

MAGNETIC, CHEMICAL AND ROTATIONAL PROPERTIES
OF THE HERBIG AE/BE BINARY SYSTEM HD 72106

by

COLIN PETER FOLSOM

A thesis submitted to the
Department of Physics, Engineering Physics and Astronomy
in conformity with the requirements for
the degree of Master of Science

Queen's University
Kingston, Ontario, Canada
September 2007

Copyright © Colin Peter Folsom, 2007

Abstract

Recently, magnetic fields have been detected in a handful of pre-main sequence Herbig Ae and Be (HAeBe) stars. This hints at an evolutionary connection between magnetic HAeBe stars and Ap and Bp stars. Ap/Bp stars are magnetic chemically peculiar main sequence stars, whose origins remain poorly understood.

In this context the HD 72106 system, a very young double star, is particularly interesting. HD 72106 consists of an intermediate mass primary with a strong magnetic field and an apparently non-magnetic Herbig Ae secondary. In this work we examine 20 high-resolution spectropolarimetric observations of HD 72106A and B, obtained with the ESPaDOnS instrument at the Canada-France-Hawaii Telescope. We find that the HD 72106 system is a true binary, based on the components' positions in space, locations on the H-R diagram, and dynamical properties. For the primary we determine an effective temperature $T_{\text{eff}} = 11000 \pm 1000$ K and a mass of $2.4 \pm 0.4 M_{\odot}$; while for the secondary we find $T_{\text{eff}} = 8750 \pm 500$ K and $M = 1.9 \pm 0.2 M_{\odot}$.

Through detailed spectral modeling, strong chemical peculiarities characteristic of Ap/Bp stars are found in the primary. Abundances of 10 times the solar value are found for Fe, Si and Ti, with Cr 100 times solar and Nd ~ 1000 times solar. Helium is found to display less than 1/10 the solar abundance. By contrast, detailed spectrum modeling of the secondary shows that it possesses approximately solar abundances.

The rotation period and magnetic field geometry of the primary are investigated in detail. A remarkably short rotation period of 0.63995 ± 0.00014 days is derived. A dipole magnetic field geometry is found, with $B_p = 1300 \pm 100$ G, $\beta = 60 \pm 5^\circ$, and $i = 23 \pm 11^\circ$. Doppler Imaging of the surface distribution of Si, Ti, Cr, and Fe is performed for the primary, and strong inhomogeneities are found. All four maps present similar abundance patterns, with a large spot near the positive magnetic pole.

Implications of these results, particularly with respect to the stage of evolution at which chemical peculiarities arise, are discussed.

Co-Authorship

The Doppler Imaging results for HD 72106A presented in this thesis were derived in collaboration with Dr. O. Kochukhov. This technique is discussed in Section 3.7, and the results are presented in Section 4.4. The spectral lines used for Doppler Imaging were identified and prepared for use by the author of this thesis, as were the Least Squares Deconvolution profiles used in the later part of the analysis. The fundamental properties of the star and the initial model parameters were also determined by the author. The execution of the Doppler Imaging code was performed by Dr. Kochukhov. Discussions with Dr. Kochukhov were critical for the interpretation of the Doppler Imaging presented here. Additionally, Dr. Kochukhov provided useful input regarding the rotation period of HD 72106A, with respect to the physicality of several different possible phasings of LSD profiles.

Acknowledgments

Firstly I would like to thank my supervisors Gregg Wade and Dave Hanes, whose knowledge, assistance and encouragement have been absolutely essential for this thesis. I would also like to thank them for their relaxed attitude towards my ‘mornings’, which has been essential for my continued mental health.

I am greatly indebted to James Silvester, Jenny Power, and Jason Grunhut. Their assistance, support and comradery has been indispensable, and this thesis could not have been completed without them.

A huge thank you goes to my family for their unflagging support and encouragement, as well as for the occasional free lunch.

I am very grateful to Oleg Kochukhov for his aid with the Doppler imaging of HD 72106A, and for fruitful discussions regarding the rotation period of that star.

Thanks are in order for observations of HD 72106A and B obtained by Evelyne Alecian, Claude Catala, Jason Grunhut, James Silvester, and Gregg Wade.

Finally I would like to thank the Queen’s Astro grads, Jennifer Shore, Shannon Nudds, Kathryn Bale, and Dominic Drouin for helping to keep the sanity.

Table of Contents

Abstract	i
Co-Authorship	iii
Acknowledgments	iv
Table of Contents	v
List of Tables	viii
List of Figures	ix
Chapter 1: Introduction	1
1.1 The Diversity of Stars	1
1.2 Diffusion	13
1.3 Magnetism in Intermediate Mass Stars	17
1.4 Herbig Ae and Be stars	19
1.5 HD 72106	27
Chapter 2: Observations	33
2.1 Observing Stellar Magnetic Fields	33
2.2 Instrumentation	38

2.3	Observations	45
2.4	Reductions	50
Chapter 3:	Analysis	67
3.1	Basic Physical Parameters	67
3.2	Binarity	76
3.3	Spectrum Synthesis and Fitting	81
3.4	Least Squares Deconvolution	89
3.5	Magnetic Field Analysis	94
3.6	Period Determination	101
3.7	Doppler Imaging	106
Chapter 4:	Results	113
4.1	Surface Chemical Abundances	113
4.2	Rotation Period of the Primary	127
4.3	Magnetic Field	134
4.4	Surface Abundance Geometry	138
Chapter 5:	Summary, Discussion and Conclusions	147
5.1	Summary of Results	147
5.2	Discussion and Conclusions	150
References	159
Appendix A:	CFHT Observing Proposal	171
Appendix B:	Computer Programs Written	179

B.1	Continuum Normalization: norm.f	179
B.2	Period Searching with Stokes I and V LSD	
	Profiles: pbp.f	187
B.3	Spectrum Fitting Through χ^2 Minimization: lma.f	197

List of Tables

1.1	Basic physical properties of main sequence stars of various spectral types.	3
2.1	Log of observations of the HD 72106 system obtained with ESPaDO nS.	47
3.1	Fundamental physical parameters for HD 72106A and B.	81
3.2	Mean longitudinal field measurements for each observation of HD 72106A and B.	96
4.1	Chemical abundances for HD 72106A in each independently fit segment of spectrum.	116
4.2	Averaged best fit chemical abundances, $v \sin i$ and microturbulence for HD 72106A and B as well as solar abundances.	118
4.3	Chemical abundances for HD 72106B in each independently fit segment of spectrum.	122

List of Figures

1.1	Sample H-R diagram illustrating main sequence stars as well as white dwarfs, giants and supergiants.	2
1.2	Typical chemical abundances of an Ap star (HD 162576) and a ‘normal’ A star (HD 162817).	8
1.3	Variability of the longitudinal magnetic field, He line intensity and u -band magnitude in the star HD 184927, from Wade et al. (1997)	10
1.4	Pre-main sequence evolutionary tracks from Palla & Stahler (1993) for a range of masses.	25
2.1	Schematic diagram of the combinations of polarization states used to calculate the Stokes parameters.	34
2.2	Illustration of the ‘normal’ Zeeman effect.	36
2.3	An observation of line splitting in HD 94660 due to the Zeeman effect.	39
2.4	Schematic of the polarization analysing optics in ESPaDOnS.	43
2.5	Schematic of the ESPaDOnS spectrograph.	45
2.6	Sample flat field and thorium argon calibration frames.	48
2.7	Unnormalized, with a polynomial fit, and normalized spectra.	55
2.8	Sample $H\beta$ and metallic lines in observations of HD 72106B on its own illustrating the stability of the spectrum.	59

2.9	Sample $H\beta$ and metallic lines in observations of HD 72106A on its own illustrating the stability of the spectrum.	60
2.10	Sample reconstructed spectra of the secondary, in a stable region of the primary's spectrum.	61
2.11	Variable metallic lines in observations of HD 72106A on its own. . . .	63
2.12	Comparison of a spectrum of the primary, combined light from both components and a reconstructed primary spectrum.	65
2.13	Reconstructed spectra of HD 72106A at different phases, illustrating variability as well as the accuracy of the reconstruction technique. . .	66
3.1	Sample Balmer line fits of $H\gamma$ for HD 72106A & B.	70
3.2	Sample best fit spectra for HD 72106B at both $T_{\text{eff}} = 8000$ K, $\log g = 4.5$ and $T_{\text{eff}} = 8750$ K, $\log g = 4.0$	71
3.3	H-R diagram containing HD 72106A and B along with pre-main sequence evolutionary tracks and isochrones.	75
3.4	An illustration of orbital geometries discussed in Section 3.2.	78
3.5	Sample best fit synthetic spectra for HD 72106A.	87
3.6	Sample best fit synthetic spectra for HD 72106B.	88
3.7	Sample LSD profiles for HD 72106A & B in both Stokes I and V. . . .	93
3.8	Sample χ^2 map in B_p and β for θ^1 Ori C, adapted from Wade et al. (2006a).	99
3.9	Periodogram for HD 72106A based on longitudinal field measurements, created using a first-order sinusoid.	103
3.10	Periodograms for HD 72106A based on the LSD Stokes I and V profile variations.	107

3.11	Illustration of the rotational Doppler shift for Doppler Imaging	108
4.1	Additional best fit spectra for HD 72106A in two windows.	117
4.2	Abundances relative to solar for HD 72106A and B, averaged over all spectral windows modeled.	119
4.3	Additional best fit spectra for HD 72106B in two windows.	123
4.4	Emission and variability in the H α Balmer line of HD 72106B.	124
4.5	Emission and variability in the OI 7773 Å triplet of HD 72106B. . .	125
4.6	Longitudinal magnetic field measurements of HD 72106A, phased with the adopted 0.63995 day period, and the best fit sinusoid.	128
4.7	Phased LSD profiles for HD 72106A with the 0.63995 day best fit period.	130
4.8	Phased LSD profiles for HD 72106A with the inferior 1.7859 day period.	131
4.9	Phased LSD profiles for HD 72106A with the inferior 1.6921 day period.	132
4.10	Phased LSD profiles for HD 72106A with the inferior 0.38983 day pe- riod.	133
4.11	Maps of reduced χ^2 for a range of dipole field models at different in- clination angles.	136
4.12	Synthetic Stokes V LSD profiles for the best fit magnetic field geometry compared with the observed profiles.	137
4.13	Doppler mapping reconstruction of Si for HD 72106A from original lines.	139
4.14	Line fits for individual Si lines used in Doppler mapping of HD 72106A.	140
4.15	Doppler mapping reconstructions of Si, Ti, Cr, and Fe for HD 72106A from LSD profiles.	145

4.16 LSD line profile fits from Doppler Imaging of Si, Ti, Cr, and Fe for HD 72106A.	146
---	-----

Chapter 1

Introduction

1.1 The Diversity of Stars

Stars exhibit a tremendous range of evolutionary and physical properties. They run from pre-main sequence stars that are still forming and have only just become visible to optical telescopes, to white dwarfs and neutron stars that are truly ancient, even by astronomical standards. Stellar masses can range from a tenth of the mass of the Sun to 100 times the Sun's mass (M_{\odot}). Radii of stars can approach 1000 times the Sun's radius (R_{\odot}) in the case of supergiants, and dwindle to the scale of 10 kilometers in the case of ultra-dense neutron stars. Many of these objects are exotic, rare, and short lived. A casual examination of the variety of known stars suggests a bewildering, and potentially incomprehensible, diversity. However, if one restricts oneself to main sequence stars, a somewhat clearer picture emerges. Main sequence stars are stars in their 'prime'; objects which are long lived, in hydrostatic equilibrium and which derive their energy from fusion of hydrogen into helium deep in their cores. These stable stars at first glance seem like the simplest objects to investigate. However,

upon closer inspection a number of complications arise.

The main sequence is defined by stars that differ primarily in age and mass. These stars occupy a diagonal strip along the Hertzsprung Russell (H-R) diagram, a plot of stellar surface luminosity versus temperature (see Figure 1.1). Differences in age and mass translate into differences in luminosity and temperature, thus defining a continuum of stars. The H-R diagram can be a very useful tool for examining large scale stellar properties. In particular, if one can create accurate models of the large scale properties of stars, one can compare a star's position on the H-R diagram with the points generated by models. Thus one can say something about a star's mass and evolutionary state based on its observed surface temperature and luminosity.

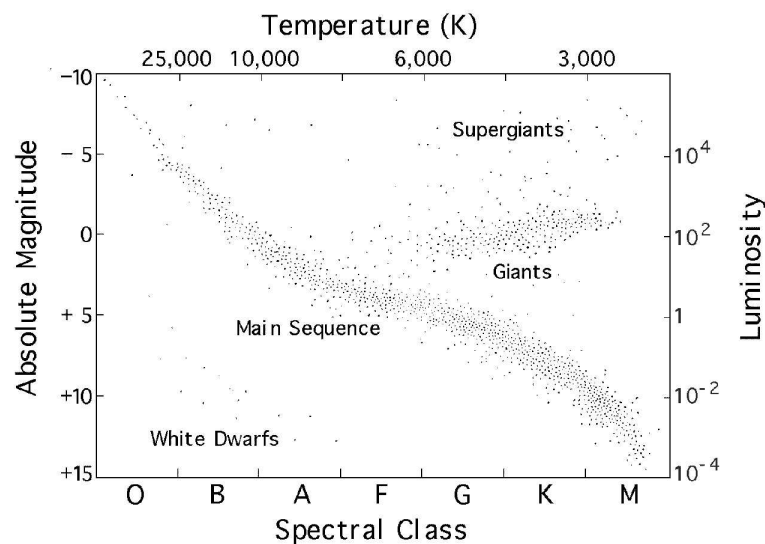


Figure 1.1: A typical H-R diagram illustrating main sequence stars, as well as white dwarfs, giants and supergiants. Luminosity is in units of solar luminosities. Image: M. Fanelli, Texas Christian University, <http://personal.tcu.edu/~mfanelli/>

Stars of different temperatures (and masses) are broadly grouped into different spectral classes, according to the characteristics of their spectra. These classes are

Spectral Type	T_{eff} (K)	Log L/L_{\odot}	Mass (M_{\odot})	Radius (R_{\odot})
O	30,000 - 60,000	6.14	60	15
B	10,000 - 30,000	4.30	18	7
A	7,500 - 10,000	1.90	3.1	2.1
F	6,000 - 7,500	0.77	1.7	1.3
G	5,000 - 6,000	0.07	1.1	1.1
K	3,500 - 5,000	-0.39	0.8	0.9
M	2,000 - 3,500	-1.39	0.3	0.4

Table 1.1: Basic physical properties of main sequence stars of various spectral types. Logarithmic luminosity, mass and radius are given in solar units, and represent upper bounds for the spectral class (adapted from Ostlie & Carroll, 1996).

labeled, from hottest to coolest, by the letters O, B, A, F, G, K, and M. Historically these classifications were based on the strengths of the Balmer absorption lines, Helium absorption lines, and a few other metallic lines. Recent discoveries of very cool brown dwarfs have led to the addition of, arguably non-canonical, classes L and T (Kirkpatrick, 2005). Sub-classes numbered 1 through 9, decreasing with temperature, are also defined. For example, our Sun is a main sequence star, with a G2 spectral type (Ostlie & Carroll, 1996). Hotter stars are often referred to as ‘early type’ stars, while cooler stars are referred to as ‘late type’. A brief overview of the physical properties of different stellar spectral types is provided in Table 1.1.

Stars are also broadly classified according to their luminosity, based on the widths of pressure broadened spectral lines. These luminosity classes are defined by Roman numerals ranging from I at the most luminous to V at the least. Main sequence stars are of luminosity class V; giants are class III, and super giants are class I (Ostlie & Carroll, 1996).

Observations of stars are obtained, almost exclusively, of the star’s *photosphere*. The photosphere is the name given to the outer layers of a star, which provide the

transition from the dense stellar interior to the vacuum of space. The photosphere is the region of the star in which the opacity becomes sufficiently low for photons to escape and eventually reach our telescopes. Thus, this is the region probed by photometric and spectroscopic measurements, and the region in which observable spectral lines are formed.

Two important definitions to provide before further discussion of stellar astrophysics are effective temperature (T_{eff}) and surface gravity ($\log g$). Effective temperature is the temperature a star would have, given its total luminosity integrated over all wavelengths, if it were a perfect spherical black body. That is:

$$L = 4\pi R^2 \sigma T_{\text{eff}}^2, \quad (1.1)$$

where L is the stars' luminosity, R is the stellar radius and σ is the Stefan-Boltzmann constant (Ostlie & Carroll, 1996). This is, of course, just the Stefan-Boltzmann equation for a uniform spherical emitter. The surface gravity, g , is simply the acceleration due to gravity at the surface of the star. In logarithmic units it is given by:

$$\log g = \log GM - 2 \log R, \quad (1.2)$$

where M is the mass of the star and G is the gravitational constant.

While this presents an apparently straightforward view of main sequence stars, the devil is in the details. A variety of physical processes can significantly modify the observable properties of stars, as well as stellar structure and evolution. Many of these properties are not included, or are included only approximately, in current stellar models. For example, in the case of massive O stars, mass loss due to strong stellar winds can complicate the picture (Massey, 2003), particularly when coupled with magnetic fields (Donati et al., 2002). In the case of very cool stars, departures

from local thermodynamic equilibrium (Asplund, 2005) and molecular bands in stellar spectra (e.g. Cushing et al., 2005) are poorly understood. Even in the case of our Sun, the internal rotation structure and details of how the solar magnetohydrodynamic dynamo generates the observed magnetic field are not clear (Thompson et al., 2003). These particular problems are minimized for main sequence A and B stars, the focus of this thesis. However, a number of interacting effects of comparable magnitude, such as atomic diffusion and magnetic fields discussed below, lead to other complications in these stars.

1.1.1 Main Sequence A and B Stars

Main sequence A and B stars are stars in the temperature range 7500 K to 30000 K (see Table 1.1). They have masses from about $1.6M_{\odot}$ to $17M_{\odot}$ and, as such, are often referred to as intermediate mass stars. The structure of these stars consists qualitatively of a convective core (which increases in volume with increasing stellar mass) with a larger overlying radiative envelope. That is to say, in the radiative envelope the star is stable against strong convection, and energy is transported primarily via radiation. In the case of cooler A-type stars, energetically weak convection can occur (Vauclair & Vauclair, 1982; Landstreet, 1998). The photospheres of A and B stars are generally in local thermodynamic equilibrium (LTE)¹. Optical spectra of these stars display very strong Balmer absorption lines, with a wide variety of metallic² absorption lines. In the large majority of A and B stars, line emission is not observed, nor

¹Local thermodynamic equilibrium is defined by a negligible temperature change over the mean free path of a photon. In general, LTE models of A and B stars reproduce detailed observations of these stars very reliably. However, some exceptions exist, for example emission lines in spectra of Herbig Ae/Be stars.

²In the astronomical community the terms ‘metals’ or ‘metallic’ refer to elements heavier than He.

is there any evidence for magnetic fields or magnetic activity (Borra et al., 1982).

1.1.2 Chemically Peculiar A and B Stars

In the early days of stellar spectroscopy it was noticed that a small number of A and B stars displayed anomalous metal line strengths in their spectra. Antonia Maury is credited with the discovery of these stars in 1897 (Maury & Pickering, 1897). She encountered them as part of a larger classification effort, and flagged them as ‘peculiar’. This historical designation has been retained in the modern label ‘chemically peculiar stars’.

Chemically peculiar stars display abundances of some elements that depart substantially from the abundances seen in the Sun, and in other main sequence stars of similar type. These abundance anomalies vary from element to element, and some elements may have nearly solar abundances. These abundance anomalies are not a result of nucleosynthetic processes in the star, or an anomalous chemical mixture of the material from which they have formed (Michaud, 1970; Landstreet, 1992). In fact, it is not uncommon to find chemically peculiar stars closely associated with ‘normal’ A and B stars in binary systems or open clusters (e.g. Silvester, 2007), where they must have shared a very similar formation and evolution. Rather, peculiarities are widely believed to be a superficial effect, resulting from chemical fractionation within the outer layers of a star. In a sufficiently stable stellar atmosphere, the competing effects of radiation pressure and gravity allow for the diffusion of elements into regions of over- or under-abundance (Michaud, 1970), producing the observed abundance anomalies.

Ap and Bp stars

Overall, chemically peculiar stars make up only about 10% of main-sequence A and B stars (Hoffleit & Jaschek, 1991). These stars can be organized into various groups based on the types of chemical peculiarity observed. The Ap and Bp star group is one of the more interesting. These stars are uniquely characterized by strong globally-ordered magnetic fields, which can usually be well approximated by a low order multipole (e.g. a dipole). Magnetic fields in Ap and Bp stars were first observed by Babcock (1947). The field strengths at the surface of the star range from several hundred gauss (Aurière et al., 2007) to greater than 10 kilogauss (Bagnulo et al., 2003, 2004). These properties stand in remarkable contrast to the magnetic fields observed in the sun and other low-mass stars. In these low-mass stars local spots with strong magnetic fields, on the order of kilogauss, are seen, but the global average magnetic field is near zero (e.g. Thompson et al., 2003). Over-abundances³ of iron peak elements, by up to 100 times the respective solar abundance, are sometimes seen in Ap and Bp stars. Over-abundances of silicon ranging above 10 times the solar abundance, and some rare earth elements, sometimes (apparently) exceeding 1000 times the solar abundance, are also seen in these stars (e.g. Folsom et al., 2007). Under-abundances of some light elements, particularly He, are often observed. Chemical abundances of a typical Ap star and a typical A star are compared in Figure 1.2. In addition to chemical abundance anomalies, Ap and Bp (often abbreviated to Ap/Bp, or simply Ap) stars display inhomogeneities in chemical abundance across the surface of the star, essentially large-scale chemical star spots (Rice et al., 1989; Hatzes et al., 1989).

All of these properties of Ap/Bp stars are stable over long periods of time; to

³Over-abundances and under-abundances are always in reference to solar abundances in this thesis.

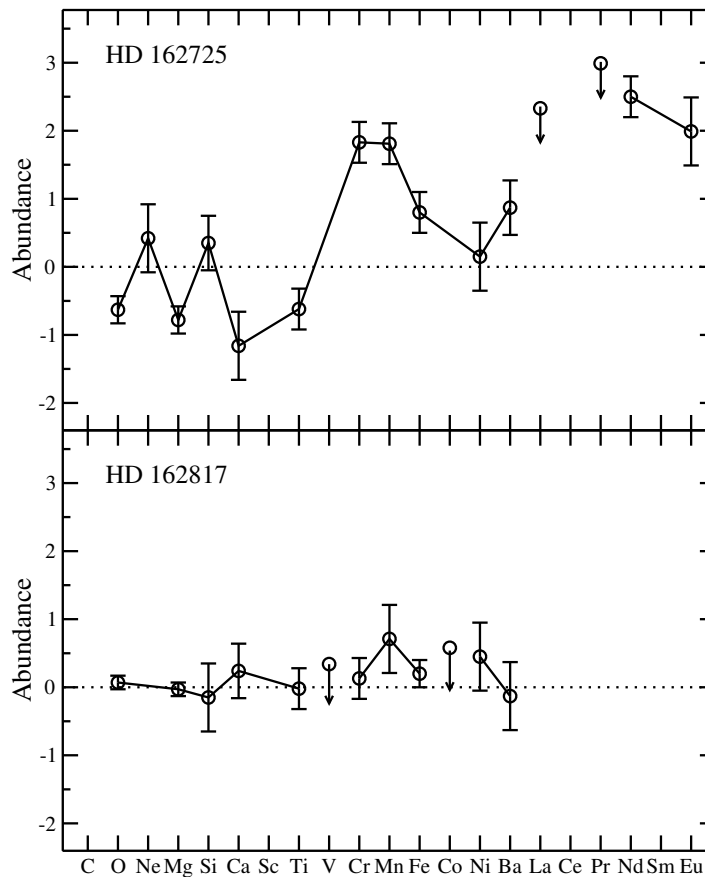


Figure 1.2: Typical chemical abundances of an Ap star, HD 162576, and a ‘normal’ A star, HD 162817, both in the open cluster NGC 6475 (from Folsom et al., 2007). Abundances are presented in logarithmic units relative to solar abundances. Downward arrows represent upper limits and the dashed line represents solar abundance values. In the peculiar star HD 162725 (the top frame) strong over-abundances of Cr, Mn, Fe, and some rare earth elements are inferred. O and Mg appear to be under-abundant in this star. In contrast, in HD 162817 these abundances are all approximately solar.

date no observations have indicated any evolution of the magnetic field, chemical abundances or surface inhomogeneities of individual stars. Periodic variability is commonly observed, particularly in photometric brightness, the observed longitudinal (line-of-sight) magnetic field, and absorption line shapes. This is due to modulation caused by the rotation of the star rather than any true variation in the underlying properties. These periodic variations are generally described as an ‘oblique rotator’ (Stibbs, 1950). In this scenario, a property, for example magnetic field, is distributed non-uniformly over the entire stellar surface. As the star rotates, different parts of the star become visible. Hence, different disk-averaged properties are observed. Such variations can extend even to photometric variability of the star. If an over-abundant spot of an element that contains many absorption lines rotates into view, the total amount of light emitted by the star in a particular wave band can decrease due to ‘line blanketing’ (e.g. Wade et al., 1997; Ryabchikova, et al., 1997). Figure 1.3 illustrates variability in several properties of the Bp star HD 184927 as the star rotates, due to non-uniform magnetic and chemical surface distributions.

Ap stars are loosely classified into several subtypes, based on some of their stronger spectral peculiarities. Most commonly, a distinction is made between SrCrEu stars and Si stars. SrCrEu stars are cooler (6500-10000 K), generally A-type and early F-type stars, while Si stars are hotter (10000-15000 K), late to mid-B-type stars. One particularly interesting subgroup is the rapidly oscillating Ap stars (roAp stars). These stars pulsate non-radially with periods on the order of minutes (Kurtz, 1990), and the excitation mechanism is still poorly understood (Kochukhov et al., 2007a).

One additional oddity seen in magnetic Ap/Bp stars is that as a group, they rotate much more slowly than normal A and B stars. Generally they have rotation

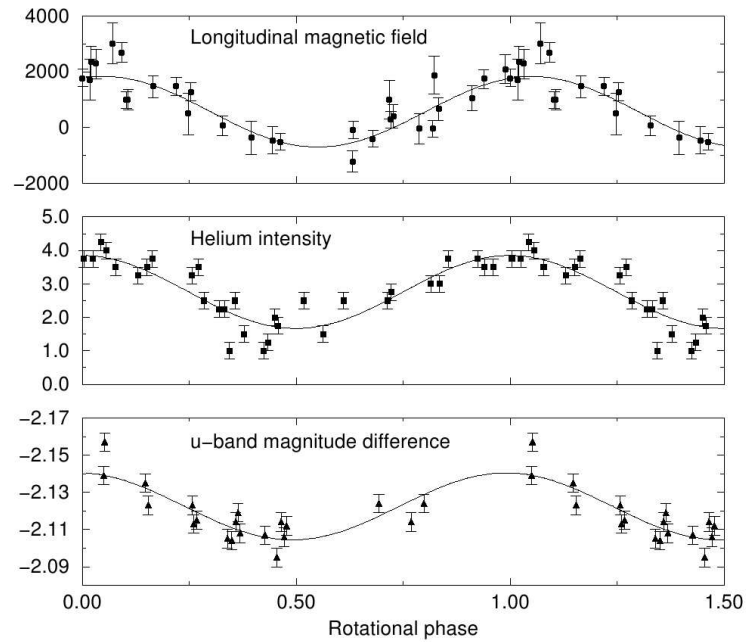


Figure 1.3: Variability in longitudinal magnetic field (in gauss), He line intensity (in arbitrary units, 1 = normal line strength, 5 = very strong) and u -band magnitude versus phase of rotation in the Bp star HD 184927, from Wade et al. (1997). This provides an illustration of the observed properties of an oblique rotator, with an inhomogeneous surface chemical abundance distribution and magnetic field.

velocities, projected along the line of sight, ($v \sin i$) of around 60 km s^{-1} or less, whereas ‘normal’ A and B stars usually have $v \sin i$ above 120 km s^{-1} (Abt & Morrell, 1995). Directly measured rotation periods of Ap/Bp stars generally are between 1 to 10 days (Power, 2007). Some Ap stars are sufficiently slowly rotating that they exhibit no measurable rotational broadening of their spectral lines, even in extremely high resolution ($R \sim 120000$) spectra. These objects often have poorly constrained, but very long (sometimes on the order of decades), rotation periods (Stępień & Landstreet, 2002; Power, 2007).

A number of enduring questions exist about Ap/Bp stars, particularly regarding the origin of the magnetic field and the detailed physical processes that produce and maintain the chemical peculiarities. These will be addressed somewhat further in Sections 1.2 and 1.3.

Other Chemically Peculiar Stars

A number of other classes of chemically peculiar stars exist. The He weak stars (sometimes called He weak SiSrTi stars), essentially a continuation of the Bp Si stars to higher T_{eff} and M , show strong under-abundances of He. These stars display over-abundances of a number of iron peak elements as well as silicon, and possess magnetic fields. He weak stars are of intermediate B-type, in the T_{eff} range 12000-19000 K (Cidale et al., 2007).

The group of He strong stars also display magnetic fields and abundance anomalies, most prominently an overabundance of He. These stars appear to be an extension of the He weak group, with temperatures in the 19000-25000 K range (Cidale et al., 2007).

There also exist a number of non-magnetic classes of chemically peculiar stars. In the cooler range, there are the Am stars. These so called metallic-line stars display over-abundances of heavier elements, particularly rare earths, and under-abundances of lighter elements. They rotate slowly (Abt & Morrell, 1995) and inhabit the 7000-10000 K temperature range (Kurtz & Martinez, 2000).

In approximately the same temperature range there exists the rare class of λ Boötis stars. These are non-magnetic stars (Bohlender & Landstreet, 1990) that display solar abundances of lighter elements, but under-abundances of iron peak elements. Non-radial pulsations have been observed in these objects (Bohlender et al., 1999).

Mercury-manganese (HgMn) stars, as the name suggests, display over-abundances of Hg and Mn, and are another class of non-magnetic chemically peculiar star (e.g. Shorlin et al., 2002). They have temperatures in the 10000-15000 K range (Kurtz & Martinez, 2000). These stars have become a subject of great interest in the last few years as they are the only non-magnetic class of star known to display chemical abundance star spots on their surfaces (Adelman et al., 2002; Wade et al., 2006b). Additionally, recent observations suggest these spots change on timescales of years (Kochukhov et al., 2007b), which is truly surprising.

The non-magnetic stars known as He weak PGa stars are characterized by over-abundances of phosphorus and gallium and under-abundances of helium. These non-magnetic objects are essentially higher temperature analogs of HgMn stars, with temperatures in the 13000-18000 K range (Kurtz & Martinez, 2000).

1.2 Diffusion

The wide range of chemical peculiarities seen in A and B stars are attributed to the effects of atomic diffusion, as described in the seminal paper by Michaud (1970). Diffusion occurs under the competing effects of gravity and radiation pressure. Under gravity alone, elements heavier than H would tend to sink in a stable star. However, the slightly anisotropic radiation field in the star provides a net outward radiative force that can potentially counter gravity, raising atoms up in the stellar atmosphere. A levitated atom of a particular species will tend to rise in the atmosphere until combined changes in the radiation field, atomic excitation and atomic ionization balance the effect of gravity, yielding a net acceleration which is null. The element will tend to accumulate in that region producing a local over-abundant layer. Thus atoms of various elements become concentrated in layers at different heights in the atmosphere, depending on the particular atomic properties of the element and physical properties of the star. When the star is examined spectroscopically, these layers are observed as general over-abundances or under-abundances if they occur in the photosphere. If an over-abundant layer of an element is located near the surface of a star, in the region in which the stellar spectrum is formed (the photosphere), then more light is absorbed by that element, and the corresponding absorption lines are seen to be stronger, and hence an over-abundance is deduced. Conversely, if a layer of local under-abundance of an element is near the surface of the star (e.g. if the net force on the element is negative and the element sinks in the photosphere), then the absorption lines formed are weaker, and hence an under-abundance is deduced.

For an atom to experience radiation pressure it must absorb photons, either through bound-bound or through bound-free transitions. Following Michaud (1970),

bound-free transitions can only occur frequently for atoms with an ionization potential less than 13.6 eV. This is the ionization potential of hydrogen, and photons above this energy are almost all absorbed by neutral H. Hence there is not enough flux above this energy to levitate atoms. Atoms with an ionization potential less than 10 eV will not acquire enough momentum from the radiation field to counter gravity, and will sink into the star⁴. Thus only atoms (or ions) with ionization potentials in the 10–13.6 eV range can be pushed up in the stellar atmosphere by bound-free radiation pressure. Species with ionization potentials in this range include C I, Ca II, Sr II, and most (singly ionized) rare earth elements. Atoms outside of this range may still absorb enough radiation in bound-bound transitions to counter gravity. Species with many absorption lines, particularly rare earth elements and some iron peak elements, can form layers of substantial over-abundance through this mechanism.

Michaud (1970) showed that this vertical diffusion process can take place on the order of 10^4 years, much shorter than the lifetime of a star. Thus, the time scale for the development of abundance anomalies by diffusion is compatible with the presence of peculiarities in the youngest intermediate mass main sequence stars, with ages of order $\sim 10^6$ years.

A critical criterion for atomic diffusion is the stability of the stellar atmosphere. Turbulence can easily overwhelm atomic diffusion, providing a homogeneous atmosphere. Turbulence tends to move material about in the stellar atmosphere, homogenizing it. Thus, for diffusion to play an important role, turbulent velocities in a star must be less than the relatively small diffusion velocities. Michaud (1970) found diffusion velocities on the order of 10^{-3} cm sec⁻¹. Intermediate mass A and B-type

⁴These models assume an A or B type stellar atmosphere, specifically $T_{\text{eff}} = 12600$ K and $\log g = 4.0$. Michaud (1970) examined a range of temperatures from 8000 K to 20000 K and found largely the same trends in all models.

stars possess radiative atmospheres, which have little turbulence and virtually no convection, allowing diffusion to potentially build up large chemical peculiarities. Lower mass stars, such as our Sun, have deep convective atmospheres. Although diffusion may occur in these lower mass stars, the deep mixing of their atmospheres homogenizes any resultant peculiarities to undetectable levels. This provides an explanation for why chemical peculiarities are not seen in these cooler classes of stars. O and early B-type stars possess large convective cores which can approach the surface of the star which, combined with the overshoot of convective cells into the radiative envelope, can disrupt the atmosphere of the star. More importantly, O and early B-type stars display significant mass loss via high-velocity stellar winds, which can lead to mixing in the stellar atmosphere, preventing the build up of chemical peculiarities (Vauclair & Vauclair, 1982).

Mixing due to rotation can also compete with diffusion. Rotation produces meridional circulation, which can vertically mix a star's atmosphere. In the case of a normal A or B star with an equatorial rotation velocity of $\sim 100 \text{ km s}^{-1}$, meridional circulation can produce velocities more than sufficient to disrupt diffusion (Michaud, 1982). However, for more slowly rotating stars (and in particular virtually all chemically peculiar stars), meridional circulation usually produces velocities less than the diffusion velocity, allowing chemical stratification to occur. This typically requires an equatorial velocity of less than 90 km s^{-1} (Michaud, 1982).

In the case of magnetic chemically peculiar stars, the magnetic field can play several important roles in the production and maintenance of chemical abundance structures. The field can help to stabilize the atmosphere of the star (Michaud, 1970), in particular by suppressing horizontal mixing. The magnetic field can also

strongly constrain atoms to follow the field lines (Michaud et al., 1981; Alecian & Stift, 2006). This may provide a mechanism for the development of surface abundance inhomogeneities, either by direct magnetohydrodynamic modification of the diffusion velocity, or by influencing other phenomena, such as a weak stellar wind. Additionally, the Zeeman splitting of atomic lines in the presence of a magnetic field can increase the opacity of some species, and hence increase the radiation pressure they experience (Alecian & Stift, 2002, 2006). This can further increase the efficiency of diffusion for some elements.

In the presence of a weak stellar wind, elements that might otherwise accumulate at the surface of a star can be ejected from the star entirely. This can cause a selective depletion of some elements (Babel, 1992). On the other hand, such a wind might drag some elements towards the surface of the star, depositing them there if they do not experience sufficient force to be ejected. Additionally, the presence of a magnetic field can affect the wind geometry, and hence modify the wind's effects.

As this overview suggests, atomic diffusion in intermediate mass stars is a rather complex mechanism, involving a large variety of competing processes. The details of these processes are generally understood only approximately (Alecian & Stift, 2006). Diffusion has a wide range of impacts on the observed properties and physical structure of stellar photospheres, and is critical to the understanding of chemically peculiar stars. Consequently, understanding the observable results of diffusion provides valuable information about poorly understood stellar physics, including rotational mixing, convection, stellar winds, and magnetic fields.

1.3 Magnetism in Intermediate Mass Stars

The first direct observation of a magnetic field in a star (besides the Sun) was obtained by Babcock (1947). In this study he used the longitudinal Zeeman effect to detect a magnetic field in the Ap star 78 Vir.

The study of stellar magnetism relies heavily on the use of astrophysical spectropolarimetry. A spectropolarimeter is essentially the combination of a spectrograph and a polarimeter. The polarimeter analyses light and splits it into the desired polarization states, then the analyzed light is dispersed and recorded by the spectrograph. In the Zeeman effect, one atomic absorption (or emission) line is split into multiple components in the presence of a magnetic field, with the spacing between the components being linearly proportional to the strength of the field. Additionally, different components of the split line have different polarization properties. The Zeeman effect is discussed further in Section 2.1.2. In a line profile broadened by the Doppler effect due to stellar rotation, the polarization properties of the Zeeman effect are much easier to observe than the wavelength splitting of the line in unpolarized light. Thus, with a spectropolarimeter, one can observe the Zeeman effect in the absorption lines of a star with high precision, and hence determine the properties of the stellar magnetic field.

Although observations of magnetic fields in Ap/Bp stars are now obtained routinely, the source of these magnetic fields remains a mystery. There are currently two broad classes of theories for the origin of the observed magnetic fields. The *fossil field theory* suggests that the observed magnetic field is a remnant from an earlier stage of stellar evolution, possibly dating back to the original gas cloud from which the star formed, that has since become ‘frozen’ into the star. Current models suggest

that fossil magnetic field configurations, which are stable over the lifetime of a star, do exist (Braithwaite & Nordlund, 2006). However, it is not clear if a magnetic field from the interstellar medium could survive the possibly violent evolution along the Hayashi track to the main sequence (mixing could cause very complex magnetic field geometries, which would be unobservable and decay quickly), or if a temporary dynamo could possibly generate an appropriate field during pre-main sequence evolution (Moss, 2003).

The *contemporaneous dynamo theory*, currently less favored than the fossil field theory, suggests that the magnetic field is generated contemporaneously by a dynamo, probably deep in the star's convective core. The field then must diffuse through the large radiative envelope to emerge at the surface of the star to become visible. It is not clear if such a dynamo generated field could produce the roughly dipolar, misaligned surface field geometries seen, or if the magnetic field could rise to the surface in a sufficiently short time to produce fields in the youngest observed magnetic stars (Moss, 2001; Charbonneau & MacGregor, 2001). Additionally, there is a lack of any significant correlation between field strength and rotation rate (Kochukhov & Bagnulo, 2006; Landstreet et al., 2007), unlike the strong correlation observed in solar-type dynamos. The ability of very slow rotating stars to possess (often very strong) magnetic fields, and the lack of a rotation period-field strength relation, casts further doubt on contemporaneous dynamo models.

In this context, the study of magnetic fields in intermediate mass pre-main sequence stars becomes particularly interesting. These stars can provide strong constraints on the origin of the observed magnetic fields in Ap/Bp stars. The presence of strong, globally-ordered magnetic fields in pre-main sequence stars is almost certainly

necessary for the fossil field hypothesis to be true. On the other hand, detections of magnetic fields in pre-main sequence stars place strong constraints on contemporaneous dynamo models. In particular, such detections require that the magnetic field diffuses through the stellar atmosphere on a time-scale shorter than the pre-main sequence lifetime of the star, quite a bit faster than the constraints obtained from the main-sequence. Additionally, such observations require that a dynamo, if it exists, ‘turns on’ early in the star’s evolution, and then persists through the pre-main sequence and the main sequence. Conversely, it may be possible to observe a pre-main sequence dynamo that ‘turns off’, leaving behind a fossil field. Furthermore, the internal structure of pre-main sequence differs significantly from that of main sequence stars, and hence these young stars can show how stellar magnetic fields behave in different conditions. Consequently, a detailed understanding of magnetic fields in intermediate mass pre-main sequence stars is of great importance. This provides one of the major motivations for the study of the HD 72106 system.

1.4 Herbig Ae and Be stars

Herbig Ae and Be stars (abbreviated as HAeBe stars) are pre-main sequence stars of intermediate mass and spectral types A and B. These objects were first identified as a stellar class by Herbig (1960). HAeBe stars evolve into A and B stars when they reach the main sequence. As such, they are higher mass analogs of the better known, lower mass, T Tauri stars.

Identifying HAeBe stars can be challenging, and there has been much discussion of the exact criteria for classification in the literature (e.g. Thé et al., 1994). Historically HAeBe stars have been identified as spectral type A or B stars with optical emission

lines, located in an obscured region, and associated with bright nebulosity (Herbig, 1960). These criteria have since been refined and supplemented. The most widely accepted criteria (Vieira et al., 2003) are currently:

1. Spectral type of A or earlier, with emission lines
2. Located in an obscured region
3. Fairly bright nebulosity nearby
4. Possess an anomalous extinction law
5. Display infrared excess
6. Are photometrically variable
7. Show emission in the Mg II λ 2800 Å line.

Very few HAeBe stars satisfy all of these criteria; generally classification of HAeBe stars only requires that several of these criteria be met. The primary objective of the selection criteria chosen is to distinguish between pre-main sequence HAeBe stars and main sequence or post-main sequence objects with circumstellar material (e.g. classical Be stars or AGB stars).

1.4.1 Observed Properties

The spectral energy distributions (SED) of HAeBe stars tend to display clear effects of circumstellar matter. Thermal emission by circumstellar dust can dominate the SED in the infrared, providing a large excess of flux. In the ultraviolet, circumstellar material can also sometimes dominate the SED. This is attributed to hot gas near

the surface of the star, exceeding the star's temperature (Meeus et al., 1998). This increase in temperature can be interpreted as heating due to accretion, implying an accretion rate on the order of $10^{-7} M_{\odot} \text{ year}^{-1}$ (Blondel & Tjin A Djie, 1994). It is important to note that the lack of veiling (emission or absorption from the hot boundary layer 'in front' of the star) in optical spectra indicates that the contribution from this hot gas at visible wavelengths is small for most stars (Böhm & Catala, 1993; Ghandour et al., 1994).

X-ray emission has been reported for a number of HAeBe stars (Zinnecker & Preibisch, 1994; Damiani et al., 1994). However, despite steadily improving observations, the source of these X-rays remains a mystery. The X-rays have been attributed to unresolved T Tauri companions (Stelzer et al., 2006), which emit X-rays in a fashion similar to the Sun. However, magnetically confined winds around the HAeBe star itself have also been used to explain this emission (Telleschi, 2007). Circumstantial supporting evidence for both hypotheses exists, but no consensus has been reached.

Photometric variability is observed in HAeBe stars, likely due to variations in extinction from circumstellar material (e.g. van den Ancker et al., 1998). Linear polarization (in the continuum) is also observed, attributed to scattering from a non-spherical distribution of dust (Grinin, 1994). Variations in the polarization are seen, often correlating with photometric variations (Grinin et al., 1994; Waters & Waelkens, 1998).

Infrared spectroscopy has been a subject of some interest, as it provides an avenue for examining the geometry and composition of circumstellar material around HAeBe stars. Absorption lines from a number of molecules have been observed. Species observed include: FeO, polycyclic aromatic hydrocarbons (PAHs), various amorphous

and crystalline silicates, and H₂O ice (e.g. Waters & Waelkens, 1998; Schütz et al., 2005).

Spectroscopy in the optical spectral region reveals spectra that bear similarities to those of main sequence A and B stars. These spectra mostly probe the photosphere of HAeBe stars, and are therefore similar to spectra of main sequence stars, outside of the emission lines. Moderate projected rotation velocities ($v \sin i$) in the range 60-200 km s⁻¹ are observed (Böhm & Catala, 1995). Photospheric chemical abundances are seen to be roughly solar in HAeBe stars (Dunkin et al., 1997; Acke & Waelkens, 2004). However, in some cases hints at departures from solar abundance have been observed (Beskrovnaya, et al., 1999); for example, a general depletion of elements relative to solar (Acke & Waelkens, 2004). Emission is seen in the Balmer series, particularly H α , as well as a number of other ions; commonly O I, Ca II, Si II, Mg II, and Fe II. The source of these emission lines is a subject of some debate. For example, Hamann & Persson (1992) favor a model in which emission lines are formed in the turbulent region where accreting matter meets the stellar surface, whereas Catala et al. (1999) argue that the emission lines are formed due to a chromospheric wind. The emission lines, and in some rare cases apparently absorption lines, display complex variability (Catala et al., 1999).

Recently magnetic fields have been detected in some HAeBe stars (Donati et al., 1997; Hubrig et al., 2004; Wade et al., 2005, 2007). Wade et al. (2005, 2007) argue that these fields are globally ordered and have longitudinal strengths of several hundred gauss. This is particularly interesting given the questions surrounding the origin of magnetic fields seen in Ap/Bp stars. Because HAeBe stars evolve into A and B stars, it may well be that the observed magnetic HAeBe stars evolve into magnetic

Ap/Bp stars. Supporting this hypothesis, the observed magnetic field strengths and geometries are approximately the same in magnetic HAeBe stars and Ap/Bp stars (Wade et al., 2005; Catala et al., 2007; Wade et al., 2007; Alecian et al., 2007, in preparation). Furthermore, the observed incidence of magnetic HAeBe stars in the set of all HAeBe stars is about the same as the incidence of Ap/Bp stars in all A and B stars (Wade et al., 2005, 2007). The observation of magnetic fields in HAeBe stars will have broader implications for models of HAeBe star X-ray emission based on magnetically confined winds, and for models of magnetically mediated accretion. However, further study is necessary before any conclusions can be drawn.

1.4.2 Physical Properties

The geometry of the circumstellar material around HAeBe stars, not surprisingly, remains somewhat controversial. It now appears that there is strong evidence for the presence of massive accretion disks around many HAeBe stars (Marsh et al., 1995; Eisner et al., 2004; Corder et al., 2005). These disks have radii on the order of several hundred astronomical units (AU), and masses in the range $0.005 M_{\odot}$ to $0.05 M_{\odot}$. The details of the disk geometries continue to be the subject of investigation (Eisner et al., 2004; Corder et al., 2005). Strong evidence for larger, more diffuse envelopes of gas around a number of HAeBe stars is also reported (Natta et al., 1993; van der Tak et al., 2000), adding another element to the picture.

In evolutionary terms, HAeBe stars are objects that have recently become observable in visible light and are evolving towards the main sequence. These stars form the middle ground in pre-main sequence objects; falling between the lower mass T Tauri stars and the (largely unobserved) higher mass pre-main sequence stars. They

are found in the mass range $\sim 2 M_{\odot}$ to $\sim 8 M_{\odot}$ (Palla & Stahler, 1993). Stars more massive than $8 M_{\odot}$ do not have an optically observable pre-main sequence life. These stars have already commenced hydrogen burning when their protostellar accretion phase ends and they become observable. Stars below $2 M_{\odot}$ are radiatively unstable, largely convective, and hence evolve as T Tauri stars. However, some authors include stars down to $1.5 M_{\odot}$ in their HAeBe samples (Thé et al., 1994; Vieira et al., 2003), despite such low-mass objects remaining largely convective for most of their pre-main sequence lifetime.

Two useful definitions to introduce are the ‘birth line’ and the zero-age main sequence (ZAMS). The birth line is the locus on the H-R diagram at which pre-main sequence stars first become visible. Upon reaching the birth line, the stars have completed most of their accretion and cleared enough of their neighborhood for their circumstellar material to become optically thin. The ZAMS is the locus on the H-R diagram at which a star first arrives at the main sequence. At this point the star has completed its contraction phase and begins core hydrogen burning. Theoretical pre-main sequence evolutionary tracks, as well as the birth line and the ZAMS are illustrated in Figure 1.4. Pre-main sequence lifetimes of HAeBe stars (the time necessary to evolve from the birth line to the ZAMS) range from 10^7 years for $\sim 2 M_{\odot}$ stars to around 10^5 years for $\sim 6 M_{\odot}$ stars (Palla & Stahler, 1993).

Following the pre-main sequence evolutionary model calculations from the classic paper of Palla & Stahler (1993), it is expected that stars with masses below $2.4 M_{\odot}$ cross the birth line fully convective and on the Hayashi evolutionary track⁵. Stars in the mass range $2.4 M_{\odot}$ to $3.9 M_{\odot}$ cross the birth line with a radiative

⁵The Hayashi track is line along which a protostar begins its life, and collapses with nearly constant effective temperature. Stars on the Hayashi track are fully convective, and depart from the Hayashi track when radiative energy transport becomes important.

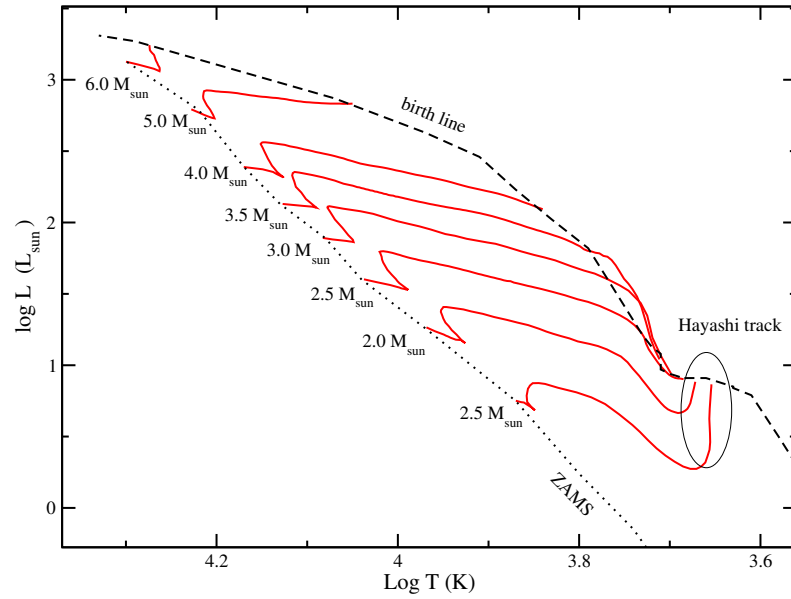


Figure 1.4: Pre-main sequence evolutionary tracks (solid lines) from Palla & Stahler (1993) along with the birth line (dashed) and the zero age main sequence (ZAMS) line (dotted) for a $10^{-5} M_{\odot} \text{ yr}^{-1}$ initial accretion rate. Evolutionary tracks have been labeled by mass, in solar masses. The Hayashi track portion of visible pre-main sequence evolution is indicated. A typical pre-main sequence star becomes optically visible at the birth line, then evolves towards the ZAMS.

core and convective outer regions, and become visible after the end of the Hayashi track evolution. Stars with masses above $3.9 M_{\odot}$ begin their pre-main sequence life fully radiative and thermally relaxed, well away from the Hayashi track. All stars then evolve towards the main sequence by undergoing a thermal readjustment, if not already thermally relaxed, and then contracting to the main sequence. The results presented here assume a $10^{-5} M_{\odot} \text{ yr}^{-1}$ initial accretion rate. In the case of larger initial accretion rates, the birth line essentially moves up, allowing for longer pre-main sequence life times, and allowing more massive stars to exist in the observable pre-main sequence phase (Palla & Stahler, 1993). The general evolutionary behavior found by Palla & Stahler (1993) is consistent with that found by other authors (e.g. Bernasconi, 1996).

There remains significant opportunity for further study of the complex physics of HAeBe stars. The current work focuses on aspects of their magnetic fields and connections to Ap/Bp stars. The role of magnetic fields in the formation of intermediate mass stars is barely understood. It is possible that magnetic fields play a role in accretion in intermediate mass stars (Muzerolle et al., 2004), but this has yet to be investigated in detail. Additionally, the role of magnetic fields in angular momentum loss for intermediate mass stars is unknown. In the case of the slow rotating Ap/Bp stars, ‘magnetic braking’ (transfer of angular momentum from the rotating star to the surrounding material via the magnetic field) seems likely, however direct observational confirmation of this has yet to be seen and the time-scale for the process is somewhat uncertain (Stepień & Landstreet, 2002). It remains unclear whether magnetic HAeBe stars evolve into Ap/Bp stars, although circumstantial evidence supporting this is mounting (Wade et al., 2007). If there is an evolutionary connection, and some

HAeBe stars are to become chemically peculiar, the timescale for the generation of chemical peculiarities in HAeBe stars is unknown.

1.5 HD 72106

HD 72106 is a visual double star system with a $0.8''$ separation between the components (Hartkopf et al., 1996). The brighter component (HD 72106A) is often referred to as the primary, and the dimmer component (HD 72106B) is often referred to as the secondary. The system is located at a right ascension of 08h:29m:34.90s and declination of $-38^{\circ}:36':21''$, placing it in the constellation Vela. The system has a combined spectral class of A0IV and was identified as having an infrared excess, based on IRAS (the Infrared Astronomical Satellite) data, by Oudmaijer et al. (1992). Blommaert et al. (1993) provided additional infrared photometric measurements of the combined system, but erroneously suggested that the object was a post-AGB (post-asymptotic giant branch) star. Torres et al. (1995) observed the system photometrically in visible light, as well as with low resolution optical spectroscopy, and noted the presence of emission in the $H\alpha$ Balmer line. They hypothesized that the system was associated with the Gum Nebula.

The HD 72106 system was observed by the Hipparcos satellite (ESA, 1997). A separation between the components of $0.805''$ was found, at a position angle of 199.4° (relative to celestial north). The system was solved as a double star system, giving a good quality solution. A parallax of 3.47 ± 1.43 mas (milli-arc seconds) was found, with a large proper motion in right ascension of -5.81 ± 1.08 mas yr $^{-1}$ (milli-arc seconds per year) and in declination of 8.73 ± 1.36 mas yr $^{-1}$. A Hipparcos magnitude $H_p = 8.937 \pm 0.005$ was observed for the primary and 9.734 ± 0.010 for

the secondary. No evidence for relative motion between the two components was observed.

Fabricius & Makarov (2000) re-reduced the Hipparcos dataset, together with data from the Tycho mission (a secondary mission on the Hipparcos satellite, ESA, 1997), providing Tycho V_T and B_T magnitudes for both components of HD 72106. For the primary they found a B_T magnitude of 8.91 ± 0.01 and a V_T magnitude of 9.00 ± 0.01 ($B_T - V_T = -0.09 \pm 0.014$). For the secondary they found $B_T = 9.82 \pm 0.02$ and $V_T = 9.62 \pm 0.02$ ($B_T - V_T = 0.20 \pm 0.03$).

Vieira et al. (2003) observed the individual components and identified HD 72106B as a HAeBe star. The authors associated it with the Gum Nebula star forming region. They observed $H\alpha$ emission, but noted that it was fairly weak for a HAeBe star. In examining HD 72106B's spectral energy distribution Vieira et al. (2003) found a very low contribution from dust. This, they hypothesized, was due to HD 72106B being an evolved HAeBe star that has cleared most of its circumstellar envelope.

Schütz et al. (2005) performed infrared spectroscopy of HD 72106B. They examined circumstellar abundances of a number of different molecules. Schütz et al. (2005) found that the circumstellar material around HD 72106B was dominated by the crystalline silicates forsterite and enstatite. They found that large grains of amorphous silicates (grain size $\sim 2.0 \mu\text{m}$) and SiO_2 were present, but that smaller grained amorphous silicates (grain size $\sim 0.1 \mu\text{m}$) were almost completely absent. When comparing the IR spectrum of HD 72106B with a linear combination of spectra from comets Hale-Bopp and Halley, Schütz et al. (2005) found an “unusually” good fit. The authors comment that such a large fraction of processed dust is seen in only a few Herbig Be stars. These results seem to support the hypothesis of Vieira et al.

(2003): that HD 72106B is a relatively evolved HAeBe star and has cleared most of the dust in its vicinity.

Recently, Drouin (2005) and Wade et al. (2005) reported a detection of a magnetic field in HD 72106A based on spectropolarimetry from FORS1 (FOcal Reducer/low dispersion Spectrograph) at the Very Large Telescope and from ESPaDOnS (Echelle SpectroPolarimetric Device for the Observation of Stars) at the Canada France Hawaii Telescope. This was one of the earliest detections of a magnetic field in a possible HAeBe star. A longitudinal field of $+195 \pm 40$ G (i.e. 4.9σ) was detected in the FORS1 spectrum. Remarkably, no significant magnetic field was detected in the secondary ($+65 \pm 55$ G was observed). In the ESPaDOnS spectrum no significant longitudinal field was detected, but clear circular polarization was detected with a very high degree of significance, unambiguously indicating the presence of a magnetic field.

A more accurate and robust analysis of the same FORS1 data by Wade et al. (2007) did not result in a longitudinal magnetic field detection at 3σ confidence in HD 72106A. Wade et al. (2007) report longitudinal fields of 166 ± 70 G from Balmer lines and -11 ± 91 G from metallic lines. They conclude that one cannot be confident of a magnetic field detection at this level, however they note that ESPaDOnS observations have shown a clear circular polarization signal, and that HD 72106A is definitely magnetic.

Wade et al. (2005) report a mass for the primary of $2.4 \pm 0.4 M_{\odot}$ and $1.75 \pm 0.25 M_{\odot}$ for the secondary, based on the stars' H-R diagram positions. They report an age of approximately 10 Myr for the system. Wade et al. (2007) accept these values, and deduce $T_{\text{eff}} = 11000 \pm 1000$ K and $3.5 \leq \log g \leq 4.5$ for the primary, and $T_{\text{eff}} = 8000 \pm 500$ K and $4.0 \leq \log g \leq 4.5$ for the secondary. Wade et al. (2005) also report

strong variability in absorption lines of the primary, and suggest that this may be due to surface chemical abundance spots. In this thesis we find that the dramatic line variability reported by Wade et al. (2005), and illustrated in their Figure 2, is largely an instrumental artifact, due to the absence of atmospheric dispersion correction in one of their two observations, as described in Section 2.3. However, in other more recently acquired spectra we do see significant variability of line profiles, and confidently interpret this as due to surface abundance inhomogeneities, as described in Section 4.4. Wade et al. (2005) suggest that the observed variability is due to rotational modulation, with a period near 2 days. Our results qualitatively support this, with periodic variability due to stellar rotation providing a good phasing of observations separated by years, but we derive a somewhat shorter rotation period, as discussed in sections 3.6 and 4.2.

Due to its young age, probable binarity, and magnetic and chemical properties, the HD 72106 system was considered to be a compelling target for further study. The discovery of magnetic fields in HAeBe stars provides a tantalizing link to Ap and Bp stars. However, an in depth study of several magnetic HAeBe objects is necessary. Such studies can provide critical evidence to support or refute proposals of an evolutionary link between some HAeBe and Ap/Bp stars. The magnetic field geometries of HAeBe stars, their rotational properties, and their surface chemistry can provide such evidence. Study of chemical abundances in HAeBe stars can help understand any link between HAeBe and Ap/Bp stars, as well as determine the time scale on which abundance peculiarities develop. The details of the chemical peculiarities seen could have important consequences for the diffusion model of abundance anomaly formation.

The HD 72106 system is a prime target for such study. The components of HD 72106 have rather similar fundamental parameters. They have similar masses and temperatures, and most likely identical ages. These similarities make the observed differences all the more striking. The hints at a magnetic field in the primary, conclusively confirmed here with further observations from ESPaDOnS, place it in an interesting class of objects. Both stars are very young, making the link to HAeBe objects, but they have spectra with very little emission, making them appealing objects for spectroscopic analysis. The binarity of the system can provide further evolutionary constraints on the formation of magnetic fields and chemical peculiarities, given the apparently normal secondary. Thus HD 72106 is a particularly interesting system, situated at an important point in its evolution, and which is especially well suited to detailed study.

This thesis presents such a detailed study of HD 72106, investigating photospheric chemical abundances, rotational characteristics, magnetic properties, and surface abundance distributions. The dynamical connection between the stars and their evolutionary state is also discussed in detail. Chapter 2 discusses the collection of observations of HD 72106 with ESPaDOnS, as well as the reduction of those observations. Chapter 3 discusses the analysis techniques used, particularly spectrum synthesis, Least Squares Deconvolution, rotation period analysis, and Doppler Imaging. This chapter also describes the determination of fundamental parameters for both stars, discusses the evolutionary state of the system, and analyses the evidence for HD 72106 being a true binary system. Chapter 4 presents the major results of this thesis: detailed mean surface abundances for both stars, the rotation period of the primary, the magnetic field strength and geometry of the primary, and surface

abundance maps for the primary. Chapter 5 summarizes and discusses these results, and draws conclusions, with implications for the formation of Ap/Bp stars.

Chapter 2

Observations

2.1 Observing Stellar Magnetic Fields

The observation of magnetic fields in stars can be challenging, but in many cases is essential for understanding the physical processes at work in a star. The presence, strength, and geometry of magnetic fields in stellar atmospheres are measured through the atomic line splitting and polarization properties of the Zeeman effect.

2.1.1 Polarization

The polarization of light is commonly described in terms of the four Stokes parameters: I, Q, U, and V. Stokes I refers to the total amount of light in all polarization states. Stokes Q is the difference between orthogonal linear polarization states. Stokes U is the same as Stokes Q but with the basis set rotated by 45° . Stokes V is the difference between right and left circular polarization (Shurcliff & Ballard, 1964). This is schematically illustrated in Figure 2.1.

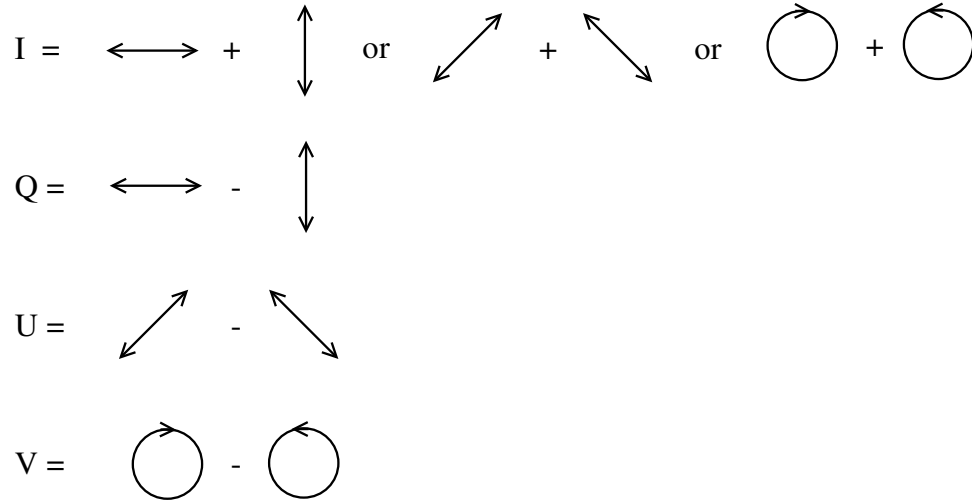


Figure 2.1: Schematic diagram of the combinations of polarization states used to calculate the Stokes parameters. I is the sum of polarizations, Q and U are the differences between orthogonal linear polarizations at two different angles, V is the difference between circular polarizations.

s The Stokes parameters can be described in a more rigorous fashion. Consider a general electromagnetic wave $\mathbf{E}(t)$ as a superposition of two orthogonal (Cartesian) components, perpendicular to the direction of travel, with magnitudes E_1 and E_2 :

$$\mathbf{E}(t) = \begin{pmatrix} E_1(t) \\ E_2(t) \end{pmatrix} = \begin{pmatrix} A_1 e^{i(\phi_1 + \omega t)} \\ A_2 e^{i(\phi_2 + \omega t)} \end{pmatrix}, \quad (2.1)$$

where components 1 and 2 have phases ϕ_1 and ϕ_2 , and amplitudes A_1 and A_2 respectively. The frequency of the wave is ω and t is time. The Stokes parameters can then be written as (Rees, 1987):

$$I = E_1^* E_1 + E_2^* E_2 = |E_1|^2 + |E_2|^2 = A_1^2 + A_2^2, \quad (2.2)$$

$$Q = E_1^* E_1 - E_2^* E_2 = |E_1|^2 - |E_2|^2 = A_1^2 - A_2^2, \quad (2.3)$$

$$U = E_1^* E_2 + E_2^* E_1 = 2 \operatorname{Re}(E_1^* E_2) = 2A_1 A_2 \cos(\phi_1 - \phi_2), \quad (2.4)$$

$$V = E_1^* E_2 - E_2^* E_1 = 2 \operatorname{Im}(E_1^* E_2) = 2A_1 A_2 \sin(\phi_1 - \phi_2), \quad (2.5)$$

where $*$ refers to the complex conjugate. Thus I is the total intensity, Q is a measure of linear polarization along the coordinate system, U is a measure of linear polarization rotated 45° to the coordinate system, and V is a measure of circular polarization.

2.1.2 Zeeman Splitting

In the presence of a magnetic field, each atomic energy level is split into multiple sub-levels with different polarization properties. This effect was first observed by Pieter Zeeman in 1897, and it now bears his name. In the Zeeman effect, the degeneracy in electron spin and angular momentum for one atomic transition is lifted by the presence of an external magnetic field. Thus one observed atomic line becomes a set of closely spaced lines, with a spacing approximately proportional to the field strength. Not only is the line split, but the light emitted (or absorbed) by each component of the line must possess a particular polarization, which is a function of the magnetic field geometry. The shift in wavelength of the Zeeman components is proportional to the magnetic field strength. Thus an observer, an astronomer for example, can measure magnetic field strength by observing the wavelength shift of the polarized components in a split absorption or emission line.

Fundamentally, the state of an electron in an atom is described by the following set of quantum numbers: n (the principal), l (azimuthal or angular momentum), and s (spin). These have the associated quantum numbers (eigenvalue for the z component of the angular momentum \mathbf{L} and spin \mathbf{S} eigenvectors), m_l and m_s . The quantum number l can range from 0 to $n - 1$ and for an electron, $s = \frac{1}{2}$. m_l runs from $-l$ to l , and m_s is $\pm\frac{1}{2}$. The total angular momentum quantum numbers j and m_j can be very useful when the spin and angular momentum (l and s) are strongly coupled. In this

case of L-S coupling, the total angular momentum quantum number can be written as: $j = l \pm \frac{1}{2}$, that is $j = 1/2 \dots n - 1/2$, and $m_j = -j \dots j$ (Griffiths, 1995).

In the ‘normal’ Zeeman effect, spin is not considered and a triplet of lines is produced. This is really a special case of the ‘anomalous’ Zeeman effect discussed below. In this simple case, with the magnetic field along the z axis, a electron changing energy levels makes a transition in m_l of $\Delta m_l = -1, 0, \text{ or } +1$ (the only allowed transitions). Due to the interaction with the magnetic field, these angular momentum transitions do not all have the same energy. Thus the line is split into three evenly spaced components, centered around the $\Delta m_l = 0$ transition at the zero-field wavelength (Ostlie & Carroll, 1996). Figure 2.2 illustrates both the splitting of atomic energy levels, and the corresponding observed absorption line splitting.

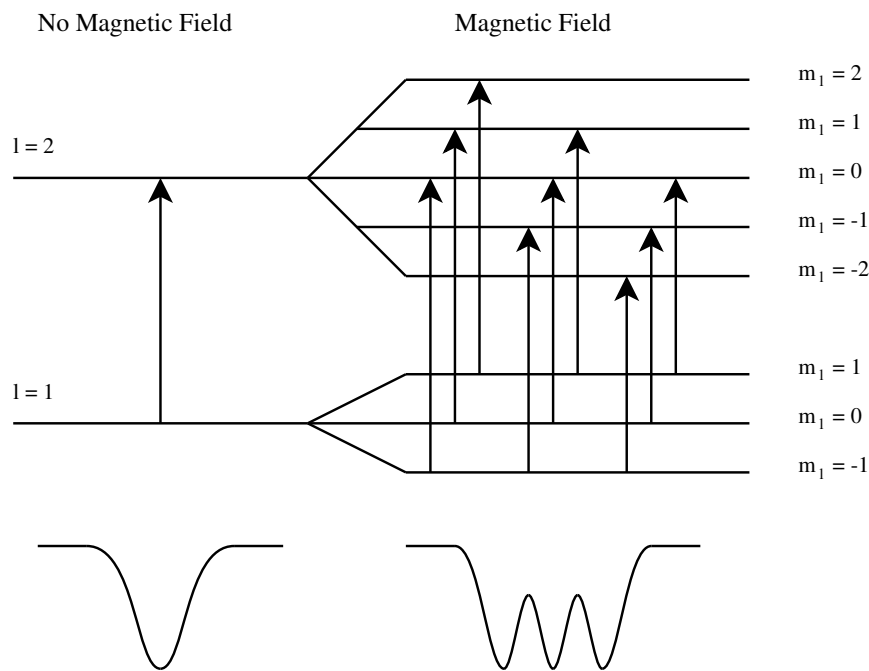


Figure 2.2: Illustration of atomic level splitting by the ‘normal’ Zeeman effect. The top half of the figure shows the splitting of energy levels with different m_l . The bottom portion of the figure illustrates splitting in the observed (Stokes I) spectrum.

In the ‘anomalous’ Zeeman effect, a transition in spin (m_s) as well as in m_l occurs, resulting in the formation of more than three lines. In this case it is more appropriate to consider the total angular momentum, since there exists strong spin-orbit coupling¹. Transitions occur with $\Delta m_j = -1, 0, \text{ or } +1$, similar to the normal Zeeman effect. The critical difference is that the spacing, in terms of energy, between the split levels depends on the l and j quantum numbers. The energy change (ΔE) in the presence of a magnetic field (B) due to the Zeeman effect is (Griffiths, 1995)

$$\Delta E = \mu_B B g_J m_j, \quad (2.6)$$

where μ_B is the Bohr magneton ($\mu_B = \frac{e\hbar}{2m}$) and g_J is the Landé g -factor (often referred to as just the Landé factor). The Landé factor is given by (Griffiths, 1995)

$$g_J = 1 + \frac{j(j+1) - l(l+1) + 3/4}{2j(j+1)}, \quad (2.7)$$

although in practice it is frequently determined experimentally, since the assumption of spin-orbit coupling is often only approximate. Due to different quantum numbers, different initial energy levels can be split into sets of sub-levels with different spacings. This allows for a wider range of transition energies (although Δm_j is still 0 or ± 1), and hence more observable components to the Zeeman split line.

The $\Delta m_j = 0$ components in a Zeeman split line are referred to as the π components. When the magnetic field is oriented along an observer’s line of sight (the ‘longitudinal’ direction), these components are not observed. In this geometry, the $\Delta m_j = \pm 1$ components, referred to as the σ components, are observed to emit or absorb left or right circularly polarized light, depending on whether Δm_j is $+1$ or

¹We consider only the Zeeman effect in the linear regime here. The Paschen-Back and intermediate field regimes are neglected. While less general, this is a safe treatment for the field strengths encountered in Ap/Bp stars (Wade et al., 2000a).

-1. In this case, the observed splitting and polarization is known as the longitudinal Zeeman effect. If the magnetic field is oriented such that it is perpendicular (i.e. transverse) to the observer's line of sight (such that it lies in the plane of the sky), the light emitted or absorbed from π components is observed to be linearly polarized, with a polarization angle parallel to the magnetic field. In this geometry the σ components are also observed to be linearly polarized, but with a polarization angle perpendicular to the field direction. This case of the Zeeman effect is referred to as the transverse Zeeman effect (e.g. Wade et al., 2000a). An observation of three Zeeman split lines in total intensity and circular polarization is presented in Figure 2.3. Because the transverse Zeeman effect is a secondary property, the linearly polarized signal is much weaker than the circularly polarized signal (Wade et al., 2000a). Additionally, in the case of a rotationally broadened line profile, it is often much easier to detect the circular polarization signature from the Zeeman effect than the wavelength splitting in total intensity. Thus, in our investigations, we have focused on circular polarization. Analysis of circular polarization is generally the method of choice for studying magnetic fields in stellar astronomy.

2.2 Instrumentation

Observations for this thesis were collected at the Canada-France-Hawaii Telescope (CFHT) with the Echelle SpectroPolarimetric Device for the Observation of Stars (ESPaDOoS) instrument.

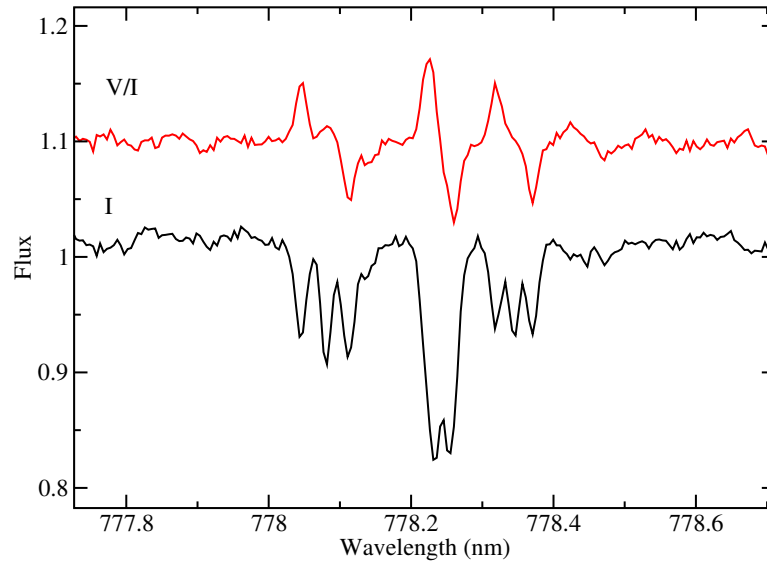


Figure 2.3: An ESPaSDOnS spectrum illustrating line splitting and polarization in HD 94660 due to the Zeeman effect. The lower line is a total intensity (Stokes I) spectrum and the upper line is a circular polarization (Stokes V divided by Stokes I) spectrum, shifted vertically for clarity. Since HD 94660 has a very low $v \sin i$, individual components of the split lines can be seen in the total intensity spectrum, as well as the change in polarization across the line profiles in the circular polarization spectrum.

2.2.1 Canada France Hawaii Telescope

The CFHT is a 3.58 meter telescope, with a Prime Focus/Cassegrain combination design, located atop Mauna Kea on the Big Island of Hawaii. The CFHT is situated at an altitude of 4204 m, a latitude of $+19^{\circ} 49' 41.86''$ and a longitude of $155^{\circ} 28' 18.00''$. The CFHT can act as a f/8 Cassegrain focus or a f/4 prime focus, and historically has also had a Coudé mode of operation. For our observations, and all observations with ESPaDOnS, the telescope operates in Cassegrain focus mode. Other instruments, notably WIRCam and MegaPrime, require the telescope to operate in prime focus mode. The telescope is controlled remotely from an operations room one floor below the dome.

2.2.2 ESPaDOnS

The Echelle SpectroPolarimetric Device for the Observation of Stars (ESPaDOnS) instrument is a high resolution spectropolarimeter that consists of two major parts. Mounted at the Cassegrain focus of the CFHT is a polarimeter module that analyses the polarization of incoming light, and passes orthogonal polarization states of the analysed light into a fiber-optic bundle. The optical fibers carry the light to a bench-mounted echelle spectrograph located in the Coudé room of the CFHT, which is located one floor below the operations room.

This design allows for the spectrograph to be well-insulated thermally and vibrationally, thereby improving the spectroscopic stability of the instrument. Placing the spectrograph in the Coudé room also reduces the stress on the telescope. Mounting the polarimeter in the Cassegrain module on the telescope allows for immediate

analysis of polarization, reducing spurious and instrumental effects caused by the optical train. The location of the Cassegrain module also allows for the easy inclusion of dedicated calibration and guiding optics. The most significant drawback of this two-piece design is that passing light into and along the optical fibers can result in a loss of flux. Problems with overly reflective and damaged fiber optic bundles have been encountered with the ESPaDOnS instrument. For example, between January and June 2005 a damaged fiber bundle resulted in a loss of throughput efficiency of about 1.0 mag. At present all known transmission problems have been corrected.

ESPaDOnS has a nominal resolving power $R = \lambda/\Delta\lambda = 68000$ when operating as a spectropolarimeter, and 80000 when operating as a spectrograph. The instrument provides nearly continuous wavelength coverage from 3700 Å to 10500 Å in 40 echelle orders. The peak throughput of the system, as measured from the telescope's aperture, is approximately 15% to 20%. The entrance aperture of the ESPaDOnS polarimeter is a 1.6 arcsecond (") pinhole with a physical size of 0.22 mm.

Polarimeter

The Cassegrain-mounted polarimeter module houses an atmospheric dispersion corrector, a compact CCD for guiding, and a calibration wheel, as well as optics for analysing the polarization of the incident light.

The Atmospheric Dispersion Corrector (ADC) consists of a pair of rotatable prisms that are used to counteract the wavelength dependence of the refractive index of air. Light passing through the earth's atmosphere is dispersed by differential refraction, causing a wavelength-dependent distortion of astronomical images. The ADC corrects for this distortion, ensuring that no extra blue or red light is systematically

lost outside of the pinhole (see e.g. Mynne & Worswick, 1986).

The guiding CCD collects light that is reflected from a tilted mirror surrounding the pinhole. Guiding images are collected in relatively short exposures (0.5 – 2 seconds), allowing for nearly real-time guiding corrections. By ensuring that the amount of light escaping around the edge of the pinhole remains symmetric, the guiding computer or observer can ensure that the target star remains centered.

The calibration wheel is used to replace the stellar beam with light from calibration sources. The standard calibration lamps are a pair of flat field tungsten lamps and a thorium-argon arc lamp for wavelength calibration.

The polarization analyzing optics consist of two half-wave Fresnel rhombs, a quarter-wave Fresnel rhomb, and a Wollaston prism, as illustrated in Figure 2.4. The half-wave Fresnel rhombs are placed on either side of the quarter-wave Fresnel rhomb, and are rotatable about the optical axis of the instrument. The half-wave Fresnel rhombs, as the name suggests, provide a $\pi/2$ retardation to the phase of the polarization, thus for example, swapping left and right circular polarization. The quarter-wave Fresnel rhomb converts circular polarization to linear polarization, much like a regular quarter-wave plate, by providing a $\pi/4$ phase retardation (Shurcliff & Ballard, 1964). Fresnel rhombs were chosen for ESPaDOnS because they behave in a less wavelength dependent fashion than quarter-wave plates. This is essential, as it allows ESPaDOnS to perform nearly achromatic polarization analysis over a large wavelength range (Alecian, 2007).

The half-wave rhombs, as mentioned, are rotatable about the optical axis of the instrument, while the quarter-wave rhomb and the Wollaston prism are fixed. This freedom of rotation allows for the optics to provide any desired retardation to the

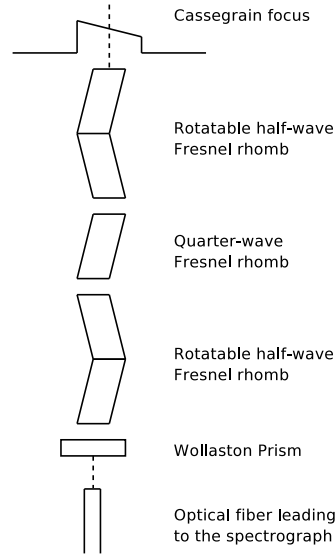


Figure 2.4: Schematic diagram of the polarization analysing optics in the Cassegrain module of ESPaDOnS. The individual optical components are labeled. Light enters from the Cassegrain focus, travels through the optical train, and exits into the fiber optic bundle for transmission to the spectrograph.

incoming beam of light. Thus one can transform any initial orthogonal pair of polarization states into any other orthogonal pair, before the light passes into the Wollaston prism, by selecting the appropriate angles for the half-wave rhombs. The choice of angle effectively reduces to a system of two equations (say the retardation of the horizontal and vertical linear polarization states) and two unknowns (the angles of the two rotatable rhombs). This allows one to easily analyse light, so as to produce Stokes I, Q, U or V spectra, without having to add or remove optical components from the path of the beam.

Upon exiting the last Fresnel rhombs, the light enters the Wollaston prism. The Wollaston prism splits linearly polarized light into its orthogonal states and produces two beams (Shurcliff & Ballard, 1964). Thus for the analysis of circular polarization, the light is first converted into linear polarization ($\pi/4$ retardation) with the Fresnel

rhombs, then the Wollaston prism produces one (linearly polarized) beam containing light that was originally left circularly polarized, and another (linearly polarized) beam that was originally right circularly polarized. These beams are then injected into separate optical fibers for transmission to the spectrograph.

The optical fiber bundle consists of three fibers, only two of which are used at a time. The bundle is approximately 30 m long, with fibers that have a 0.1 mm core diameter and 0.11 mm diameter including cladding. ESPaDOnS uses low-OH H-treated fibers produced by CeramOptec, allowing for very good throughput over a wide spectral domain (Donati, 2007). Peak throughput of the fibers is around 90%.

Spectrograph

Light entering the spectrograph from the optical fibers first encounters a Bowen-Walraven image slicer (Donati, 2007). The image slicer transforms the round images from the two fiber heads into a set of three narrow elongated slices (when the instrument is operating in spectroscopic ‘star only’ mode this is doubled to six slices). This is done by slightly redirecting portions of the beams from the fiber heads with a set of two prisms and a parallel plate.

The light is then collimated with a parabolic collimator and passed to the diffraction grating. The diffraction grating is an R2 echelle grating with a 204x408 mm ruled area, 79 lines/mm, and a 63.4 degree blaze angle. The dispersed light then passes through a prism cross-disperser to separate the spectral orders. Light finally enters the f/2 camera and is collected by a 2000x4500 pixel CCD detector with 13.5 μm square pixels (Donati, 2007). The optical path through the major components of the spectrograph is illustrated in Figure 2.5

This design of the spectrograph provides a total of 40 orders projected onto the CCD. Wavelength coverage runs from 372 nm to 1029 nm with three small gaps at 922.4 - 923.4 nm, 960.8 - 963.6 nm, and 1002.6 - 1007.4 nm. The CCD pixels correspond to 2.6 km s^{-1} and are extracted at 1.8 km s^{-1} (that is 0.6923 CCD pixels per spectral pixel, see Section 2.4 for the extraction process) (Donati, 2007). The spectrograph has a peak throughput of about 40% to 45%, giving the total peak throughput of the telescope and instrument of 15% to 20%.

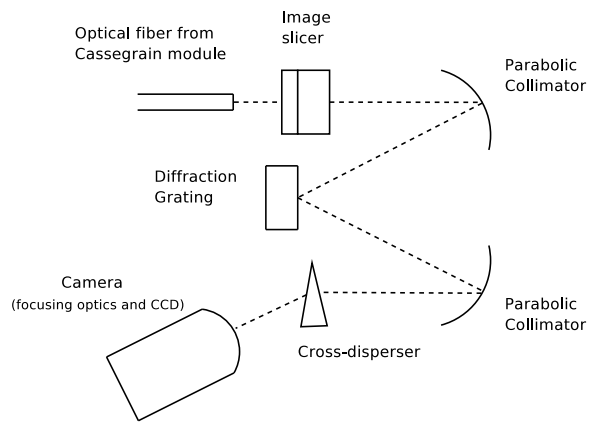


Figure 2.5: Schematic diagram of the major components in the ESPaDOnS spectrograph. The individual optical components are labeled. Light enters from the fiber optic bundle, passes through the spectrograph, and is collected by the CCD in the camera.

2.3 Observations

Observations were collected during four different observing missions (runs) between February 2005 and March 2007. All runs used the same instrument, ESPaDOnS, and all observations were collected and reduced in the same manner. Approximately half the observations (those in the March 2007 run) were obtained during a time

allocation for which the author of this thesis wrote the proposal and was the principal investigator. A copy of this proposal is included in Appendix A. The journal of observations is reported in Table 2.1.

The initial setup at the start of a night of observations is heavily automated. The appropriate directory structure for acquired images and data reduction must be created. The dewar of liquid nitrogen used to cool the CCD must be filled. After that is complete the automatic focusing routine is executed and the telescope is ready to acquire calibration images.

A full set of calibration frames was collected at the beginning and end of each observing night. This consisted of 3 bias frames, one thorium argon lamp exposure, 20-40 internal tungsten lamp flat field frames, and about 4 Fabry-Perot exposures. A sample flat field frame and a sample thorium argon frame are presented in Figure 2.6. The bias frames are used to correct for detector background and readout noise. However, rather than averaging over multiple bias frames (to reduce noise in the bias frame), the ESPaDOnS bias frames are averaged over 8 pixel by 8 pixel squares, before subtraction from science images. The thorium argon arc lamp exposure provides a set of well known emission lines used for wavelength calibration. The wavelength calibration is refined in science images with the use of telluric lines (terrestrial atmospheric absorption lines due to water vapor) in the science images themselves. The flat field frames are also used to identify the orders on the CCD chip, and fit them to produce a geometric model of the frame. The Fabry-Perot frames, which contain a large number of very sharp ‘lines’, are used to fit the shape and orientation of the ‘slit’ image on the CCD.

All observations were made in polarimetric mode, as ‘Stokes V’ observations, using

UT Date	HJD (-2 450 000)	Component (HD 72106)	Integration Time (s)	Peak S/N I	Peak S/N V
21 Feb. 05	3422.9730	A&B	2400	222	208
22 Feb. 05	3423.9248	A&B	2400	201	186
09 Jan. 06	3745.02967	A&B	2400	219	219
11 Jan. 06	3747.02034	A&B	3200	143	116
12 Jan. 06	3747.99629	A	1200	149	149
12 Jan. 06	3748.01496	B	1200	76	88
11 Feb. 06	3777.87860	A&B	2000	238	221
11 Feb. 06	3777.95149	A&B	2400	253	239
12 Feb. 06	3778.86172	A&B	2400	282	259
13 Feb. 06	3779.87202	A&B	2400	184	175
13 Feb. 06	3779.95052	A&B	2400	107	15
13 Feb. 06	3779.98127	A&B	2400	128	79
02 Mar. 07	4161.77282	A&B	2400	254	248
02 Mar. 07	4161.80256	A&B	2400	265	255
02 Mar. 07	4161.90282	A&B	2400	297	285
03 Mar. 07	4162.85713	A&B	2400	208	195
04 Mar. 07	4163.83561	A&B	2400	322	308
05 Mar. 07	4164.84650	B	3200	209	200
05 Mar. 07	4164.88387	A	2400	248	241
05 Mar. 07	4164.90961	A&B	1600	277	272
09 Mar. 07	4168.85791	A&B	2400	283	278
09 Mar. 07	4168.90947	A&B	2400	272	258

Table 2.1: Log of observations of the HD 72106 system obtained with ESPaDOnS. Column 1 is the date the observation was obtained on, column 2 is the heliocentric Julian date of the observation, and column 3 indicates which component(s) of the double star were observed. Integration times are given in column 4 and refer to the complete set of 4 sub-exposures required to produce each Stokes V spectrum. Peak signal-to-noise ratios are given for the Stokes I spectra in column 5 and Stokes V spectra in column 6, and are reported for 1.8 km s^{-1} spectral pixels.

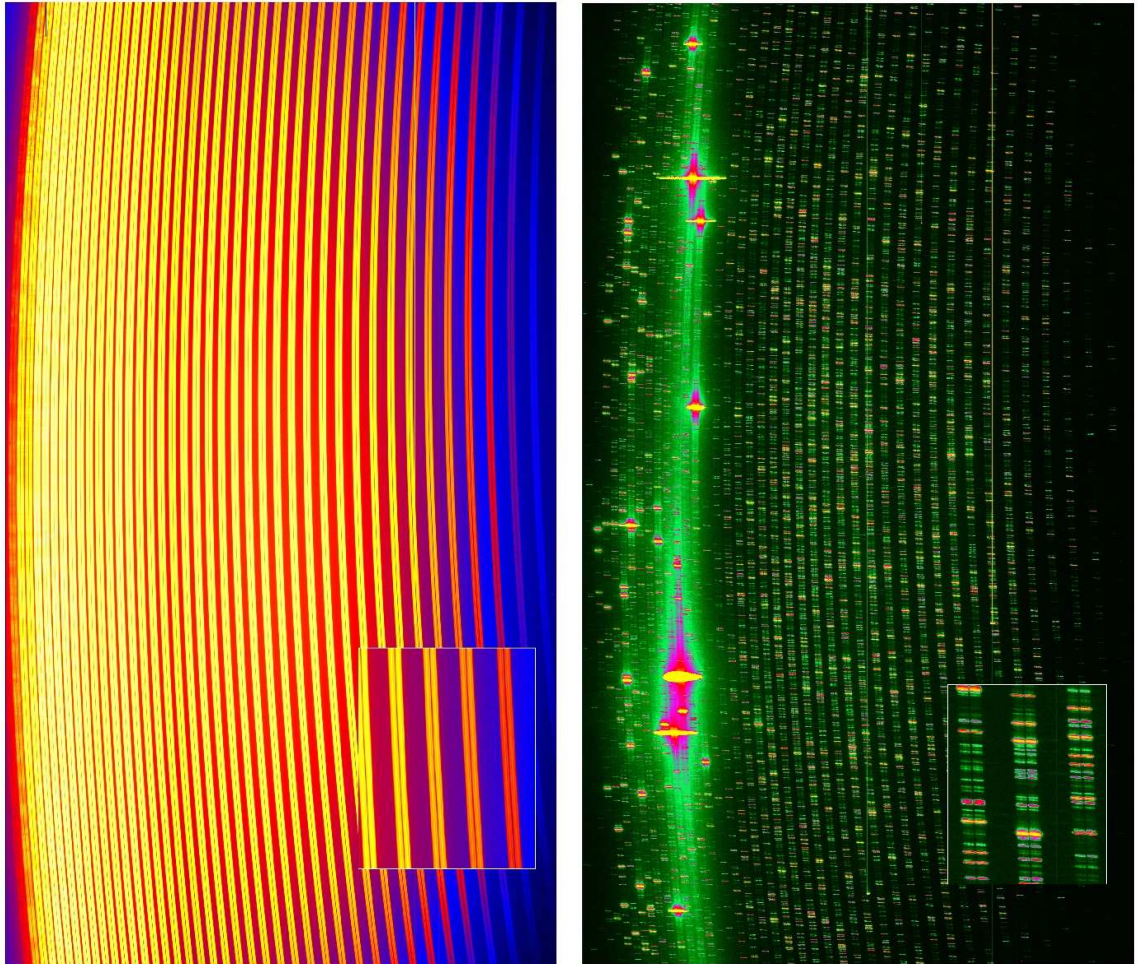


Figure 2.6: Sample flat field (left) and thorium argon (right) calibration frames. Both frames have a zoomed in detail in their lower right. The flat field frame illustrates the geometry of the spectral orders, with the closely spaced pairs corresponding to opposite polarization states. The thorium argon frame illustrates the ‘slit’ shape from individual emission lines. The heavily saturated lines are not used for data reduction. Images: N. Manset, Canada-France-Hawaii Telescope, <http://www.cfht.hawaii.edu/Instruments/Spectroscopy/Espadons/>

the 40 second ‘normal’ readout mode. Each ‘Stokes V’ observation produces both a real circular polarization Stokes V spectrum and a total intensity Stokes I spectrum. A complete Stokes V observation consists of 4 sub-exposures, between each of which the angles of the half-wave rhombs are chosen so as to produce either a $\pi/4$ or a $-\pi/4$ retardation, in the sequence: $\pi/4$, $-\pi/4$, $-\pi/4$, $\pi/4$. Exposure times for each observation (i.e. the complete set of 4 sub-exposures) are given in Table 2.1.

All observations listed in Table 2.1 (with one exception, discussed below) were made with the atmospheric dispersion corrector in place and the fiber agitator on. The fiber agitator jiggles the fiber optic bundle to eliminate any modal noise in the cable. Modal noise is caused by the interference of different optical modes in a fiber. Varying the physical geometry of the fiber changes the preferred modes and can average out this noise.

As indicated in Table 2.1, both components of the HD 72106 system were usually observed together, due to the small separation of the components. For the observations of the combined system, the photo-center of the system was centered in the pinhole. In these observations atmospheric conditions (worse than $0.5''$ seeing) were insufficient to resolve the individual components properly. However, with a $1.6''$ pinhole and a separation between components of $0.8''$, keeping both components in the pinhole did not pose a problem.

Observations of the individual components were made on nights with particularly good seeing. With seeing better than $0.4''$ it is possible to resolve the two components of the binary. With careful guiding, one can exclude one component from the pinhole. Manual guiding and careful monitoring are necessary to ensure flux from the undesired component does not enter the pinhole.

Ultimately, two of the observations were rejected as unsuitable for science. The observation at HJD 2453779.95052 (second observation on 13 Feb. 2006) was rejected due to cloud cover during part of the exposure, which resulted in a very low signal-to-noise ratio (S/N). The observation at HJD 2453422.9730 (21 Feb. 2005) was rejected because it was the one case in which the ADC (atmospheric dispersion corrector) was accidentally not used. The observation was of the combined HD 72106 A & B system. As a result of the atmospheric distortions, the amount of flux recorded from each of the two components varied with wavelength. Thus some observed spectral lines were primarily contributed by the primary and some were primarily from the secondary. This effect cannot be reliably corrected for, and thus the observation was discarded.

The observation collected without the use of the ADC was discussed by Wade et al. (2005). The authors erroneously diagnosed very strong variability in HD 72106 due to this observation. While we do find substantial variability in HD 72106A, the differences in spectra seen by Wade et al. (2005) are primarily a result of the unused ADC, not intrinsic variability in either star.

2.4 Reductions

Basic data reductions were performed with the Libre-ESpRIT data reduction package. This is a nearly-automatic dedicated data reduction package for ESPaDOnS, which performs a complete calibration and optimal spectrum extraction. Continuum normalization of the resulting unnormalized spectra was performed with a ‘home made’ routine, tailored by hand to HD 72106A and B. This routine, described in Section 2.4.1 and included in Appendix B, fits low-order polynomials to the continuum in each spectral order and then divides the spectrum by the polynomial, hence normalizing

the continuum to unity. Observations of the primary were reconstructed by subtracting the (assumed constant) spectrum of the secondary, using appropriate weighting, from the spectra of the combined system, as described in Section 2.4.2.

2.4.1 Spectrum Extraction and Normalization

The Libre-ESpRIT data reduction package is based on the ESpRIT (Echelle Spectra Reduction: an Interactive Tool) package (Donati et al., 1997), but it has been tailored specifically for ESPaDOnS and has been further automated. This package allows for fully reduced spectra to be available within minutes after an exposure sequence is complete.

Libre-ESpRIT begins by performing a bias subtraction. The software then calculates the geometry of the orders on the CCD, producing a best fit model, and pixel-to-pixel sensitivity variations are corrected with the mean flat field. Flat field and thorium argon frames are illustrated in Figure 2.6. The slit geometry is then modeled with the Fabry-Perot images and bad pixels are rejected. A wavelength calibration is applied using the thorium argon frame, defining the dispersion relation and providing a relationship between CCD position and spectral wavelength. The robustness of the calibration is verified using regions of wavelength with overlap of different spectral orders.

Once the initial calibration is complete, optimal spectrum extraction is performed, producing a 1D spectrum from each of the four 2D sub-exposures. The spectra from the individual sub-exposures are combined as follows. To produce the (total intensity) Stokes I spectrum (I), the flux from individual sub-exposures is added:

$$I = i_{1,\perp} + i_{1,\parallel} + i_{2,\perp} + i_{2,\parallel} + i_{3,\perp} + i_{3,\parallel} + i_{4,\perp} + i_{4,\parallel}, \quad (2.8)$$

where $i_{k,\perp}$ and $i_{k,\parallel}$ are the two spectra of orthogonal polarization obtained in sub-exposure k . The polarization rate V/I is given by

$$\frac{V}{I} = \frac{R - 1}{R + 1}, \quad (2.9)$$

where $R = R_V$ and

$$R_V^4 = \frac{i_{1,\perp}/i_{1,\parallel} \ i_{4,\perp}/i_{4,\parallel}}{i_{2,\perp}/i_{2,\parallel} \ i_{3,\perp}/i_{3,\parallel}}, \quad (2.10)$$

as described by Donati et al. (1997). This method requires more sub-exposures than is strictly necessary to produce V/I , however it corrects for systematics much better than is otherwise possible. In particular, swapping optical paths in two sets of sub-exposures allows for the suppression, at least to first order, of spurious polarization signals due to variations in optical path, including CCD sensitivity. Repeating this process allows for the canceling out of time dependent effects, again to first order (see Semel et al., 1993; Donati et al., 1997).

The ‘null polarization’ spectrum N/I is also calculated by replacing R in equation 2.9 with R_N^4 (Donati et al., 1997) where:

$$R_N^4 = \frac{i_{1,\perp}/i_{1,\parallel} \ i_{2,\perp}/i_{2,\parallel}}{i_{4,\perp}/i_{4,\parallel} \ i_{3,\perp}/i_{3,\parallel}}. \quad (2.11)$$

In this case, rather than multiplying together coherent polarization states as for V/I , we divide coherent polarization states, hence canceling out any real signal. N/I is useful for ensuring that a signal in V/I is in fact real. In general, N/I should contain no signal. If a signal is observed in the N/I spectrum then some systematic error is likely present, and it must be corrected if the data is to be used.

The individual $i_{k,\perp}$ and $i_{k,\parallel}$ spectra are extracted by fitting a (model) spectrum to the observed CCD orders. In this ‘inverse problem’ the model spectrum is processed through the previously calculated model slit and order geometries, and then

compared, via χ^2 , to the observed CCD image. The autocorrelation matrix from this fitting process is used to derive error bars for each individual pixel. Error bars on the final I and V/I spectra are then computed from the individual sub-exposure error bars. Once the optimal extraction process is complete, a wavelength correction to the heliocentric rest frame is applied. A final optional step is continuum normalization. The quality of the Libre-ESpRIT normalization is not sufficiently good for the detailed analysis that we will perform, therefore we only use unnormalized output.

Continuum Normalization

In general, it is very difficult to accurately define the continuum level in absolute units in high resolution stellar spectroscopy. The continuum recorded on the CCD is a product of the true continuum of the star, the interstellar transmission, the terrestrial atmospheric transmission, the system transmission of both the telescope and instrument, and the response of the CCD. Furthermore, most of the important information for stellar spectroscopy is contained in individual absorption (or emission) lines. Thus, rather than deal with the difficult problem of absolutely fixing the continuum, it is common practice to normalize the continuum to unity. Then the properties of absorption and emission lines are analysed relative to the normalized continuum.

The general procedure is to fit an appropriate (but ad hoc) function through regions identified as continuum, then to divide the entire observed spectrum by the function. A smooth (low-degree) polynomial function is often used, since the continuum changes very slowly with wavelength compared to the (relatively sharp) absorption lines of interest. In echelle spectroscopy, relatively steep order profiles make normalization somewhat more challenging, particularly at the ends of orders.

A home made routine written in Fortran and tailored for HD 72106A & B was used. A copy of the normalization routine can be found in Appendix B, Section B.1. This routine follows the basic strategy outlined above, with low-degree polynomials as the fitting function. The function used ($y(x)$) for a degree of n is

$$y(x) = \sum_{i=0}^n a_i x^i, \quad (2.12)$$

with $a_0 \dots a_n$ as the free parameters to be fit. The routine operates on one spectral order at a time. This avoids the problem of order overlap, and the much higher-degree polynomials needed to deal with changes in the continuum level between orders. It also has the advantage that the robustness of the normalization for each order can be checked in the overlapping regions of successive orders.

Points in the continuum are identified by first taking a running average (over 17 pixels) of the spectrum, smoothing out the noise. Then the pixel with the greatest flux in a moderately large (200 pixel) region is identified. The size of the region is chosen to be larger than the spacing between most lines; thus there usually is some real continuum to be identified in each region. These points are then used to find the polynomial fit. The points chosen are much fewer than the actual number of points in the continuum, however they are chosen with some care so as to ensure that they are representative of the true continuum.

The degree of the polynomial used is determined manually for each order of the spectrum. Usually a degree between 3 and 5 was chosen. Additionally, regions of the spectrum with emission lines or particularly broad absorption features can be excluded from the fit by hand. Figure 2.7 illustrates fits to the continuum in a segment of unnormalized ESPaDOnS spectrum, as well as the subsequently normalized spectrum. Note that the S/N in this segment is 220 (based on spectral pixels) and the error bar

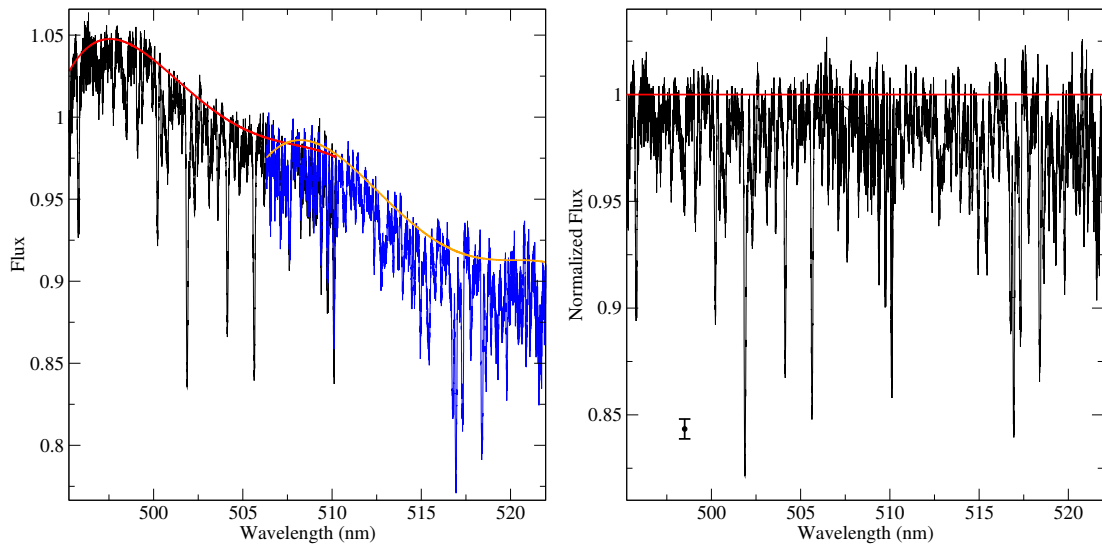


Figure 2.7: An unnormalized spectrum with polynomial fits to the continuum (smooth lines) is presented in the left frame. Two spectral orders are shown, using different colors. In the right frame, the same spectrum, now with the normalization applied, is shown. A typical error bar for this segment of spectrum is illustrated in the right frame.

associated with each pixel is approximately 0.0045, as illustrated in Figure 2.7.

2.4.2 Spectrum Reconstruction

The majority of our spectra correspond to the combined light of both components of the HD 72106 system. Analysis of the system requires that we recover the spectra of the individual components.

The recovery of the spectrum of HD 72106A from the combined spectrum relies on our observation that the spectrum of the secondary remains stable over long periods of time². This is illustrated by the two nearly identical spectra of HD 72106B collected in January 2006 and March 2006. In these two spectra, all of the Balmer lines other than H α were identical within the uncertainties. In H α we see clear emission which displays some variability. The metallic lines are also all identical except for the O line at 7771 Å, in which a small amount of variable emission is seen. The stability between observations is illustrated in Figure 2.8. This stability is not surprising; later results show the secondary to be a normal Herbig Ae star (see Section 4.1.2), and thus one would not expect significant variability outside of emission lines.

Having established the stability of the spectrum of the secondary, we can subtract it from each of the combined spectra, weighted by its relative contribution, to obtain spectra of the primary. We begin by modeling the intensity I_T at any point in the combined spectrum according to

$$I_T L_T = I_1 L_1 + I_2 L_2, \quad (2.13)$$

where I_2 refers to the normalized observed flux of the secondary and L_2 refers to the

²There are two exceptions to this: the H α Balmer line and the O 7771 Å line, both of which are observed to be variable in emission.

luminosity of the secondary; thus the product $I_2 L_2$ gives the total observed flux of the star as a function of wavelength. I_1 refers to the normalized flux of the primary (our unknown), while L_1 is the luminosity of the primary. I_T and L_T are the total normalized flux of the system and the total luminosity of the system respectively. The total luminosity can be written as $L_T = L_1 + L_2$. It is elementary to rearrange equation 2.13 to obtain I_1 :

$$I_1 = I_T \left(1 + \frac{L_2}{L_1} \right) - I_2 \frac{L_2}{L_1}. \quad (2.14)$$

The magnitude difference between components is well known from Hipparcos data (ESA, 1997; Fabricius & Makarov, 2000). In the Hipparcos V band the apparent magnitude of the primary is 8.937 and the secondary is 9.734 (ESA, 1997). In the Tycho V band the apparent magnitudes are 9.00 and 9.62 respectively (Fabricius & Makarov, 2000). This allows us to easily determine the ratio L_2/L_1 using the standard relation:

$$L_2/L_1 = 100^{(m_1 - m_2)/5}, \quad (2.15)$$

where $m_1 - m_2$ is the difference in apparent magnitude between the primary and secondary. A bolometric correction is not necessary here, as we are interested in the relative luminosities in a particular wavelength range - the spectral range of the ESPaDOnS instrument. The procedure described here, when used with V band photometry, is not expected to work outside of the bandpass of the V filter.

This procedure allows us to reconstruct 18 spectra of the primary from the combined spectra, rather than using just the 2 observations of the primary on its own. However, we cannot generally use the same technique to reconstruct spectra of the secondary. The primary displays clear variability of its absorption lines. Hence the observations of the (variable) primary, obtained at an arbitrary date, cannot be used

with observations of the combined system to reconstruct spectra of the secondary. In addition, subtracting a reconstructed spectrum of the primary from its original combined spectrum simply recovers the original observation of the secondary used in the initial reconstruction. However, regions of the primary's spectrum that exhibit no detectable variability can be used to recover small parts of the spectrum of the secondary. This was used to further verify the non-variability of the secondary.

2.4.3 Quality Control

Because of the complexity of the procedure described in Section 2.4.2, we have performed a number of checks to ensure the accuracy of the reconstructed spectra.

The first check performed was a comparison of the observed spectra of just the primary (obtained on nights of excellent seeing, Julian date 2453747.99629 and Julian date 2454164.88387) with each other, and those of just the secondary (Julian date 2453748.01496 and Julian date 2454164.84650) with each other. Careful monitoring at the time of observation makes us confident that the observations of one component were not contaminated by light from the other. This was confirmed by comparing observations of the same object. At the level of the S/N (76 in the worst observation), the two observations of the secondary were identical outside of H α and OI 7771 Å, the two clear emission lines observed in the star. A careful examination of every angstrom of these two spectra by eye revealed no other variations above the noise level. Figure 2.8 illustrates the stability of the spectra of HD 72106B between our observations, obtained 417 days apart. Thus we conclude that the spectrum of the secondary is constant within the noise, outside of emission lines.

Regions in which the spectra of the primary displayed little to no variability

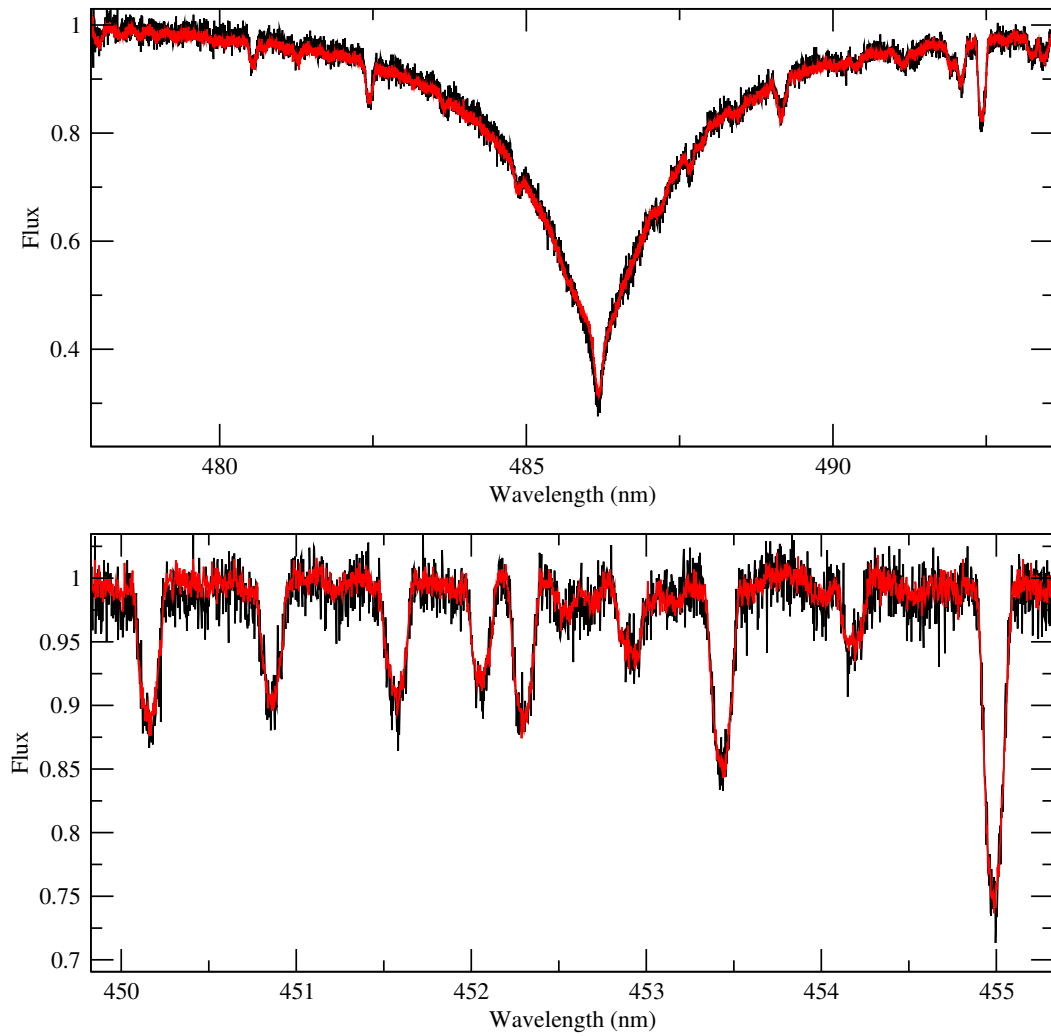


Figure 2.8: Sample H β and metallic lines in observations HD 72106B on its own. The black spectra were obtained on 12 Jan. 2006, the red (gray) spectra were obtained on 5 Mar. 2007. A very good correspondence can be seen between the observations.

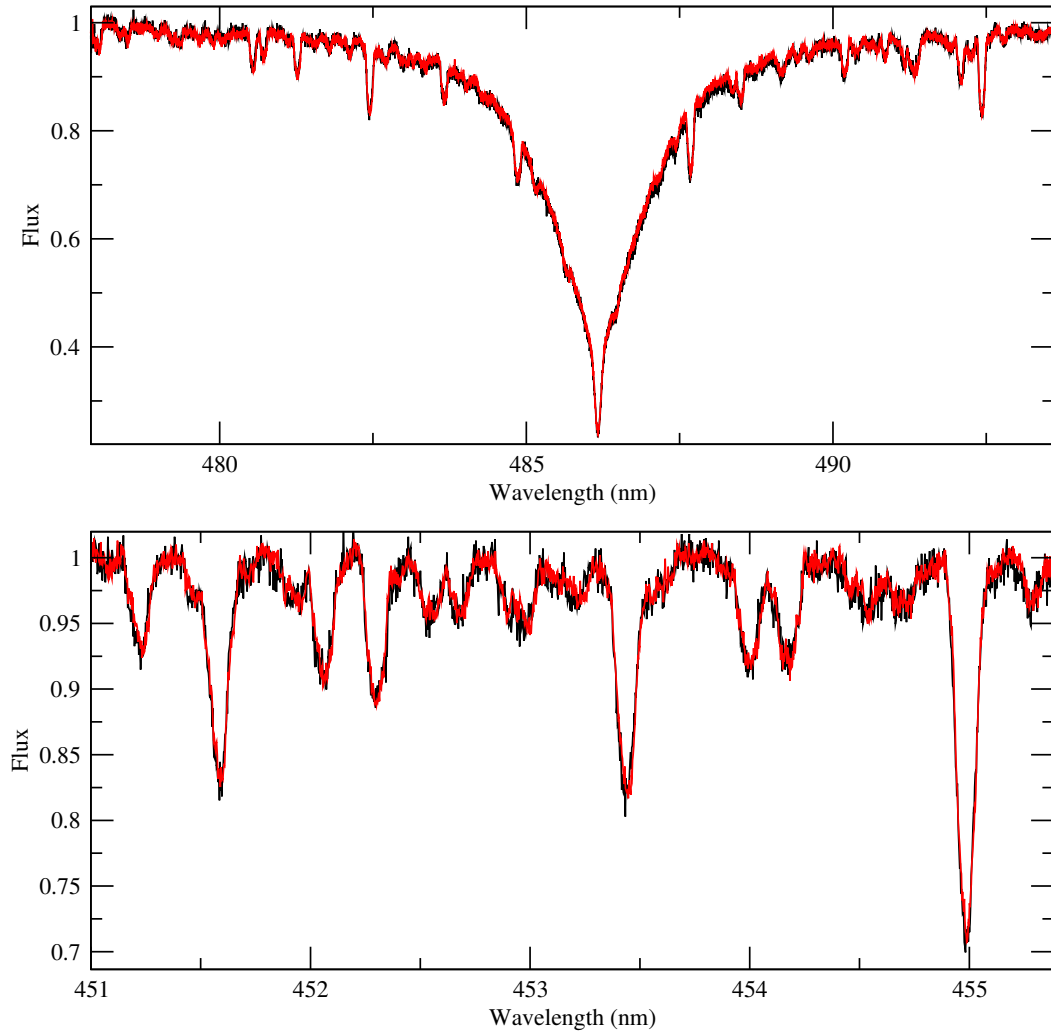


Figure 2.9: Sample H β and non-variable metallic lines in observations HD 72106A on its own. The black spectra were obtained on 12 Jan. 2006, the red (gray) spectra were obtained on 5 Mar. 2007. In these ‘stable’ regions of spectrum, a good correspondence can be seen.

were used to reconstruct spectra of the secondary, as discussed in Section 2.4.2. In general, reconstructed spectra of the secondary are not useful due to unaccounted for variability in the primary's spectrum. However, in these segments of spectral stability, the process can reliably be performed. In these small regions, no variability was seen in any reconstructed observation of the secondary, down to the noise level of the observation. The stability of one such region is illustrated in Figure 2.10. The lack of variability in these regions provides further support for the conclusion that the secondary is non-variable, at least to the noise level in our observations.

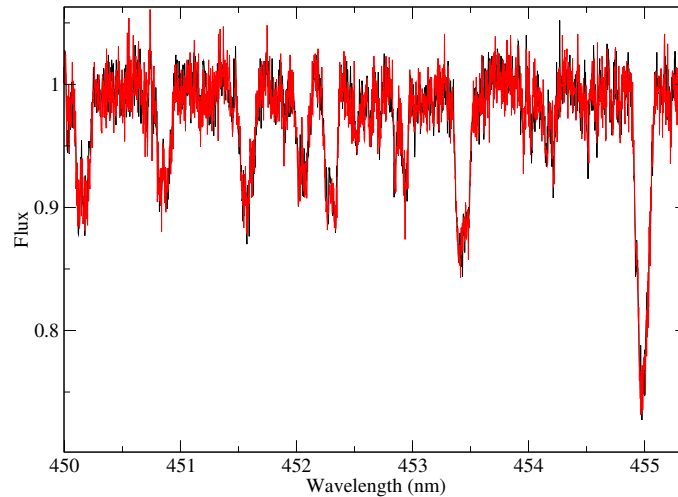


Figure 2.10: Sample reconstructed spectra of the secondary, in a stable region of the primary's spectrum. The black line is based on the observation from 4 March, 2007 and the red line is based on the second observation from 11 February, 2006. In general, reconstructed spectra of the secondary are not useful due to unaccounted for variability in the primary's spectrum. However, in a few spectral regions where the primary displays little to no variability, one can reliably reconstruct spectra of the secondary. In these regions we seen no variability in the secondary, providing further support to the conclusion that HD 72106B is non-variable.

A similar examination of spectra from the primary found that they displayed identical Balmer line profiles, and a number of identical metal lines. This is illustrated in Figure 2.9, which compares stable segments of spectra in observations of HD 72106A on its own. However, unlike the spectrum of the secondary, changes in a significant number of metal lines were observed. These changes are attributed to intrinsic variability of the primary’s spectrum. Several examples of this are illustrated in Figure 2.11 using spectra of just HD 72106A. Asymmetric line profiles were observed in the majority of these cases (particularly clear in the segment of spectrum centered at ~ 443 nm, shown in Figure 2.11), leading us to infer intrinsic variability. The variability being restricted to only lines of some species (such Si) also suggests that it is intrinsic, rather than an artefact of the observation, reduction, or reconstruction techniques.

Reconstructed spectra of the primary were compared to observations of the primary on its own, as well as to each other. An observation of HD 72106A compared to an observation of the combined system and a reconstructed spectrum are shown in Figure 2.12. Neither the core depth nor the wing shape of the Balmer lines seen in the combined spectra match the observations of the primary on its own. Reconstructed spectra, on the other hand, provide excellent matches to the spectra of the primary on its own. Additionally, the majority of metallic lines in the combined spectra do not match the spectra of the primary on its own. However, reconstructed spectra (at the correct rotation phase of the primary³) provide nearly perfect matches.

³The rotation phases of our observations and the rotation period of HD 72106A are discussed in detail in Sections 3.6 and 4.2. In these sections we find that the variability observed here is due to rotational modulation of HD 72106A. As the star rotates the visible portion of the stellar surface changes, and hence the observed properties vary. The rotational phase ϕ is defined $\phi = t/P$, where t is the time of observation and P is the rotation period. Thus ϕ runs from 0.0 to 1.0 during one rotation.

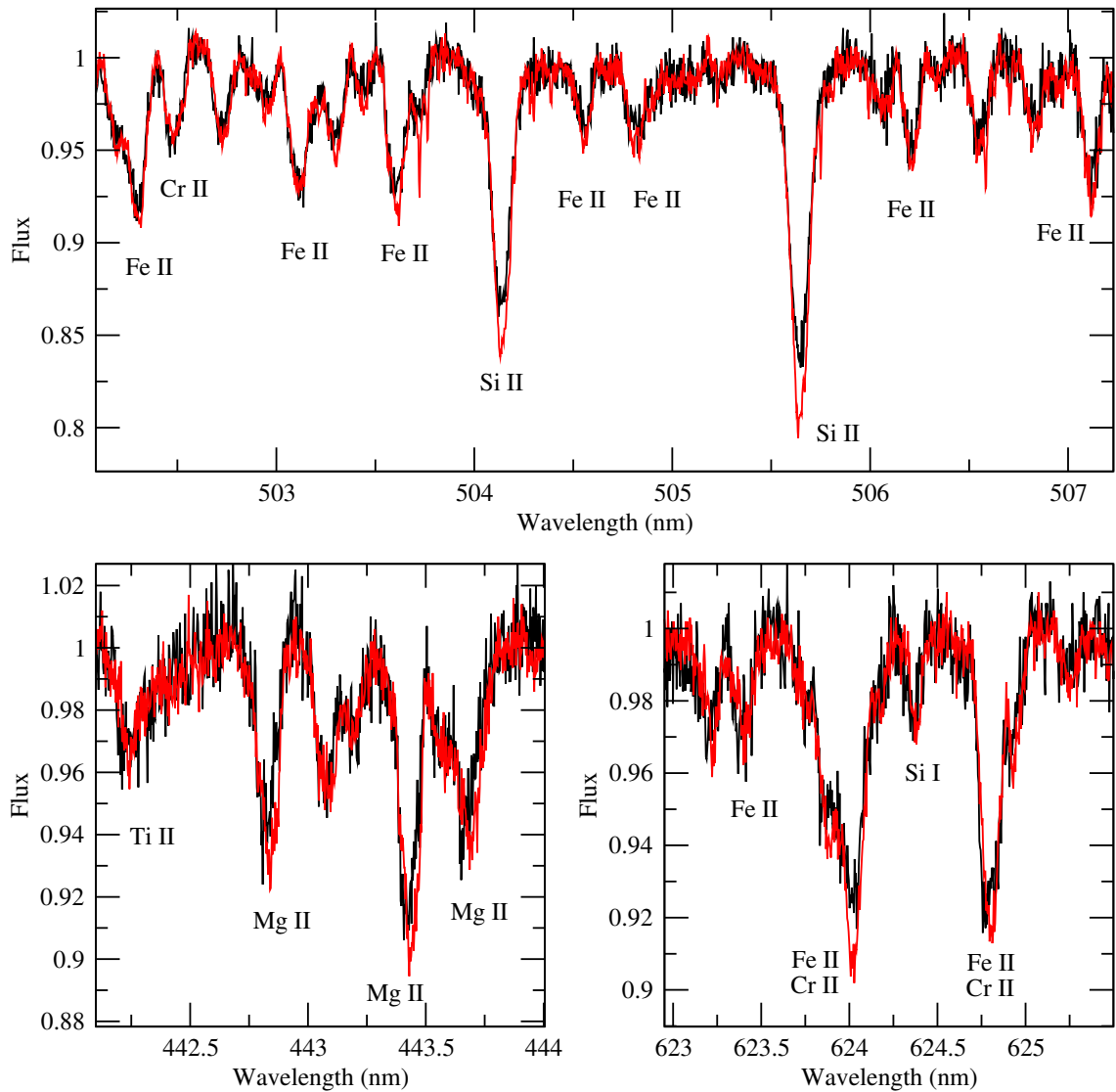


Figure 2.11: Variable metallic lines in observations of HD 72106A on its own. The black spectra were obtained on 12 Jan. 2006, the lighter (red) spectra were obtained on 5 Mar. 2007. Clear variability can be seen in lines of some species, while other lines have not varied substantially between observations. Some lines show clear variations in strength, some in radial velocity, and some vary in both. Major contributors to the stronger lines are labeled, in order of importance.

Reconstructed spectra at widely separated rotation phases do not display matching metallic line profiles, due to the profile variability established above, but the Balmer lines do not vary. Pairs of reconstructed spectra at nearly the same phase (and at diametrically opposite phases) are shown in Figure 2.13. From this we conclude that the spectrum recovery process is necessary to produce usable spectra, and that the process provides very good results.

Comparing recovered observations of HD 72106A at the same phase or opposite phases, as determined in Section 4.2, highlights the accuracy of the reconstructed spectra, as well as the intrinsic variability in HD 72106A. Figure 2.13 presents the same spectral region, in one case with two observations separated by 0.50 in phase and in another case with observations separated by only 0.03. The spectra in both comparisons were obtained over a year apart. In the first case, strong variability can be seen, as well as asymmetric line profiles. In the second case, while asymmetric line profiles are seen, the spectra are virtually identical. This provides further clear evidence for the variability of HD 72106A. As well, this further demonstrates that the spectrum reconstruction technique is sufficiently accurate to provide nearly identical spectra of the primary at the the same rotation phase. Thus systematic errors due to spectrum reconstruction are small, at or below the noise level.

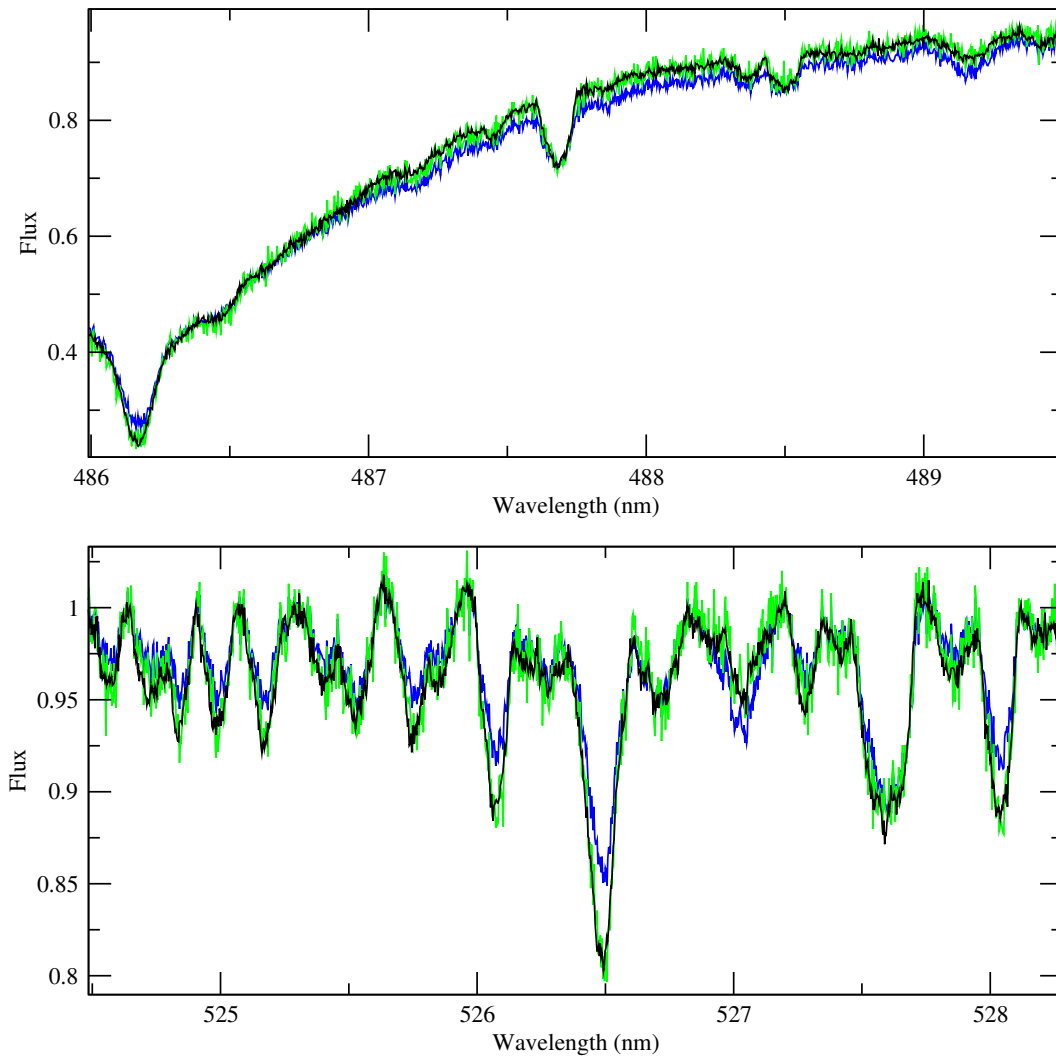


Figure 2.12: Comparison of $H\beta$ and metallic lines in an observation of just HD 72106A, a combined observation of HD 72106A & B, and a reconstructed spectrum of HD 72106A. The black spectrum is of just the primary, from 5 March, 2007. The darker blue (gray) spectrum is an observation of the primary and secondary combined, obtained on 11 January, 2006. The green (lighter gray) spectrum is the reconstructed spectrum of the primary from the combined spectrum. The two observations were obtained at nearly the same rotation phase of the star, with only a difference in phase of 0.04 cycles. The reconstructed spectrum matches the observed primary spectrum almost perfectly, despite the original combined spectrum it was produced from being a poor match.

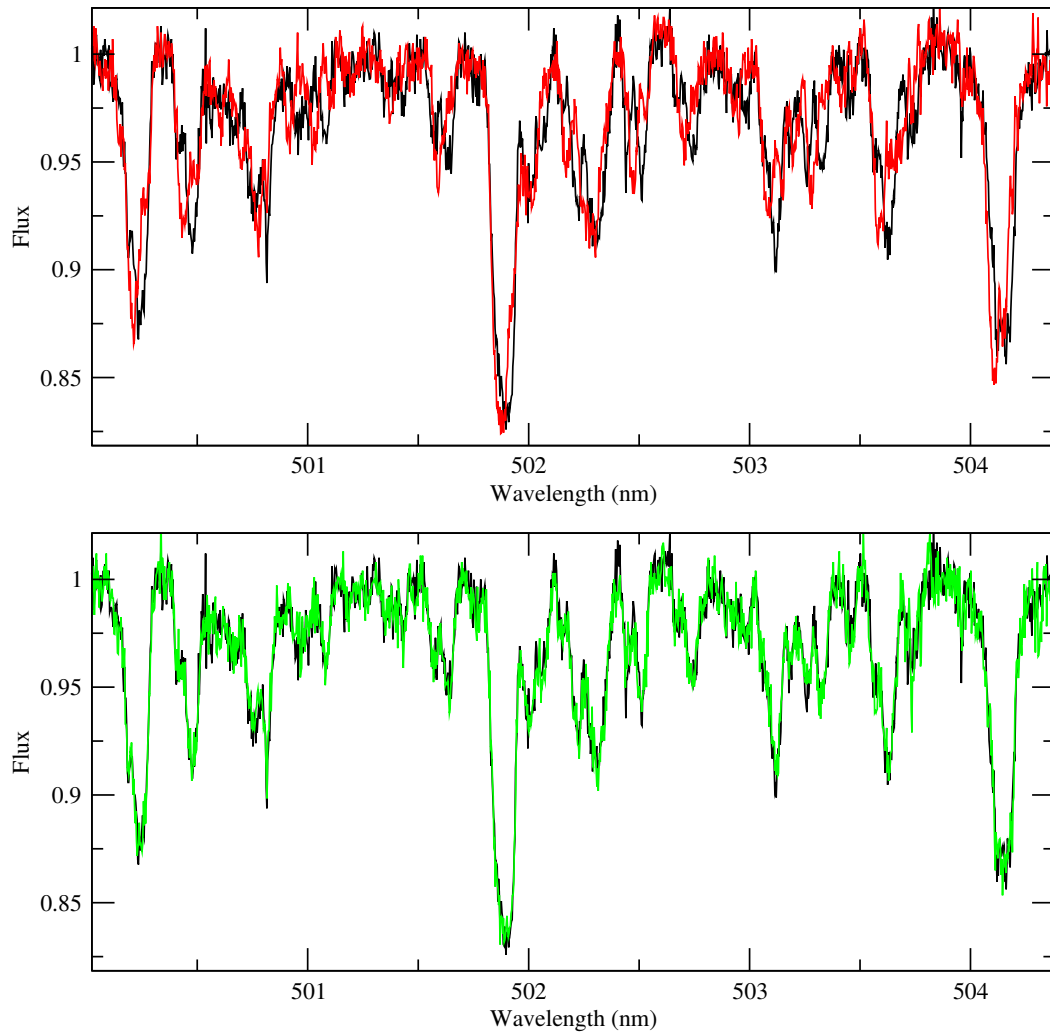


Figure 2.13: Reconstructed spectra of HD 72106A at different rotational phases. In the top frame, spectra with a separation in phase of 0.50, from 9 March, 2007 (black) and 12 February, 2006 (gray/red) are compared. Strong variability and asymmetric line profiles can be seen. In the bottom frame, spectra with a separation in phase of 0.03, from 9 March, 2007 (black) and 11 February, 2006 (gray/green) are compared. While asymmetric line profiles are still present, the spectra are almost identical.

Chapter 3

Analysis

Having demonstrated our ability to accurately recover the individual spectra of the two components of HD 72106, we now discuss the techniques used to analyse the spectra and interpret the properties of the stars. These techniques will allow us to determine the fundamental parameters of both stars, the surface chemical abundances of both stars, the rotational properties of the primary, the magnetic field geometry and strength of the primary, and the surface chemical abundance distribution for the primary.

3.1 Basic Physical Parameters

3.1.1 Effective Temperature and Surface Gravity

Determining fundamental physical parameters for HAeBe stars is very challenging. Initially, we require effective temperature (T_{eff}) and surface gravity ($\log g$ in logarithmic units) to characterize the stellar atmosphere. Photometric methods, using

photometry in several different bands and an appropriate photometric calibration, are unreliable. This is due to contributions to the energy distribution from circumstellar emission and absorption from dust and gas (e.g. van den Ancker et al., 1998). Fitting a model spectral energy distribution to an observed one can in principle be used to derive a temperature, however no appropriate observations exist for the individual components of HD 72106. Balmer line fitting is the remaining commonly used technique. This is also an unreliable technique, as many HAeBe stars display emission in their Balmer lines, and Balmer lines generally don't provide a unique solution for T_{eff} and $\log g$. However, the HD 72106 system is fairly evolved, to the point that the primary is at about the zero age main sequence, and hence one expects little emission in the Balmer lines of either component. Observationally, the primary displays no observable emission in Balmer lines; the secondary has observable emission only in $\text{H}\alpha$ and the $\text{OI } 7771 \text{ \AA}$ lines in our spectra.

Balmer line fitting was performed by Wade et al. (2005) for both the secondary and the primary of HD 72106. Following Wade et al. (2005), we attempted to constrain T_{eff} and $\log g$ using the Balmer lines in the observed spectra. The observed Balmer lines were compared to theoretical models computed with the ATLAS9 code (Kurucz, 1993), calculated with solar metallicity model atmospheres. The theoretical spectra, were convolved with a Gaussian instrumental profile, with a full width at half-maximum adjusted to match the resolution of the observations. Balmer lines in ESPaDOnS spectra are generally recorded in multiple spectral orders, as mentioned earlier. Normalization of echelle spectra between orders can be unreliable. The normalization is further complicated by the lack of true continuum for large portions of the orders due to the broad Balmer line wings. Consequently, the modeling results

from the ESPaDOnS Balmer lines were viewed as tentative at best.

Observations from the FORS1 (FOcal Reducer/low dispersion Spectrograph) instrument at the Very Large Telescope (VLT) in Chile were obtained from Wade et al. (2005). The observations were obtained with the grism GRIS 600B+12, providing a resolving power of about 815 from 345 nm to 590 nm. Individual spectra of both HD 72106A and HD 72106B were obtained. As FORS1 is a single order spectrograph, these spectra were collected in a single order. Therefore, they do not suffer from the normalization effects that afflict the ESPaDOnS Balmer lines. Balmer line fitting was performed on these spectra by Wade et al. (2005) and Drouin (2005). For the primary they find: $T_{\text{eff}} = 11000 \pm 1000$ K and $3.5 \leq \log g \leq 4.5$, (best fit $T_{\text{eff}} = 11000$ K, $\log g = 4.0$). For the secondary they find $T_{\text{eff}} = 8000 \pm 500$ K and $4.0 \leq \log g \leq 4.5$, (best fit $T_{\text{eff}} = 8000$ K, $\log g = 4.5$). We repeated the fitting procedure with the FORS1 spectra ourselves, using the method outlined above, and arrived at results identical to Wade et al. (2005) and Drouin (2005) for the primary. For the secondary we find the temperature range 7500 K to 9000 K more realistic, with a best fit value of 8000 K at $\log g = 4.5$. The $\log g$ of the secondary we find to be in the range 4.0 to 4.5 range, with smaller values being more appropriate for hotter temperatures. These values are also consistent with the values determined by Balmer line fitting in the ESPaDOnS spectra. Sample fits from of the FORS1 Balmer lines are shown in Figure 3.1 for the best fit values, as well as the $T_{\text{eff}} = 8750$ K, $\log g = 4.0$ model discussed below.

When spectrum synthesis was performed for HD 72106B, it became apparent that the Balmer line best fit T_{eff} and $\log g$ were not able to reproduce the detailed line profiles. The spectrum synthesis procedure is discussed in more detail in Section

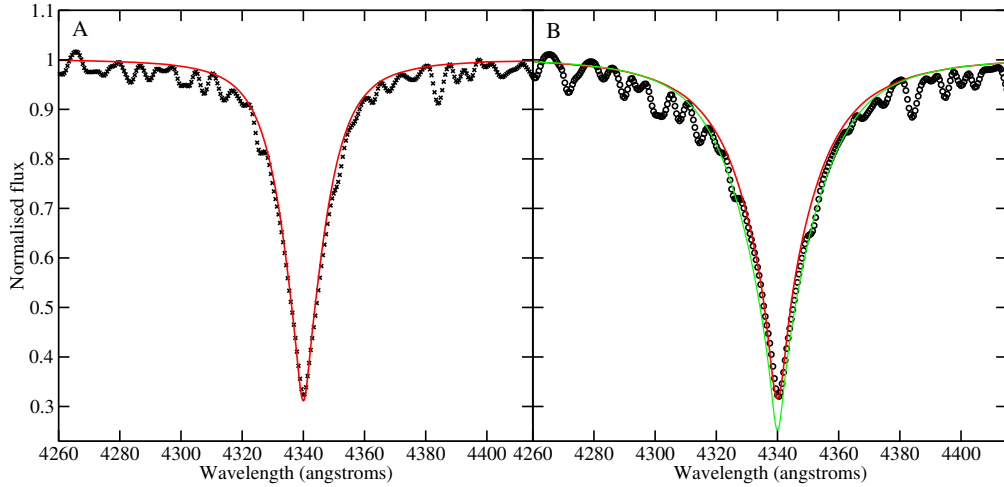


Figure 3.1: Sample Balmer line fits of $H\gamma$ for HD 72106A in frame A and HD 72106B in frame B. The solid lines represent best fit models and the points represent the observed spectra. In frame A the model is $T_{\text{eff}} = 11000$ K $\log g = 4.0$. In frame B the darker (red) line represents a $T_{\text{eff}} = 8000$ K $\log g = 4.5$ model and the lighter (green) line represents a $T_{\text{eff}} = 8750$ K $\log g = 4.0$ model.

3.3.2, with results discussed in Section 4.1. After extensive spectrum modeling in 7 independent spectral windows, with the range of T_{eff} and $\log g$ allowed by the error bars from Balmer line fitting, it was found that the values $T_{\text{eff}} = 8750$ K and $\log g = 4.0$ gave a substantially better fit to lines across the spectrum of HD 72106B. Even with chemical abundance, projected rotational velocity, and microturbulence as free parameters, an 8000 K temperature resulted in systematic inconsistencies between the model and observed spectra, as did a $\log g$ of 4.5. As a consequence, we adopt $T_{\text{eff}} = 8750$ K and $\log g = 4.0$ as the most accurate effective temperature and surface gravity for the secondary. Best fit synthetic spectra for both the initial $T_{\text{eff}} = 8000$ K, $\log g = 4.5$ model and the best fit $T_{\text{eff}} = 8750$ K, $\log g = 4.0$ model are shown in Figure 3.2. However, a temperature of 9000 K and $\log g$ of 4.0 provides almost as good a fit as the 8750 K model. Including the full range of T_{eff} and $\log g$ which

provide at least marginally acceptable fits to the modeled metallic lines in HD 72106B, we find a conservative uncertainty in T_{eff} of 500 K and in $\log g$ of 0.5. While the best fit values of $T_{\text{eff}} = 8750 \pm 500$ K and $\log g = 4.0 \pm 0.5$ produce a somewhat poorer fit to the Balmer lines, the fit to metallic lines is improved substantially, hence we conclude that the higher temperature and lower $\log g$ are more accurate.

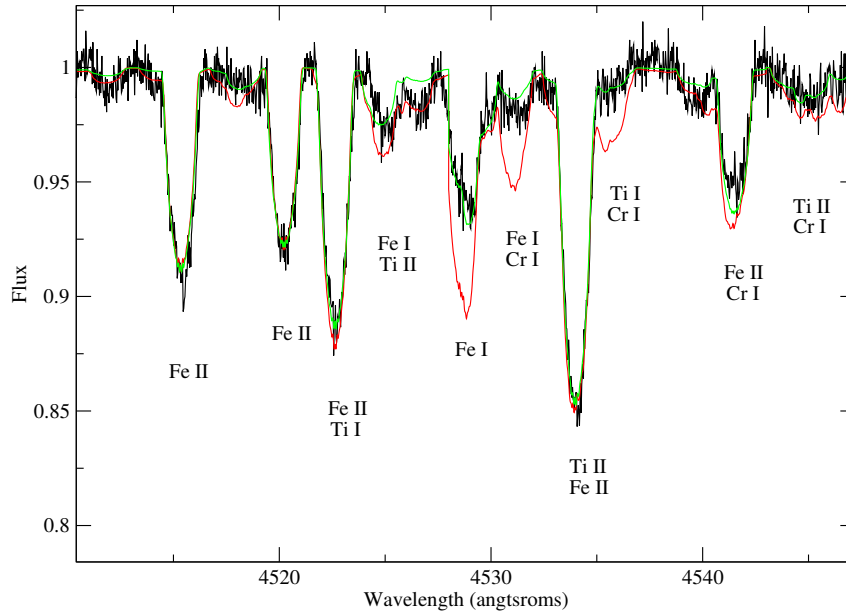


Figure 3.2: Sample best fit spectra for HD 72106B at both the original $T_{\text{eff}} = 8000$ K and $\log g = 4.5$ in (in red/darker gray) as well as the best fit $T_{\text{eff}} = 8750$ K $\log g = 4.0$ (in green/lighter gray). Major contributors to each line are labeled, in order of importance. This represents a segment of a larger 100 \AA region that was fit simultaneously. For both T_{eff} and $\log g$ values, $v \sin i$, microturbulence, and chemical abundances were fit. Even with these free parameters, clear discrepancies between lines of different ionization states of the same element can be seen in the $T_{\text{eff}} = 8000$ K and $\log g = 4.5$ case. The $T_{\text{eff}} = 8750$ K $\log g = 4.0$ model resolved these discrepancies, and hence we adopt it as the best fit effective temperature and surface gravity.

3.1.2 Mass, Radius and Age

With an effective temperature and luminosity it is straightforward to place a star on the Hertzsprung-Russell (H-R) diagram, which allows for the determination of other physical parameters (by comparison with evolutionary models) such as mass and age. In the case of the HD 72106 system, Hipparcos parallax measurements exist, allowing one to determine luminosity using the inverse square law.

The observed Hipparcos parallax of the HD 72106 system is 3.47 ± 1.43 mas (ESA 1997), which indicates that the system is situated at a heliocentric distance of 288_{-84}^{+202} pc.

Using this distance, one can convert the apparent (observed) magnitude to an absolute magnitude, with the standard distance modulus relation:

$$M_v = m_v - 5 \log d + 5, \quad (3.1)$$

where d is the heliocentric distance of the object, m_v is the apparent magnitude and M_v is the absolute magnitude (Ostlie & Carroll, 1996). To obtain the luminosity of an object one requires a bolometric (i.e. integrated across all wavelengths) magnitude. The bolometric absolute magnitude (M_{bol}) is calculated from the absolute magnitude by addition of the appropriate bolometric correction (BC) (Ostlie & Carroll, 1996):

$$M_{\text{bol}} = M_v + BC. \quad (3.2)$$

Before applying a bolometric correction we first converted the Tycho V magnitude, available for HD 72106 from Fabricius & Makarov (2000), into a standard Johnson V magnitude. This is necessary because bolometric correction tabulations are general for the Johnson V band. The Tycho V and Johnson V filters are very similar, so a linear conversion can be used unless extreme accuracy is required. In the case of the

HD 72106 system the uncertainties in distance dominate any uncertainties due to the conversion from Tycho to Johnson V magnitudes. We therefore used the empirical relation:

$$V = V_T + 0.09(B_T - V_T), \quad (3.3)$$

where V is the Johnson V magnitude, V_T is the Tycho V magnitude and B_T is the Tycho B magnitude (ESA, 1997).

For the primary, the bolometric correction relation of Landstreet et al. (2007) was used. This calibration is tailored specifically for magnetic chemically peculiar A and B type (Ap and Bp) stars, hence it is the most appropriate calibration available for the primary¹. Due to the strong chemical over-abundances seen in Ap/Bp stars, many abnormally strong metallic lines are present in their spectra. These lines absorb flux in one wave band, which is then re-emitted in other wavebands. This ‘line blanketing’ effect results in Ap/Bp stars having spectral energy distributions that differ somewhat from normal A and B stars, hence they require a special bolometric correction. The bolometric correction $BC_{\text{Ap}}(T_{\text{eff}})$ (in magnitudes) from Landstreet et al. (2007) is given by:

$$BC_{\text{Ap}}(T_{\text{eff}}) = -4.891 + 15.147\theta - 11.517\theta^2, \quad (3.4)$$

where $\theta = 5040.0/T_{\text{eff}}$.

For the secondary, the bolometric correction for main sequence stars from Gray (2005) was used. The correction is as follows:

$$\begin{aligned} BC = & -64741.46 + 67717 \log T_{\text{eff}} - 26566.141 \log^2 T_{\text{eff}} \\ & + 4632.926 \log^3 T_{\text{eff}} - 303.0307 \log^4 T_{\text{eff}}, \end{aligned} \quad (3.5)$$

¹The strong chemical peculiarities of the primary, and their similarity to those of Ap/Bp stars, are discussed further in Section 4.1

where T_{eff} is the effective temperature of the star.

With the bolometric magnitudes for both stars one can finally determine the luminosity (L) of the two stars, using the relation:

$$\frac{L}{L_{\odot}} = 10^{(M_{\text{bol}} - M_{\text{bol}}^{\odot})/2.5}, \quad (3.6)$$

where L_{\odot} is the luminosity of the sun and M_{bol}^{\odot} is the bolometric magnitude of the sun ($L_{\odot} = 3.826 \times 10^{26}$ W, $M_{\text{bol}}^{\odot} = 4.76$ mag) (Ostlie & Carroll, 1996). The luminosity of the primary determined from equation 3.6 is $23^{+31}_{-13} L_{\odot}$, and the luminosity of the secondary is $9.9^{+12.7}_{-5.6} L_{\odot}$.

The radius of each star can be computed directly from the Stefan-Boltzmann equation:

$$L = 4\pi R^2 \sigma T_{\text{eff}}^2, \quad (3.7)$$

where R is the stellar radius and σ is the Stefan-Boltzmann constant. This produces a radius of $1.3 \pm 0.6 R_{\odot}$ for the primary and $1.4 \pm 0.6 R_{\odot}$ for the secondary.

The stars can be placed on an H-R diagram using the derived values of T_{eff} and L , as shown in Figure 3.3. The H-R diagram positions can be compared with theoretical evolutionary tracks and isochrones, allowing the determination of mass and age. We use the pre-main sequence evolutionary model calculations of Palla & Stahler (1993). We find the age of the HD 72106 system to be between 3 and 13 Myr, based on the position of the secondary in the H-R diagram. The mass of the primary is $2.4 \pm 0.4 M_{\odot}$ and mass of the secondary is $1.9 \pm 0.2 M_{\odot}$. The position of the primary falls mostly below the zero age main sequence line (ZAMS), but is still consistent with the ZAMS within 1σ uncertainties. If one compares the H-R diagram position of the primary to main sequence evolutionary tracks, one can constrain its age to be less than $8.2 \log$ yr (~ 160 Myr). However, if the system is truly a binary, the constraint on the age

of the system derived from the secondary (3 to 13 Myr) is much more precise. Error bars associated with T_{eff} , $\log g$, luminosity, radius, and mass are all approximately 1σ .

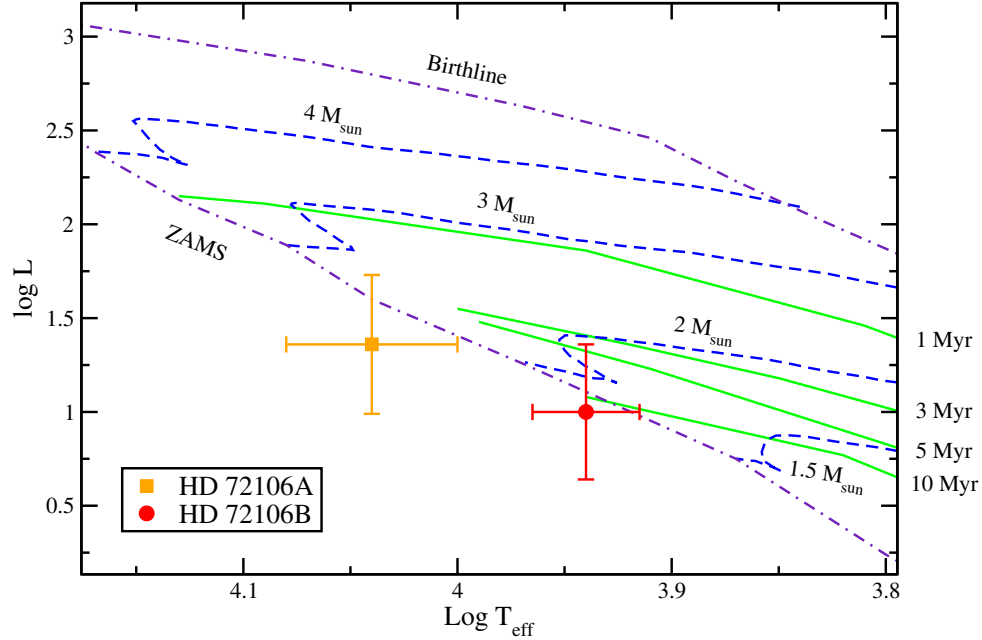


Figure 3.3: An H-R diagram containing both components of the HD 72106 system. Isochrones (solid lines) and evolutionary tracks (dashed lines), as well as the birth line (for an accretion rate of $10^{-5} M_{\odot} \text{ yr}^{-1}$) and the zero age main sequence (ZAMS) line, are taken from Palla & Stahler (1993).

It is worth noting that, while the absolute luminosities of the components are poorly determined, their ratio is very well determined. This is because the major uncertainty in the absolute luminosity is the distance to the stars, and the stars are situated at the same distance. Thus the uncertainties on the radii or masses derived for the two stars are not independent. If the primary has a higher mass then, due to

the highly accurate ratio of luminosities, so does the secondary. The spacing between the components in $\log L$ on the H-R diagram must remain essentially fixed.

Given the importance of the evolutionary status of these stars, a somewhat more in-depth discussion is necessary. The presence of circumstellar material around the HAeBe secondary assures us of its very young age, justifying the use of pre-main sequence evolutionary tracks. For the primary we do not have the same strong justification. Given its H-R diagram position, the primary could be as young as ~ 3 Myr (as measured from the birth line), and in that case have $\sim \frac{1}{4}$ of its pre-main sequence lifetime remaining. The most likely case (from ‘best fit’ positions) is that the system is ~ 10 Myr old, thus the primary has just entered the main sequence and the secondary is on its final approach to the ZAMS. In this case the primary would have spent ~ 6 Myr on the main sequence, giving it a fractional age on the main sequence (τ) of 0.01. In the oldest limiting case, the system is ~ 13 Myr old and secondary is just reaching the ZAMS. In this scenario, the primary has been on the main sequence for up to ~ 9 Myr and has fractional age of 0.015. Further study, particularly a more accurate distance measurement, is necessary to more precisely determine the evolutionary status of the primary. Regardless, if HD 72106A is not on the pre-main sequence, it is certainly one of the youngest main sequence stars of its type.

3.2 Binarity

Determining whether the HD 72106 system is truly a binary or just a double star (i.e. an accidental conjunction of 2 stars at different distances along the line of sight) is critical. If the system is a binary it allows us to constrain the age of the primary

much more precisely than would otherwise be possible, as demonstrated in Section 3.1.2. Additionally, it implies that both components formed from approximately the same material, making HD 72106 an interesting system from the point of view of stellar magnetic and chemical evolution.

As mentioned previously, the system has a (projected) separation of $0.8''$, and thus is fairly widely separated. Given the Hipparcos parallax of 3.47 ± 1.43 mas, this implies a minimum possible physical separation of 232 ± 96 AU.

The Hipparcos solution for the system finds that the stars have the same parallax and proper motions. In the spectrum fitting (to be described in Section 3.3) we included heliocentric radial velocities for each star as a free parameter. From this fitting, we find identical radial velocities of 22 ± 1 km s⁻¹ for both components. Thus the stars are in the same point in space and moving together (in three dimensions), strongly suggesting that they are in fact physically associated.

For the system to be a true binary, the stars must be orbiting one another. We must check if the apparent lack of relative motion is consistent with the stars being gravitationally bound. Assuming a circular orbit, and that the minimum possible separation is the true separation (r), one can easily calculate the relative velocity of the components of the binary (v). This is given by (Ostlie & Carroll, 1996):

$$v^2 = G(m_1 + m_2) \left(\frac{2}{r} - \frac{1}{a} \right), \quad (3.8)$$

where m_1 and m_2 are the masses of the primary and secondary respectively, G is the gravitational constant, and a is the semimajor axis of the orbit of the reduced mass about the center of mass of the system; in our circular case $a = r$. This equation follows directly from the virial theorem. The true separation and orbits of the components are unknown, and cannot be determined without accurate measurements

of the relative motion of the components. In this assumed geometry, the relative velocity of the stars is $4.0 \pm 0.9 \text{ km s}^{-1}$ and the orbital period is 1700 ± 800 years.

If one considers the case in which system is inclined with the orbital plane along the line of sight and, as assumed above, the observed separation of the stars is the full physical separation in a circular orbit, then one can calculate the maximum radial velocity possible. In this geometry, illustrated in Figure 3.4, the relative velocity between the stars is completely projected along the line of sight, and hence is larger than the observed radial velocities. However, if the plane of the orbit is tilted by only 15° then the values become consistent with the observed velocities, within uncertainty. Furthermore, if the stars' physical separation is larger than we have assumed then the velocities can be consistent with smaller inclination angles.

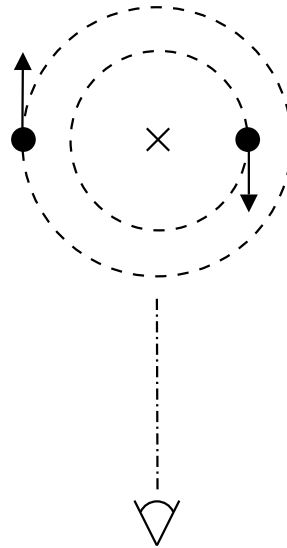


Figure 3.4: A schematic diagram of the orbital geometries considered for HD 72106. For the first case discussed in Section 3.2, with the orbital plane aligned along the line of sight, the observer would be looking along the dot dashed line. For the second case discussed, the observer would be looking down on the page, towards the 'X'.

In the other extreme, if the plane of orbit of the stars lies in the plane of the sky, as

illustrated in Figure 3.4, then an observed relative proper motion of $2.9 \pm 1.4 \text{ mas yr}^{-1}$ should be seen. One can calculate this simply by converting the relative motion given above into a proper motion across the sky, at the appropriate distance. The result of this calculation is marginally consistent with the Hipparcos proper motion reported in Section 1.5. While the observed relative proper motion is zero, the uncertainties on this value are significant. This results in a difference between the two values of 1.3σ . Again, if the physical separation of the stars is larger, or if the orbit is inclined away from ‘face on’, the discrepancies become smaller.

Dr. Brian Mason at the United States Naval Observatory kindly provided a list of separation and position angle observations from the Washington Double Star Catalog, dating back to 1902 (private correspondence, Mason, 2006). These have been compiled from a number of sources in the literature, such as Hartkopf et al. (1996) and the Hipparcos mission (ESA, 1997), as well as a large number of observatory bulletins that are no longer readily accessible, such as the Republic Observatory at Johannesburg Circular. These observations indicate no change in the separation of the components, but hint at a possible change in position angle of roughly $+10^\circ$. Unfortunately, the accuracy of the older observations in this catalog is unclear. If a 10° position angle change over 90 years (1902-1992) has occurred, that is very much consistent with the range of possible relative motions between components of HD 72106. We shall consider the scenario presented above, in which the orbital plane is in the plane of the sky and the stars are minimally separated on circular orbits. In this case the change in position angle per year can be trivially calculated from the relative motion and separation of the two stars. This produces a change of $19 \pm 9^\circ$ in 90 years. This is in good agreement with the $\sim 10^\circ$ value. Again, the theoretical value would be

somewhat smaller if the orbit were inclined further or if the physical separation were larger. There is clearly a large range of models that could fit this observation.

Generally one ought to consider elliptical orbits, however with the limited observations available for HD 72106 it is difficult to do so with any accuracy. Considering an orbit with an eccentricity 0.5 and the system at periastron, no major changes are seen to the above results, and a wide range of models are still allowed. The inclinations discussed above are restricted only by roughly another 5° .

One final constraint is that the stars must have consistent positions on the H-R diagram. As discussed in Section 3.1.2 and shown in Figure 3.3, this is the case. The ages of the stars are consistent, implying that the system can be co-eval, hence providing further evidence for binarity.

Thus we conclude that HD 72106 is almost certainly a true binary system. The observations are, admittedly, not sufficient to guarantee that the stars are physically associated with complete certainty. However, there is very strong evidence that this is truly a binary system. The stars are at the same position in space, moving in the same (three dimensional) direction at the same speed, and allow for a wide range of gravitationally bound orbits. While we cannot determine the geometry of the orbit, the small relative radial velocity and possible change in position angle suggest that the binary may be closer to ‘face on’ than to ‘edge on’. The physical parameters of HD 72106A and HD 72106B, as well as some of the orbital constraints, are summarized in Table 3.1

	HD 72106A	HD 72106B
T_{eff} (K)	11000 ± 1000	8750 ± 500
$\log g$	4.0 ± 1.0	4.0 ± 0.5
R (R_{\odot})	1.3 ± 0.6	1.4 ± 0.6
M (M_{\odot})	2.4 ± 0.4	1.9 ± 0.2
Age	10^{+3}_{-7} Myr	
Orbital Constraints		
Minimum possible separation	232 ± 96 AU	
Maximum Relative velocity	4.0 ± 0.9 km s $^{-1}$	
Minimum Orbital period	1700 ± 800 years	

Table 3.1: Fundamental physical parameters for HD 72106A and B, and orbital constraints on the system. The orbital constraints derived assume that the minimum possible separation between the stars is their true physical separation, as well as assuming circular orbits for both stars.

3.3 Spectrum Synthesis and Fitting

The observed total intensity (Stokes I) spectrum of a star contains a tremendous amount of information about the photosphere of the star. In recent years the most common, and arguably the most accurate, method of accessing information about conditions near the surface of a star has been to model the spectrum in detail. Computer modeling of spectra can provide accurate information about surface chemical abundances, projected rotation velocity ($v \sin i$), velocity fields and the magnetic field. Effects of chemical stratification near the surface of the star are sometimes detectable (e.g. Babel, 1992; Ryabchikova et al., 2002; Kochukhov et al., 2006). Magnetic field strength, effective temperature and surface gravity also play important roles in the formation of absorption lines, but are best constrained before extensive metallic line modeling is undertaken, so as to simplify the parameter space of possible models.

In this work, modeling was performed using the ZEEMAN2 spectrum synthesis code (Landstreet, 1988; Wade et al., 2001). Fitting of the model spectrum to the observed spectrum was performed using a Levenberg-Marquardt χ^2 minimization method.

3.3.1 ZEEMAN2

ZEEMAN2 is a local thermodynamic equilibrium (LTE) spectrum synthesis code that solves the fully polarized radiative transfer equations. The code is descended from the ZEEMAN code, written by Landstreet (1988) and then updated by Wade et al. (2001). ZEEMAN2 is written in FORTRAN 77, and calculates Stokes I, Q, U, and V spectra for an arbitrary set of rotational phases of a rotating magnetic star.

The ZEEMAN2 code takes as input a pre-computed plane parallel model atmosphere, as well as a table of atomic line data for the spectral line profiles to be computed. The model atmospheres used in this thesis were computed using Atlas9 (Kurucz, 1993) for solar abundances and 2 km s^{-1} microturbulence. Atomic data was extracted from the Vienna Atomic Line Database (VALD) (Kupka et al., 1999). The “extract stellar” utility in VALD was used with a line depth threshold of 0.01. For the primary, a T_{eff} of 11000 K was used with a $\log g$ of 4.0; a 2 km s^{-1} microturbulence was used to simulate the desaturation effect of the magnetic field², and very strong chemical over-abundances were included, to ensure the completeness of the line list. For the secondary a $T_{\text{eff}} = 8500 \text{ K}$ and $\log g = 4.0$ were used with a 2 km s^{-1} microturbulence. Initially strong chemical over-abundances were included to

²Magnetic desaturation is the increase in equivalent width seen in stronger absorption lines due to the presence of a magnetic field. Such saturated lines, which are no longer on the linear part of their curve of growth, are split by the Zeeman effect. This increases the wavelength range over which the line can absorb light, and hence the total amount of light absorbed, if the line is saturated.

ensure completeness of the line list, however when the abundances in the secondary proved to be normal, line requests were altered to only use solar abundances for line selections.

The ZEEMAN2 code calculates Zeeman splitting patterns of atomic lines using the total angular momentum (j) quantum number for the lower and upper levels of the transition. Experimental Landé factors for both levels are used to calculate the strength of the splitting. Partition functions are calculated from the polynomial approximation of Bolton (1970, 1971) for many lighter elements up to Zr. For heavier elements, the approximations of Aller & Everett (1972) (for many neutral and singly ionized rare earths), Cowley & Adelman (1983) (for a variety of heavier species), and Cowley (1994) (for doubly ionized rare earths) are used. Species not included in these sources use the approximations of Irwin (1981). Ionic populations are calculated with the Saha equation for ions up to the triply ionized state. Radiation damping, quadratic Stark damping and van der Waals damping are included, using constants supplied by VALD. If the constants are not available, various approximations are used (see Wade et al., 2001). Line opacity and anomalous dispersion profiles for metallic elements are calculated using Voigt and Faraday-Voigt functions, implemented with the numerical recipe of Humlicek (1982).

Continuous opacities are calculated from bound-free and free-free transitions for neutral H, neutral He, and H^- , as well as Rayleigh scattering from neutral H, and electron scattering. These opacity sources are implemented using a variety of standard algorithms, as detailed by Wade et al. (2001).

Numerical integration of the polarized radiative transfer equations is performed using the semi-analytic method of Martin & Wickramasinghe (1979). The algorithm

described by Martin & Wickramasinghe (1979) has been augmented to better handle a number of special cases by Landstreet (1988) and Wade et al. (2001).

The magnetic field is included as an axisymmetric oblique multipole, with terms up to octupole. Surface chemical abundance inhomogeneities can be described in a simple parameterized fashion, usually by rings in magnetic latitude. Vertical chemical stratification can be described using a simple two-step model. These last two features were not used in this project, as there was no clear evidence for vertical chemical stratification, and surface inhomogeneities were investigated in a more detailed fashion with Doppler Imaging (see Section 3.7).

At each rotational phase, the visible disk of the star is divided into several hundred to several thousand surface elements of approximately equal projected area. The radiative transfer equation is integrated through the model atmosphere, with the local magnetic field vector and chemical abundance included, for each of these elements in their frame of reference. Large scale velocity fields, particularly $v \sin i$, can then easily be applied by Doppler shifting the local spectrum computed for individual surface elements. The final step in the calculation of the synthetic flux spectrum is to convolve the disk-integrated spectrum with an instrumental profile (assumed to be Gaussian, with a width appropriate to the observed spectra).

The ZEEMAN2 code as been widely tested over a number of years and is now considered very robust (e.g. Wade et al., 2001; Bagnulo et al., 2003; Folsom et al., 2007; Silvester, 2007).

3.3.2 Fitting Procedure

For both components of the HD 72106 system, surface chemical abundances and $v \sin i$, as well as microturbulence for the secondary, were determined by fitting a synthetic spectrum from ZEEMAN2 to an observed spectrum. The high S/N observation of the primary at JD 2453747.99629 and the secondary at JD 2454164.84650 were used. Effective temperature and surface gravity were determined as described in Section 3.1.1. The magnetic field of the primary was determined as described in Section 3.5 and assumed to be null for the secondary, since there is no evidence for the presence of a magnetic field in HD 72106B (see Section 4.3). As previously mentioned, no attempt was made to model the surface abundance inhomogeneities of the primary. Therefore, the chemical abundances of the primary derived here are, strictly speaking, only mean surface abundances for one phase. However, a comparison of the JD 2453747.99629 spectrum to the average of all our spectra of HD 72106A shows a particularly good correspondence. Fitting synthetic spectra to both the average observed spectrum and the JD 2453747.99629 spectrum gives a difference in the inferred abundances between the two spectra of at most 0.05 dex. Thus the abundances presented here are roughly representative of the global mean surface abundances of HD 72106A. A detailed investigation of surface abundance inhomogeneities is discussed in Section 3.7, with results described in Section 4.4.

Initially, for each star, direct comparison of the synthetic and observed spectra by eye was used to determine approximate best fit values for relevant abundances, $v \sin i$ and microturbulence. Once approximate values were determined, either from manual fitting or fitting of another spectral region of the same object, the values were passed as initial values to an automatic Levenberg-Marquardt χ^2 minimization routine.

The Levenberg-Marquardt fitting routine uses the recipe of Press et al. (1992). The routine is designed as a Fortran 90 wrapper around the preexisting ZEEMAN2 code, thus leaving the ZEEMAN2 source code virtually unaltered, allowing for easy upgrades as ZEEMAN2 is improved. Comparisons of the results of the Levenberg-Marquardt fitting routine to careful fits by eye show very good agreement, well within the uncertainties. Best fit model spectra, found using the Levenberg-Marquardt routine, are shown in Figures 3.5 and 3.6; further examples can be seen in Figures 4.1 and 4.3.

Despite the fact that χ^2 values are calculated, they cannot be used to determine reliable quantitative uncertainty estimates. The problem of spectrum synthesis is sufficiently non-linear that something as simple as the covariance matrix cannot reliably be used. Moreover, the uncertainties are often dominated by uncertainties in spectrum normalization or errors and omissions in the atomic line data, which are not reflected in the observational error bars. This produces large values of χ^2 , and makes a formal uncertainty based on changes in χ^2 unrealistic. Consequently, we base uncertainties on the standard deviation of best fit values from a number of independently fit spectral regions. This accounts for intrinsic noise in the data, uncertainties in atomic line data, and uncertainties in continuum normalization, as well as uncertainties (although not systematic errors) in other parameters such as T_{eff} and $\log g$. In cases where the abundance of a particular element was determined using only a few lines, uncertainties were based on a conservative estimate of the change in abundance necessary to shift the synthetic spectrum beyond any noise in the observed spectrum, or any possible normalization errors. These uncertainty values represent approximately a 2σ confidence level, and are indicated by an asterisk (*) in Table

4.2. All other uncertainties in abundances, $v \sin i$, and microturbulence are reported in Table 4.2 at the 1σ confidence level.

Good, unique fits to the observed spectra are generally achievable. Figure 3.5 shows a good sample fit of a synthetic to an observed spectrum of the primary, Figure 3.6 shows a good fit to an observation of the secondary. Figures 4.1 and 4.3 present additional high quality fits.

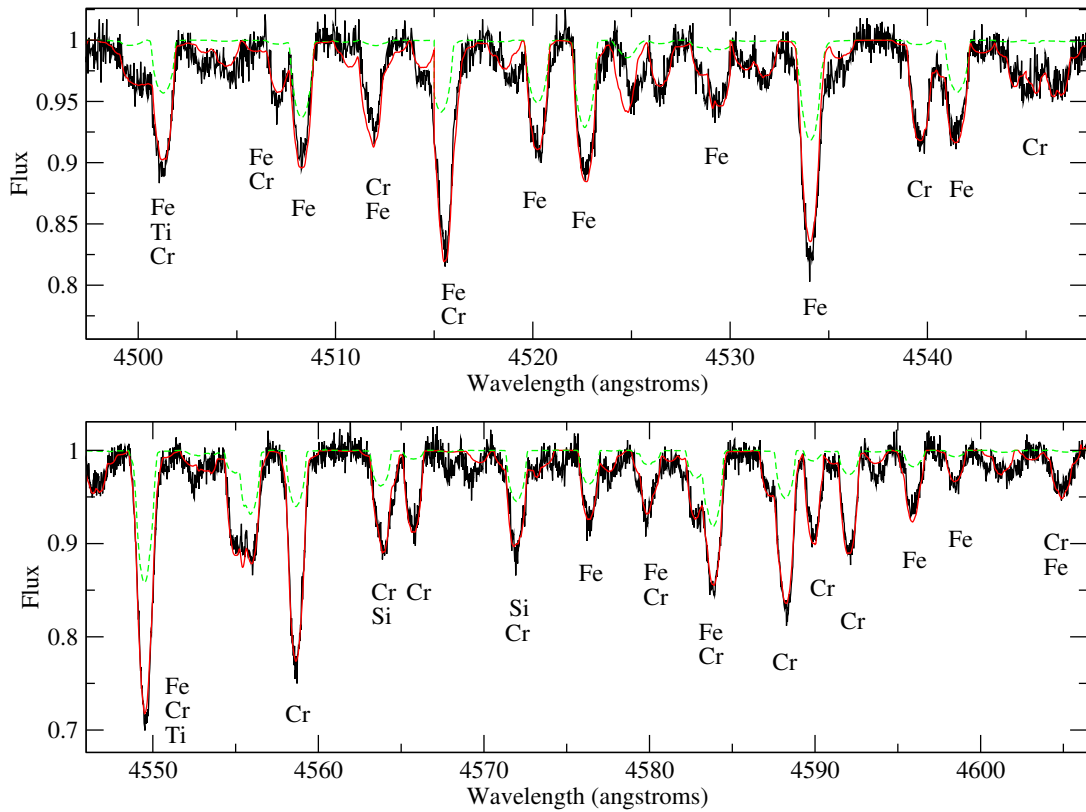


Figure 3.5: Sample synthetic spectra fit to observations of HD 72106A, in two independently fit spectral regions. Major contributors to each line have been labeled, in order of importance. The smooth solid line is the best fit spectrum in this region, the dashed line is a spectrum computed with solar chemical abundances. These represent sections of larger 100 \AA regions that were fit simultaneously. The parameters for these spectra were determined using the Levenberg-Marquardt fitting routine.

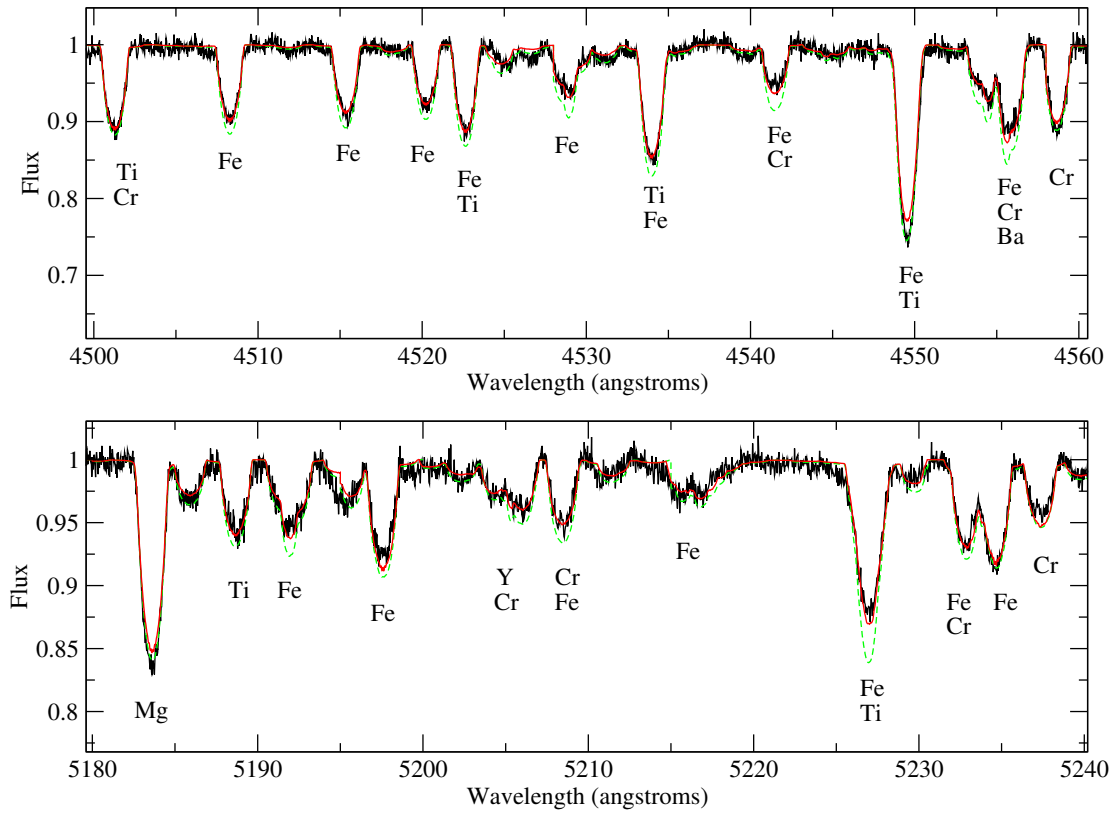


Figure 3.6: Sample synthetic spectra fit to observations of HD 72106B, in two independently fit spectral regions.. Major contributors to each line have been labeled, in order of importance. The smooth solid line is the best fit spectrum in this region, the dashed line is a spectrum computed with solar chemical abundances. These represent sections of a larger 100 Å regions that were fit simultaneously. The parameters for these spectra were determined using the Levenberg-Marquardt fitting routine.

In the case of HD 72106B, poor fits to the observed spectrum were found initially, despite including $v \sin i$, microturbulence, and chemical abundance as free parameters. Eventually it was found that the T_{eff} and $\log g$ values from Balmer line fitting were insufficiently constrained for accurate spectrum synthesis. Seven independent regions of spectrum were fit for all allowed T_{eff} and $\log g$ values from Balmer line fitting, in steps of 500 K in T_{eff} and 0.5 in $\log g$. An extra step in temperature at 8750 K was included when both 8500 K and 9000 K (at $\log g = 4.0$) were found to provide close to acceptable fits. The $T_{\text{eff}} = 8750$ K and $\log g = 4.0$ model was found to give a visibly better fit than other models tested, and hence has been adopted as the best fit temperature. The difference in fits between the initial and best fit models is illustrated in Figure 3.2. The $T_{\text{eff}} = 9000$ K and $\log g = 4.0$ model was only marginally worse than the best fit case, and cannot be completely ruled out. Additionally, the sensitivity of the fit to $\log g$ is weaker than the sensitivity to temperature. However, $\log g = 4.5$ did produce several small discrepancies that were corrected by a decrease to $\log g = 4.0$, thus we prefer the $T_{\text{eff}} = 8750$ K and $\log g = 4.0$ model.

3.4 Least Squares Deconvolution

For the typical field strength and rotation velocity observed for magnetic intermediate mass stars (~ 1 kG and ~ 40 km s $^{-1}$), the circular polarization signal due to a magnetic field in any given line in an ESPaSO n S spectrum is very small. In the case of HD 72106A, which has a field strength typical of Ap/Bp stars, the amplitude of the Stokes V signal is about 0.1-0.3 percent of the Stokes I continuum level (a typical absorption line in Stokes I has a depth of $\sim 10\%$ of the continuum). Consequently, a technique

that can effectively average over many lines in a spectrum to produce a high signal-to-noise ratio would be very valuable. Least Squares Deconvolution (LSD) does this (Donati et al., 1997). This averaging is possible because most metallic lines in a spectrum have approximately the same Stokes I and V profile shape. The spectrum of a star can very approximately be described as a convolution of an average line profile and a set of delta functions, located at each individual line's wavelength and with an amplitude equal to the line's depth. The objective of LSD is to reverse this process and deconvolve the average line profile from the observed spectrum, using a theoretical set of delta functions (referred to as a line mask). The details of the procedure are outlined here for the Stokes V spectrum, although the procedure can also be applied to Stokes I, Q, and U with minimal modification (Wade et al., 2000a)

In the weak-field regime (when magnetic line splitting is much less than thermal Doppler broadening), the Stokes V profile of a line, local to one point on a star's surface, follows the relation (Landstreet, 1982):

$$V_{\text{loc}}(v) \propto g\lambda \frac{\partial I_{\text{loc}}(v)}{\partial v} B_z, \quad (3.9)$$

where $I_{\text{loc}}(v)$ is the local Stokes I profile of the line, g is the Landé factor (magnetic sensitivity), B_z is the line-of-sight (longitudinal) magnetic field strength, and v is the velocity coordinate $c\Delta\lambda/\lambda$ (with $\Delta\lambda$ being the wavelength shift relative to the center of the line at wavelength λ) (Donati et al., 1997). The proportionality constant is the same for all lines. If one assumes that $I_{\text{loc}}(v)$ has the same shape for all lines and simply scales with line depth d then one can write:

$$V_{\text{loc}}(v) = g\lambda dk_{\text{B}}(v), \quad (3.10)$$

where $k_{\text{B}}(v)$ is a proportionality function, the same for all lines, which includes the effect of the longitudinal field. This assumption is strictly true only for optically

thin lines. However, for profiles dominated by rotational broadening it is not a bad approximation (Donati et al., 1997). Integrating $V_{\text{loc}}(v)$ over the surface of a star can effectively be done by integrating over M points in brightness b_M and radial velocity v_M to produce the global $V(v)$. Brightness and radial velocity are used since they provide simpler coordinates for local profiles, which are generated at one particular radial velocity and brightness from the point of view of the observer. The global $V(v)$ can be written as:

$$\begin{aligned} V(v) &= \iint b_M V_{\text{loc}}(v - v_M) dS \\ &= g\lambda d \iint b_M k_B(v - v_M) dS \\ &= w Z(v). \end{aligned} \tag{3.11}$$

If limb darkening is assumed to be constant for all wavelengths, then $Z(v)$, the Zeeman signature (or LSD profile), is constant for all lines. In that case the shape of the Zeeman signature is reproduced by all Stokes V profiles ($V(v)$) scaled by the factor $w = g\lambda d$ (Donati et al., 1997).

The line mask can be represented as:

$$M(v) = \sum_i w_i \delta(v - v_i), \tag{3.12}$$

where v_i is the position, in velocity units, of the i^{th} line, w_i is the weighting (depth) of that line, and δ is the Dirac delta function (Donati et al., 1997). This effectively gives a list of center wavelengths and weightings for all lines of interest. The Stokes V spectrum can then be described as the convolution of $Z(v)$ and $M(v)$ (that is $V = M * Z$), or in terms of a linear system: $\mathbf{V} = \mathbf{M} \cdot \mathbf{Z}$. This assumes that line intensities add linearly, which is clearly not true, especially for stronger, more saturated lines. In intermediate mass stars with moderate rotation rates, such as HD

72106 A and B, there are many unblended or weakly blended lines available in the spectrum, lessening this concern somewhat. In practical experiments, Donati et al. (1997) found that good results were achieved despite this assumption. Other authors, for example Wade et al. (2000a) and Shorlin et al. (2002), support this conclusion. One can then seek the best fit least-squares solution by minimizing the χ^2 function (Press et al., 1992):

$$\chi^2 = {}^t(\mathbf{M} \cdot \mathbf{Z} - \mathbf{V}) \cdot \mathbf{S}^2 \cdot (\mathbf{M} \cdot \mathbf{Z} - \mathbf{V}), \quad (3.13)$$

with \mathbf{Z} (the Zeeman signature) as the matrix of free parameters and the observed Stokes V spectrum (\mathbf{V}). The matrix \mathbf{S} is a square diagonal matrix whose elements S_{jj} are the inverse error bars ($1/\sigma_j$) of the j^{th} pixel in the spectrum. Since our model is linear, the χ^2 problem can be solved using the method of normal equations (e.g. Press et al., 1992) (essentially setting the derivative of χ^2 to 0). This gives the result:

$$({}^t\mathbf{M} \cdot \mathbf{S}^2 \cdot \mathbf{M}) \cdot \mathbf{Z} = {}^t\mathbf{M} \cdot \mathbf{S}^2 \cdot \mathbf{V}, \quad (3.14)$$

or equivalently:

$$\mathbf{Z} = ({}^t\mathbf{M} \cdot \mathbf{S}^2 \cdot \mathbf{M})^{-1} {}^t\mathbf{M} \cdot \mathbf{S}^2 \cdot \mathbf{V}. \quad (3.15)$$

The term ${}^t\mathbf{M} \cdot \mathbf{S}^2 \cdot \mathbf{V}$ is the cross correlation of the observed spectrum (\mathbf{V}) with the line mask (\mathbf{M}). Uncertainties can be estimated from the diagonal elements of the ${}^t\mathbf{M} \cdot \mathbf{S}^2 \cdot \mathbf{M}$ matrix (the auto-correlation matrix). In the case when blending of lines is minimal and photon noise dominates uncertainties, as is often seen in Stokes V spectra, this gives a good estimate of the real uncertainty (Donati et al., 1997). Cases when photon noise is small and improperly calculated blends and other systematic limitations of the model become significant can be diagnosed by large values of χ^2 . In these cases, photon noise based error bars systematically underestimate the true

uncertainty. Therefore the photon noise error bars are scaled up to compensate for the large χ^2 values, in the manner described by Wade et al. (2000a).

LSD analysis was performed on all spectra obtained. Observations of the combined system were transformed into reconstructed spectra of the primary before LSD was performed. A line mask tailored to a star with $T_{\text{eff}} = 10000$ K and Ap-like overabundances (see Shorlin et al., 2002) was used for the primary. An 8000 K line mask with solar abundances was used for the secondary. Sensitivity to line mask details is small, thus discrepancies in temperature or abundance of line masks have little impact on the resulting profiles. Sample LSD profiles for both components are shown in Figure 3.7.

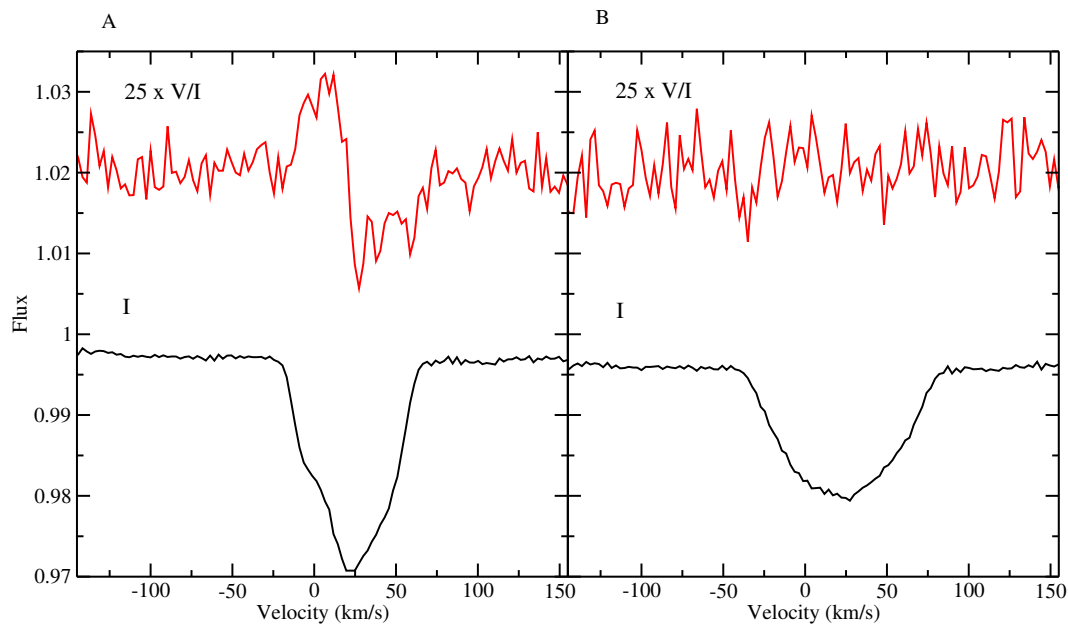


Figure 3.7: Sample Stokes I and V LSD profiles for HD 72106A (in the left frame, labeled A) and HD 72106B (in the right frame, labeled B). A Zeeman signature, indicating the presence of a magnetic field, is clearly visible in frame A, but absent in frame B. A line asymmetry is visible in the Stokes I profile in frame A, due to surface abundance non-uniformities.

3.5 Magnetic Field Analysis

Analysis of a single Stokes V profile can be used to determine the mean longitudinal magnetic field (the surface component of the magnetic field, projected onto the line of sight, and integrated over the visible disk of the star) at one point in time (phase). For our purposes, we wish to calculate the longitudinal field from the LSD profiles discussed in the previous section. This is necessary, as the original spectra have too poor a S/N in individual lines to determine precise magnetic field strengths. The mean longitudinal field strength ($\langle B_z \rangle$) can be calculated from the first-order moment of the LSD Stokes V profile (Mathys, 1989) as follows:

$$\langle B_z \rangle = -2.14 \times 10^{11} \frac{\int vV(v)dv}{\lambda gc \int [I_c - I(v)]dv}, \quad (3.16)$$

where g and λ (in nm) are respectively the *average* Landé factor and wavelength for all lines used in the LSD mask (Donati et al., 1997; Wade et al., 2000b). In equation 3.16 c is the speed of light, v is the wavelength in velocity units, $I(v)$ and $V(v)$ are the Stokes I and V LSD profiles, and I_c is the Stokes I continuum level (which should be unity for a well normalized spectrum). For the primary the values $g = 1.27$ and $\lambda = 527$ nm were used, for the secondary $g = 1.21$ and $\lambda = 535$ nm were used. Longitudinal magnetic field measurements, obtained using equation 3.16, are presented in Table 3.2. Integration was performed through the portion of the line profile that exceeded 15% of the total line depth, with an additional 5 km s^{-1} on either end. This was done to avoid integration over the continuum, ‘diluting’ the longitudinal magnetic field’s signal by increasing the noise. The continuum level I_c is taken from the average value of the Stokes I LSD profile far from the absorption line. The integration (in the velocity coordinate) is performed with respect to the

‘center-of-gravity’ (cog) of the line. The center-of-gravity is calculated by evaluating the expression:

$$\text{cog} = \frac{\int v |V(v) (I_c - I(v))| dv}{\int |V(v) (I_c - I(v))| dv}. \quad (3.17)$$

Using the center-of-gravity provides an accurate value for the velocity at the center of the line, even for complicated asymmetric line profiles. This allows one to correct for the (usually unknown) Doppler shift of the star. Uncertainties are determined by propagating the error bars on the LSD profile through the numerical integration and arithmetic of equation 3.16.

Longitudinal magnetic fields are detected, at 3σ or better, in nearly all our observations of the primary, but no longitudinal field is detected in the secondary. Additionally, the Stokes V profiles of HD 72106B are consistent with a null field hypothesis. Wade et al. (2007) find no magnetic field in HD 71206B with their FORS1 observation. They report longitudinal magnetic fields of 52 ± 90 G from an analysis of Balmer lines and 3 ± 122 G from an analysis of metallic lines. This result is consistent with the earlier analysis of HD 72106B by Wade et al. (2005), in which no magnetic field was detected.

One can constrain the geometry of a stellar magnetic field using a series of longitudinal field observations with known rotation phases. In the case of a tilted, centered dipole field, the longitudinal field will vary sinusoidally with the rotation period of the star (P_{rot}). Models of this type are known as oblique dipole rotators. The well-known relation of Preston (1967) describes the variation of the mean longitudinal magnetic field $\langle B_z \rangle$ as a function of rotation phase ϕ . The rotation phase is given by:

$$\phi = \frac{t - t_0}{P_{rot}}, \quad (3.18)$$

where t is the time of interest and t_0 is some reference time. For simplicity, values

UT Date	HJD (-2 450 000)	Component	B_z (G)	Significance of B_z	LSD Detection
22 Feb. 05	3423.9248	A	300 ± 60	5.3	D
09 Jan. 06	3745.02967	A	410 ± 50	9.1	D
11 Jan. 06	3747.02034	A	320 ± 80	3.8	D
12 Jan. 06	3747.99629	A	-10 ± 40	0.2	D
11 Feb. 06	3777.87860	A	200 ± 50	4.4	D
11 Feb. 06	3777.95149	A	90 ± 40	2.2	D
12 Feb. 06	3778.86172	A	260 ± 40	6.6	D
13 Feb. 06	3779.87202	A	140 ± 60	2.4	D
13 Feb. 06	3779.98127	A	120 ± 170	0.7	N
02 Mar. 07	4161.77282	A	330 ± 40	8.1	D
02 Mar. 07	4161.80256	A	270 ± 40	7.1	D
02 Mar. 07	4161.90282	A	190 ± 40	5.3	D
03 Mar. 07	4162.85713	A	230 ± 50	4.7	D
04 Mar. 07	4163.83561	A	180 ± 30	5.6	D
05 Mar. 07	4164.88387	A	340 ± 30	13.5	D
05 Mar. 07	4164.90961	A	350 ± 40	9.3	D
09 Mar. 07	4168.85791	A	280 ± 40	7.6	D
09 Mar. 07	4168.90947	A	230 ± 40	5.8	D
12 Jan. 06	3748.01496	B	0 ± 170	0.0	N
05 Mar. 07	4164.84650	B	-50 ± 60	0.9	N

Table 3.2: Mean longitudinal field measurements for each observation of HD 72106A and B. The significance of B_z is the number of standard deviations that the detection corresponds to, we consider 3σ necessary for a confident detection. The letter D in the LSD detection column indicates that the Stokes V LSD profile is inconsistent with a flat profile at the 99.99% confidence limit, as determined by its χ^2 statistic. This indicates the presence of a magnetic field, even if the mean longitudinal component not clearly detected. The letter N indicates that the inconsistency was at the 99.9% limit or less, and hence cannot be take as strong evidence for the detection of a magnetic field (Donati et al., 1997).

of ϕ between 0 and 2π are often used. One can then write the variation of the mean longitudinal magnetic field as

$$\langle B_z \rangle = B_p \frac{15 + u}{20(3 - u)} (\cos \beta \cos i + \sin \beta \sin i \cos 2\pi\phi), \quad (3.19)$$

where B_p is the strength of the dipole magnetic field at the magnetic pole, u is the limb darkening parameter, i is the inclination of the rotation axis of the star to our line of sight, and β is the angle between the rotation axis and magnetic dipole's axis (the obliquity angle). For equation 3.19, the t_0 term in ϕ (see equation 3.18) must be set such that the maximum longitudinal field strength is observed when $\phi = 0$. The angles i and β are related by (Preston, 1967):

$$\tan \beta = \frac{1 - r}{1 + r} \cot i, \quad (3.20)$$

where $r = \frac{B_z^{min}}{B_z^{max}}$ is the ratio of the smallest (B_z^{min}) to the largest (B_z^{max}) absolute longitudinal field strengths from the complete sinusoidal curve. Determining i is discussed in Sections 3.6 and 4.2. Thus if one has a good set of observations describing the sinusoidal variability of the longitudinal magnetic field in a star, the dipole field parameters (B_p and β) can be calculated straightforwardly, with a priori knowledge of i . This analysis was performed for HD 72106A, but not for HD 72106B because we do not detect a magnetic field in the secondary.

As seen in Table 3.2, a Stokes V signature from a magnetic field can often be detected when a mean longitudinal field cannot. In an effort to verify the validity of the dipole magnetic field model, and possibly to constrain the field geometry further, direct modeling of the Stokes V LSD profiles was undertaken.

Modeling of the LSD Stokes V profiles of HD 72106A was performed with the ZEEMAN2 spectrum synthesis code, described in Section 3.3. This process was not

performed for HD 72106B since there was no evidence for a magnetic field in that star. Mean atomic line data from the LSD process were used. Chemical abundance, and hence line depth, for our synthetic LSD line was fixed by fitting the equivalent width of the Stokes I LSD profile. For the magnetic field geometry, initially the oblique dipole rotator model derived from the longitudinal magnetic field measurements was used. Comparison of the set of phased Stokes V LSD profiles with model profiles at corresponding phases showed acceptable agreement, as discussed in Section 4.3. This suggests that a dipole field is a sufficient model, within the uncertainty of our observations.

A grid of dipole models was constructed by generating many synthetic time series of Stokes V profiles by varying β and B_p . Model Stokes V profiles were calculated for the same rotational phases as the observations. Initially a grid spacing of 100 G and 10 degrees was used; this was refined to 20 G and 1 degree near the best fit model. The reduced χ^2 of the model³, including all points in the line profiles (and excluding points in continuum) from all rotation phases, was calculated for each point in β and B_p , producing a map of reduced χ^2 . The best fit model was then simply selected by finding the minimum χ^2 value. An illustrative map of χ^2 for β and B_p in the star θ^1 Ori C (adapted from Wade et al., 2006a) is shown in Figure 3.8. When the range of models were examined by eye, significant departures from the best fit model (by a few hundreds of gauss or a few tens of degrees) showed clear discrepancies between modeled and observed profiles at several phases.

One can use the change in χ^2 away from the minimum in χ^2 to place limits, at a specific confidence level, on a model. This is described by Press et al. (1992,

³Reduced χ^2 is simply the standard χ^2 value divided by the number of ‘degrees of freedom’ (the number of observed data points minus the number of fit parameters)

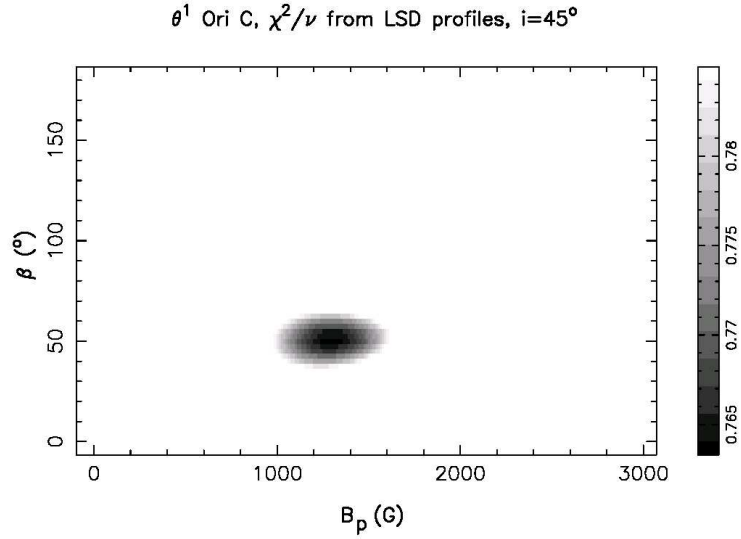


Figure 3.8: A sample χ^2 map in B_p and β for θ^1 Ori C, adapted from Wade et al. (2006a). The gray-scale axis represents reduced χ^2 . Values outside the 95% confidence limit are white. Synthetic model profiles, using an inclination angle of 45° , were compared to observed LSD Stokes V profiles to produce this plot.

Section 15.6) and was originally developed by Avni (1976) and Lampton et al. (1976). Based on the number of free parameters in the model, one can use χ^2 statistics to calculate the change in χ^2 that corresponds to a specific confidence limit. The change in χ^2 ($\Delta\chi^2$) can be determined by finding the point in the cumulative χ^2 distribution function, with the degrees of freedom equal to the number of free model parameters, that has a probability equal to the desired confidence limit. The equation governing this is (Press et al., 1992):

$$P\left(\frac{\nu}{2}, \frac{\Delta\chi^2}{2}\right) \equiv \frac{\gamma(\nu/2, \Delta\chi^2/2)}{\Gamma(\nu/2)} = p, \quad (3.21)$$

where P is the ‘regularized’ gamma function, γ is the lower incomplete gamma function, Γ is the ‘complete’ gamma function, ν is the number of free model parameters, and p is the desired confidence limit. Thus for a given p one must solve for $\Delta\chi^2$. For

example, with 2 free parameters at a 99.73% confidence limit ($\sim 3\sigma$) one requires a change in χ^2 of 11.8. The limiting value of χ^2 (χ_{lim}^2), at confidence p , is then simply the sum of the minimum χ^2 (χ_{min}^2) and $\Delta\chi^2$, that is $\chi_{lim}^2 = \chi_{min}^2 + \Delta\chi^2$. This produces a boundary in parameter space that can be used to determine error bars. Figure 3.8 provides an illustration of such a boundary in two dimensions. The error bars (i.e. confidence intervals for individual parameters) are, in general, the projection of the extrema of the confidence boundary onto the relevant coordinate axis.

This method of determining uncertainties for our model was used, providing much more rigorous error bars than the ‘by eye’ method. To properly include the substantial uncertainty in inclination angle, we recalculate the grid of models at the maximum and minimum values of i allowed by its error bars. Our final uncertainties then run from the 3σ limit at one inclination angle extreme to the 3σ limit at the other inclination angle extreme. The results from this are discussed in Section 4.3. The greatest limitation in these models is the inaccurately modeled Stokes I profiles. Equivalent width was accurately modeled, however line asymmetries due to surface abundance inhomogeneities were not modeled. As a consequence of the unmodeled surface abundance inhomogeneities, there was a limitation on the accuracy of the Stokes V profile shapes (which are also affected by the presence of abundance spots). Hence the true error bars on the magnetic geometry may be larger than the formal uncertainties derived above. The technique outlined above has been employed by a number of authors (e.g. Donati et al., 2001; Wade et al., 2006a) with good results.

3.6 Period Determination

In order to determine the inclination angle i of HD 72106A, it was necessary to determine the rotation period of the star. Additionally, to determine the phase of each observation, necessary for magnetic field modeling or Doppler Imaging, a rotation period is required.

In order to determine the rotation period of a star, one needs an observable property of the star that varies with the star's rotation. In a normal main sequence A or B star such a property often does not exist. However, in the case of Ap/Bp stars, and in the case of HD 72106A, we have a detectable longitudinal magnetic field with presumably periodic variability, as well as presumably periodic variability in the line profiles of the star. The periodicity (illustrated by the similarities between some profiles separated by two nights), and stability between cycles (illustrated by the similarities between some profiles separated by over a year), of the magnetic field and line variability (in absorption) strongly suggests that they are intrinsic to the star (e.g. Preston, 1967; Hatzes et al., 1989), thus we adopt an oblique rotator model. That is, simply put, that the property in question varies across the surface of the star. As the star rotates at some inclination angle, periodic variability is observed due to different parts of the stellar surface being visible at different times.

The simplest data-set to investigate is the set of longitudinal magnetic field measurements. The variability of a centered dipole magnetic field should be a first-order sinusoid. If the magnetic field is a low-order multipole, then the observed longitudinal field varies as a low-order sinusoid.

In order to find the best fit rotation period, a periodogram (a graph of χ^2 versus period) was constructed for a first-order sinusoid fitting function. A first-order

sinusoid with a fixed period was fit through the longitudinal field observations and reduced χ^2 calculated. The phase, amplitude and average value of the sinusoid were taken as free parameters. This was repeated for many period values, with a logarithmic sampling from 0.3 to 10 days, to produce a graph of reduced χ^2 versus period. One cannot simply use a χ^2 minimization routine to find the best period because there are a great many local minima in the parameter space. Any reasonably efficient χ^2 minimization routine would find it almost impossible to reliably find the global χ^2 minimum. The resulting periodogram, based on longitudinal field measurements, is shown in Figure 3.9. The procedure described here is similar to performing a Fourier analysis on the set of longitudinal field measurements and dates, however there are a few differences (Press et al., 1992).

This method of fitting sinusoids through the data points is essentially a Lomb-Scargle method (Press et al., 1992). This method has the advantages of working well with unevenly sampled data and being sensitive much below a Nyquist frequency calculated from the average data point spacing. The Nyquist frequency, f_c , is defined by (Press et al., 1992):

$$f_c = \frac{1}{2\Delta} \quad (3.22)$$

where Δ is the spacing in time between data points. In a uniformly sampled data set, frequency components above the Nyquist frequency are falsely shifted into the range below the Nyquist frequency, a process known as aliasing (Press et al., 1992). Thus in a search for periodicity, if the period is shorter than the Nyquist period one can see false peaks in a power spectrum. In the case of a rotating star, the star would be completing multiple rotations between observations. For non-uniformly sampled data, periodicity can be found via the Lomb-Scargle method, much below the Nyquist

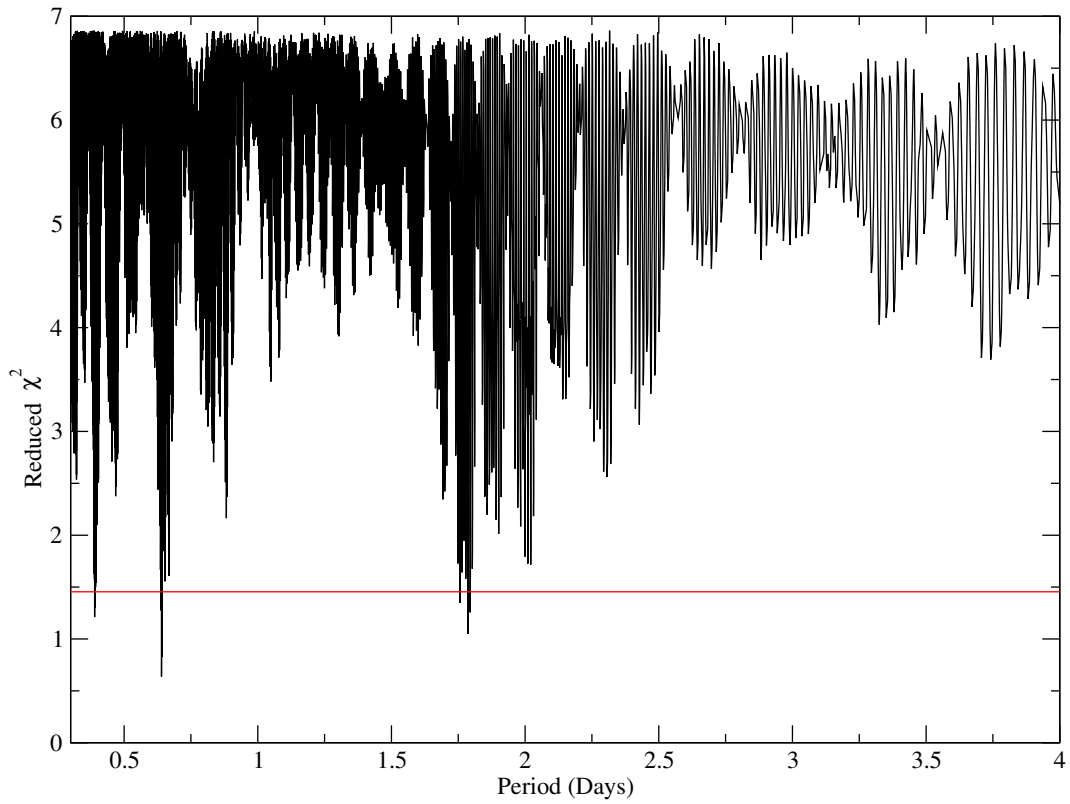


Figure 3.9: Periodogram for HD 72106A, using a first-order sinusoid, based on longitudinal field data. A number of strong minima are apparent between 0.4 and 2 days, with the ~ 0.64 day period giving the strongest minimum. The horizontal line represents the 99% confidence limit, based on the minimum at ~ 0.64 days.

frequency from the average spacing of data points (Press et al., 1992). Since some data points are more closely spaced than the average, they provide constraints below the Nyquist frequency based on the average spacing. In principle one can determine a period down to nearly two times the smallest data spacing, but in practice, with limited noisy data sets and a limited number of points, this is overly optimistic. With this advantage comes two drawbacks. The Lomb-Scargle method is computationally much slower than Fourier methods (which can make efficient use of Fast Fourier Transforms; Press et al., 1992). More importantly, the significance of periods found with the Lomb-Scargle method depends on the number of data points used (Press et al., 1992), thus a large number of observations is necessary for accurate period determination.

The dependence of the Lomb-Scargle method's accuracy on the number of observations proved to be problematic for us. Specifically, we found many minima with almost identical reduced χ^2 in the periodogram. One can assign confidence limits in terms of χ^2 (or reduced χ^2), using the minimum χ^2 value and the number of free fitting parameters, as described by Press et al. (1992, Section 15.6) and discussed near the end of Section 3.5. However, in the case of the longitudinal field data we could not draw any useful conclusions, at the 99% confidence level, since there were several periods with suitable reduced χ^2 values.

A full Stokes V LSD profile contains significantly more information than the corresponding single derived longitudinal field datum. In light of this, we hoped to improve the periodogram analysis by searching for periodic variability in the Stokes V and Stokes I LSD profiles. The method developed for this is based on the fitting of sinusoids as described above. However, rather than fitting the sinusoid through

a time series of longitudinal field measurements, it is fit through the times series of observations at one particular point ('pixel') in the LSD profile. Again a wide range of periods are used, creating a periodogram for one particular pixel. The phase, amplitude and average value of the sinusoid were used as free parameters for the fit, and the periods considered were logarithmically sampled from 0.3 to 10 days. Periodograms are created in this fashion independently for all the pixels across the LSD profile. Then, so as to improve the S/N, the periodograms for all of the pixels are averaged together, weighted by the significance (in standard deviations) of the variability in each pixel. This produces an average periodogram for the LSD profile. This procedure is performed independently for the Stokes I and Stokes V LSD profiles. The method described here was in part inspired by Adelman et al. (2002) and described briefly by Aurière et al. (2007).

The technique was tested on a number of 'normal' main sequence Ap and Bp stars, with good results (Aurière et al., 2007; Power, 2007). Additional tests using synthetic I and V profiles with artificial noise and realistically sparse phase coverage were also performed. In these tests the true period was identified unambiguously, with no other minima below the 99% cutoff level. Stokes I and V based periodograms have produced unambiguous periods from a number of observations for which longitudinal field based periodograms were insufficient (Aurière et al., 2007; Power, 2007). The technique performs quite well for Stokes V profiles, in which approximately sinusoidal variability in individual pixels is expected for a low-order multipole magnetic field. Stokes I profile based periodograms perform well at identifying the proper period, but generally have large χ^2 values. A pixel in a Stokes I profile will not, in general, vary in a sinusoidal fashion. However, the fitting of a sinusoid picks out periodicity well.

Thus one sees large χ^2 values, but reliable minima in the periodogram. The LSD pixel average periodograms described here are equivalent to averaging together Fourier transforms of the data for each individual pixel in the LSD profile. Periodograms based on LSD Stokes I and V profiles, using a first-order sinusoid, for HD 72106A can be seen in Figure 3.10.

Despite this more advanced technique, some ambiguity in the rotation period of HD 72106A remained. Several candidate periods with strong minima in all periodograms still could not be ruled out at the 99% confidence limit. These periods were investigated for non-physical variations of their LSD profiles, as detailed in Section 4.2. Dramatic changes in profile shape with correspondingly small changes in rotation phase, or features moving counter to the Doppler motion expected due to stellar rotation (from red to blue) were considered grounds for rejecting a period as unphysical. This was finally sufficient to eliminate all but one period, 0.63995 days, as discussed in Section 4.2.

3.7 Doppler Imaging

Doppler Imaging is a technique for indirectly reconstructing surface features of a star by using a series of spectra obtained at different rotation phases, and exploiting the rotational Doppler effect. As the star rotates, a surface feature, for example a spot of chemical overabundance, moves across the visible disk of the star. This change is reflected in a rotationally broadened line profile, as different points on the star's surface have different radial velocities as seen by an observer, and hence different Doppler shifts. Thus the rotational longitude of a surface feature can be deduced from the corresponding spectral feature's position in a rotationally broadened line

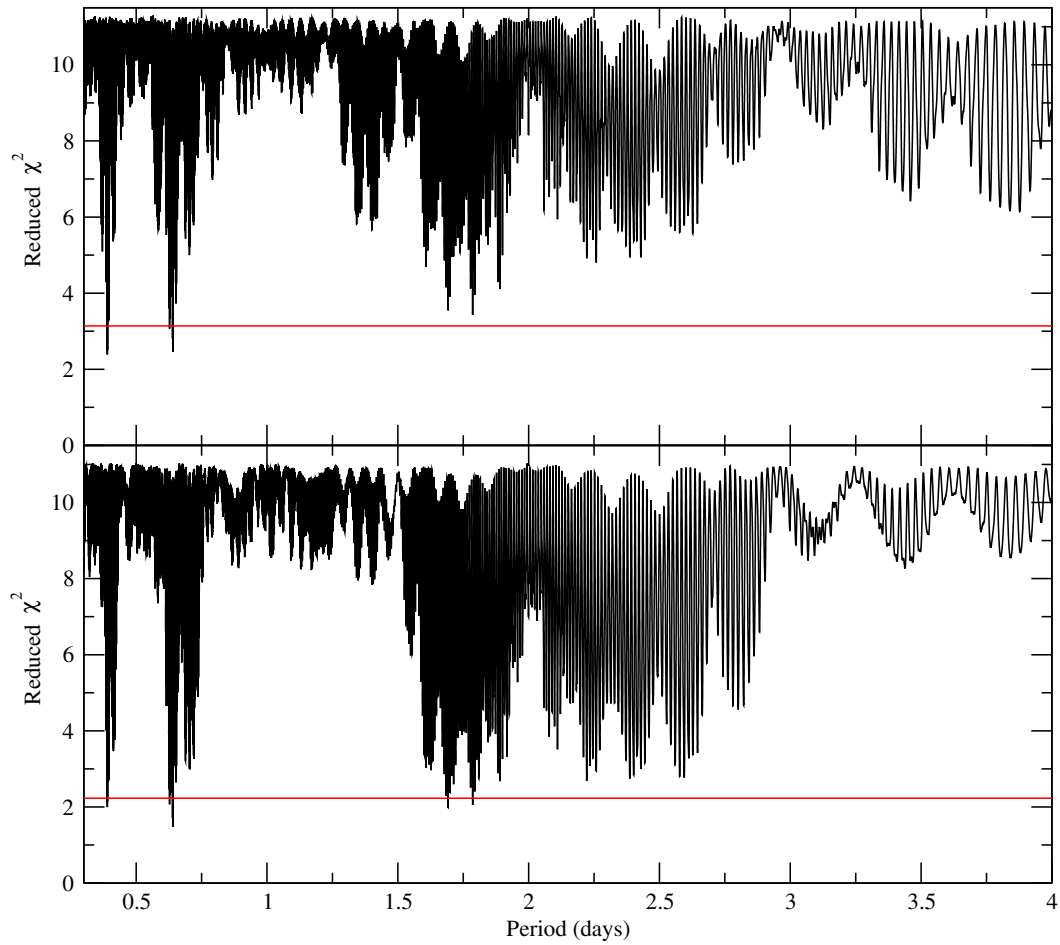


Figure 3.10: Periodogram for HD 72106A, using a first-order sinusoid, based on the LSD Stokes I (top frame) and Stokes V (bottom frame) variations. The horizontal lines represents the 99% confidence limits, based on the deepest minimum in each plot. A number of comparable minima are still present, however the scaling in χ^2 is larger, and fewer minima fall below the 99% confidence limit.

profile. Latitudinal information is contained in the variation with phase of a feature in a line profile. A feature near the rotational pole would present smaller Doppler shifts, move more slowly across the line profile, and be visible longer.

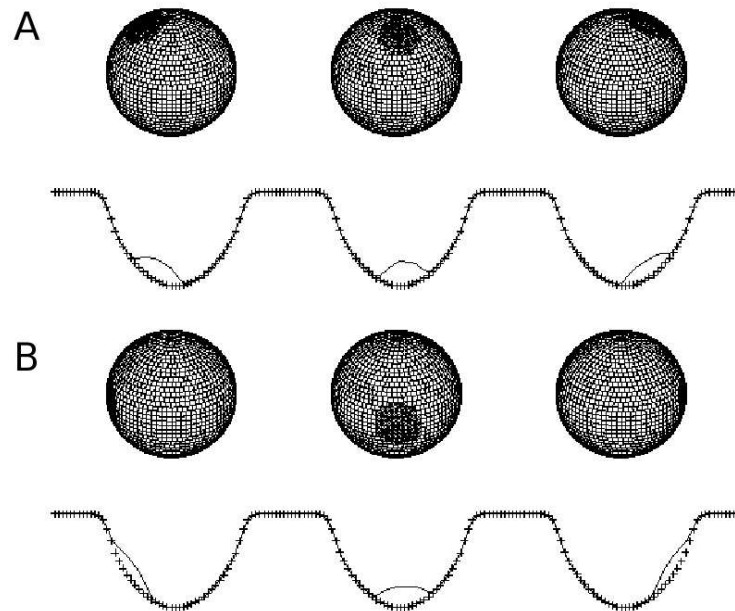


Figure 3.11: Illustration of Doppler Imaging. As the model star rotates, the spot of under-abundance moves across the visible disk of the star. The ‘bump’ in the synthetic line profile, corresponding to the spot of under-abundance, moves across the line profile as the star rotates, due to the rotational Doppler shift. In the case in which the spot is at higher latitude, (case A rather than case B) the ‘bump’ is restricted to the center of the line profile, since it never achieves as large a Doppler shift as the equator. Image: A. P. Hatzes, Thüringer Landessternwarte Tautenburg (http://www.tls-tautenburg.de/research/artie/di_technique.html).

In Doppler Imaging, the information contained in the time series of variable line profiles is extracted by inverting the line profiles to produce a surface map of the star. In the case of abundance Doppler Imaging this is, in essence, done by fitting the set of unknown abundances across the surface of the star to the observed series of line profiles. At the rotation phase of each observation, a synthetic line profile can be

calculated from an assumed model surface abundance distribution. By varying the surface abundance distribution one can then fit the synthetic line to the observed line profile. This is done simultaneously for all observed rotation phases to produce the best fit surface abundance map.

In mathematical terms, this inverse problem is solved by minimizing the quantity (e.g. Kochukhov et al., 2004):

$$\begin{aligned} E &= \sum_{\phi} \sum_{\lambda} [I_{\text{calc}}(\lambda, \phi) - I_{\text{obs}}(\lambda, \phi)]^2 / \sigma_{\text{obs}}^2(\lambda, \phi) + R(\varepsilon) \\ &= \chi^2 + R(\varepsilon), \end{aligned} \tag{3.23}$$

where $I_{\text{calc}}(\lambda, \phi)$ and $I_{\text{obs}}(\lambda, \phi)$ are the calculated and observed line profiles at wavelength λ and phase ϕ , and $\sigma_{\text{obs}}^2(\lambda, \phi)$ is the uncertainty associated with the observed profile at wavelength λ . The sums over phases (ϕ) and wavelengths (λ) cover all observed data points, and thus summation yields χ^2 . The last term in equation 3.23, $R(\varepsilon)$, is the regularization function, and warrants further discussion.

In general, the inversion required for Doppler Imaging is an ‘ill-posed’ problem. The large number of surface elements necessary for a map with reasonable resolution produces several thousand free parameters, which are not uniquely constrained by the relatively small number of observed data points⁴. In principle there can be many solutions which provide equally good fits to the observed line profiles. Thus a unique, stable solution cannot be achieved without the addition of some further constraint: the regularization function. Regularization provides a scheme for selecting a particular solution from a number of possible solutions that fit the data. Most possible solutions present large variations between nearby points on the stellar surface. These

⁴In the case of our observations we have approximately 20 points across a line profile and observations at 18 phases, hence 360 data points.

solutions are usually non-physical, and contain variations below the true resolution of the Doppler map. Thus most regularization schemes search for the most smooth or uniform solution that fits the observations. A number of regularization schemes for Doppler Imaging exist (e.g. Vogt et al., 1987; Piskunov et al., 1990), however the differences are minimal when the line profile variability is large compared to the noise in the observation (Piskunov et al., 1990; Korhonen et al., 1999).

In this thesis we used the the Doppler Imaging code INVERS12, developed by O. Kochukhov and N. Piskunov (Kochukhov et al., 2004), for surface chemical abundance mapping. This program performs accurate LTE spectrum synthesis, using pre-calculated model stellar atmospheres. INVERS12 allows for simultaneous modeling of multiple chemical elements and multiple wavelength regions, and takes into account blended lines. Tikhonov regularization is used, which has the functional form (Tikhonov, 1963; Kochukhov et al., 2004):

$$R(\varepsilon) = \iint \|\nabla\varepsilon(M)\|^2 dM, \quad (3.24)$$

where $\varepsilon(M)$ is the surface distribution of the relevant element, the integration is performed over latitude and longitude (i.e. M), and $\|\cdot\|$ indicates the absolute value of a vector. This regularization essentially constrains the reconstructed abundances to change slowly over the surface of the star. Thus Tikhonov regularization selects the ‘smoothest’ solution that still fits the data.

The disk integrated synthetic line profiles are calculated from local synthetic line profiles, integrated across the visible surface of the star. Surface features are then included by their effect on the local line profiles. Mathematically this can be written as (Kochukhov et al., 2004):

$$I_{\text{calc}}(\lambda, \phi) = \frac{\iint I_{\text{L}}(M, \varepsilon, \lambda + \Delta\lambda_{\text{D}}(M, \phi)) \cos\theta dM}{\iint I_{\text{C}}(M) \cos\theta dM}, \quad (3.25)$$

where I_L and I_C are the line and continuum intensities, the latter assumed to be independent of the local chemical composition. Division is necessary to produce a continuum normalized line profile. M is the position on the stellar surface in longitude and latitude, θ is the angle between the line of sight and the normal to the surface at point M , and $\Delta\lambda_D(M, \phi)$ is the Doppler shift of the surface element M at phase ϕ . Integration is performed over the hemisphere of the star visible at rotation phase ϕ .

For input into the Doppler Imaging computations for HD 72106A we used the adopted effective temperature and surface gravity from Section 3.1.1: $T_{\text{eff}} = 11000$ K and $\log g = 4.0$. An initial $v \sin i$ of 41 km s^{-1} and abundances, for the treatment of blended lines, were taken from the results of our abundance analysis of HD 72106A, presented in Section 4.1.1. A further discussion of the input parameters can be found in Section 4.4. Initially, five Si II lines were used simultaneously to construct a Doppler Imaging map of Si across the surface of HD 72106A. However, the noise level in the observed spectra proved to be too high for very accurate Doppler Imaging. To remedy this, we performed Doppler Imaging using LSD profiles, constructed using lines of individual elements. LSD produces line profiles with a much higher S/N than individual spectral lines, which can be used much like regular spectral line profiles (e.g. Barnes et al., 1998; Donati et al., 2000; Marsden et al., 2005). Ultimately, high quality maps were constructed for Si, Ti, Cr, and Fe from LSD profiles. These results are presented in Section 4.4, along with a further discussion of the challenges faced.

The identification of individual lines for Doppler Imaging, preparation of those lines for analysis, construction of LSD profiles, the determination of fundamental stellar parameters, and determination of initial parameters for Doppler Imaging were all performed by the author. The execution of the Doppler Imaging code was performed

by Dr. O. Kochukhov. Discussions with Dr. Kochukhov about the interpretation of the Doppler Imaging results were invaluable.

Chapter 4

Results

4.1 Surface Chemical Abundances

Detailed chemical abundance analyses were performed for both components of HD 72106, simultaneously fitting $v \sin i$, surface chemical abundances for many species, and microturbulence (for HD 72106B). The abundances of HD 72106A represent mean surface abundances, as there exists strong evidence for the presence of surface abundance inhomogeneities. For the primary, abundances for 13 elements in 7 independent spectral windows were modeled. For the secondary, abundances for 15 elements in 7 windows were obtained.

4.1.1 Primary

Clear chemical peculiarities in HD 72106A, as hinted at by the observed line profile variability, were discovered early in the spectrum modeling process. In particular, Fe over-abundances with respect to the solar abundance of +1 dex (1 dex = 1 order of

magnitude), Cr over-abundances of +2 dex, and Nd over-abundances of about +3 dex were obtained. When one considers that these values are in logarithmic units, it is apparent that the departures from solar abundances in the atmosphere of HD 72106A are quite strong. The abundance patterns observed are characteristic of main sequence Ap and Bp stars, although remarkably strong.

HD 72106A was modeled using an Atlas9 model atmosphere with a temperature of 11000 K and $\log g = 4.0$. A 1 kG dipole magnetic field was included, with an obliquity angle $\beta = 90^\circ$. While later results show this magnetic field geometry is not perfectly correct, it provides a good approximation for the magnetic desaturation which will affect the Stokes I profiles. A modification of the field geometry to $B_p = 1300$ G and $\beta = 60^\circ$ (the final adopted geometry) has a negligible impact on the results, well below the level of the uncertainties. No microturbulence was included, as magnetic intermediate mass stars (particularly Ap and Bp stars) do not display any evidence of microturbulence (e.g. Ryabchikova et al., 2000). The strong, globally ordered magnetic field seen in these stars is sufficient to suppress microturbulence (e.g. Ryabchikova et al., 2000). Moreover, no evidence for microturbulence was found during the modeling process. Fitting the radial velocity of the star, by adjusting the net Doppler shift of the observed spectrum, produced a value of 22 ± 1 km s⁻¹. As described in Section 3.3.2, individual regions ranging from ~ 100 Å to ~ 200 Å of the observed spectrum were fit independently. The observation of the spectrum of HD 72106A on January 12, 2006 was used for fitting. As discussed in Section 3.3.2, this spectrum is representative of the average spectrum (over all observations) of the star.

Results for each individual segment of spectrum fit can be seen in Table 4.1.

Abundances are presented in units of $\log \frac{N_{\text{el}}}{N_{\text{H}}}$, where N_{el} is the number of atoms of the element in question and N_{H} is the number of H atoms present. Spectrum-averaged abundances are presented numerically in Table 4.2, and graphically in Figure 4.2. The spectrum averaged values should be taken as the most accurate abundances. Example segments of fit spectrum can be seen in Figure 4.1.

As discussed in Section 3.3.2, uncertainties on the spectrum-averaged, best fit values are based on the standard deviation of the values from individual windows. Exceptions to this rule are marked with an * in Table 4.2. In these cases only a few lines were available for modeling, so the uncertainties were estimated by taking the change in abundance necessary to shift the synthetic line well beyond any noise or normalization errors in the observed spectrum. Thus the uncertainties in these special cases represent the $\sim 2\sigma$ confidence level, while all other uncertainties are at 1σ .

Remarkably strong over-abundances of Cr, Fe and Nd are found. The Si abundance appears to be above solar by 0.8 dex, whereas He appears to be ~ 1.5 dex under-abundant. A number of elements, such as Al, Sc and Sr, appear to have solar abundances. A couple of elements, particularly Mg and O, hint at possible peculiarity but require further study before concrete conclusions can be drawn. The $v \sin i$ value of $41.0 \pm 0.7 \text{ km s}^{-1}$ is very low for a main sequence B star, but within the normal range of values for a Bp star. The strong over-abundances in Si, Cr, Fe, and Nd, as well as the under-abundance in He, are common features of cooler Bp stars (Jaschek & Jaschek, 1995).

Strong chemical peculiarities, particularly in He, and magnetic fields can affect the structure of a stellar model atmosphere, which can in turn modify the derived

	4170-4265 Å	4400-4500 Å	4500-4600 Å	4600-4700 Å	5000-5200 Å	5200-5400 Å	5400-5600 Å
$v \sin i$ (km s ⁻¹)	41.4	40.1	41.0	41.0	41.9	40.1	41.4
He		-2.8					
O						-3.0	
Mg		-4.1			-3.6	-4.5	-3.9
Al				-5.8			
Si	-3.5			-3.5	-4.1		-3.8
Ca	-5.1						
Sc	-8.6						
Ti	-6.0	-6.2	-6.0		-5.9	-6.1	
Cr	-4.4	-4.5	-4.2	-4.4	-4.4	-4.3	-4.1
Fe	-3.5	-3.5	-3.6	-3.5	-3.5	-3.5	-3.4
Sr	-8.7						
Ba			-8.5				
Nd					-7.4	-7.6	

Table 4.1: Chemical abundances for HD 72106A in each independently fit segment of spectrum. Clear over-abundances in a number of elements can be seen.

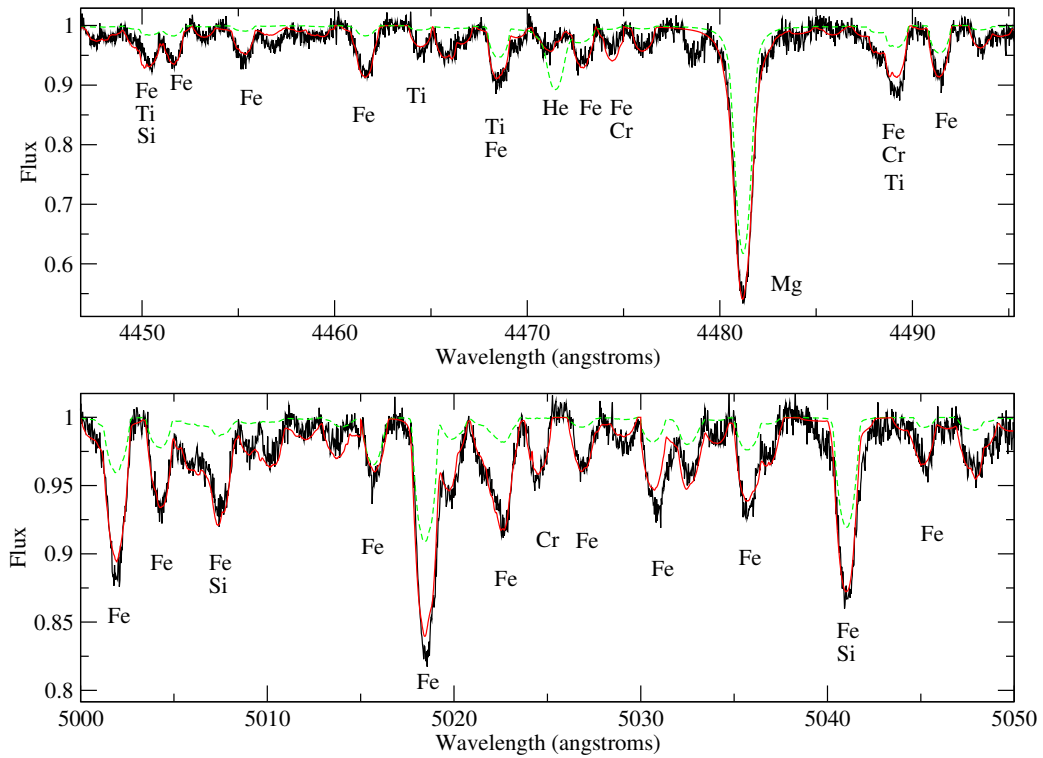


Figure 4.1: Sample best fit synthetic spectra for HD 72106A in two independently fit spectral windows. Major contributors to each line have been labeled, in order of importance. The smooth solid line is the best fit spectrum in this region, the dashed line is a spectrum computed with solar chemical abundances.

temperature for the star as well as chemical abundances (Shulyak et al., 2004; Khan & Shulyak, 2006). These effects tend to be small, on the order of 0.1 dex, and hence would have a minimal impact on our results. However, peculiar He abundance can have a larger effect. Thus future studies would be well advised to take our results as a starting point for model atmosphere calculations.

	HD 72106A	HD 72106B	Solar
$v \sin i$ (km s ⁻¹)	41.0 ± 0.3	53.9 ± 1.0	
ξ (km s ⁻¹)		2.3 ± 0.6	
He	-2.8 ± 0.3 *		-1.07
C		-3.40 ± 0.08	-3.61
O	-3.0 ± 0.2 *		-3.34
Mg	-4.0 ± 0.3	-4.60 ± 0.16	-4.47
Al	-5.8 ± 0.4 *		-5.63
Si	-3.73 ± 0.14	-5.2 ± 0.6	-4.49
Ca	-5.1 ± 0.5 *	-6.0 ± 0.2	-5.69
Sc	-8.6 ± 0.3 *	-9.13 ± 0.08	-8.83
Ti	-6.04 ± 0.10	-7.21 ± 0.09	-7.10
Cr	-4.33 ± 0.13	-6.3 ± 0.3	-6.36
Mn		-6.7 ± 0.5 *	-6.61
Fe	-3.49 ± 0.07	-4.64 ± 0.17	-4.55
Ni		-6.3 ± 0.3	-5.77
Sr	-8.7 ± 0.6 *	-9.2 ± 0.6 *	-9.08
Y		-10.0 ± 0.3	-9.79
Ba	≤ -8.5 *	-10.2 ± 0.5 *	-9.83
Ce		≤ -9.0 *	-10.30
Nd	-7.5 ± 0.4 *	≤ -9.2 *	-10.54

Table 4.2: Averaged best fit chemical abundances, $v \sin i$ and microturbulence (ξ) for HD 72106A and B as well as solar abundances from Grevesse et al. (2005). Entries marked by an * are based on only a few lines, and hence have larger $\sim 2\sigma$ error bars.

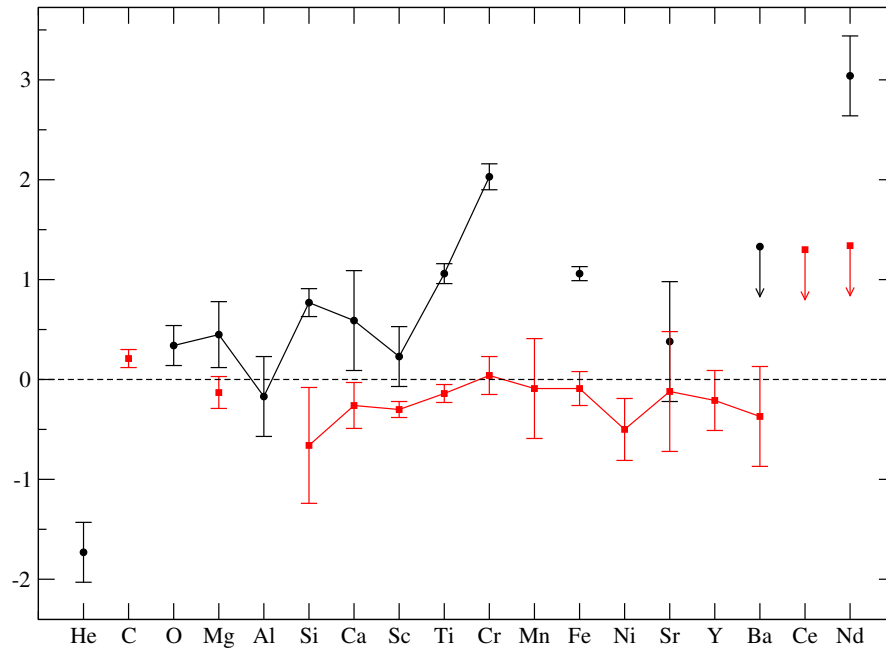


Figure 4.2: Abundances relative to solar for HD 72106A (black circles) and HD 72106B (red/gray squares), averaged over all spectral windows modeled. The dashed line at 0 represents solar abundance. Points marked with only an arrow indicate the value is an upper limit only. Strong departures from solar abundance can be seen for HD 72106A, whereas HD 72106B has largely solar abundances.

4.1.2 Secondary

Initial spectrum modeling suggested that the secondary possessed roughly solar chemical abundances. More detailed modeling showed that our initial temperature and $\log g$ values gave poor fits, and produced abundance values inconsistent with solar, as described in Sections 3.1.1 and 3.3.2. In particular, multiple lines of a single element often could not be fit well with the same abundance. A closer inspection showed that lines of lower ionization states tended to be too deep when lines of higher ionization states were well fit; strongly suggesting an incorrect temperature and $\log g$. A revised effective temperature of 8750 K was adopted with $\log g = 4.0$. No magnetic field was included in these models, since there is no evidence for the presence of a magnetic field in this star. Microturbulence (ξ) was included as a free parameter in the models as well as $v \sin i$. One expects a non-zero microturbulence in HD 72106B, as microturbulence is usually seen in cool, non-magnetic A type stars (Gray, 2005; Landstreet, 1998).

As for HD 72106A, large regions of HD 72106B's spectrum were modeled in several independent segments, following the procedure outlined in Section 3.3.2. The observation of HD 72106B from March 5, 2007 was used. Best fit results for individual windows are presented in Table 4.3. Sample best fits of models to the observed spectrum can be seen in Figure 4.3. Abundances, $v \sin i$ and Microturbulence averaged over all modeled windows are presented in Table 4.2 and can be seen graphically in Figure 4.2.

The large majority of elements are consistent with solar abundances, within 2σ at most. A few elements appear to depart marginally from solar values, with a significance slightly greater than 2σ . C appearsers to be over-abundant with $\sim 2\sigma$

significance, whereas Sc is under-abundant by $\sim 3\sigma$. Nevertheless, nearly all the elements are within 2σ of solar abundance, and no elements display the strong peculiarities seen in HD 72106A. We find $v \sin i = 53.9 \pm 1.0$, which is larger than that of the primary, but not dramatically so.

One other trend of possible significance is that the best fit abundances are consistently below solar. The abundances are, as mentioned, almost all within uncertainty of solar, however the distribution of abundances is clearly not Gaussian around the solar values. This may be indicative of a still incorrect temperature, or an overly large microturbulence. An increase in temperature to 9000 K increased the best fit abundances by 0.1 dex or 0.2 dex depending on the element. This temperature results in a marginally worse fit to the observed spectrum, but may be the simplest explanation for the trend of under-abundance. Alternately, since excellent fits of the synthetic to the observed spectra are generally seen, the trend may in fact reflect a systematic lower metallicity in HD 72106B near the surface.

Emission Features in HD 72106B

Emission was observed in the $H\alpha$ Balmer line and the OI 7773 Å triplet of HD 72106B. A careful examination of the spectrum of the secondary revealed no other emission lines, at the level of the noise in our spectra. Small amounts of emission infilling in a small number of lines cannot be completely ruled out, but must not be much beyond the noise in our observations. Variability between observations in the emission lines, both in $H\alpha$ and in the OI 7773 Å triplet, was noted. Observations of the $H\alpha$ emission line in the secondary are illustrated in Figure 4.4, and observations of the OI 7773 Å triplet are illustrated in Figure 4.5.

	4170-4265 Å	4400-4500 Å	4500-4600 Å	4600-4700 Å	5000-5200 Å	5200-5400 Å	5400-5600 Å
$v \sin i$ (km s ⁻¹)	54.2	52.1	54.3	53	54	55.2	54.5
ξ (km s ⁻¹)	2.1	2.5	3.0	1.2	2.8	2.6	2.0
C					-3.4	-3.3	-3.5
Mg		-4.8			-4.6		-4.4
Si		-4.6			-4.7	-5.7	-5.6
Ca	-5.7	-6.0	-6.3				-5.8
Sc	-9.3			-9.1	-9.0		-9.2
Ti	-7.2	-7.3	-7.2	-7.1	-7.2	-7.3	-7.4
Cr	-6.5		-6.5	-6.0		-6.4	-6.2
Mn		-6.7					
Fe	-4.7	-4.7	-4.9	-4.4	-4.7	-4.7	-4.4
Ni				-6.0	-6.1		-6.7
Sr	-9.3						
Y	-9.7					-10.3	
Ba			-10.2				
Ce						≤ -9.0	≤ -8.5
Nd						≤ -9.2	

Table 4.3: Chemical abundances for HD 72106B in each independently fit segment of spectrum. Solar abundances for virtually all elements are found.

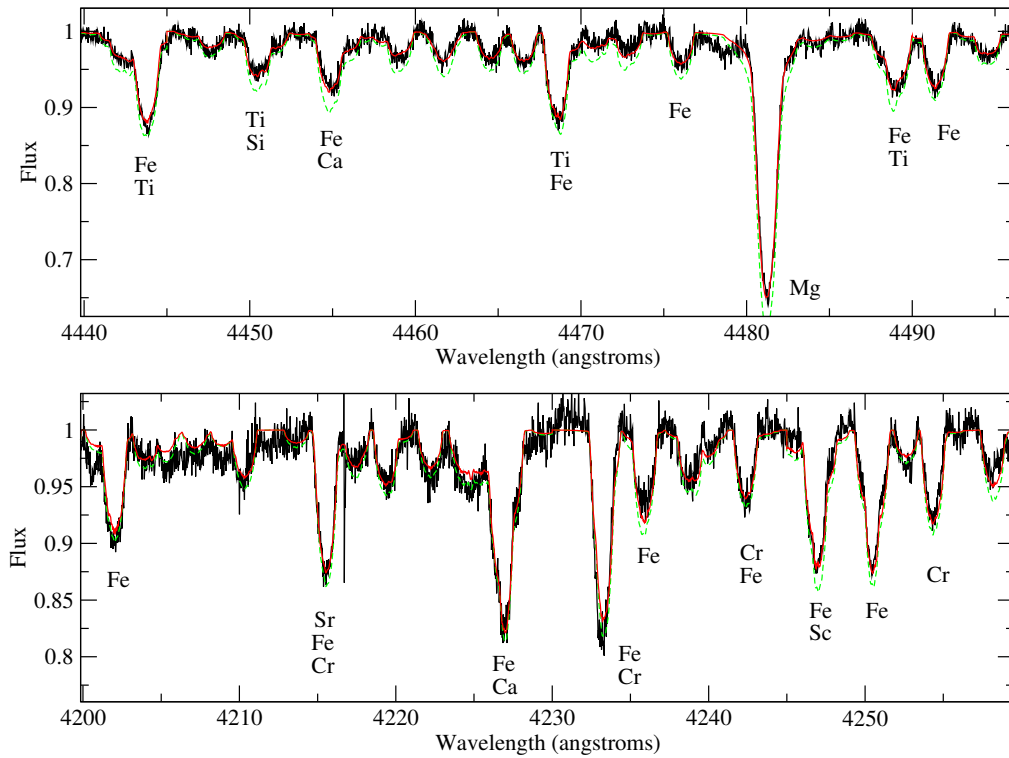


Figure 4.3: Sample best fit synthetic spectra for HD 72106B in two independently fit spectral windows. Major contributors to each line have been labeled, in order of importance. The smooth solid line is the best fit spectrum in this region, the dashed line is a spectrum computed with solar chemical abundances.

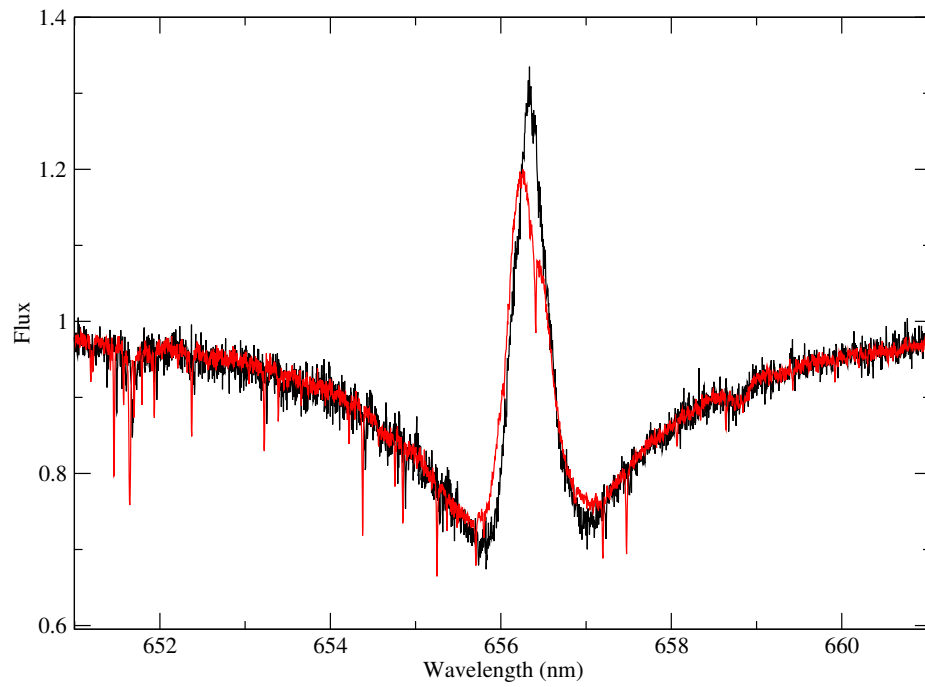


Figure 4.4: Emission and variability in the H α Balmer line of HD 72106B. The black line represents the individual observation of the secondary from JD 2453748.01496 and the red/gray line is the spectrum of just the secondary from JD 2454164.84650.

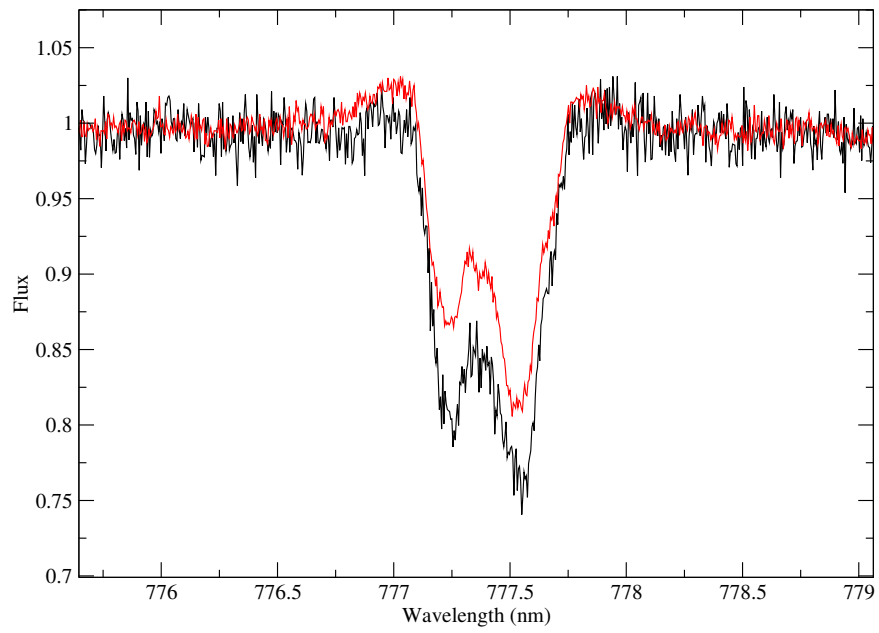


Figure 4.5: Emission and variability in the OI 7773 Å triplet of HD 72106B. The black line represents the individual observation of the secondary from JD 2453748.01496 and the red/gray line is the spectrum of just the secondary from JD 2454164.84650.

The emission in $H\alpha$ is by far the more prominent. The wings of the $H\alpha$ line are observed in absorption and the core contains a large single peaked emission feature. There is a hint of an absorption core superimposed on the emission peak in our second individual observation of the secondary (at JD 2454164.84650). However, this absorption feature is very sharp and somewhat off center, thus it may be a telluric line. Comparing the $H\alpha$ lines in observations of the combined HD 72106 system suggests that variability occurs on time scales as short as one day. However, larger, longer term trends are also present, as the variation between observations separated by months or years is larger than the variation between days. Comparison of $H\alpha$ lines in observations of the combined system, for the purposes of investigating variability in the secondary, is fairly safe since there is no evidence for variability in the $H\alpha$ line of the primary. No clear periodicity is seen in the $H\alpha$ line variability.

The emission in the OI 7773 Å triplet is more subtle than that of the $H\alpha$ line. In our second individual observation of the secondary, a rise above the continuum level is seen around the edges of the OI 7773 Å triplet. A careful examination of the unnormalized spectrum shows that this is not a result of the normalization process. It is unlikely that this is an instrumental artifact, as this rise is observed only in this line of the secondary, and the feature is too broad to be a result of a bad pixel, a cosmic ray, or the terrestrial atmosphere. This, combined with the variability in the OI 7773 Å triplet in the observations of the secondary individually, leads us to conclude that we are observing a small amount of emission in this triplet. The variability in line depth we attribute to emission infilling of the absorption line. Furthermore, no such rise above the continuum level is observed in our spectra of the primary on its own, and while there may be some variability in the OI 7773 Å triplet of the primary,

it is of much smaller amplitude than that observed in the secondary. This provides further evidence that the observed feature is indeed emission, and that it is intrinsic to HD 72106B.

The observed emission in $H\alpha$ and the OI 7773 Å triplet of HD 72106B, combined with the star's H-R diagram position, fully support this star's classification as a HAeBe star. This combined with the star's infrared excess (Oudmaijer et al., 1992), and the presence of molecular bands in the star's infrared spectrum (Schütz et al., 2005), place HD 72106B firmly in the HAeBe class.

4.2 Rotation Period of the Primary

The rotation period of HD 72106A was determined using the procedure described in Section 3.6. Mean periodograms based on the time series of pixels comprising the Stokes I and V profiles, illustrated in Figure 3.10, display a few minima with reduced χ^2 values of about 2. Following the method described by Press et al. (1992) and Avni (1976) (discussed in Section 3.6), confidence limits of constant χ^2 were placed on the periodogram. The χ^2 minima at 0.38983 days, 0.63995 days, 1.6921 days and 1.7859 days were all within the 99% confidence limit, and hence were considered to be possible rotation periods.

The phase variation of the Stokes I and V LSD profiles for each candidate period was examined visually. The data were phased according to each rotation period, and the LSD profiles plotted according to phase. Phased LSD profiles were then examined to verify that the resultant variation was qualitatively consistent with rotational modulation. The 0.63995 day period produced the best phasing of the profiles, as

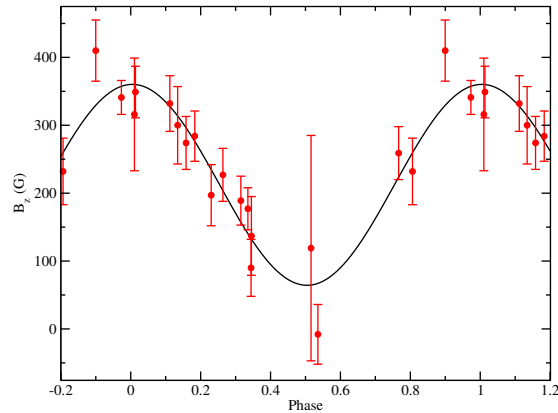


Figure 4.6: Longitudinal magnetic field measurements of HD 72106A, phased with the adopted 0.63995 day period, and the best fit sinusoid. A good fit of the sinusoid to the data is seen with a reduced χ^2 of 0.86.

illustrated in Figure 4.7. This period also provided a good phasing of the longitudinal magnetic field data, illustrated in Figure 4.6. The 1.6921 and 1.7859 day periods produced less satisfactory variations. Each of these periods resulted in small phase differences between observations exhibiting large profile differences. These variations were considered unphysical and the associated periods were discarded. Figure 4.8 illustrates the phasing of profiles for the 1.7859 day period and highlights LSD profiles in an unphysical order, Figure 4.9 does the same for the 1.6921 day period. The 0.38983 day period produced also unphysical variations at a few phases, as illustrated in Figure 4.10. Additionally, the 0.38983 day period would require an inclination $i \sim 0^\circ$ to be compatible with the observed $v \sin i$. Finally, this period is remarkably short - smaller than that of any known Ap star. The shortest known rotation periods of Ap stars are around 0.5-0.6 days (Adelman et al., 1992; North, 1998; Kochukhov & Bagnulo, 2006; Power, 2007).

Thus we conclude that the 0.63995 day minimum represents the most probable

rotation period of HD 72106A. Using the 99% confidence limits described above, we obtain the rotation period of 0.63995 ± 0.00014 days (3σ). This is notable in that it is one of the shortest rotation periods seen in any Ap/Bp star.

Wade et al. (2005) reported a possible rotation period near 2 days. This period can be confidently ruled out by both the periodograms and the phasing of LSD profiles it produces. However, given the authors' limited data set, it is not surprising that they found this period. The star, with our 0.63995 ± 0.00014 day period, rotates approximately three times in two days, and ~ 1.5 times in one day. So observations on consecutive nights reveal approximately diametrically opposite phases and observations spaced two nights apart reveal the same rotation phase. Thus Wade et al. (2005) observed an alias of the true period. Our data set remedies this problem by having observations that are more closely spaced in time than one day.

With an accurate rotation period, it is now possible to calculate the inclination angle (i) of the star's rotation axis to our line of sight. Given the radius of $1.3 \pm 0.6 R_{\odot}$, as determined in Section 3.1.2, one can calculate the circumference of the star. Using the rotation period one can then easily calculate the rotation velocity at the equator of the star (v). Then using the definition of $v \sin i$ and the value $v \sin i = 41.0 \pm 0.7$ km s⁻¹ from Section 4.1.1, one can calculate i . That is:

$$\sin i = \frac{P v \sin i}{2\pi R}, \quad (4.1)$$

where P is the rotation period and R is the stellar radius. Performing this calculation produces the value $i = 23 \pm 11^{\circ}$. Knowledge of the inclination angle is essential for accurate modeling of the magnetic field geometry.

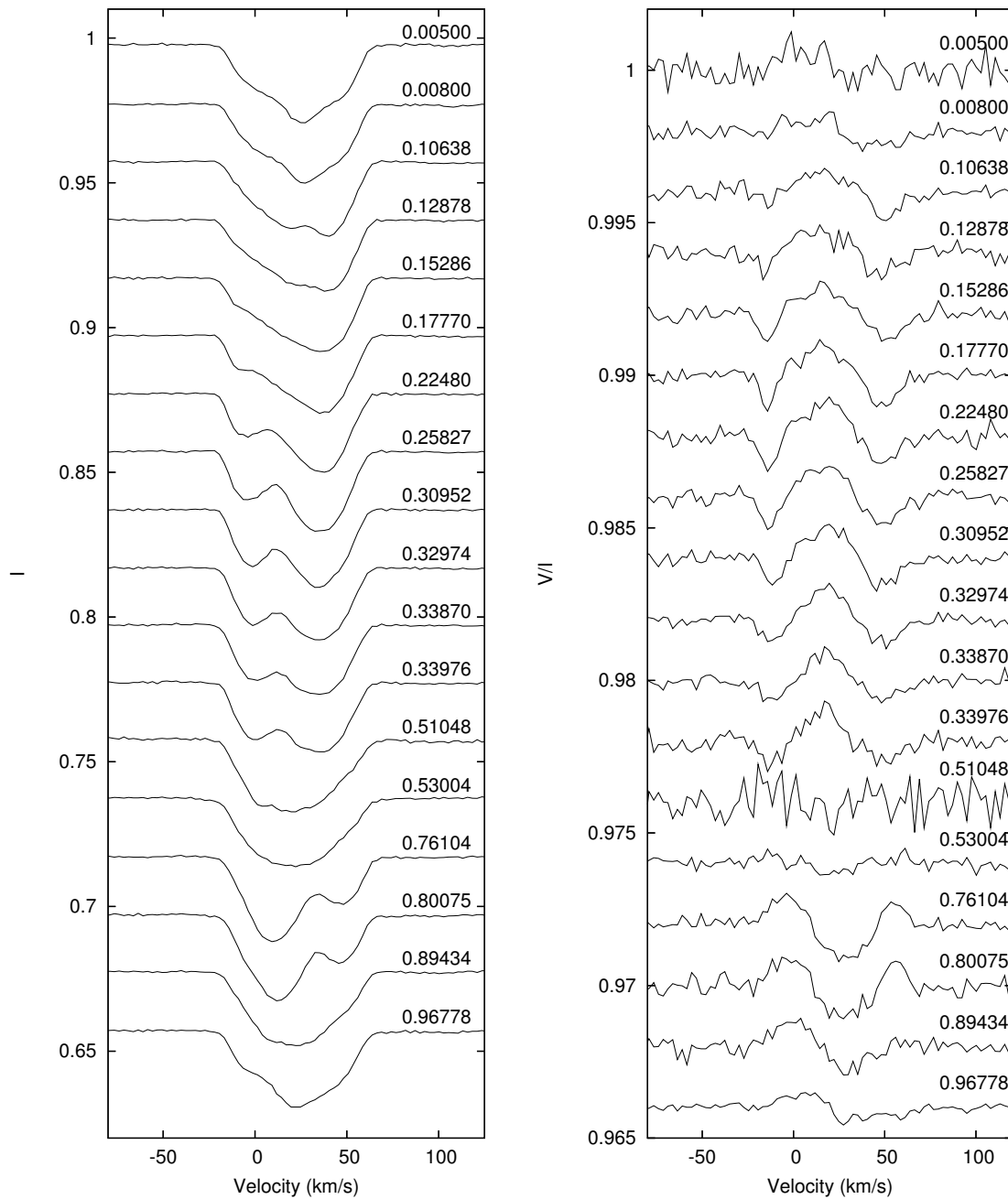


Figure 4.7: Phased LSD profiles (Stokes I on the left and Stokes V on the right) for HD 72106A with the adopted 0.63995 day best fit period. The profiles are labeled according to phase, and have been shifted vertically for display purposes.

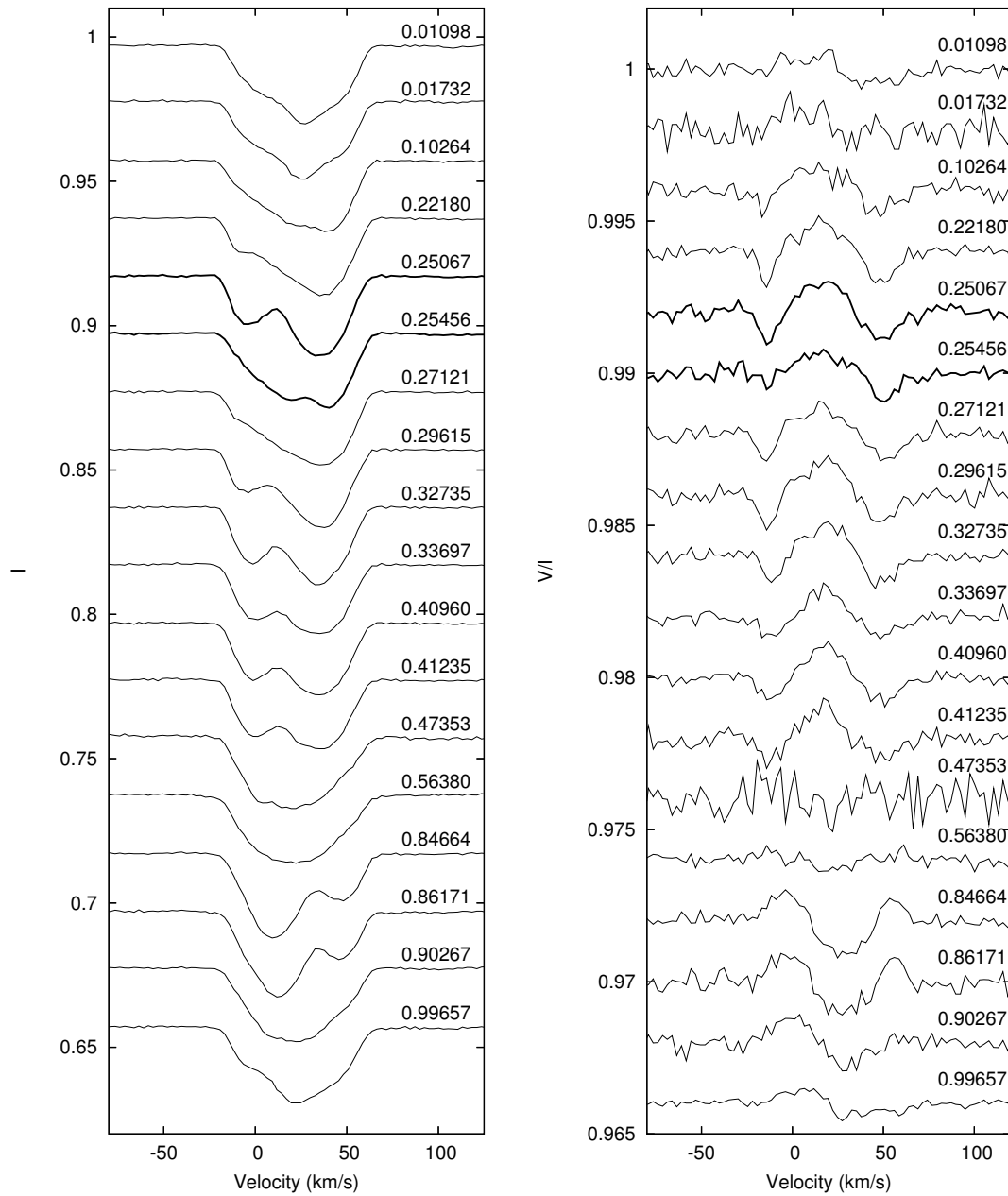


Figure 4.8: Phased LSD profiles (Stokes I on the left and Stokes V on the right) for HD 72106A with the incorrect 1.7859 day period. The profiles are labeled according to phase, and have been shifted vertically for display purposes. Note the inconsistencies between phases 0.22180 and 0.27121 (profiles in bold). Such large changes, particularly noticeable in the set of Stokes I profiles, over only 5% of the star’s rotation are highly unlikely.

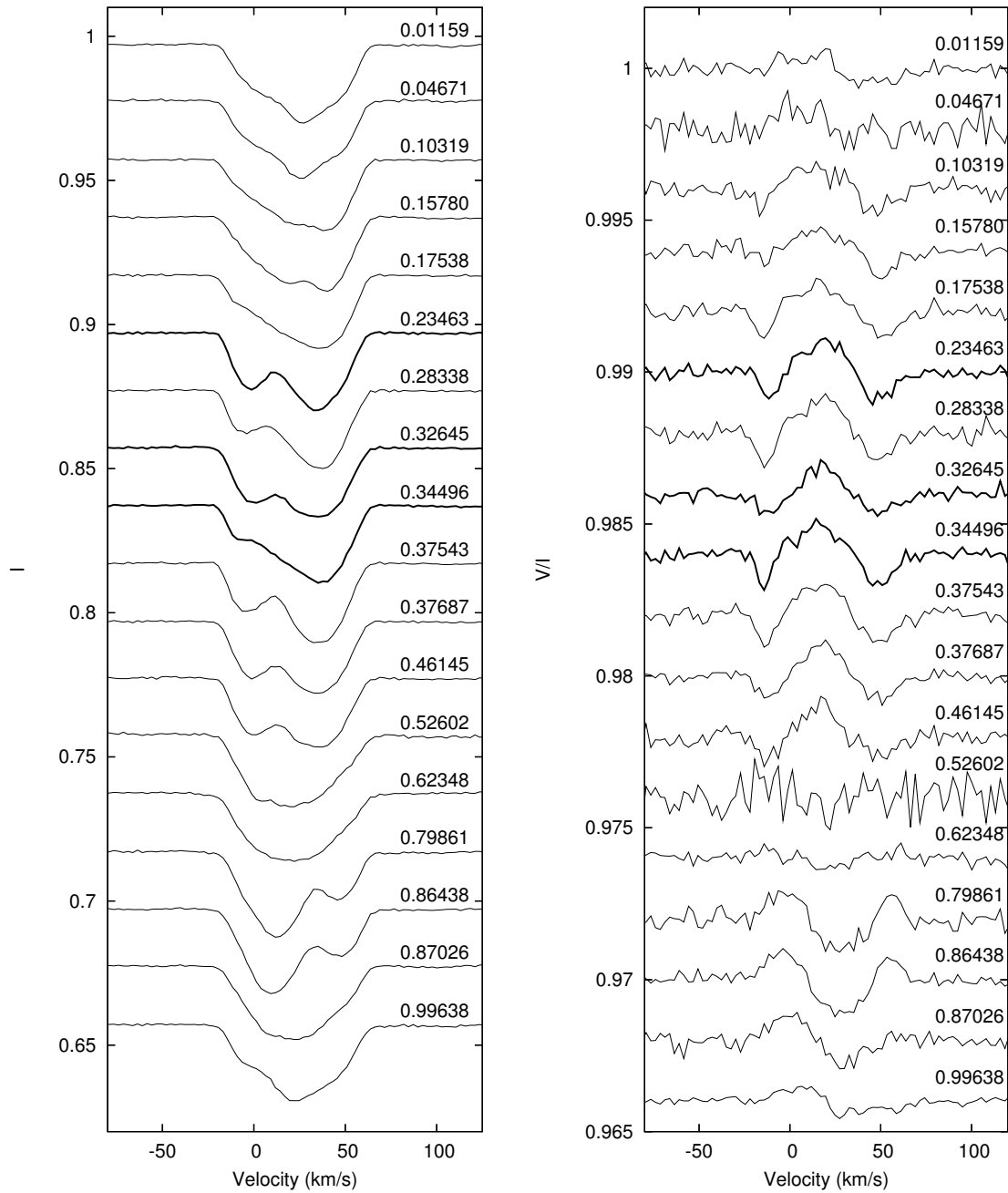


Figure 4.9: Phased LSD profiles for HD 72106A with the incorrect 1.69219 day period, as in Figure 4.8. Note the inconsistencies at phases 0.23465, 0.32845 and 0.34496.

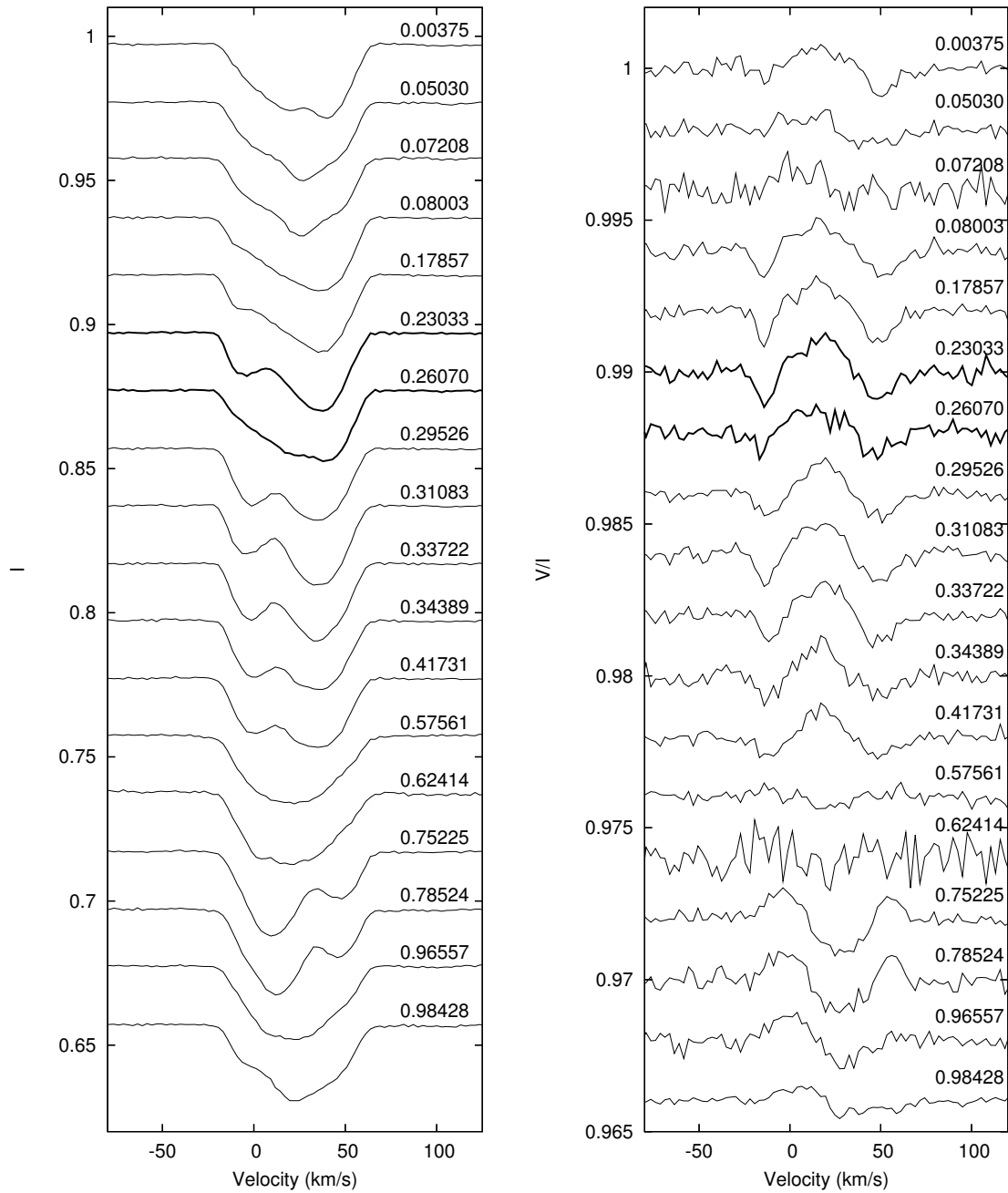


Figure 4.10: Phased LSD profiles for HD 72106A with the incorrect 0.38983 day period, as in Figure 4.8. Note the inconsistencies between phases 1.7857 and 0.28070.

4.3 Magnetic Field

The phase variation of the longitudinal field of HD 72106A exhibits an approximately sinusoidal form. This implies that the underlying field has an important large scale dipole component. Therefore we adopt an oblique dipole rotator model, as discussed in Section 3.5, to describe the magnetic field of HD 72106A. A first-order sinusoid was fit by least squares through the longitudinal field data, as discussed in Section 4.2. The 0.63995 day rotation period was used, with the phase, amplitude and mean value of the sinusoid as the free parameters in the fit. This produced a good fit (reduced $\chi^2 = 0.86$) which is shown in Figure 4.6. According to this fit, the maximum longitudinal field is $+360 \pm 40$ G while the minimum is $+65 \pm 40$ G. Computing the r parameter, described in Section 3.5, we obtain $r = 0.18 \pm 0.11$. From equation 3.20 with the inclination angle, discussed in Section 4.2, $i = 23 \pm 11^\circ$ we find $\beta = 58 \pm 15^\circ$. Then from equation 3.19 we compute the polar dipole field strength, $B_p = 1490 \pm 360$ G. A standard limb darkening coefficient for a late B star, $u = 0.4$, was used (Gray, 2005). These values are all given with 1σ error bars.

This dipole field model was verified by using ZEEMAN2 to model the full set of phased Stokes V LSD profiles, as described in Section 3.5. First, a dipole field with the values $i = 23^\circ$, $\beta = 58^\circ$, and $B_p = 1490$ G were used for the input geometry. Profiles were synthesized with ZEEMAN2 for all observed LSD profiles of the primary, resulting in 18 different phases. The models were compared by eye and by χ^2 to the Stokes V LSD profiles. No major discrepancies were observed in either the shapes or amplitudes of the Stokes V profiles, and a reduced χ^2 of 2.87 was calculated. From this we concluded that the dipole field model derived from the longitudinal field measurements is able to fit the Stokes V observations to nearly within the error

bars. It is not surprising that the fit is less than perfect, because the Stokes I profiles were fit only approximately.

Additionally, a grid of dipole field models was calculated and compared to the observed Stokes V LSD profiles. A coarse grid using 100 G steps in the dipole strength and 10° steps in β was first calculated to search from 0 to 2500 G and 0° to 180° . A finer grid, using 20 G steps in B_p and 1° steps in β was calculated, centered on the χ^2 minimum from the coarse grid. A map of χ^2 for the models tested is shown in Figure 4.11. A minimum was found at $B_p = 1300$ G and $\beta = 60^\circ$, with a reduced χ^2 of 2.6184 (for 522 data points: 29 points per profile at 18 different phases). A comparison of the best fit model Stokes V profiles to the observed profiles can be seen in Figure 4.12. Uncertainties were determined following the method described by Press et al. (1992), which was also used for the period determination in Section 4.2. To take into include the large uncertainty on the inclination angle ($i = 23 \pm 11^\circ$), a grid of models was calculated at the maximum and minimum allowed i . The χ^2 minimum was found, and confidence ellipses at the 3σ level were calculated. The final uncertainty is then the total range of values allowed, at the 3σ limit, at the extrema in i . From this we derive the values $B_p = 1300 \pm 100$ G, and $\beta = 60 \pm 5^\circ$. However, as described in Section 3.5 the shapes of the Stokes I profiles were not modeled, hence our confidence in the details of the Stokes V profile models is decreased. Consequently, the formal uncertainties presented here may be somewhat too small. However, the derived field parameters are in good agreement with those derived from the longitudinal magnetic field measurements, therefore the true magnetic field geometry cannot depart radically from the one presented here.

In HD 72106B we detect no magnetic field. Our two observations of the secondary

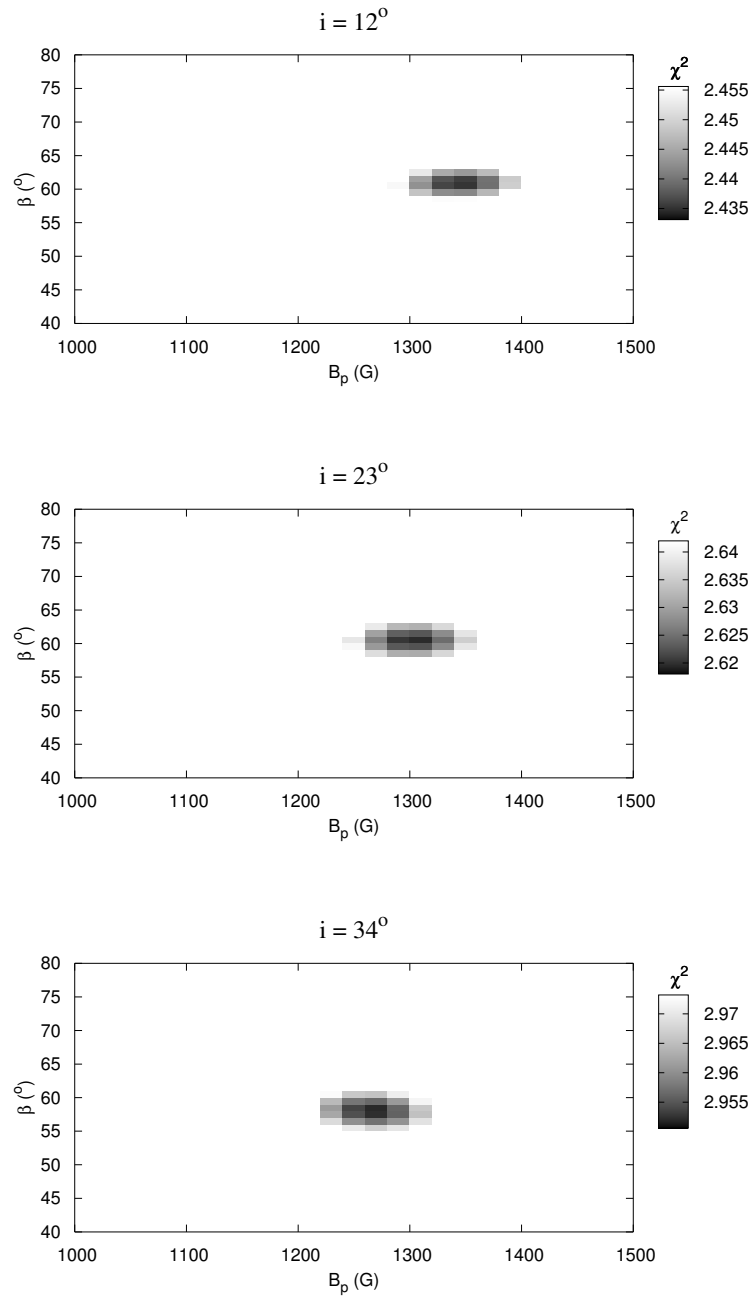


Figure 4.11: Maps of reduced χ^2 for a range of dipole field models for HD 72106A at different inclination angles. The minimum in χ^2 can be seen in the $i = 23^\circ$ map at $B_p = 1300$ G and $\beta = 60^\circ$. The reduced χ^2 scales correspond to the 3σ ($\sim 99.75\%$) confidence limit, calculated using the probability tables of Press et al. (1992).

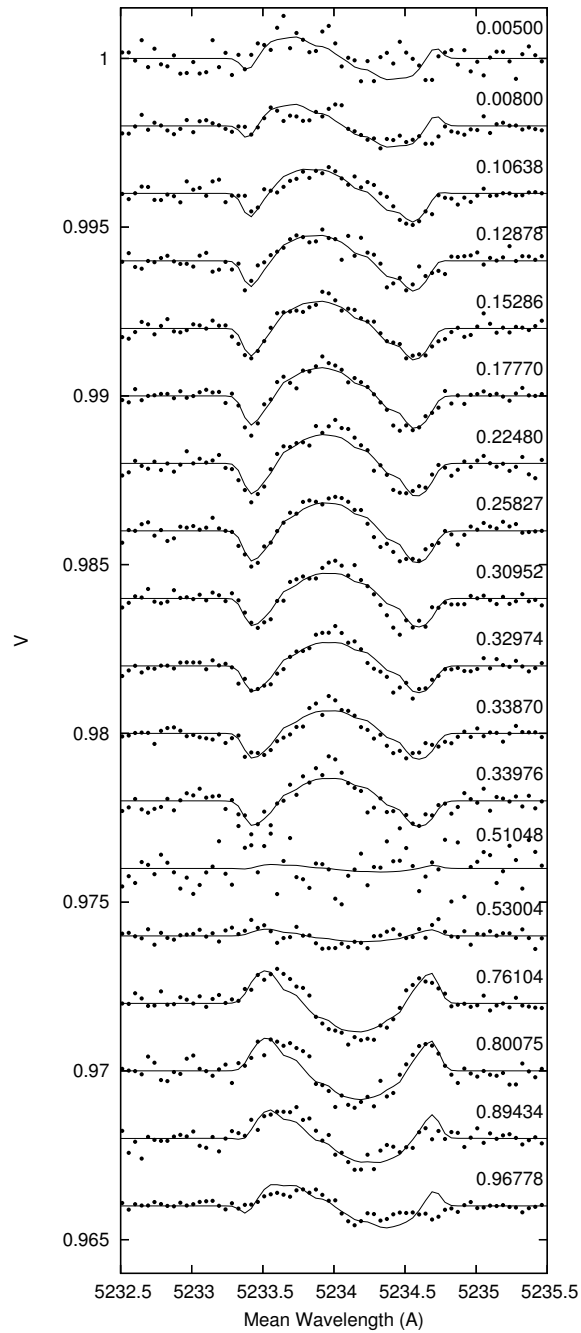


Figure 4.12: Synthetic Stokes V LSD profiles (lines) corresponding to the best fit magnetic field geometry ($i = 23^\circ$, $B_p = 1300$ G, $\beta = 60^\circ$) compared with observed profiles (points). The profiles are labeled by phase, and acceptable fits are obtained at all phases.

individually yield longitudinal magnetic field measurements of 0 ± 170 G and -50 ± 60 G. Thus we can place an upper (1σ) limit on the longitudinal field in the secondary at 170 G (since the star may have been at a less favorable rotation phase when the more accurate measurement was made). Additionally, the Stokes V LSD profiles for both observations are consistent with the null field hypothesis. This rules out the possibility of a large scale field being present but undetected due to the rotation phase of the star (such as a dipole aligned perpendicular to the line of sight). If such a magnetic field were present, one would still see a ‘cross-over signature’ in the Stokes V profile.

In their FORS1 observation of HD 72106B Wade et al. (2005) find no magnetic field detection, reporting a longitudinal field measurement of 60 ± 55 G. Wade et al. (2007) re-analyzed the same observation, in a more robust fashion, and report longitudinal fields of 52 ± 90 G from an analysis of Balmer lines and 3 ± 122 G from an analysis of metallic lines. These results provide further evidence that the secondary is non-magnetic, further decreasing the chance that it was simply observed at an inopportune rotation phase. Thus we conclude that if the secondary has a magnetic field, either it is not globally ordered, or it has a longitudinal field strength that never exceeds ~ 200 G.

4.4 Surface Abundance Geometry

Motivated by the asymmetries and phase variability seen in many metallic line profiles, we undertook a detailed analysis of the surface abundance distribution of several elements in HD 72106A. Doppler Imaging with the INVERS12 code was used to perform this analysis, as described in Section 3.7. For these models a 30° inclination

angle was assumed, the adopted 0.63995 day rotation period was used, and $T_{\text{eff}} = 11000$ K, and $\log g = 4.0$ were assumed for the model atmosphere. This inclination angle is not quite our best fit value, but it is well within uncertainty, and the difference would have a minimal impact on our results. The initial value for $v \sin i$ was 41 km s^{-1} , and abundances for the treatment of blends were taken from Table 4.2.

Initially the Doppler Imaging procedure was performed using five Si II lines: 4128 Å, 4130 Å, 5056 Å, 5041 Å, and 6371 Å. These lines were strong enough to have sufficient S/N for Doppler Imaging, and also possessed strong variability. The five lines were modeled simultaneously. The reconstructed surface abundance distribution for Si is illustrated in Figure 4.13. The best fit models of the Si lines used are presented in Figure 4.14. A clear spot of over-abundance can be seen in the northern hemisphere, with a ring of Si over-abundance near the equator. The Si depletion visible in the southern hemisphere is likely an artifact of the poor sensitivity of the procedure to this mostly hidden region of the star.

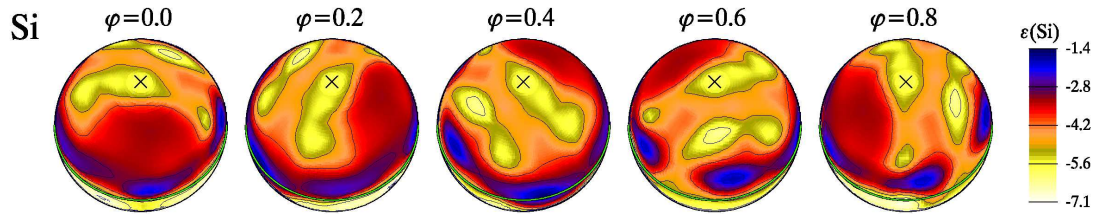


Figure 4.13: Surface abundance map of Si for HD 72106A. This map is based on five Si II lines: 4128 Å, 4130 Å, 5056 Å, 5041 Å, and 6371 Å. A good agreement of the large scale abundance distribution is obtained with the Si map reconstructed from the LSD profiles (see Figure 4.15), although the scale of the abundances does not match (for reasons described in the text). The ‘X’ represents the rotational pole, the green circle indicates the rotational equator. The abundance scale on the right is in units of $\log \frac{N_{\text{Si}}}{N_{\text{tot}}}$.

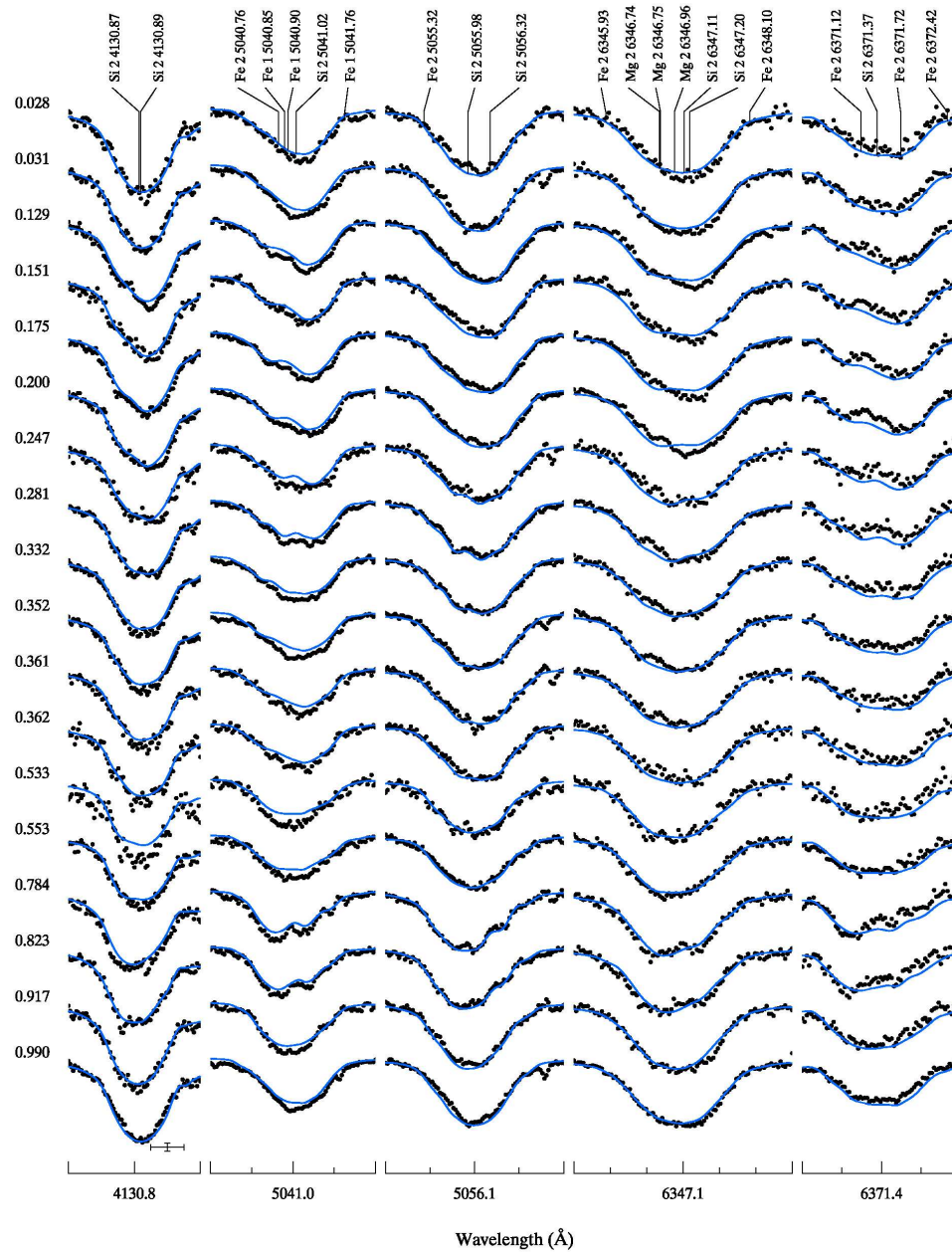


Figure 4.14: Line fits for individual Si II lines used in Doppler mapping of HD 72106A. Observed line profiles are points and synthetic profiles are solid lines. Contributors to each line have been labeled. The bars in the lower left indicate the vertical and horizontal scale, 2.5% of the continuum and 0.5 Å respectively. Fairly good fits to the line profiles can be seen. However, there is a large amount of noise relative to the observed variability.

Problematically, there were very few strong lines with both very high S/N and large variability in our spectra of HD 72106A. Stronger, more saturated lines inherently display less variability than their weaker, less saturated counterparts. This, combined with the relatively low S/N ratio of the observed spectra, resulted in very few lines being suitable for Doppler Imaging. The limited suitability of our spectra for Doppler Imaging is largely due to the use of Doppler Imaging not being foreseen when many of the spectra were originally collected. HD 72106A, at almost 9th magnitude, is a relatively faint target for Doppler Imaging. Originally, shorter exposure times, allowing for better phase coverage, were chosen. Our ability to perform Doppler Imaging at all is largely a ‘bonus’, thanks to the large number of spectra collected for rotation period determination and magnetic field modeling.

Doppler Imaging using LSD profiles, as described in Section 3.7, was undertaken to remedy the problem of insufficient S/N. Suitable LSD profiles, constructed with line masks containing lines of individual elements, were generated for Si, Ti, Cr, and Fe. These LSD profile time series were then used as the input data for Doppler Imaging. Adopted atomic data were constructed from the average properties of the lines used in LSD for each element. The depth of the LSD profile is a complex function of the lines used in the analysis. It is therefore not possible to assign a realistic oscillator strength to the LSD profiles. Consequently a $\log gf$ of 1 was adopted for all elements, and abundances were scaled to fit the LSD profile. Therefore the maps reconstructed by Doppler Imaging from LSD profiles should reflect the correct distribution of surface features (patches of over- or under-abundance), and probably the correct abundance contrast, but the absolute abundance scale is unknown.

Surface abundance maps inferred from Doppler Imaging of LSD profiles for Si, Ti,

Cr, and Fe are illustrated in Figure 4.15. Fits of the synthetic to the observed LSD Stokes I profiles are shown in Figure 4.16. Several interesting features are evident from the Doppler Imaging maps. Ti, Cr, and Fe all seem to share very similar abundance patterns in the northern hemisphere. This is reflected in the similar phase variations of the LSD profiles in Figure 4.16. A large patch of over-abundance centered near phase 0 is apparent in all three maps, with another somewhat smaller over-abundance spot about 180° away in longitude, at the same latitude, around phase 0.6. The Si map shares the larger spot but not the smaller, as reflected in its LSD profiles. The large over-abundance ring at the equator in the Si map, and set of spots around the equator in the Ti map, are probably real. The ring is not evident in the Cr and Fe maps, but one is apparent in the Si map based on several lines in the original spectra. However, such equatorial features are vulnerable to systematic effects, as are features centered at the rotational pole. There appears to be a large over-abundance spot in the southern hemisphere for both Fe and Cr, although the sensitivity of the map is poor in that location. When the magnetic field geometry, determined in Section 4.3, is compared to the Doppler maps, it appears that the positive magnetic pole lies near the large spot of over-abundance at phase 0 in all four maps. However, the magnetic pole lies roughly to the south and west of the center of the abundance spot, thus the relationship is not entirely clear. The over-abundance spots cannot be aligned with the rotational pole, as they would not generate the observed variability in that position..

Substantial abundance contrasts are observed in the Doppler Imaging maps. Ti shows a 2 dex contrast. Fe shows a 2.5 dex contrast, if the spots of strong over- and under-abundance in the southern hemisphere are to be believed, and a 1.5 dex

contrast in the northern hemisphere. Cr displays a 4 dex contrast overall, but only a 2 dex contrast in the more reliable northern hemisphere. Similarly, Si displays a 4.5 dex contrast overall, with a contrast of 1.5 dex in the northern hemisphere

It is useful to consider HD 72106A in the context of other Ap/Bp stars for which multi-element Doppler Imaging has been performed. The elements He, Mg, Si, Cr, and Fe were mapped in the Bp star CU Virginis (HD 124224) with Doppler Imaging by Kuschnig et al. (1999). They found a temperature of 13000 K, a $\log g$ of 4.0 and quote a rotation period of 0.5207038 days, making CU Virginis somewhat similar to HD 72106A. Triglio et al. (2000) found a dipole magnetic field strength of 3000 ± 200 G and an obliquity of $74 \pm 3^\circ$. The Doppler maps of Si, Cr, and Fe for CU Virginis were all very similar to one another. For all three elements, a large region of depletion, relative to the global average, was seen near the magnetic pole, at $\sim 60^\circ$ latitude. A large spot of over-abundance was seen for all three elements at the same latitude, but 180° away in longitude. Helium had an opposite pattern to that observed in Si, Cr, and Fe, with a large over-abundance spot near the magnetic pole and a large depletion 180° away. In light of this, it is perhaps not surprising that Si, Cr, and Fe display similar surface abundance distributions in HD 72106A.

Lueftinger et al. (2003) found somewhat similar results for ϵ Ursae Majoris. ϵ Ursae Majoris (HD 112185) is a 9000 K ($\log g = 3.6$) Ap star with ~ 5 day period and a dipole field strength of several hundred gauss. Lueftinger et al. (2003) constructed surface maps of Ti, Cr and Fe, among other elements, with Doppler Imaging. They found distributions of Cr and Fe very similar to each other, with two large spots of over-abundance near the longitude of the magnetic poles. Ti was roughly anti-correlated with Fe and Cr, displaying two large spots of under-abundance at the

same positions as the over-abundance spots of Cr and Fe.

In the cooler roAp star HR 3831 (HD 83368) Kochukhov et al. (2004) found somewhat different results. HR 3831 is a rapidly oscillating Ap star (roAp), with a ~ 2.9 day rotation period, a 11.67 min pulsation period and a temperature of 7700 K. As such, it may provide a poor comparison to HD 72106A. However, a brief mention of this star is worthwhile, if only to illustrate the differences observed between Ap/Bp stars. In this star Kochukhov et al. (2004) found no clear correlation between the distribution of Si, Ti, Cr, or Fe. The authors found over-abundance features near the magnetic poles for many elements, but the details varied widely.

In this context, the surface abundance distribution patterns seen in HD 72106A are roughly consistent with those seen in similar Bp stars. However, the details are particular to HD 72106A itself. For example, over-abundances of Fe and Cr are seen near the north magnetic pole, as in ϵ Ursae Majoris, however the pattern of Ti follows that of Cr and Fe, unlike in the case of ϵ Ursae Majoris. It remains unclear whether these discrepancies represent the range of variation intrinsic to Ap/Bp stars, or if they are a result of HD 72106A's young evolutionary status.

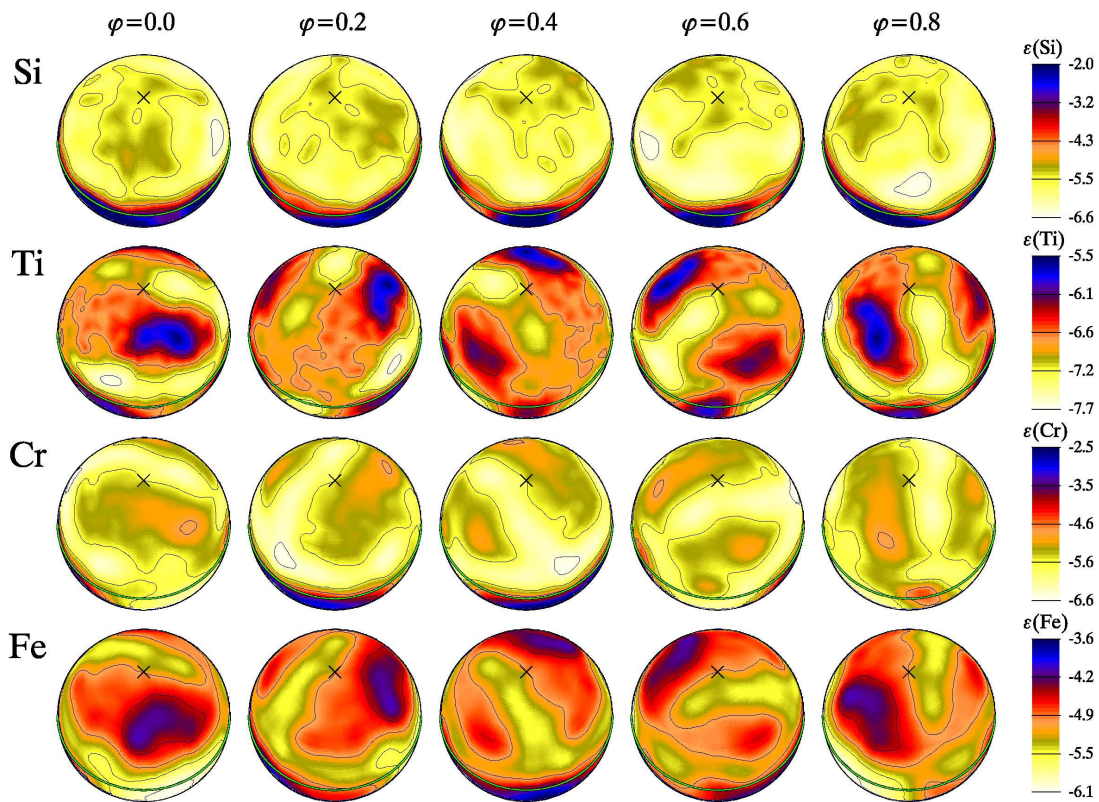


Figure 4.15: Surface abundance maps of HD 72106A for Si, Ti, Cr and Fe. The maps are all based on fits to LSD profiles. The ‘X’ represents the rotational pole, the green circle indicates the rotational equator. The abundance scale on the right is in units of $\log \frac{N_{\text{Si}}}{N_{\text{tot}}}$.

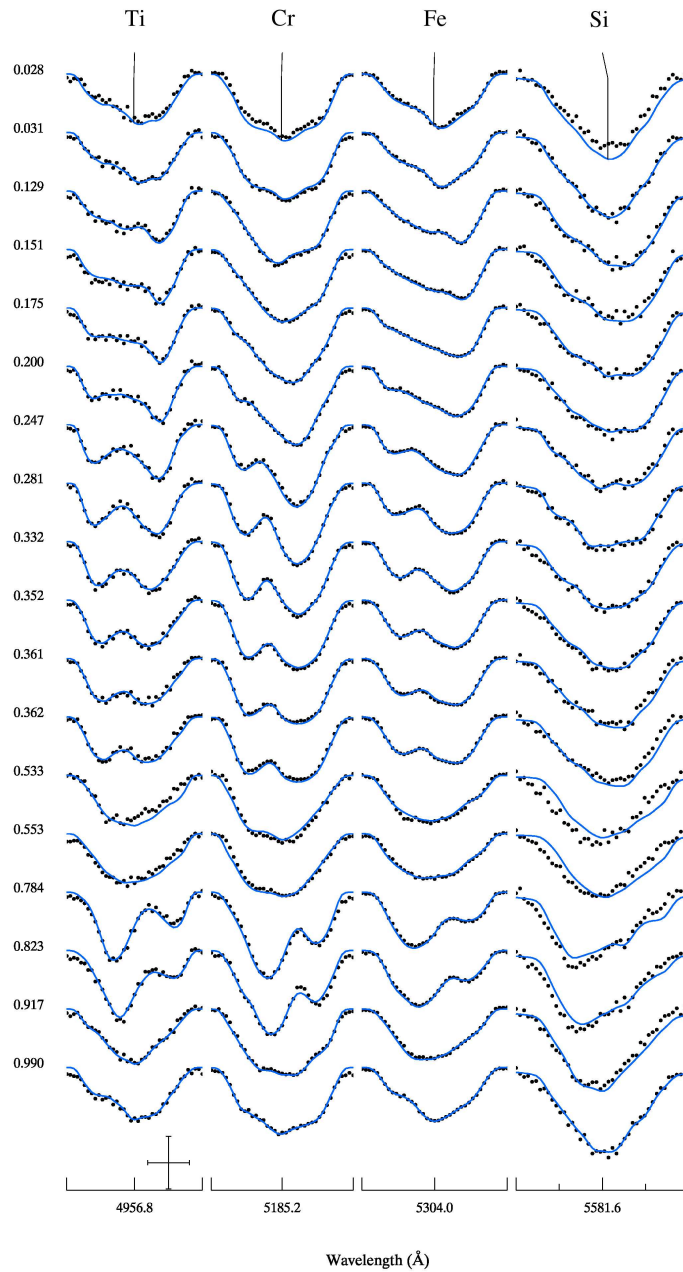


Figure 4.16: Fits of synthetic Stokes I LSD profiles to observed LSD profiles for Si, Ti, Cr, and Fe. The profiles are labeled according to element and phase. The bars in the lower left indicate the vertical and horizontal scale, 5% of the continuum and 0.5 Å respectively. Generally good fits can be seen, ranging from the high S/N Fe profiles at the best to the noisy Si profiles at the worst.

Chapter 5

Summary, Discussion and Conclusions

5.1 Summary of Results

In this thesis 22 high resolution spectropolarimetric observations of the HD 72106 system were analyzed in detail. This system is composed of a Herbig Ae secondary and a magnetic, chemically peculiar primary. The observations were obtained with the ESPaDOnS instrument at the CFHT. Spectra were recorded in circular polarization as well as total intensity.

Based on Balmer line fitting we determined $T_{\text{eff}} = 11000 \pm 1000$ K and $\log g = 4.0 \pm 0.5$ for the primary. For the secondary, with the additional aid of spectrum synthesis, we determined $T_{\text{eff}} = 8500 \pm 500$ K and $\log g = 4.0 \pm 0.5$. Using Hipparcos measurements and placing the stars on the H-R diagram, we found a mass of $2.4 \pm 0.4 M_{\odot}$ and a radius of $1.3 \pm 0.6 R_{\odot}$ for the primary. For the secondary we found $M = 1.8 \pm 0.2 M_{\odot}$ and $R = 1.4 \pm 0.6 R_{\odot}$. If one calculates $\log g$ from mass and

radius one finds values consistent with those presented above, with comparable error bars, thus we prefer the more directly inferred $\log g$ values.

We find that HD 72106B is conclusively a Herbig Ae star. The emission in both the H α Balmer line and the OI 7773 Å triplet, together with the star's H-R diagram position strongly support the HAeBe nature of the star. In addition HD 72106B displays an infrared excess (Oudmajer et al., 1992), and has an infrared spectrum containing a number of molecular lines (Schütz et al., 2005). Thus there is little doubt of HD 72106B's true HAeBe nature.

The age of the HD 72106 system, a critical parameter for this analysis, proved to be somewhat uncertain. We find the range 3 Myr to 13 Myr consistent with the H-R diagram positions of the stars, with a best fit value of 10 Myr. Taking the younger end of this range implies that the entire system is on the pre-main sequence, and that the primary has about 1 Myr left before it reaches the main sequence. In the older limit, the secondary is nearing the ZAMS and the primary has been on the main sequence for about 9 Myr, giving it a fractional main sequence age (τ) of 0.015. In the most likely case (10 Myr) the primary reached the main sequence about 6 Myr ago and has a fractional age τ of 0.01. Thus we cannot confidently conclude that HD 72106A is a pre-main sequence object, but even if it is on the main sequence it is still very young.

Surprisingly strong over-abundances, relative to solar abundances, of a number of chemical elements were found in the photosphere of HD 72106A. Fe was found to be over-abundant by almost 10 times, as was Si. Cr was over-abundant by 100 times and Nd was over-abundant by 1000 times. Conversely, He was found to be under-abundant, well below 0.1 times solar. A number of other elements, such as

Al and Sc, have solar abundances within their uncertainties. These peculiarities are characteristic of Ap and Bp stars, although the peculiarities seen in HD 72106A would be fairly strong by Ap/Bp standards. This makes their appearance in this very young star that much more surprising.

HD 72106B, unlike HD 72106A, shows abundances that are generally within uncertainty of solar abundances. A few marginal departures may exist, particularly for C and Sc. On average, the abundances derived are slightly below solar. This may indicate a truly lower metallicity in the star, not inconsistent with that observed in normal A stars, or it may be only an artifact due to the uncertainty in the temperature of this star. The existence of this chemically normal A-type star in a binary system with a strongly chemically peculiar primary adds to the list of interesting properties of HD 72106.

The rotation period of HD 72106A was carefully examined. Based on longitudinal field measurements, as well as variability in the set of Stokes I and V LSD profiles, we determined the rotation period to be 0.63995 ± 0.00005 days. This value is notable in that it is a particularly short rotation period for an Ap/Bp star. The most rapidly rotating Ap star in our vicinity (within 100 pc of the Sun) is HD 124224 (Power, 2007), rotating once in 0.52068 days (Adelman et al., 1992). The majority of Ap/Bp stars have periods in the range 1 to 10 days, although much longer periods are observed in some cases (Kochukhov & Bagnulo, 2006).

The magnetic field geometry of HD 72106A was determined by fitting both the longitudinal field curve and the set of phased Stokes V profiles. Based on the derived rotation period, radius, and $v \sin i$, the inclination angle of the star is $i = 23 \pm 11^\circ$. We then find that the dipole magnetic field has an obliquity of $\beta = 60 \pm 5^\circ$ and a

polar field strength of $B_p = 1300 \pm 100$ G. A simple centered oblique dipole magnetic field reproduces all observations very well. Thus we conclude that, if higher order components to the field exist, they are much weaker than the dipole component. We also conclude that the magnetic field is stable on time scales of several years. The fact that we find a good phasing for the longitudinal field measurements and Stokes V profiles with a single period, despite observations being separated by up to two years, suggest that the magnetic field cannot have changed much over that time period.

Doppler Imaging of surface abundance inhomogeneities was performed for HD 72106A. While Doppler Imaging using individual lines was attempted, superior results were achieved by using LSD profiles tailored to specific elements. Surface abundance maps were made for Si, Ti, Cr, and Fe, all of which showed clear inhomogeneities. Patches of overabundance corresponding roughly to the positive magnetic pole were seen for all four elements. As well, patches or rings around the rotational equator were seen for a few elements, and were particularly clear for Si. However, a number of surface abundance features with no obvious correlation to magnetic field or rotation were also seen. These maps clearly show that HD 72106A possesses surface abundance inhomogeneities similar to Ap/Bp stars, in addition to peculiar abundances and a dipolar magnetic field.

5.2 Discussion and Conclusions

These results show that HD 72106A is one of the youngest intermediate mass stars observed to have a magnetic field. Even if the star has reached the pre-main sequence, it has a remarkably small fractional age. The oblique dipolar geometry of the magnetic field seen in HD 72106A has only been conclusively shown in one younger

star, HD 200775A (Alecian et al, 2006; Alecian, 2007). HD 72106A is most likely the youngest star in which strong chemical peculiarities have been observed. Certainly it has a fractional age, even with the large uncertainties, that can only be approached by very few known Ap stars (Bagnulo et al., 2003, 2004; Landstreet et al., 2007). Of these stars with rival fractional ages, NGC 2244-334 is the only one for which a detailed abundance analysis has been performed (Bagnulo et al., 2004). Additionally, HD 72106A is the youngest star for which surface abundances inhomogeneities have unequivocally been shown. The Doppler reconstructions presented here are the earliest stage of intermediate mass stellar chemical evolution ever mapped.

The set of properties observed in HD 72106A is perfectly characteristic of a main sequence Ap/Bp star. Thus we conclude that HD 72106A is, for all intents and purposes, a Bp star. If it is still on the pre-main sequence one could debate the semantics, however all observations indicate that the photosphere of HD 72106A is identical to that of a Bp star. This makes HD 72106A possibly the youngest known Ap/Bp star; certainly it has one of the smallest fractional ages (Bagnulo et al., 2004; Landstreet et al., 2007). The classification of HD 72106A as a Bp star lends strong support to the identification of magnetic HAeBe stars as the precursors to main sequence Ap/Bp stars. The existence of this star suggests that there may be a continuum of Ap/Bp-like stars back into the late pre-main sequence.

For comparison, consider the Bp star NGC 2244-334. This star has been on the main sequence for only 2.3 ± 0.3 Myr (Bagnulo et al., 2004; Hensberge et al., 2000), implying a fractional main sequence age $\tau = 0.02 \pm 0.01$. Thus HD 72106A is most likely the younger star, or at least has a younger fractional age, however that is not entirely certain. Bagnulo et al. (2004) found that NGC 2244-334 has a mass of 4.0 ± 0.5

M_{\odot} , a temperature of 15000 ± 1000 K, and observed a longitudinal magnetic field of 9000 G, implying a dipole field strength significantly of at least 30 kG. Bagnulo et al. (2004) derive a strong under-abundance of He (-2.45 ± 0.3 dex, 1.38 dex below solar) and remarkably strong over-abundances of Si (-3.5 ± 0.3 dex, 1.0 dex above solar), Ti (-5.1 ± 0.3 dex, 2.0 dex above solar), Cr (-3.9 ± 0.3 dex, 2.5 dex above solar), and Fe (-3.3 ± 0.2 dex, 1.3 dex above solar). These abundances are similar to those of HD 72106A: Ti is even more abundant in NGC 2244-334, however abundances for the other elements are roughly within uncertainty of each other. This suggests that there are important similarities between these two very young stars, despite their difference in mass and large difference in magnetic field strength.

Several pre-main sequence stars also provide useful comparisons. The star HD 200775A is the pre-main sequence magnetic primary of a double-lined binary system (Alecian et al, 2006; Alecian, 2007). It has a temperature of 18600 ± 2000 K, a mass of $10 \pm 2 M_{\odot}$ and an age of about 0.1 Myr (Hernández et al., 2004; Alecian et al., 2007, in preparation). Alecian et al. (2007, in preparation) find that a dipole magnetic field of $\beta = 90^{\circ}$ and $B_p = 400$ G, coupled with a 4.3 day rotation period and $i = 17^{\circ}$, reproduce their 21 observations well. The star V380 Ori is a $2.8 \pm 0.3 M_{\odot}$ star with a temperature of about 10700 K and an age of about 1 Myr as measured from the birth line (Wade et al., 2005). Wade et al. (2005) find a longitudinal magnetic field of 460 ± 70 G, and Alecian et al (2006) find that the magnetic field has a major dipole component, but were unable to derive an accurate geometry from their observations. Wade et al. (2005) and Wade et al. (2007) detect a magnetic field in the star HD 101412, with a longitudinal strength of 512 ± 111 G. Wade et al. (2007) report a mass of $2.6 \pm 0.3 M_{\odot}$ and an age of about 2 Myr for HD 101412, however they could not

constrain the magnetic field geometry. A magnetic field was reported in the star HD 104237 by Donati et al. (1997), and confirmed by Donati (2000), with a longitudinal strength of ~ 50 G. This star has a mass of about $2.3 M_{\odot}$ and an age of about about 2 Myr (van den Ancker et al., 1998). Acke & Waelkens (2004) studied chemical abundances in HD 104237, using equivalent widths. They find approximately solar abundances for a range of elements, including Si, Cr, and Fe. The star HD 190073 was reported to possess a magnetic field by Catala et al. (2007). They find a longitudinal magnetic field strength of 74 ± 10 G, with no variability in either the longitudinal field measurements or the Stokes V profiles in 13 months of observation. Catala et al. (2007) derive a mass of $2.85 \pm 0.25 M_{\odot}$ and an age of 1.2 ± 0.6 Myr (measured from the birth line). Acke & Waelkens (2004) also studied chemical abundances in this star using equivalent widths, and found roughly solar abundances. Thus we see magnetic field strengths (and in the case of HD 200775A a magnetic field geometry) in most other magnetic HAeBe stars that are similar to that observed in HD 72106A. However, there may be significant differences in surface chemistry between HD 72106A many other magnetic HAeBe stars.

Another important comparison to make is between HD 72106A and HD 72106B. The stars have similar masses ($2.4 \pm 0.4 M_{\odot}$ and $1.8 \pm 0.2 M_{\odot}$ respectively) and temperatures (11000 ± 1000 K and 8750 ± 500 K respectively), and identical ages. The stars also have very similar $v \sin i$ values (41.0 ± 0.3 km s $^{-1}$ and 53.9 ± 1.0 km s $^{-1}$ respectively). The existence of HD 72106A and B in such a young a binary system suggests that the two stars formed together. This implies that the initial gas both stars formed out of was very similar (e.g. Carrier et al., 2002). It is improbable that there were any great contrasts in temperature, density, abundance, or magnetic field

between the two stars initially. This makes it all the more surprising that the primary displays a strong dipolar magnetic field and very strong chemical peculiarities, while the secondary has no observable magnetic field, at the level of the noise in our observations, and it displays solar chemical abundances. Such results have been seen in other Ap/Bp stars for both binary systems and clusters (e.g. Carrier et al., 2002; Silvester, 2007). However, HD 72106 is one of, youngest case of this phenomenon known. The system HD 200775 the only other intermediate mass pre-main sequence binary known to possess a star with a strong globally ordered magnetic field (the primary in that case). Interestingly, the stars in this system are also fairly similar to each other in both mass and age. It remains an open question why the stars of HD 72106 are so similar in some respects and so different in others.

These observational results make some suggestions about the underlying physical processes at play. The conclusion that strong, globally ordered magnetic fields exist on the pre-main sequence for some HAeBe stars is supported. This conclusion is perfectly consistent with the fossil field theory for the origin of the magnetic field. The contemporaneous dynamo theory, on the other hand, is presented with further difficulties in timescale. A strong magnetic field must be generated, propagate to the surface, and become predominantly an oblique dipole, all before the star reaches the main sequence. While this is not conclusive evidence against contemporaneous dipole models, it does provide strong constraints on any such models.

The presence of chemical peculiarities in HD 72106A indicates that atomic diffusion can generate peculiarities on very short time scales, relative to the stellar life time. This is not especially surprising given the theoretical discussion presented in Section 1.2 (e.g. Michaud, 1970), however this is some of the first observational

evidence to constrain the timescale. HD 72106A raises the possibility that atomic diffusion can generate peculiarities on the pre-main sequence; that is, on time scales substantially shorter than the pre-main sequence lifetime of the star. Additionally, these results show that inhomogeneities can develop on such short timescales in the horizontal direction as well as the vertical. This suggests the effects of rotation and magnetic fields on diffusion also operate very quickly.

The possibility of diffusion generated peculiarities on the pre-main sequence raises questions about the impact of accretion. A heavily accreting star almost certainly does not possess a sufficiently stable atmosphere for chemical peculiarities to build up via atomic diffusion (e.g. Vauclair, 1981). However, in a star that is nearing the main sequence, accretion may fall off enough for the stellar atmosphere to become sufficiently stable for diffusion to begin generating peculiar abundances..

The similar strong chemical peculiarities seen in NGC 2244-334 (Bagnulo et al., 2004) and HD 72106A seem to support the very early appearance of chemical peculiarities. However the magnetic HAeBe stars HD 190073 and HD 104237, with ages 1.2 ± 0.6 Myr and ~ 2 Myr respectively, both appear to have solar abundances (Acke & Waelkens, 2004). This suggests that chemical peculiarities may arise between ~ 2 and ~ 10 Myr from the birth line. HD 190073 and HD 104237 both display emission lines, suggesting they may still be accreting, while NGC 2244-334 and HD 72106A do not. This raises an alternate possibility: if accretion effectively inhibits the buildup of chemical peculiarities through diffusion, then chemical peculiarities may simply arise shortly after a star stops accreting. Thus the observation of chemical peculiarities may provide information about accretion.

The Ap/Bp type chemical peculiarities in such a young star raise the question of

whether other types of chemical peculiarities can be seen in the pre-main sequence or on the ZAMS. In particular, are there non-magnetic species of chemically peculiar stars on the pre-main sequence or zero age main sequence? The underlying mechanism of diffusion is the same for both magnetic and non-magnetic chemically peculiar stars. However, the presence of a magnetic field could provide additional stability to the stellar atmosphere, allowing Ap/Bp style chemical peculiarities to arise earlier than non-magnetic patterns of chemical peculiarity.

Given the remarkably strong chemical peculiarities observed in HD 72106A, as well as in the very young star NGC 2244-334 (Bagnulo et al., 2004), it is interesting to speculate whether chemical peculiarities are initially very strong in young stars (near the ZAMS) and then decay as stars age. To properly investigate this speculation one would require detailed chemical abundances, as well as accurate ages, for a large number of stars.

The particularly short rotation period of HD 72106A, when compared to other main sequence Ap stars (Abt & Morrell, 1995), or HD 200775A, is intriguing. One can speculate that this fast rotation rate may be due to the star still being in the process of magnetic braking (angular momentum transfer from the star to surrounding material via the stellar magnetic field). Evidence for angular momentum loss in main sequence Ap stars has been seen in some cases (Wolff, 1981; Kochukhov & Bagnulo, 2006). However, given the lack of emission, HD 72106A appears to have largely cleared its immediate neighborhood of circumstellar material. Thus if magnetic braking is ongoing in HD 72106A, it must be a weak effect, and it must proceed slowly over a long period of time.

Implications for accretion in the presence of a strong globally ordered photospheric

magnetic field are not clear (Wade et al., 2007; Catala et al., 2007). While accretion does not appear to be ongoing in HD 72106A, a clear picture of the magnetic geometry in such a young star could be valuable in diagnosing the presence and extent of magnetospheric accretion in similar stars on the pre-main sequence. In contrast, HD 72106B displays emission and infrared excess (Oudmaijer et al., 1992), suggesting it may still be accreting. However we detect no magnetic field in the secondary, down to ~ 200 G. Thus, if accretion is occurring in the star, it seems unlikely that it is mediated by a strong globally organized magnetic field.

To resolve these questions detailed chemical abundance analysis, as well as an examination of magnetic fields, must be performed on a wide range of HAeBe stars. Varying ages, amounts of circumstellar material, and rates of accretion should be studied. Examining stars of different ages could determine at what point in time chemical peculiarities arise. Examining different levels of accretion and circumstellar activity could provide constraints on the stability of the atmosphere needed for diffusion to take place. As well, this may hint at the degree of turbulence caused by low levels of accretion. Studying a large number of HAeBe stars, both with and without magnetic fields, can demonstrate which species of chemical peculiarity can arise on the pre-main sequence. Such a study may also provide indirect information about accretion and mass loss in HAeBe stars.

In an extension of this study, it would be wise to focus on very young clusters of stars. In these cases, all the member stars formed at approximately the same time and in approximately the same environment. Thus one can use cluster average ages, and in some cases cluster average distances, to eliminate some of the large uncertainties present in this work. In addition, the cluster provides a context for studies of

individual stars, for example one could compare apparently peculiar chemical abundances to the cluster's average abundances. Studying cluster members should allow for more accurate dating of stars, and possibly improve mass determination, allowing for more precise conclusions to be drawn.

While there is clearly much work to be done in the study of magnetic pre-main sequence stars, there are potentially great rewards. Such stars provide the opportunity to examine diffusion and magnetic field formation in ways previously impossible. Additionally, these stars may supply critical information about the accretion processes by which stars form, with wide ranging implications. We are only beginning to see the range of interesting results that pre-main sequence magnetic stars can provide.

References

- Abt, H.A., & Morrell, N.I., 1995 ApJS, 99, 135A
- Acke, B. & Waelkens, C., 2004, A&A 427, 1009
- Adelman, S. J., Dukes, R. J. Jr., & Pyper D. M., 1992, AJ, 104, 314
- Adelman, S. J., Gulliver, A. F., Kochukhov, O. P., & Ryabchikova, T. A., 2002, ApJ, 575, 449
- Alecian, E., 2007, PhD thesis, Observatoire de Paris
- Alecian, E. et al, 2007, in preparation
- Alecian, E., Wade, G. A. , Catala, C., Bagnulo, S., Bohm, T., Bouret, J.-C., Donati, J.-F., Folsom, C. P., Landstreet, J. D., Silvester, J., 2006, in the proceedings of *Stellar Magnetic Fields* held at the Special Astrophysical Observatory, in press (astro-ph/0612186)
- Alecian, G., & Stift, M. J., 2006, A&A, 454, 571
- Alecian, G., & Stift, M. J., 2002, A&A, 387, 271
- Aller, M.F., & Everett, C. H. M., 1972, ApJ, 172. 447

Asplund, M., 2005, *ARA&A*, 43, 481

Aurière, M., Wade, G. A., Silvester, J., Lignières, F., Bagnulo, S., Bale, K., Dintrans, B., Donati, J.-F., Folsom, C. P., Gruberbauer, M., Hui Bon Hoa, A., Jeffers, S., Johnson, N., Landstreet, J. D., Lèbre, A., Lüftinger, T., Marsden, S., Mouillet, D., Naseri, S., Paletou, F., Petit, P., Power, J., Rincon, F., & Toqué, N., 2007, *A&A*, submitted

Avni, Y., 1976, *ApJ*, 210, 642

Babcock, H. W., 1947, *ApJ*, 105, 105

Babel, J., 1992, *A&A*, 258, 449

Bagnulo, S., Hensberge, H., Landstreet, J. D., Szeifert, T., & Wade, G. A., 2004, *A&A*, 416, 1149

Bagnulo, S., Landstreet, J. D., Lo Curto, G., Szeifert, T., & Wade, G. A., 2003, *A&A*, 403, 645

Barnes, J. R., Collier Cameron, A., Unruh, Y. C., Donati, J. F., & Hussain, G. A. J., 1998, *MNRAS*, 299, 904

Bernasconi, P. A., 1996, *A&AS*, 120, 57

Beskrovnaya, N. G., Pogodin, M. A., Miroshnichenko, A. S., Thé, P. S., Savanov, I. S., Shakhovskoy, N. M., Rostopchina, A. N., Kozlova, O. V., & Kuratov, K. S., 1999, *A&A*, 343, 163

Blommaert, J. A. D. L., van der Veen, W. E. C. J., & Habing, H. J., 1993, *A&A*, 267, 39

- Blondel, P. F. C. & Tjin A Djie, H. R. E., 1994, in the proceedings of '*The nature and evolutionary status of Herbig Ae/Be stars*', ASP Conference Series, 62, 211
- Bohlender, D. A., Gonzalez, J.-F., & Matthews, J. M., 1999, *A&A*, 350, 553
- Bohlender, D. A., Landstreet, J. D, 1990
- Böhm, T. & Catala, C., 1993, *A&AS*, 101, 629
- Böhm, T. & Catala, C., 1995, *A&A*, 301, 155
- Böhm-Vitense, E., 1989, *Introduction to Stellar Astrophysics: Vol 1*, Cambridge University Press
- Bolton, C. T., 1970, *ApJ*, 161, 1187
- Bolton, C. T., 1971, *A&A*, 14, 233
- Borra, E. F., Landstreet, & J. D., Mestel, L., 1982, *ARA&A* 20, 191
- Braithwaite, J. & Nordlund, Å, 2006, *A&A*, 450, 1077
- Carrier, F., North, P., Udry, S., & Babel, J., 2002, *A&A*, 394, 151
- Catala, C., Alecian, E., Donati, J.-F., Wade, G. A., Landstreet, J. D., Böhm, T., Bouret, J.-C., Bagnulo, S., Folsom, C., & Silvester, J., 2007, *A&A*, 462, 293
- Catala, C., Donati, J. F., Böhm, T., Landstreet, J., Henrichs, H. F., Unruh, Y., Hao, J., Collier Cameron, A., Johns-Krull, C. M., Kaper, L., Simon, T., Foing, B. H., Cao, H., Ehrenfreund, P., Hatzes, A. P., Huang, L., de Jong, J. A., Kennelly, E. J., ten Kulve, E., Mulliss, C. L., Neff, J. E., Oliveira, J. M., Schrijvers, C., Stempels, H. C., Telting, J. H., Walton, N., & Yang, D., 1999, *A&A*, 345, 884

- Charbonneau, P & MacGregor, K. B., 2001, *ApJ* 559, 1094
- Cidale, L. S., Arias, M. L., Torres, A. F., Zorec, J., Frmat, Y., & Cruzado, A., 2007, *A&A*, 468, 263
- Corder, S., Eisner, J., & Sargent, A., 2005, *ApJ*, 622, 133
- Cowley, C.R., 1994, *Obs.*, 114, 308
- Cowley, C.R. & Adelman, S.J., 1983, *QJRAS*, 24, 393
- Cushing, M. C., Rayner, J. T., & Vacca, W. D., 2005, *ApJ*, 623, 1115
- Damiani, F., Micela, G., Sciortino, S., & Harnden, F. R., Jr., 1994, *ApJ*, 436, 807
- Donati, J.-F., 2000, Thèse d'habilitation, Observatoire Midi-Pyrénées
- Donati, J.-F., 2007, <http://www.ast.obs-mip.fr/projets/espadons/espadons.html>,
in preparation as: Donati J.-F., Catala C., Landstreet J. D. et al., 2007, *MNRAS*
- Donati, J.-F., Babel, J., Harries, T. J., Howarth, I. D., Petit, P., & Semel, M., 2002, *MNRAS*, 333, 55
- Donati, J.-F., Mengel, M., Carter, B. D., Marsden, S., Collier Cameron, A., & Wichmann, R., 2000, *MNRAS*, 316, 699
- Donati, J.-F., Semel, M., Carter, B. D., Rees, D. E., & Collier Cameron, A., 1997, *MNRAS*, 291, 658
- Donati, J.-F., Semel, M., & Rees, D. E., 1992, *A&A*, 265, 669
- Donati, J.-F., Wade, G. A., Babel, J., Henrichs, H. F., de Jong, J. A., Harries, T. J., 2001, *MNRAS*, 326, 1265

- Drouin, D., 2005, MSc thesis, Royal Military College of Canada
- Dunkin, S. K., Barlow, M. J., & Ryan, S. G., 1997, MNRAS, 290, 165
- Eisner, J. A., Lane, B. F., Hillenbrand, L. A., Akeson, R. L., & Sargent, A. I., 2004, ApJ, 613, 1049
- ESA 1997, The Hipparcos and Tycho Catalogues, ESA SP-1200
- Fabricius, C., & Makarov, V.V., 2000, A&A, 356, 141
- Folsom, C. P., Wade, G. A., Bagnulo, S., & Landstreet, J. D., 2007, MNRAS, 376, 361
- Ghandour, L., Strom, S., Edwards, S., & Hillenbrand, L., 1994, in the proceedings of '*The nature and evolutionary status of Herbig Ae/Be stars*', ASP Conference Series, 62, 223
- Gray, D. F., 2005, *The Observation and Analysis of Stellar Photospheres 3rd Edition*, Cambridge University Press
- Grevesse, N., Asplund, M., & Sauval, A. J., 2005, in the proceedings of '*Element Stratification in Stars: 40 Years of Atomic Diffusion*', EAS 17, 21
- Griffiths, D. J., 1995, *Introduction to Quantum Mechanics*, Prentice Hall Inc.
- Grinin, V. P., 1994, in the proceedings of '*The nature and evolutionary status of Herbig Ae/Be stars*', ASP Conference Series, 62, 63
- Grinin, V. P., Thé, P. S., de Winter, D., Giampapa, M., Rostopchina, A. N., Tambovtseva, L. V., & van den Ancker, M. E., 1994, A&A, 292, 165

- Hamann, F & Persson, S. E., 1992, ApJS, 82, 285
- Hartkopf W.I., Mason B.D., McAlister H.A., Turner N.H., Barry D.J., Franz O.G.,
& Prieto C.M., 1996, AJ, 111, 936
- Hatzes, A. P., Penrod, G. D., & Vogt, S. S., 1989, ApJ, 341, 456
- Herbig, G. H., 1960, ApJS, 4, 337
- Hernández, J., Calvet, N., Briceño, C., Hartmann, L., & Berlind, P., 2004, AJ, 127,
1682
- Hensberge, H., Pavlovski, K., & Verschueren, W., 2000, A&A, 358, 553
- Hoffleit, D., Jaschek, C. V., 1991, *The Bright Star Catalogue*, Yale University Observ-
atory
- Hubrig, S., Schiller, M., & Yudin, R. V., 2004, A&A, 428, 1
- Humlicek., 1982, J. Queant. Spec. Rad. Trans. 27, 437
- Irwin, A. W., 1981, ApJS, 45, 621
- Jaschek, C., & Jaschek, M., 1995, *The behavior of chemical elements in stars*, Cam-
bridge University Press
- Khan, S. A. & Shulyak, D. V., 2006, A&A, 448, 1153
- Kirkpatrick, D. J., 2005, ARA&A, 43, 245
- Kochukhov O., Adelman, S. J., Gulliver, A. F., & Piskunov N., 2007b, Nature Physics,
in press

- Kochukhov, O., & Bagnulo, S., 2006, *A&A*, 450, 763
- Kochukhov, O., Drake, N. A., Piskunov, N., & de la Reza, R., 2004, *A&A*, 424, 935
- Kochukhov, O., Ryabchikova, T., Weiss, W. W., Landstreet, J. D., & Lyashko, D., 2007a, *MNRAS*, 376, 651
- Kochukhov, O., Tsymbal, V., Ryabchikova, T., Makaganyk, V., & Bagnulo, S., 2006, *A&A*, 460, 831
- Korhonen, H., Berdyugina, S. V., Hackman, T., Duemmler, R., Ilyin, I. V., & Tuominen, I., 1999, *A&A*, 346, 101
- Kupka, F., Piskunov, N. E., Ryabchikova, T. A., Stempels, H. C., & Wiess, W. W., 1999, *A&AS*, 138, 119
- Kurtz, D. W., 1990, *ARA&A*, 28, 607
- Kurtz, D. W., & Martinez, P., 2000, *Baltic Astronomy*, 9, 253.
- Kurucz, R. 1993, *CDROM Model Distribution*, Smithsonian Astrophys. Obs.
- Kuschnig, R., Ryabchikova, T. A., Piskunov, N. E., Weiss, W. W., & Gelbmann, M. J., 1999, *A&A*, 348, 924
- Lampton, M., Margon, B., & Bowyer, S., 1976, *ApJ*, 208, 177
- Landstreet, J. D., 1982, *ApJ*, 258, 639
- Landstreet, J. D., 1988, *ApJ*, 326, 967
- Landstreet, J. D., 1992, *A&ARv*, 4, 35

- Landstreet, J. D., 1998, *A&A*, 338, 1041
- Landstreet, J. D, Bagnulo, S., Andretta, V., Fossati, L., Mason, E., Silaj, J., & Wade, G. A., 2007, *A&A*, 470, 685
- Lueftinger, T., Kuschnig, R., Piskunov, N. E., & Weiss, W. W., 2003, *A&A*, 406, 1033
- Marsden, S. C., Waite, I. A., Carter, B. D., & Donati, J.-F., 2005, *MNRAS*, 359, 711
- Marsh, K. A., Van Cleve, J. E., Mahoney, M. J., Hayward, T. L., & Houck, J. R., 1995, *ApJ*, 451, 777
- Martin, B., & Wickramasinghe, D.T., 1979, *MNRAS*, 189, 883
- Mason, B., 2006, Washington Double Star Catalogue, private correspondence
- Massey, P., 2003, *ARA&A*, 41, 15
- Mathys, G., 1989, *Fund. Cosmic Phys.* 13, 143
- Maury, A. C. & Pickering, E. C., 1897, *Annals of Harvard College Observatory*, 28, 1
- Meeus, G., Waelkens, C., & Malfait, 1998, *A&A*, 329, 131
- Michaud, G., 1970, *ApJ*, 160, 641
- Michaud, G., 1982, *ApJ*, 258, 349
- Michaud, G., Charland, Y., & Megessier, C., 1981, *A&A*, 103, 244
- Moss, D., 2003, *A&A*, 403, 693

- Moss, D., 2001, in the proceedings of *Magnetic Fields Across the Hertzsprung-Russell Diagram*, ASP Conference Proceedings, 248, 305
- Muzerolle, J., D'Alessio, P., Calvet, N., & Hartmann, L., 2004, *ApJ*, 617, 406
- Natta, A., Palla, F., Butner, H. M., Evans, N. J., II, & Harvey, P. M., 1993, *ApJ*, 406, 674
- North, P., 1998, *A&A*, 334, 181
- Ostlie, D. A., & Carroll, W. C., 1996 *An Introduction to Modern Stellar Astrophysics*, Addison-Wesley Publishing Company, Inc.
- Oudmaijer, R. D., van der Veen, W. E. C. J., Waters, L. B. F. M., Trams, N. R., Waelkens, C., & Engelsman, E., 1992, *A&AS*, 96, 625
- Palla, F. & Stahler, S. W., 1993, *ApJ* 418, 414
- Piskunov, N. E., Tuominen, I., & Vilhu, O., 1990, *A&A*, 230, 363
- Power, J., 2007, MSc thesis, Queen's University, Canada
- Press, W. H., Teukolsky, S. A., Vetterling, W. T., & Flannery, B. P., 1992, *Numerical Recipes in FORTRAN 2nd Edition*, Cambridge University Press
- Preston, G. W., 1967, *ApJ*, 150, 547
- Rees, D. E., 1987, *A Gentle Introduction to Polarized Radiative Transfer in Numerical radiative transfer*, p. 213, Kalkofen Ed., Cambridge University Press
- Rice, J. B., Wehlau, W. H., & Khokhlova, V. L., 1989, *A&A*, 208, 179

- Ryabchikova, T. A., Landstreet, J. D., Gelbmann, M. J., Bolgova, G. T., Tsymbal, V. V., & Weiss, W. W., 1997, *A&A*, 327, 1137
- Ryabchikova, T., Piskunov, N., Kochukhov, O., Tsymbal, V., Mittermayer, P., & Weiss, W. W., 2002, *A&A*, 384, 545
- Ryabchikova, T. A., Savanov, I. S., Hatzes, A. P., Weiss, W. W., & Handler, G., 2000, *A&A*, 357, 981
- Schütz, O., Meeus, G., & Sterzik, M. F., 2005, *A&A*, 431, 165
- Semel, M., Donati, J.-F., & Rees, D. E., 1993, *A&A*, 278, 231
- Shorlin, S. L. S., Wade, G. A., Donati, J.-F., Landstreet, J. D., Petit, P., Sigut, T. A. A., & Strasser, S., 2002, *A&A*, 392, 637
- Shulyak, D., Tsymbal, V., Ryabchikova, T., Stütz, Ch., & Weiss, W. W., 2004, *A&A*, 428, 993
- Shurcliff, W. A., Ballard, S. S., 1964, *Polarized Light*, D. van Nostrand Inc.
- Silvester, J., 2007, MSc thesis, Queen's University, Canada
- Stelzer, B., Micela, G., Hamaguchi, K., & Schmitt, J. H. M. M., 2006, *A&A*, 457, 223
- Stepień, K. & Landstreet, J. D., 2002, *A&A*, 384, 554
- Stibbs, D. W. N., 1950, *MNRAS*, 110, 395
- Telleschi, A., Gdel, M., Briggs, K. R., Skinner, S. L., Audard, M., & Franciosini, E., 2007, *A&A*, 468, 541

- Thé, P. S., de Winter, D., & Perez, M. R., 1994, *A&AS*, 104, 315
- Thompson, M. J., Christensen-Dalsgaard, J., Miesch, M. S., & Toomre, J., 2003, *ARA&A*, 41, 599
- Tikhonov, A. N., 1963, *Soviet Math. Dokl.*, 4, 1624
- Torres, C. A. O., Quast, G., de La Reza, R., Gregorio-Hetem, J., & Lepine, J. R. D., 1995, *AJ*, 109, 2146
- Trigilio, C., Leto, P., Leone, F., Umana, G., & Buemi, C., 2000, *A&A*, 362, 281
- van den Ancker, M. E., de Winter, D., & Tjin A Djie, H. R. E., 1998, *A&A*, 330, 145
- van der Tak, F. F. S., van Dishoeck, E. F., Evans, N. J., II, & Blake, G. A., 2000, *ApJ*, 537, 283
- Vauclair, S., 1981, *AJ*, 86, 513
- Vauclair, S. & Vauclair, G., 1982, *ARA&A*, 20, 37
- Vieira, S. L. A., Corradi, W. J. B., Alencar, S. H. P., Mendes, L. T. S., Torres, C. A. O., Quast, G. R., Guimarães, M. M., & da Silva, L., 2003, *AJ*, 126, 2971
- Vogt, S. S., Penrod, G. D., & Hatzes, A. P., 1987, *ApJ*, 321, 496
- Wade, G. A., Aurire, M., Bagnulo, S., Donati, J.-F., Johnson, N., Landstreet, J. D., Lignières, F., Marsden, S., Monin, D., Mouillet, D., Paletou, F., Petit, P., Toqu; N., Alecian, E., & Folsom, C., 2006b, *A&A*, 451, 293
- Wade, G. A., Bagnulo, S., Drouin, D., Landstreet, J. D., Monin, D., 2007, *MNRAS*, 376, 1145

- Wade, G. A., Bagnulo, S., Kochukov, O., Landstreet, J. D., Piskunov, N., & Stift, M. J., 2001, *A&A*, 374, 265
- Wade, G. A., Bohlender, D. A., Brown, D. N., Elkin, V. G., Landstreet, J. D., & Romanyuk, I. I., 1997, *A&A*, 320, 172
- Wade, G. A., Donati, J.-F., Landstreet, J. D., & Shorlin, S. L. S., 2000a, *MNRAS*, 313, 823
- Wade, G. A., Donati, J.-F., Landstreet, J. D., & Shorlin, S. L. S., 2000b, *MNRAS*, 313, 851
- Wade, G. A., Drouin, D., Bagnulo, S., Landstreet, J. D., Mason, E., Silvester, J., Alecian, E., Böhm, T., Bouret, J.-C., Catala, C., & Donati, J.-F., 2005, *A&A*, 442, 31
- Wade, G. A., Fullerton, A. W., Donati, J.-F., Landstreet, J. D., Petit, P., & Strasser, S., 2006a, *A&A*, 451, 195
- Waters, L. B. F. M. & Waelkens, C., 1998, *ARA&A*, 36, 233
- Wolff, S. C., 1981, *ApJ*, 244, 221
- Wynne, C. G. & Worswick, S. P., 1986, *MNRAS*, 220, 657
- Zinnecker, H. & Preibisch, T., 1994, *A&A*, 292, 152

Appendix A

CFHT Observing Proposal

The following is the observing time request submitted to the Canada-France-Hawaii Telescope by the author of this thesis. The request was for additional ESPaDOnS observations of the HD 72106 system, with the primary goal of obtaining a precise rotation period for the HD 72106A. The request was submitted as a joint Canadian and French proposal. Dr. Evelyne Alecian kindly agreed to be the principal investigator for the French half of the proposal. The author of this thesis wrote both the Canadian and French versions of the proposal, and was principal investigator for the Canadian portion of the proposal. The two versions of the observing proposal are virtually identical, so for brevity only the Canadian version is included. Our request for observing time was granted, allowing us to obtain the observations of HD 72106A and B from March 2007 listed in Table 2.1.

Date: September 21, 2007 Category: Stars - Individual, Binaries, Clusters Proposal: C2036

CFHT
OBSERVING TIME REQUEST
Semester: 2007A Agency: Canada

1. Title of the Program (*may be made publicly available for accepted proposals*):
Investigating the magnetic chemically peculiar HAeBe star HD 72106A

2. Principal Investigator: **Colin Folsom**
 Postal address: Royal Military College, Station Forces P.O. Box 17000 K7K 7B4 Kingston
 Fax: Phone: 613-530-3540 E-mail: Colin.Folsom@rmc.ca

3. Co-Investigators:

Evelyne Alecian	Institute: Observatoire de Paris	E-mail: Evelyne.Alecian@obspm.fr
Wade Gregg	Institute: Royal Military College	E-mail: Gregg.Wade@rmc.ca
Claude Catala	Institute: Observatoire de Paris	E-mail: Claude.Catala@obspm.fr
John Landstreet	Institute: University of Western Ontario	E-mail: jlandstr@astro.uwo.ca

4. Summary of the Program (*may be made publicly available for accepted proposals*):
 Recent groundbreaking observations with ESPaDOnS have shown that about 10% of the pre-main sequence Herbig Ae/Be (HAeBe) stars display strong globally ordered magnetic fields. This suggests that the progenitors of the main sequence magnetic Ap and Bp stars are the newly discovered magnetic HAeBe stars. The first HAeBe star in which a magnetic field was discovered with ESPaDOnS, HD 72106A, has very recently been found to possess strong chemical peculiarities, up to 2 dex above solar. The pattern of abundance anomalies seen, including overabundances of Si, Cr, and Fe, is characteristic of Ap and Bp stars. HD 72106A is the only HAeBe star known to display chemical peculiarities. Consequently, an investigation of this unique link between Ap and HAeBe stars is necessary. An accurate rotation period, magnetic field geometry, and surface abundance map are required. However, due to the limited number of observations and aliasing effects from the star's ~ 2 day rotation period, it is impossible to determine these properties from current data. Therefore we propose to observe the star and collect 14 additional spectra. Numerical experiments show that this will be sufficient to accurately determine the period of HD 72106A, and allow us to determine the magnetic field geometry and to map the surface abundance distributions of this remarkable star.

5. Summary of the Observing Run Requested:

Instrument	Detector	Moon (d)	Filters		Grisms		
ESPaDOnS	EEV1	14					
Time Req.	Service/Queue?	Queue Mode	Image Quality	Opt. LST	Min. LST	Max. LST	
0.5 nights	No	—	—	08:00	04:00	12:00	

6a. Is this a joint proposal? YES 6b. If yes, total number of nights or hours requested from all agencies? 1 nights

7a. Is this a Thesis Project? YES 7b. If yes, indicate supervisor: Wade

8. Special instrument or telescope requirements:
 polarimetric mode

9. Scheduling constraints:
 Scheduling for optimal phase coverage: three consecutive 1/3 nights

10. Scientific Justification (*science background and objectives of the proposed observations: 1 page maximum*):

About 10% of main sequence A and B stars display strong globally ordered magnetic fields - these are the so-called Ap and Bp stars. The origin and evolution of these magnetic fields is currently the subject of intensive research. An important avenue of this research is the investigation the progenitors of Ap and Bp stars. Herbig Ae and Be (HAeBe) stars are the pre-main progenitors of the main sequence A and B type stars. As such, HAeBe stars have intermediate masses and display emission, infrared excess, and tend to be associated with dust and nebulosity. It has been long suggested that some HAeBe stars may evolve into magnetic main sequence Ap and Bp stars. If this were the case, it was hoped that there would be some distinguishing observable feature in HAeBe stars linking them to Ap stars.

Pioneering ESPaDOnS observations in 2005 and 2006 successfully detected magnetic fields in 4 HAeBe stars (Wade et al. 2005, Catala et al. 2006, Alecian et al. 2006). The detected fields display similar intensities and geometries to those of Ap stars (Alecian et al. 2006, Folsom et al. 2006). The longitudinal field strengths detected are on the order of hundreds of gauss, and the geometries are predominantly dipolar. Additionally, the frequency of magnetic HAeBe stars is similar to the frequency of magnetic Ap and Bp stars in the set of all A and B stars, around 10% (Wade et al. 2005). This strongly supports the idea that magnetic HAeBe stars do in fact represent the progenitors of main sequence magnetic Ap and Bp stars.

The HAeBe star HD 72106A was the first of four HAeBe stars in which magnetic fields were detected with ESPaDOnS (Fig. 1). It is the *only* magnetic HAeBe that displays clear chemical peculiarities of the type seen in Ap stars. Specifically, overabundances in Fe, Ti, and Si of 10 times above solar and Cr of 100 times above solar have been inferred (Folsom et al. 2006). Sample spectrum synthesis is shown in Fig. 2. Additionally, strongly non-uniform surface abundance distributions are inferred for Cr and Fe. Non-uniform surface abundances are also characteristic of Ap stars. Therefore, HD 72106A represents a unique opportunity to study the early development of both chemical peculiarities and magnetic fields in intermediate-mass stars. The HD 72106 system is a close but optically resolved (0.8") binary. The secondary, HD 72106B, is a chemically normal A type HAeBe star. A single ESPaDOnS observation, obtained during conditions of very good seeing, shows no magnetic field in the secondary, with a 168 gauss limit (at 1σ). Abundance analysis shows solar concentrations of Cr, Fe, Ti, and Ba (Folsom et al. 2006). Additionally, no asymmetries have been observed in the line profiles of the star, implying a uniform surface distribution of elements. Thus we have a normal HAeBe star that is contemporaneous and co-eval with a magnetic chemically peculiar HAeBe star. This scenario can potentially provide strong additional constraints on the formation of magnetic fields and chemical peculiarities in A and B stars.

Currently 9 observations have been obtained of HD 72106A. Mean photospheric abundances have been calculated, longitudinal magnetic field measurements obtained, and a rotation period estimated. Despite this, an unambiguous rotation period cannot be determined from the current data. The Hipparcos photometric variability of HD 72106A is also too weak to produce a definite period. A periodogram based on longitudinal field measurements produces many acceptable periods around 2 days (Fig. 3). A more sophisticated technique looking at the variability in each pixel across the Stokes I and V line profiles also fails to produce a unique period. Although it is clear that the period is close to 2 days, the lack of a precise period presents a major obstacle, as this is *absolutely* necessary to determine the magnetic field geometry and to map the surface abundance distribution, using a technique like Doppler Imaging.

Numerical experiments show that the period ambiguity results directly from the current time sampling (window function) and the near-integer period in days. Further experiments show that an additional 14 observations, distributed over three consecutive nights, will allow us to unambiguously determine a precise rotation period for HD 72106A (Fig. 3). Moreover, dense spectroscopic coverage is needed to perform Doppler Imaging. This is *the* necessary piece of information for us to begin mapping the surface chemical abundance distribution and modelling the magnetic field of this unique and remarkable star.

11. References (1 page maximum):

- Alecian, E., Catala, C., Donati, J.-F., Wade, G. A., Landstreet, J. D., Böhm, T., Bouret, J.-C., Bagnulo, S., Folsom, C. P., Silvester, J. 2006, A&A, in preparation
- Catala, C., Alecian, E., Donati, J.-F., Wade, G.A., Landstreet, J.D., Böhm, T., Bouret, J.-C., Bagnulo, S., Folsom, C. P., Silvester, J. 2006, A&A, submitted
- Donati, J.-F., Semel, M., Carter, B. D., Rees, D. E., Collier Cameron, A. 1997, MNRAS, 291, 658
- Folsom, C. P., Wade, G. A., Hanes, D. A., Catala, C., Alecian, E., Bagnulo, S., Böhm, T., Bouret, J.-C., Donati, J.-F., Landstreet, J. D. 2006, MNRAS in preparation
- Wade, G. A., Donati, J.-F., Landstreet, J. D., Shorlin, S. L. S. 2000, MNRAS, 313, 823
- Wade, G. A., Drouin, D., Bagnulo, S., Landstreet, J. D., Mason, E., Silvester, J., Alecian, E., Böhm, T., Bouret, J.-C., Catala, C., Donati, J.-F. 2005, A&A, 442, L31
- Wade, G. A., Bagnulo, S., Drouin, D., Landstreet, J. D., Monin, D., 2006, MNRAS, submitted

12. Figures (all figures must appear on a single page):

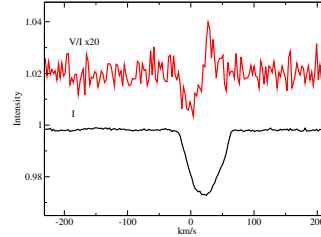


Figure 1: Illustrative mean LSD Stokes I (bottom) and V (top) profiles of HD 72106A. This observation corresponds to a longitudinal magnetic field value of 391 ± 65 gauss.

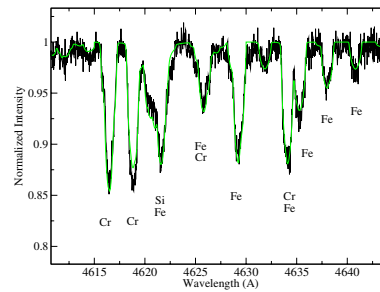


Figure 2: Example observed spectrum of HD 72106A, in black, and best fit synthetic spectrum, in green. The major elements contributing to each line have been labeled. The unusually strong Cr lines are notable.

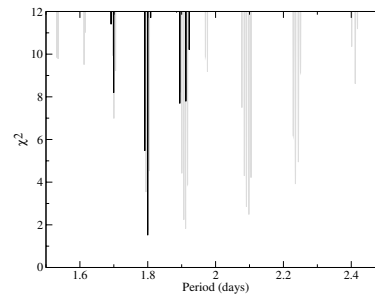


Figure 3: Periodograms based on longitudinal magnetic field data. A periodogram based on our current 9 observations is presented in grey. A periodogram including 14 additional proposed observations, based on numerical experiments with a period of 1.8 days, is presented in black. These new observations allow a unique, unambiguous rotation period to be determined, 1.8000 ± 0.0001 days. Such an improvement is the primary goal of this proposal.

13. Technical Justification

(provide technical details of the proposed observations; justify the use of the CFHT, the requested instrument configuration, and the amount of telescope time requested: 1 page maximum):

The aim of the proposed observations is twofold. The primary objective is to accurately determine the rotation period of the magnetic HAeBe star HD 72106A. The secondary objective of this program is to acquire additional high-resolution spectra of HD 72106A for the purposes of Doppler Imaging. To accomplish this we will acquire a series of observations of the spectrum of HD 72106A in circular polarisation. We will use the circular polarisation induced in the metallic absorption lines of the star by the longitudinal Zeeman effect to deduce the longitudinal magnetic field in the star. The longitudinal magnetic field strength varies with the stellar rotation; thus we can use the variation in the longitudinal field strength over the course of our observations to determine the rotation period of the star. Addition of the left and right circularly polarised spectra provides the total intensity (Stokes I) spectrum for free, allowing us to perform Doppler Imaging.

It is important to note that, while ideal, it is not necessary to resolve both components of the HD 72106 binary system for these observations. The spectrum of the secondary appears to be stable, with symmetric line profiles, except for emission in H α . Thus if we obtain spectra of the combined light from the system, we can subtract our existing observation of the secondary off of the combined observation, weighted by the relative luminosities of the components. Thus we can reconstruct the spectrum of the primary if the seeing is not sufficiently good to separate the primary from the secondary (Folsom et al. 2006).

We will carry out these observations with ESPaDOnS, the new high-resolution spectropolarimeter at CFHT. Previous observations of HD 72106A and B in 2005 and 2006 show that ESPaDOnS is fully capable of carrying out the necessary observations for this program.

ESPaDOnS is essentially the only instrument in the world capable of providing both the polarisation and the high-resolution spectrum observations necessary for this program. The low-resolution spectropolarimeter at the VLT, FORS1, may be capable of providing the necessary magnetic field data, however ESPaDOnS provides some major advantages. ESPaDOnS can resolve the rotationally broadened metallic line profiles in HD 72106A, allowing us to detect a magnetic field even when the longitudinal field value is zero (e.g. dipolar fields at “crossover” phases). Moreover, there has been some concern raised regarding the suitability of FORS1 for observations of pre-main sequence objects (Wade et al. 2006), thus we can be more confident in the precision of our results with ESPaDOnS. Further observations with ESPaDOnS also allow us to maintain a more homogeneous data set when combined with our previous observations of HD 72106A from the same instrument. Finally and most importantly, observations with FORS1 would require a second observing campaign to acquire the high-resolution spectra necessary for Doppler mapping. Narval, the copy of ESPaDOnS being installed at TBL/Pic du Midi, is not suitable for these observations because the target is too far south to be accessible. We will use the observing procedure described by Wade et al. (2000), with each exposure divided up into 4 subexposures and the quarter wave plate rotated by ± 90 degrees between each subexposure. The data reduction will be performed with Libre-ESPRIT (Donati et al. 1997; Donati et al., in preparation). If observations of the individual components of the system are not possible due to the seeing conditions, the spectrum of the primary will be reconstructed. Least-Squares Deconvolution (Donati et al. 1997) and complementary techniques will be used to determine longitudinal magnetic field values. The rotation period will then be found by fitting models thorough the magnetic field data and constructing a periodogram, and by direct modelling of Stokes V profiles. Doppler Imaging will be performed using the code “Inverse” with which we and our collaborators have past expertise. All the members of our team are experts at data reduction and analysis of spectropolarimetric observations.

Based on our previous observations of HD 72106A, to achieve a peak S/N ratio of about 250 we will require an exposure time of 600x4 seconds. Including a 160 second readout time and an additional 30 seconds of overhead we will require 2590 seconds per exposure. Thus we can acquire the necessary 14 observations in 10 hours, or about one night, However, for optimal phase coverage, we request that this be distributed uniformly over 3 consecutive nights, *and spread evenly between the Canadian and French agencies.*

Page 6

Proposal: C2036

14. Targets:					
Object/Field	α	δ	Epoch	Mag/Flux	Comment
HD 72106	08:29:34.9	-38:36:21.1	2000	8.58	

15. General Target Information:
The target details represent both components of this 0.8" separation binary system. The V magnitude of the primary, our principal object of interest, is 9.00 and the magnitude of the secondary is 9.62. To obtain a peak S/N ratio of 250 in the primary we require a 600x4 second exposure.

16. Is this program conducted in relation with other observations (optical, radio, space)?
YES: This program follows up earlier discovery observations obtained with ESPaDOnS.

17. How many additional nights or hours at CFHT would be required to complete this project? 0 nights

18a. Is an extension of the one-year proprietary period required? NO 18b. Proposed proprietary period? 12 months
18c. If yes, justify the request for an extension:

19. Recent Allocations on CFHT and Other Telescopes:

1. CFHT, 2005A, 2005B, 6 nights, (Wade et al.), "Seeking the progenitors of magnetic Ap stars", CFHT, 2005A, 2005B, 7 nights, (Catala et al.), "Magnetic fields in the pre-main sequence Herbig Ae/Be stars", observations obtained for approximately 60 Herbig Ae/Be stars, data fully reduced, magnetic fields detected in 4 stars (modelling is in progress). One paper has been published (Wade et al., 2005, A&A, 442, L31) + 3 papers (Catala et al. 2006, Alecian et al. 2006, Folsom et al. 2006) and 3 theses (2 MSc - C. Folsom and K. Bale, 1 PhD - E. Alecian) in preparation.
2. CFHT, 2005A, 3 nights, (Landstreet et al.), "A spectropolarimetric survey of magnetic stars in open clusters", Lots of stars observed, a number of new magnetic field detections and confirmations. Data reduction was performed at CFHT and subsequent magnetic field measurements were made. We are incorporating these data into a cluster database and they will appear in a forthcoming paper. (Thesis of an undergraduate student)
3. CFHT, 2005B, 2 nights, (Wade et al.), "Magnetic fields of massive stars in the ONC", data fully reduced and currently being analyzed, magnetic field detected in at least one star. (PhD thesis - V. Petit)
4. CFHT, 2005B, 1.5 nights, (Wade et al.), "Magnetic Doppler Imaging of Ap stars", no program data acquired due to instrument problems, excellent backup program data acquired which is now fully reduced and under analysis.
5. CFHT, 2006B, 3 nights, (Catala et al.), "Magnetism of pre-main sequence A and B stars in young open clusters: the influence of environment age and rotation", the first part of a multi-semester project. 1 night already secured in Aug. 2006, 8 stars observed, 1 magnetic field detection; 2 nights remaining in Dec. 2006.

20. Publications Resulting from CFHT Observations (only the 12 most recent contained in the database are displayed):

Donati, J.-F., Howarth, I. D., Bouret, J.-C., Petit, P., Catala, C., Landstreet, J. 2006, MNRAS, 365, L6
 C. Catala, E. Alecian, J.-F. Donati, G.A. Wade, J.D. Landstreet, T. Böhm, J.-C. Bouret, S. Bagnulo, C. Folsom, J. Silvester 2006, A&A, submitted
 Wade, G.A., Drouin, D., Bagnulo, S., Landstreet, J.D., Mason, E., Silvester, J., Alecian, E., Böhm, T., Bouret, J.-C., Catala, C., Donati, J.-F. 2005, A&A, 442, L31
 Unruh, Y. C. and 23 others 2004, MNRAS, 348, 1301
 Kochukhov, O., Ryabchikova, T., Landstreet, J. D. , Weiss, W. W. 2004, MNRAS, 351, L34
 Kochukhov, O., Landstreet, J. D., Ryabchikova, T., Weiss, W. W., Kupka, F. 2002, MNRAS, 337, L1
 Sigut, T. A. A., Landstreet, J. D. and Shorlin, S. L. S. 2000, ApJ, 530, L89
 Catala, C. and 26 others 1999, A&A, 345, 884
 Landstreet, J.D. 1998, A&A, 338, 1041
 Hill, G. M., Bohlender, D. A., Landstreet, J. D., Wade, G. A., Manset, N., Bastien, P. 1998, MNRAS, 297, 236
 Ryabchikova, T. A., Landstreet, J. D., Gelbmann, M. J., Bolgova, G. T., Tsymbal, V. V. and Weiss, W. W. 1997, A&A, 327, 1137
 Mathys, G., Hubrig, S., Landstreet, J. D., Lanz, T. and Manfroid, J. 1997, A&AS, 123, 353

Disclaimer: *In submitting this application, I acknowledge that I am aware of CFHT's policy concerning public access to data after a proprietary period of one year. I recognize that each individual reacts differently to working at high altitude and that some individuals may experience potentially severe altitude sickness or other medical problems. I agree that observers proposing to work at Mauna Kea should be medically fit for such work and not have conditions which would be inconsistent with work at high altitude. I understand and agree that Canada-France-Hawaii Telescope Corporation and those acting in its behalf have no liability with respect to the risks associated with work at the telescope by observers or others, and that every participant in an observing run at Mauna Kea should follow the policy of his or her own employer or sponsoring agency with respect to medical examinations and other requirements for work at high altitude.*

Signature: signed via "POOPSY"

Appendix B

Computer Programs Written

Included here are the raw Fortran source codes use for the continuum normalization, LSD profile period searching, and spectrum fitting routines. Hard-coded parameters are set to typical values used in this thesis.

B.1 Continuum Normalization: `norm.f`

The continuum normalization routine used for all spectra in this thesis. The routine fits a low order polynomial through carefully selected points in the continuum of the star, then divides the spectrum by the polynomial. This is done for each order individually. Points in the continuum are selected by finding the pixel with the most flux in a large segment of spectrum, once a running average has been applied to the spectrum.

```
c   Originally from Kathryn Bale (April 2006)
c   Heavily Modified by Colin Folsom (May 2006)
c
c   Colin's Change Log:
c   Added flexibility for slightly different sized files
c   (uses over sized arrays and the number of lines in the file header)
c   Fixed the read in, uncertainty (rmaxdy), and write out to include the
c   uncertainty column from ESPADONS spectra
```

```

c      Capped the output values at +/- 10 for easy reading.
c      Now takes a running average of several (17) points and finds the highest point in a large
c      (200 point) bin. These points are used to fit the polynomial (this should give points
c      that are ~ noise free and not in absorption lines)
c      Uncertainties for the points are calculated accordingly.
c      Changed the excluded regions to read use the highest point in this bin, not the last
c      (important for larger bins).
c      Now includes the 'balmer' subroutine which looks ahead/back to the far side of a
c      Balmer line to fit the continuum in this region
c      (assumes that you will use a low order (2nd) polynomial)
c      If the calibration between orders is good it gives a straight line across the Balmer line,
c      and hence a '1st order' approximation of the continuum
c      Uses 5 points on the far side found with a copy of the regular point finding code
c      (if you change the regular point finding routine change this too!)

C      My apologies to the reader for the legacy goto statements!
C      I'll clean it up soon, I promise!

      implicit real*8(a-h,o-z)
      implicit integer(i-n)
      character*15 filename
      character*50 junk1,junk2
      dimension rstart(1),rend(1),fn(9)
      dimension wl(220000),r1(220000),r2(220000),r3(220000),r4(220000),
1         rn(220000),x(2000),y(2000),dy(2000),coeff1(10),coeff2(10),
2         r5(220000)
      dimension nos(40),noe(40),ff(40),coeff3(10)
      character*2 fn
      character*2 ff
      data ff/'01','02','03','04','05','06','07','08','09',
1         '10','11','12','13','14','15','16','17','18','19',
2         '20','21','22','23','24','25','26','27','28','29',
3         '30','31','32','33','34','35','36','37','38','39','40'/

c      Continuum normalise Esprit-reduced spectra using polynomial fit.
c      This version selectes continuum points from x40x pixel bins for the fit,
c      useful for rich-spectrum stars.

      mode=+1
      nclips=1

100  format(a15)

c      read input filename (now hard coded... was a loop here reading from the file flistE)
      filename = 'in.s'
      open(10,file='N'//filename,status='unknown')
c      7 is the file containing the unnormalized spectrum
      open(7,file=filename,status='old')

      read(7,101) junk1
      read(7,102) iflen, ncol
      write(10,101) junk1
      write(10,102) iflen, ncol

101  format(a50)
102  format(I7,1X,I1)

c      numorder = the order that we are on, initially one
      numorder=1

c      nos = the start line for each order (first one starts at one)
      nos(numorder)=1

c      finds the beginning and ending lines of each order
      do i=1,iflen
         read(7,1105) wl(i),r1(i),r2(i),r3(i),r4(i), r5(i)
c      if the space between the wavelengths is bigger than 0.2nm
         if (i.ne.1.and.(wl(i)-wl(i-1))**2.gt.0.04) then
            write(*,*) 'Order: ', numorder, ', Wavelength: ', wl(i)
c      noe is the line the order ends on

```

```

        noe(numorder)=i-1
        numorder=numorder+1
        nos(numorder)=i
    end if
end do

noe(numorder)=iflen

write(*,*) 'There are ',numorder,' orders.'

close(7)

do i=1,numorder

c   write to the files numbered 01 to 40
    open(14,file=ff(i),status='unknown')

c   npts is the total number of points in the order
    npts=0
    rmaxy=-1000.0

c   set the number of points per bin
    nbin=200

c-----
    write(*,*) i, nbin
c-----

c   initialize counters for the number of pointes on the edges of the Balmer lines
c   necessary for the blamer subroutine
    iHbeta1 = 0
    iHbeta2 = 0
    iHalpha1 = 0
    iHalpha2 = 0
    iHgamma1 = 0
    iHgamma2 = 0
    iHdelta1 = 0
    iHdelta2 = 0

c   Throw out the first x20 and last x20 points in the order to get a
c   better fit. Then pick the highest point in each set of x40 points.

    do k=nos(i)+40,noe(i)-40

c   17 pt running average
    ravg = 0.0
    ravgdy = 0.0
    do j=-8,8
        ravg =ravg +r1(k+j)
        ravgdy = ravgdy + r5(k+j)*r5(k+j)
    enddo
    ravg=ravg/17.0
    ravgdy = sqrt(ravgdy)/17.0

c   if it's the highest point so far
    if(ravg.gt.rmaxy) then
        rmaxy=ravg
        rmaxx=w1(k)-w1(nos(i))

        rmaxdy=ravgdy
    end if

c   if it's evenly divisible by nbin, hence every nbinth point
    if(real(k/nbin).eq.real(k)/real(nbin)) then

c   get rid of Balmer lines and other large absorption lines
    if(rmaxx+w1(nos(i)).gt.371.8.and.
1      rmaxx+w1(nos(i)).lt.372.5) goto 91
    if(rmaxx+w1(nos(i)).gt.372.9.and.
1      rmaxx+w1(nos(i)).lt.374.0) goto 91
    if(rmaxx+w1(nos(i)).gt.374.5.and.
1      rmaxx+w1(nos(i)).lt.375.9) goto 91

```

```

1         if(rmaxx+wl(nos(i)).gt.376.3.and.
1           rmaxx+wl(nos(i)).lt.378.1) goto 91
1         if(rmaxx+wl(nos(i)).gt.378.6.and.
1           rmaxx+wl(nos(i)).lt.380.6) goto 91
1         if(rmaxx+wl(nos(i)).gt.381.7.and.
1           rmaxx+wl(nos(i)).lt.382.2) goto 91
1         if(rmaxx+wl(nos(i)).gt.382.3.and.
1           rmaxx+wl(nos(i)).lt.385.1) goto 91
1         if(rmaxx+wl(nos(i)).gt.387.0.and.
1           rmaxx+wl(nos(i)).lt.391.0) goto 91
1         if(rmaxx+wl(nos(i)).gt.395.0.and.
1           rmaxx+wl(nos(i)).lt.400.0) goto 91
1         if(rmaxx+wl(nos(i)).gt.400.5.and.
1           rmaxx+wl(nos(i)).lt.401.3) goto 91
1         if(rmaxx+wl(nos(i)).gt.402.1.and.
1           rmaxx+wl(nos(i)).lt.403.1) goto 91
c   H delta
1         if(rmaxx+wl(nos(i)).gt.405.2.and.
1           rmaxx+wl(nos(i)).lt.414.0)then
1           wlstart = 405.2
1           wlend = 414.0
2           call balmer(wlstart, wlend, iHdelta1, iHdelta2, i,
1             k, nos, noe, wl, r1, r5, rmaxy, rmaxx, rmaxdy)
1           if(rmaxy.eq.-1000.0) goto 91
1         endif
1         if(rmaxx+wl(nos(i)).gt.417.0.and.
1           rmaxx+wl(nos(i)).lt.417.5) goto 91
1         if(rmaxx+wl(nos(i)).gt.419.8.and.
1           rmaxx+wl(nos(i)).lt.421.2) goto 91
c   H gamma
1         if(rmaxx+wl(nos(i)).gt.428.0.and.
1           rmaxx+wl(nos(i)).lt.438.0)then
1           wlstart = 428.0
1           wlend = 438.0
2           call balmer(wlstart, wlend, iHgamma1, iHgamma2, i,
1             k, nos, noe, wl, r1, r5, rmaxy, rmaxx, rmaxdy)
1           if(rmaxy.eq.-1000.0) goto 91
1         endif
c   H beta
1         if(rmaxx+wl(nos(i)).gt.478.5.and.
1           rmaxx+wl(nos(i)).lt.494.5)then
1           wlstart = 478.5
1           wlend = 494.5
2           call balmer(wlstart, wlend, iHbeta1, iHbeta2, i,
1             k, nos, noe, wl, r1, r5, rmaxy, rmaxx, rmaxdy)
1           if(rmaxy.eq.-1000.0) goto 91
1         endif
1         if(rmaxx+wl(nos(i)).gt.501.3.and.
1           rmaxx+wl(nos(i)).lt.502.6) goto 91
1         if(rmaxx+wl(nos(i)).gt.516.6.and.
1           rmaxx+wl(nos(i)).lt.517.4) goto 91
1         if(rmaxx+wl(nos(i)).gt.587.0.and.
1           rmaxx+wl(nos(i)).lt.590.0) goto 91
1         if(rmaxx+wl(nos(i)).gt.626.9.and.
1           rmaxx+wl(nos(i)).lt.629.4) goto 91
c   H alpha
1         if(rmaxx+wl(nos(i)).gt.643.5.and.
1           rmaxx+wl(nos(i)).lt.669.5)then
1           wlstart = 643.5
1           wlend = 669.5
2           call balmer(wlstart, wlend, iHalpha1, iHalpha2, i,
1             k, nos, noe, wl, r1, r5, rmaxy, rmaxx, rmaxdy)
1           if(rmaxy.eq.-1000.0) goto 91
1         endif
1         if(rmaxx+wl(nos(i)).gt.686.5.and.
1           rmaxx+wl(nos(i)).lt.695.2) goto 91
1         if(rmaxx+wl(nos(i)).gt.759.2.and.
1           rmaxx+wl(nos(i)).lt.766.8) goto 91
1         if(rmaxx+wl(nos(i)).gt.769.2.and.
1           rmaxx+wl(nos(i)).lt.771.5) goto 91

```

```

1         if(rmaxx+wl(nos(i)).gt.775.8.and.
           rmaxx+wl(nos(i)).lt.778.5) goto 91
1         if(rmaxx+wl(nos(i)).gt.812.7.and.
           rmaxx+wl(nos(i)).lt.814.0) goto 91
1         if(rmaxx+wl(nos(i)).gt.813.8.and.
           rmaxx+wl(nos(i)).lt.814.6) goto 91
1         if(rmaxx+wl(nos(i)).gt.816.0.and.
           rmaxx+wl(nos(i)).lt.816.7) goto 91
1         if(rmaxx+wl(nos(i)).gt.818.2.and.
           rmaxx+wl(nos(i)).lt.819.1) goto 91
1         if(rmaxx+wl(nos(i)).gt.822.6.and.
           rmaxx+wl(nos(i)).lt.851.8) goto 91
1         if(rmaxx+wl(nos(i)).gt.839.1.and.
           rmaxx+wl(nos(i)).lt.839.9) goto 91
1         if(rmaxx+wl(nos(i)).gt.843.3.and.
           rmaxx+wl(nos(i)).lt.845.0) goto 91
1         if(rmaxx+wl(nos(i)).gt.844.9.and.
           rmaxx+wl(nos(i)).lt.845.4) goto 91
1         if(rmaxx+wl(nos(i)).gt.847.9.and.
           rmaxx+wl(nos(i)).lt.850.8) goto 91
1         if(rmaxx+wl(nos(i)).gt.853.3.and.
           rmaxx+wl(nos(i)).lt.880.1) goto 91
1         if(rmaxx+wl(nos(i)).gt.857.7.and.
           rmaxx+wl(nos(i)).lt.862.5) goto 91
1         if(rmaxx+wl(nos(i)).gt.863.5.and.
           rmaxx+wl(nos(i)).lt.870.7) goto 91
1         if(rmaxx+wl(nos(i)).gt.871.8.and.
           rmaxx+wl(nos(i)).lt.878.8) goto 91
1         if(rmaxx+wl(nos(i)).gt.881.7.and.
           rmaxx+wl(nos(i)).lt.890.4) goto 91
1         if(rmaxx+wl(nos(i)).gt.894.3.and.
           rmaxx+wl(nos(i)).lt.911.0) goto 91
1         if(rmaxx+wl(nos(i)).gt.899.8.and.
           rmaxx+wl(nos(i)).lt.903.3) goto 91
1         if(rmaxx+wl(nos(i)).gt.916.6.and.
           rmaxx+wl(nos(i)).lt.926.9) goto 91
1         if(rmaxx+wl(nos(i)).gt.927.2.and.
           rmaxx+wl(nos(i)).lt.941.3) goto 91
1         if(rmaxx+wl(nos(i)).gt.946.5.and.
           rmaxx+wl(nos(i)).lt.957.8) goto 91

           npts=npts+1
           x(npts)=rmaxx
           y(npts)=rmaxy
           dy(npts)=rmaxdy

91        rmaxy=-1000.0

           end if
         end do

c
c  Fit...
c

           do ik=1,10
             coeff1(ik)=0.
           end do

c  set the number of terms used in polyfit
           nterms=4

           if(i.eq.1) nterms=2
           if(i.eq.2) nterms=3
           if(i.eq.3) nterms=2
           if(i.eq.4) nterms=2
           if(i.eq.5) nterms=2
           if(i.eq.6) nterms=2
           if(i.eq.7) nterms=2
           if(i.eq.8) nterms=5
           if(i.eq.9) nterms=2

```

```

    if(i.eq.10) nterms=2
    if(i.eq.11) nterms=5
    if(i.eq.12) nterms=5
    if(i.eq.13) nterms=5
    if(i.eq.14) nterms=5
    if(i.eq.15) nterms=2
    if(i.eq.16) nterms=2
    if(i.eq.17) nterms=5
    if(i.eq.18) nterms=6
    if(i.eq.19) nterms=5
    if(i.eq.20) nterms=5
    if(i.eq.21) nterms=5
    if(i.eq.22) nterms=5
    if(i.eq.23) nterms=5
    if(i.eq.24) nterms=5
    if(i.eq.25) nterms=5
    if(i.eq.26) nterms=5
    if(i.eq.27) nterms=2
    if(i.eq.28) nterms=2
    if(i.eq.29) nterms=5
    if(i.eq.30) nterms=5
    if(i.eq.31) nterms=5
    if(i.eq.32) nterms=5
    if(i.eq.33) nterms=3
    if(i.eq.34) nterms=2
    if(i.eq.35) nterms=2
    if(i.eq.36) nterms=2
    if(i.eq.37) nterms=2
    if(i.eq.38) nterms=2
    if(i.eq.39) nterms=3
    if(i.eq.40) nterms=3

    call polyfit(x,y,dy,npts,nterms,mode,coeff1,chisq)

c   output the renormalized values
    do k=nos(i),noe(i)
c   calculate the value of the fit polynomial at this point
        rfit1=0.
        nhow=nterms
        do nfit=1,nhow
            rfit1=rfit1+coeff1(nfit)*(wl(k)-wl(nos(i)))**(nfit-1)
        end do

c   then apply the polynomial and write the result !!!Limiting the extrema to +/-10!!!
        if( (r1(k)/rfit1).gt.10.0 )then
            write(10,1105) wl(k),10.0,10.0
1           ,10.0,10.0, 10.0
            write(14,1051) wl(k),r1(k),rfit1
        elseif( (r1(k)/rfit1).lt.-10.0 )then
            write(10,1105) wl(k),-10.0,-10.0
1           ,-10.0,-10.0, -10.0
            write(14,1051) wl(k),r1(k),rfit1
        else
            write(10,1105) wl(k),r1(k)/rfit1,r2(k)/r1(k)
1           ,r3(k)/r1(k),r4(k)/r1(k), r5(k)/rfit1
            write(14,1051) wl(k),r1(k),rfit1
        endif

        end do

        close(14)

c   (end the loop over orders)
    end do

    close(10)

    close(20)
    close(21)
    close(22)

1051 format(f11.4,1x,3(f12.5,1x))
1105 format(f10.4,1x,5(e11.4,1x))

```

end

```

subroutine polyfit(x,y,sigmay,npts,nterms,mode,a,chisqr)
implicit real*8(a-h,o-z)
implicit integer(i-n)
dimension x(1),y(1),sigmay(1),a(1)
dimension sumx(19),sumy(10),array(10,10)

c
c From Bevington 1st edition
c
c   Accumulate weighted sums
c
11  nmax=2*nterms-1
do 13 n=1,nmax
13  sumx(n)=0.
do 15 j=1,nterms
15  sumy(j)=0.
chisq=0.
21  do 50 i=1,npts
xi=x(i)
yi=y(i)
31  if (mode) 32, 37, 39
32  if (yi) 35,37,33
33  weight=1./(yi)
go to 41
35  weight=1./(-yi)
go to 41
37  weight=1.
go to 41
39  weight=1./sigmay(i)**2
41  xterm=weight
do 44 n=1,nmax
sumx(n)=sumx(n)+xterm
44  xterm=xterm*xi
45  yterm=weight*yi
do 48 n=1,nterms
sumy(n)=sumy(n)+yterm
48  yterm=yterm*xi
49  chisq=chisq+weight*yi**2
50  continue
c
c Construct matrices and calculate components
c
51  do 54 j=1,nterms
do 54 k=1,nterms
n=j+k-1
54  array(j,k)=sumx(n)
delta=determ(array,nterms)
if(delta) 61,57,61
57  chisqr=0.
do 59 j=1,nterms
59  a(j)=0.
go to 80
61  do 70 l=1,nterms
62  do 66 j=1,nterms
do 65 k=1,nterms
n=j+k-1
65  array(j,k)=sumx(n)
66  array(j,l)=sumy(j)
70  a(l)=determ(array,nterms)/delta
c

```

```

c Calculate chi**2
c
71  do 75 j=1,nterms
      chisq=chisq-2.*a(j)*sumy(j)
      do 75 k=1,nterms
          n=j+k-1
75  chisq=chisq+a(j)*a(k)*sumx(n)
76  free=npts-nterms
77  chisqr=chisq/free

80  return
    end

    function determ(array,norder)
    implicit real*8(a-h,o-z)
    implicit integer(i-n)
    dimension array(10,10)
c
c Calculate the determinant of a square matrix
c
110  determ=1.
111  do 150 k=1,norder
      if(array(k,k)) 141,121,141
121  do 123 j=k,norder
      if(array(k,j)) 131,123,131
123  continue
      determ=0.
      go to 160
131  do 134 i=k,norder
      save=array(i,j)
      array(i,j)=array(i,k)
134  array(i,k)=save
      determ=-determ
141  determ=determ*array(k,k)
      if (k-norder) 143,150,150
143  k1=k+1
      do 146 i=k1,norder
          do 146 j=k1,norder
146  array(i,j)=array(i,j)-array(i,k)*array(k,j)/array(k,k)
150  continue
160  return
    end

    subroutine balmer(wlstart, wlend, ih1, ih2, i, k,
2  nos, noe, wl, r1, r5, rmaxy, rmaxx, rmaxdy)
C  Looks ahead/behind to the far side of the Balmer line to finde a few (5) good points.
C  returns a good point per call, untill ih1 = 5 (for the blue side)
C  and ih2 = 5 (for the red side)

c  wlstart, wlend = starting and ending wavelengths of the balmer line
c  i, k = the order and point we're currently on
c  ih1, ih2 = the number of points at the start and end of the balmer line use so far
c  (gets modified) (goes up to 5 total)
c  wl, r1, r5 = wavelength, intensity, and uncertainty arrays
c  rmaxy, rmaxx, rmaxdy = vales fot the best point in this bin (200 point bins)
c  (gets modified and returned)
c  returns rmaxy = -1000.0 if we are on more then the 5th point

    implicit real*8(a-h,o-z)
    implicit integer(i-n)

    real*8 wlstart, wlend, wl(220000), r1(220000),
2  r5(220000), rmaxy, rmaxx, rmaxdy
    integer i, k, ih1, ih2, nos(40), noe(40)

    if(ih1.lt.5.and.ih2.lt.5)then
c  if this order is on the blue side
      if(wl(nos(i)).lt.wlstart)then
c  advance past the balmer line
        jend=k

```

```

        do while (wl(jend).lt.wlend)
            jend=jend+1
        enddo
c      and skipp ahead iH1 bins
        jend=jend+200*iH1
        iH1 = iH1+1
c      if this order is on the red side
        elseif (wl(noe(i)).gt.wlend)then
c      rewinde past the balmer line
        jend=k
        do while (wl(jend).gt.wlstart)
            jend=jend-1
1      enddo
c      iH2 = iH2+1
        and step back iH2 bins (starting at -200)
        jend=jend-200*iH2
    endif

c      search for best point (out of 200) with parameters stolen from the body of this code
        rmaxy=-1000.0
        do j=jend,jend+200
c      17 pt running average
            ravg = 0.0
            do j2=-8,8
                ravg=ravg +r1(j+j2)
            enddo
            ravg=ravg/17.0
c      if it's the highest point so far keep it
            if(ravg.gt.rmaxy) then
                rmaxy=ravg
                rmaxx=wl(j)-wl(nos(i))
                rmaxdy=r5(j)
            end if
        enddo
c      if we have enough points just skipp all this and return -1000
        else
            rmaxy=-1000.0
        endif
    endif

end

```

B.2 Period Searching with Stokes I and V LSD

Profiles: pbp.f

This routine searches for periodicity in the Stokes I and V LSD profiles independently. Sinusoids with a range of periods are fit through the time series of observations at one particular pixel in the LSD profile, and the reduced χ^2 is calculated. This is then repeated for each pixel individually. The reduced χ^2 values for each period are averaged over all pixels, and a periodogram (plot of reduced χ^2 versus period) is output.

```

implicit none
c LSD version - cleaned up a bit (April 4 2007)
c Things that may change: nLines, nFiles, vmin, vmax, read format,
C individual pixel writing (currently #100)
c See ./Test/pbpt.f for the version with multiple pixel phases output
C Interpolation Added. Uses the 1st input LSD profile wavelenght scale

integer iFLenght, nColumn, n, nLines, nFiles, nDates, i, ipNum,
c iminI, iminV, iFito, iFitod, iCount, pix1, pix2
character*45 txt
double precision period0, jd0, pMin, pMax, vmin, vmax,
c fminI, fminV, limI, limV, sign, maxVarIT, maxVarVT, wtI, wtV

c set the number of lines in the input spectra (excluding header)
parameter(nLines=188)
c set the number of observations (points in the time series)
parameter(nFiles=18)
c set the start and end of the line in velocity units relative to the line
c center in the star's frame
parameter(vmin = -30.0)
parameter(vmax = 70.0)
c set the order of the fit polynomial
parameter(iFito = 1)
parameter(pix1 = 57)
parameter(pix2 = 66)
c pix2 = pix1 +10 (start and end pixels for the list of phased I and V curves)

character*40 fnames(nFiles)
double precision wl(nFiles,nLines),int(nFiles,nLines),
c eint(nFiles,nLines), vi(nFiles,nLines), evi(nFiles,nLines),
c no(nFiles,nLines), eno(nFiles,nLines), JD(nFiles),
c dint(nFiles), deint(nFiles), dvi(nFiles), devi(nFiles),
c maxVarI(nLines), maxVarV(nLines), avgI(nLines), avgV(nLines),
c tint(nLines), teint(nLines), tvi(nLines), tevi(nLines)

real, allocatable :: pspecI(:,,:), pspecIT(:,,:), pspecV(:,,:),
c pspecVT(:,,:), phasesI(:,,:), phasesV(:,,:)

avgI = 0.0
avgV = 0.0
wtV = 0.0
wtI = 0.0

C Read in the input files

c read the 1st line of flist...
open(20, file="flist", status='unknown')

99 read(20,99) nDates, period0, jd0
format(I4, 1X, F10.4, 1X, F16.4)
if(nDates.ne.nFiles)then
write(*,*) 'Warning: number of files inconsistant with the nFile
*s parameter'
endif

c loop over all observations
do n=1,nFiles
c read the flist line corrsponding to this observation
read(20,103) JD(n), fnames(n)

c read the observed LSD file
open(21, file=fnames(n), status='unknown')
c comment out these two line if there is no header on the LSD profiles
read(21,*)
read(21,54) iFLenght, nColumn
54 format(I4,I2)

do i=1,nLines
read(21,102) wl(n,i), int(n,i), eint(n,i), vi(n,i),
c evi(n,i), no(n,i), eno(n,i)
c while we're looping through pixels, lets find the average value in I and V for this pixel
c (just a sum weighted by 1/uncertainty for now...)

```

```

        avgI(i) = avgI(i)+int(n,i)/eint(n,i)
        avgV(i) = avgV(i)+vi(n,i)/evi(n,i)
    enddo
    close(21)

    enddo
c    read the last line of flist
    read(20,104) pMin, pMax, ipNum
104 format(F10.4,F10.4,I10)

    close(20)

102 format(F10.4,1X,E11.4,1X,E11.4,1X,E11.4,1X,E11.4,1X,E11.4,1X,
c    E11.4)
103 format(F13.5,1X,A40)

c    allocate the result arrays
    ALLOCATE(pspecI(ipNum,2),pspecIT(ipNum,2))
    ALLOCATE(pspecV(ipNum,2),pspecVT(ipNum,2))
    ALLOCATE(phasesI(nFiles,ipNum),phasesV(nFiles,ipNum))

c    initialize the arrays to 0 (aren't array operations fun?)
    pspecIT = 0.0
    pspecI = 0.0
    pspecVT = 0.0
    pspecV = 0.0

    iCount = 0

    maxVarIT = 0.0
    maxVarVT = 0.0
    maxVarI = 0.0
    maxVarV = 0.0

    tint=0.0

c    Interpolate to common wavelength points, use the 1st LSD profile
    do i=2, nFiles
        call interp(wl(1,:), int(1,:), nLines, wl(i,:), int(i,:),
1         nLines, tint)

        int(i,:) = tint

        call interp(wl(1,:), eint(1,:), nLines, wl(i,:), eint(i,:),
1         nLines, tint)

        eint(i,:) = tint

        call interp(wl(1,:), vi(1,:), nLines, wl(i,:), vi(i,:),
1         nLines, tint)

        vi(i,:) = tint

        call interp(wl(1,:), evi(1,:), nLines, wl(i,:), evi(i,:),
1         nLines, tint)

        evi(i,:) = tint

        wl(i,:) = wl(1,:)

    enddo

c    then find the maximum variation in I and V
    do i=1,nLines
c    but first finish calculating that average
c    (divide by sum of weighting (ie sum of 1/uncertainty))
    wtI = 0.0
    wtV = 0.0
    do n=1,nFiles
        wtI = wtI + 1/eint(n,i)
        wtV = wtV + 1/evi(n,i)
    enddo
    enddo

```

```

        enddo
        avgI(i) = avgI(i)/wtI
        avgV(i) = avgV(i)/wtV
c      Now look for the observation with the largest _sigma_ difference from the mean
        do n=1,nFiles

            sign = ABS(int(n,i)-avgI(i))/eint(n,i)
            if(sign.gt.maxVarI(i))then
                maxVarI(i)=sign
            endif

            sign = ABS(vi(n,i)-avgV(i))/evi(n,i)
            if(sign.gt.maxVarV(i))then
                maxVarV(i)=sign
            endif

        enddo

c      And the largest sigma difference of all
        if(maxVarI(i).gt.maxVarIT)then
            maxVarIT = maxVarI(i)
        endif
        if(maxVarV(i).gt.maxVarVT)then
            maxVarVT = maxVarV(i)
        endif

        enddo

        wtV = 0.0
        wtI = 0.0

c      loop over all pixels in the LSD spectrum
        do i=1,nLines
            write(*,*) 'On pixel: ', i

            if( (wl(1,i).gt.vmin).and.(wl(1,i).lt.vmax) )then
                iCount = iCount+1
                write(*,*) 'Pixels included: ', iCount
            end

c          use a copy of the intensity and error (error gets modified in the subroutine)
            dint = int(:,i)
            deint = eint(:,i)
            iFitod = iFito

            *****
            call fsrch(nFiles, period0, jd0, iFitod, JD, dint,
                1      deint, pMin, pMax, ipNum, pspecI, phasesI,
                2      iCount)
            *****

c          Weighted average, by the variation(/uncertainty) of the point
c          as a fraction of the largest variation of any point
            pspecIT = pspecIT + pspecI*(maxVarI(i)/maxVarIT)
            wtI = wtI+(maxVarI(i)/maxVarIT)

c      And do the same for stokes V
            dvi = vi(:,i)
            devi = evi(:,i)
            iFitod = iFito
            *****
            call fsrch(nFiles, period0, jd0, iFitod, JD, dvi,
                1      devi, pMin, pMax, ipNum, pspecV, phasesV,
                2      iCount)
            *****

c          Weighted average, by the varyation(/uncertainty) of the point
c          as a fraction of the largest variation of any point
            pspecVT = pspecVT + pspecV*(maxVarV(i)/maxVarVT)
            wtV = wtV+(maxVarV(i)/maxVarVT)

        endif

    enddo

```

```

c   Divide by the sum of the weighting
   pspecIT = pspecIT/wtI
   pspecVT = pspecVT/wtV

c   Finally parse and output the results
   fminI = pspecIT(1,2)
   iminI = 0
   fminV = pspecVT(1,2)
   iminV = 0
   open(31, file="avg_periodsI", status='unknown')
   open(32, file="avg_periodsV", status='unknown')
c   loop over all lines
   do i=1,ipNum
c   write the ones that are not zero (skip the remainder)
       if(pspecIT(i,2).ne.0.0)then
           write(31,200) pspecIT(i,1), pspecIT(i,2)
c   and find the minimum chi^2 point
           if(pspecIT(i,2).lt.fminI)then
               fminI = pspecIT(i,2)
               iminI = i
           endif
       endif
c   and do the same for the stokes V spectrum too
       if(pspecVT(i,2).ne.0.0)then
           write(32,200) pspecVT(i,1), pspecVT(i,2)
           if(pspecVT(i,2).lt.fminV)then
               fminV = pspecVT(i,2)
               iminV = i
           endif
       endif
   enddo
200  format(F13.7,1X,E16.8)
   close(31)
   close(32)

C   Final comments written to terminal

c   write the phases of the observations at the best fit point for I and V
   write(*,*) 'Phases at mininum from I: '
   do i=1,nFiles
       write(*,*) 'JD: ', JD(i), 'phase: ', phasesI(i,iminI)
   enddo
   write(*,*) 'Phases at mininum from V: '
   do i=1,nFiles
       write(*,*) 'JD: ', JD(i), 'phase: ', phasesV(i,iminV)
   enddo

c   write the mininum points in the periodogram
   write(*,*) 'Minimum in I at ', pspecIT(iminI,1), 'days, chi^2: ',
*   pspecIT(iminI,2)
   write(*,*) 'Minimum in V at ', pspecVT(iminV,1), 'days, chi^2: ',
*   pspecVT(iminV,2)

c   and the statistical limit based on those points (for a 1st order fit)
   if(iFito.eq.1)then
       limI = pspecIT(iminI,2)+11.3/(real(nFiles) -3.0)
       limV = pspecVT(iminV,2)+11.3/(real(nFiles) -3.0)
   elseif(iFito.eq.2)then
       limI = pspecIT(iminI,2)+15.1/(real(nFiles) -5.0)
       limV = pspecVT(iminV,2)+15.1/(real(nFiles) -5.0)
   endif

   write(*,*) '99% confidance limit on I:', limI,
1     '99% confidance limit on V:', limV

   DEALLOCATE(pspecI, pspecIT)
   DEALLOCATE(pspecV, pspecVT)
   DEALLOCATE(phasesI, phasesV)

end

```

```

*****
C   Subroutine-ized (badly) by Colin for pbp.f (for pixel by pixel period searching)
C   (hacked for g95 compatibility by Colin)
C
C   MODIFIED AND UPDATED FOR EXECUTION IN UNIX BY GREGG WADE 1993.
C
C   INPUT IS FROM 'FOUFITDATA'. FORMAT MUST BE:
C   NUMBER OF DATA, PERIOD AND EPOCH ON LINE 1, THEN DATE..DATA..WEIGHT
C   FOR EACH ENTRY. OUTPUT FILE IS 'periods'.o
C
c   Takes: NMAX (number of points in the time series)(usually N=NMAX),
c   P (a guss period, input is vestigial, used in a large loop),
c   FJDL (a referance julian date),
c   M (order of the function used to fit),
c   FJD(N) (the julian date of each point),
c   V(N) (the amplitude of each point),
c   WT(N) (the error on each point, 1 sigma) Note: this gets modified!,
c   pmin (the starting period of the search),
c   pmax (the ending period of the search),
c   ipnum (the number of points in the search)
c   pspec (the returned power spectrum) (no input only output)
c   phases (the phases for each observation at each ipnum period)
c
c   Changed the way the loop over phases is set up to avoid overflowing
c   Now we loop ipnum times and then calculate which period the current
c   loop should be based on pmin+(# loops)*(period change per point)
c   This should be safe up to ~1e9 points and
c   the limit of single float (real) precision in period
c
c   subroutine fsrch(NMAX,P,FJDL, M, FJD,V,WT,
c   pmin,pmax,ipnum,pspec,phases,iteration)
c
c   IMPLICIT REAL*8(A-H,O-Z)
c
c   DIMENSION Z(18,18)
c   DIMENSION Q(17)
c   DIMENSION RC(17),RS(17)
c   DIMENSION S(17),C(17)
c   DIMENSION OC(1000),PH(1000)
c   INTEGER x,ipmin,ipmax,istep,lp, a,b, M, count, iteration, ipnum
c
c   COMMON Z,S,C
c
c   real pspec(ipnum,2)
c   real*8 WT(NMAX), V(NMAX), FJD(NMAX)
c   double precision rpmin,rpmax,rstep,pmin,pmax
c   real phases(NMAX,ipnum)
c
C   DEFINING FREQUENTLY USED CONSTANTS
C   PI2=6.283185
c
c   count = 1
1   Q(1)=1.0
C
C   Number of data, period and epoch WERE read from first 3 elements in file.
C
c   WRITE (*,92)NMAX,P,FJDL
92  format(I5,2x,F12.5,2x,f20.6)
C
C   ENTERING ALL INPUT FOR HARMONIC ANALYSIS
C
22  N=0
FFN1=0.0
199 N=N+1

```

```

      epha=(FJD(N)-FJDL)/P
      if(epha.lt.0.0) epha=epha+int(epha)+1
c      write(*,996)FJD(N),epha,V(N),WT(N)
      wt(N)=1/(wt(N)*wt(N))
996  FORMAT(4F16.5)
      FFN1=FFN1+1.0
      IF(WT(N).NE.0.0)GO TO 201
      FFN1=FFN1-1.0
201  IF(N.LT.NMAX)GO TO 199

8887  format(f10.2,f10.2,i10)
c      write(*,*) 'PMIN=',pmin,' PMAX=',pmax,' # periods:',ipnum

      BOCWT=SIGMA*SIGMA*(N-1)

3      M2=2*M
      M21=M2+1
      M22=M2+2
      M23=M2+3
C      SET THE Z MATRIX EQUAL TO ZERO
      DO I=1,M23
        DO J=1,M23
          Z(I,J)=0.0
        enddo
      enddo
C      FROM HERE EACH OBS IS DEALT WITH ONE AT A TIME

c      new hottness:
      rstep = (pmax-pmin)/dble(ipnum)
c      write(*,*) pmin,pmax,rstep,ipnum

c      loop over the periods to be searched
      do lp = 1,ipnum
c      scale steps exponentially increasing from pmin to pmax
        p = real(pmin*(pmax/pmin)**(dble(lp)/dble(ipnum)))
c      simplistic error trapping
        if(p.gt.pmax) then
          write(*,*) 'WARNING: periodogram exceeding max period'
          write(*,*) p
        endif

        r1=0.0
        y=0.0
        bocwt=0.0

        do a=1,18
          do b=1,18
            z(a,b)=0.0
          end do
        end do
c      loop over the observed data points
      DO I=1,N
C      FINDING THE PHASE
        EPPH=(FJD(I)-FJDL)/P

        x=EPPH
        EPPH=EPPH-FLOAT(X)
        if (EPPH.lt.0) EPPH=EPPH+1.
        EPPH=dabs(EPPH)

        PH(I)=EPPH
        IF(PH(I).GT.0.0)GO TO 54
        PH(I)=PH(I)+1.0
54      FM=PH(I)*PI2
C      FINDING C1 AND S1 COEFF
        Q(2)=DCOS(FM)
        Q(3)=DSIN(FM)
C      FINDING C2 AND S2 TO CM AND SM COEFF
        DO J=4,M2,2
          J1=J-1
          J2=J1-1
C      BY THE SIN & COS OF SUMS OF ANGLES

```

```

        Q(J)=Q(J2)*Q(2)-Q(J1)*Q(3)
        Q(J+1)=Q(J1)*Q(2)+Q(J2)*Q(3)
    enddo
    Q(M22)=V(I)
C   SETTING UP NORMAL EQUATIONS FOR LSTSQ SOLN
    DO J=1,M22
        DO K=J,M22
            Z(J,K+1)=WT(I)*Q(J)*Q(K)+Z(J,K+1)
        enddo
    enddo
C
C   SOLN BY LSTSQ AND RELABELLING
    CALL LSTSQ(M21,FFN1)

c   loop over the terms in the fit function
    DO J=1,M
        C(J)=Z(M22,2*J)
        S(J)=Z(M22,2*J+1)
        RC(J)=Z(M23,2*J)
        RS(J)=Z(M23,2*J+1)
    enddo
C   DATA, RESULTS & STATISTICS TABULATION
    BOCWT=0.0

c   loop over the observed data points
    DO I=1,N
        Y=Z(M22,1)
        FM=PI2*PH(I)
        DO J=1,M
            Y=Y+S(J)*DSIN(J*FM)+C(J)*DCOS(J*FM)
        enddo
        OC(I)=V(I)-Y
        BOCWT=BOCWT+WT(I)*OC(I)*OC(I)
        phases(I,count)=PH(I)
    enddo
C   CALCULATION OF THE ERROR
    NN=N-2*M-1
    GNN=NN
    R1=BOCWT/GNN

    pspec(count,1) = p
    pspec(count,2) = r1
    count = count+1

C   EQUAL PHASE INCREMENT RESULTS
    V0=Z(M22,1)
    END do

end

C
C   LEAST SQUARES SUBROUTINE
C
SUBROUTINE LSTSQ(N,FNO)
IMPLICIT REAL*8(A-H,O-Z)
DIMENSION Z(18,18)
COMMON Z
C   CONTROL FROM MAIN PROGRAM TRANSFERRED TO HERE
M=N+1
M1=M+1
FN=N
DO7 I=1,M
    L=I+1

C   COMPUTATION OF DIAGONAL MATRIX ELEMENTS
    DO1 K=1,I
        IF(I.LE.K)GO TO 2
1       Z(I,L)=Z(I,L)-Z(K,L)*Z(K,L)
2       IF(M.LE.I)GO TO 8
        Z(I,L)=DSQRT(Z(I,L))
        L1=L+1
    DO4 J=L1,M1

C   COMPUTATION OF ELEMENTS TO RIGHT OF DIAGONAL

```

```

      DO3 K=1,I
      IF(I-K)4,4,3
3     Z(I,J)=Z(I,J)-Z(K,L)*Z(K,J)
4     Z(I,J)=Z(I,J)/Z(I,L)
      Z(I,I)=1.0/Z(I,L)
      DO6 J=1,I
      IF(I.LE.J)GO TO 7
      PP=0.0
      L1=I-1
C     COMPUTATION OF ELEMENTS TO LEFT OF DIAGONAL
      DO5 K=J,L1
5     PP=PP+Z(K,L)*Z(K,J)
6     Z(I,J)=-Z(I,I)*PP
7     CONTINUE
C     EVALUATION OF R1
8     Z(M1,M1)=0.675*DSQRT(Z(M,M1)/(FNO-FN))
      DO10 I=1,N
      Z(M,I)=0.0
      PP=0.0
      DO9 J=I,N
C     EVALUATION OF THE UNKNOWNNS
      Z(M,I)=Z(M,I)+Z(J,I)*Z(J,M1)
C     EVALUATION OF RECIPROCAL WEIGHTS
9     PP=PP+Z(J,I)*Z(J,I)
C     EVALUATION OF PROBABLE ERRORS OF UNKNOWNNS
10    Z(M1,I)=Z(M1,M1)*DSQRT(PP)
C     RETURN CONTROL TO MAIN PROGRAM
      RETURN
      END

```

```

*****
      subroutine interp(w11, f11, len1, w12, f12, len2, f13)
C     assumes 1 is longer then 2 (or equal to)

      integer len1, len2, start, jump
      double precision w11(len1), w12(len2), f11(len1), f12(len2),
2       f13(len1)

      integer first, i,j

c     initialize to 0
      do i=1,len1
         f13(i) = 0.0
      enddo

c     advance 1 untill it overlaps with 2
      start=1
      do while(w11(start).lt.w12(1))
         start=start+1
      enddo

      j=1
      jump = 0
      do i=start, len1

c         if we're in range and 1 is increasing
c         if( (j.le.len2).and.(w11(i).ge.w11(i-1)) )then
c             advance to the next point in 2
c             do while( (w12(j).lt.w11(i)).and.(j.lt.len2) )
c                 j=j+1
c             if there is a discontinuity we will want to remeber this
c             if(w12(j).lt.w12(j-1))then
c                 jump = j
c                 write(*,*) 'Warning: Discontinuity'
c             endif
c             now w12(j-1) < w11(i) and w12(j) >= w11(i)
c             enddo
c             if exact then use it
c             if(w12(j).eq.w11(i))then
c                 f13(i) = f12(j)

```

```

c           otherwise interpolate
c           else
c             f13(i) = (w11(i)-w12(j-1))*(f12(j)-f12(j-1))/
2             (w12(j)-w12(j-1))+f12(j-1)
c           endif

c           if we're in range but 1 is decreasing
c           Note: This implementation assumes that 2 and 1 have similar overlap in their orders.
c           The number of overlapping reigons in 1 and 2 must be the same.
c           The resulting overlap follows 1's lambda values.
c           Any points in 2's 1st order after 1 stopps overlapping will be ignored
c           (only the second order is used)
c           Any points in 2's 2nd order berore 1 starts overlapping will be ignored
c           (only the 1st order is used)
c           Interpolation of end points is (almost) usless
c           Any points in 1's 2nd order before 2's 2nd order begins will exist
c           with (almost) junk values
c           Any points in 1's 1st order after 2 stops will have values from 2's second order
c           elseif( (j.le.len2).and.(w11(i).lt.w11(i-1)) )then
c           advance untill we decend in 2 too, unless we allready have then go to where we did decend
c           if(jump.eq.0)then
c             do while( (w12(j).gt.w12(j-1)).and.(j.lt.len2) )
c               j=j+1
c             enddo
c           else
c             j=jump
c           endif

c           advance to the next point in 2 straddeling this point in 1
c           do while( (w12(j).lt.w11(i)).and.(j.lt.len2) )
c             j=j+1
c           enddo

c           if exact then use it
c           if(w12(j).eq.w11(i))then
c             f13(i) = f12(j)
c           otherwise interpolate
c           else
c             f13(i) = (w11(i)-w12(j-1))*(f12(j)-f12(j-1))/
2             (w12(j)-w12(j-1))+f12(j-1)
c           endif
c           reset jump for the next overlap
c           jump = 0

c           if we're out of range
c           else
c           if we've ran out of points use 0
c           f13(i)=0.0
c           endif
c           endif

c           enddo

c           end

```

B.3 Spectrum Fitting Through χ^2 Minimization:

lma.f

This routine uses the Levenberg-Marquardt χ^2 minimization method, presented in Press et al. (1992), to fit a synthetic spectrum to an observed spectrum. Synthetic spectra are calculated by ZEEMAN2. Free parameters in the fit are chemical abundances, $v \sin i$, and microturbulence. The radial velocity of the star must be determined in advance, as must T_{eff} , $\log g$, and the magnetic properties of the star.

The program is broken into three files. The file lma.f performs the χ^2 minimization and calls all other files. The file rewriter.f formats the input for ZEEMAN2 and writes it to the file 'inzmodel.dat' in the 'data' directory. The file z2.1v2mod1b-sub.f contains the ZEEMAN2 synthesis code itself. ZEEMAN2 writes synthetic spectra to a file where it is read back in by the 'interp' subroutine in lma.f. While this is moderately inefficient it allows one to examine spectra as the routine operates, and moreover it requires the minimum of modifications to ZEEMAN2.

Note that the ZEEMAN2 code itself has been omitted, as the author made only minimal modifications to it for this thesis. In the source code of lma.f the ZEEMAN2 subroutine is named 'ZeeModel'.

B.3.1 Levenberg-Marquardt χ^2 Minimization

The lma.f file, containing the majority of the spectrum fitting routine.

```
C Compilation Requires z2.1v2mod1b-sub.f and rewriter.f
C Execution requires inlma.dat ./data/newatom.dat ./data/irwinpf.dat ./data/inzmodel.dat

C   CHECK LIST
C   Have you:
C   [ ] put the right file in observed.dat
C   [ ] input your initial estimate parameters
C   [ ] set the appropriate elements to be fitable
```

```

C      [ ] set vsini to be fitable or fixed
C      [ ] set ma to the number of input parameters
C      [ ] set ndata to the length of observed.dat
C      [ ] set Itot in zeeman
C      [ ] checked the success criteria
C      [ ] checked the continuum cutoff level
C      [ ] checked the read format for observed.dat
C      [ ] backed up results.dat and inzmodel.dat
C      [ ] deleted any leftover w0* files

C      TO DO:

C      TO MAYBE DO:
C      Base continuum decision on whether the spectrum changes under spectrum synthesis
C      (% of deepest line?)
C      Auto fit for Vr (before everything else re: Gregg's suggestion)
C      Check success criteria
C      Check numerical derivative lambda shift values
C      Make 'observed' sigma values dynamic / more sensible
C      Read in success criteria, derivative shift, & sigma values from file (no longer hard coded)
C      IF you don't care about the covariance matrix then there is 1 iteration more the necessary
C      (last derivatives and prettifying call)

      IMPLICIT NONE

      integer ndata, ma, nca, fnCall, n, m
      real chisq, alambda

      integer stab
      real chio, inichi, xlast, success, contcut

c      My attempt at fancy fortran 90 style dynamic arrays
      REAL, DIMENSION(:), ALLOCATABLE :: x, y, sig, a
      REAL, DIMENSION(:,:), ALLOCATABLE :: covar, alpha
      integer, DIMENSION(:), ALLOCATABLE :: ia
c      these three are passed in and out of mrqmin to preserve values
c      (could use SAVE if they were not dynamic)
      REAL, DIMENSION(:), ALLOCATABLE :: atry, beta, da

C      Commonly Changed Values
c      success: Fractional change in chi^2 less than which we say the fit is ok
c      (or not likely to get significantly better) Must occur 2 times in a row (by default) to terminate
      success = 0.005
c      contcut: The continuum level cutoff. Used to reject points that are just continuum from the fit
c      can be set to >> 1 and (virtually) the entire spectrum in the synthesized range will be fit
      contcut = 10.0

c      ndata = # obs. data pts. ma = # input param. nca = fitting matrix size (>=ma),
c      fcCall = function call counter, n,m=counters, stab = 'stability' check counter
c      chisq = chi squared, alambda = shift in lambda / flag, chio = old chisq,
c      inichi = initial chisq, xlast = last x (checks for overlap in observed.dat)
c      x,y = observed data points (wavelength, normalized intensity)(ndata long)
c      sig = standard deviation on y (presently just made up) a = input parameters
c      ia = input parameters to fit (0=no/1=yes), covar = covariance matrix (output ignored),
c      alpha = augmented (w lambda) Hessian matrix  $\sim (d^2(\chi^2)/(da_i)(da_j))$ 

c      Definition of parameters in a(n) and ia(n):
c      n=1 => radial velocity (m/s)
c      n=2 => vsini (cm/s)
c      n=3 => micro turbulence (cm/s)
c      n=i (i=4,6,8,...) => atomic number
c      n=i+1 abundance for atom # in n=i

      open(15, file="observed.dat", status='unknown')
      open(16, file="results.dat", status='unknown')
      open(17, file="inlma.dat", status='unknown')
c      open(19, file="dump.dat", status='unknown')

C      Read in the input parameters and dimensions file.
      read(17,219)
      read(17,210) ndata, ma

```

```

        ALLOCATE(a(1:ma))
        ALLOCATE(ia(1:ma))
c      And the three storage arrays for mrqmin
        ALLOCATE(atry(1:ma))
        ALLOCATE(beta(1:ma))
        ALLOCATE(da(1:ma))

        read(17,219)
        read(17,211) a(1), ia(1)
        read(17,219)
        read(17,211) a(2), ia(2)
        read(17,219)
        read(17,211) a(3), ia(3)
        read(17,219)
        do n=4,ma,2
c          read(17,212) a(n), a(n+1), ia(n+1)
          never fit the atomic #
          ia(n) = 0
        enddo

        close(17)

c      set size of fitting matrix, >= ma
        nca = ma

210 format(I7,1X,I3)
211 format(E11.2,1X,I2)
212 format(F3.0,6X,F9.6,1X,I2)
219 format(1X)

        write(*,*) 'Initial Param:'
        write(16,*) 'Initial Param:'
        write(*,*) a
        write(16,*) a

        write(*,*) 'Free Param:'
        write(16,*) 'Free Param:'
        write(*,*) ia
        write(16,*) ia

c      There are 10 arrays (5 here 2+3 above)
c      be kind and deallocate them all (though it should happend automatically)
        ALLOCATE(x(1:ndata))
        ALLOCATE(y(1:ndata))
        ALLOCATE(sig(1:ndata))
        ALLOCATE(covar(1:nca,1:nca))
        ALLOCATE(alpha(1:nca,1:nca))
c      ... that was too easy...

c      Read in observed data (assumes wavelength in angstroms, no overlap, normalized to 1)
        xlast = 0.0
        do n=1,ndata
            read(15,200) x(n), y(n)
200          format(F10.4,1X,E11.4)
c 200          format(f21.16,1x,f10.7)
c 200          format(3X,E13.7,3x,E13.7)
c 200          format(f11.6,1x,f8.6)
c          convert nm to angstroms
            x(n)=x(n)*10.0
c          simple error trapping
            if(x(n).lt.xlast)then
                write(*,*)"ERROR! overlap in the observed data"
                write(16,*)"ERROR! overlap in the observed data"
            endif
            xlast = x(n)
        enddo

        close(15)

c      Apply the doppler shift correction to the observed data
        do n=1,ndata
            x(n) = x(n)- x(n)*a(1)/2.99792458E8

```

```

        enddo

c      Estimate sigma (the uncertainty on y) (to improve...)
      do n=1,ndata
        sig(n) = 1.000
      enddo

c      Initialize everything else to 0
      do n=1,nca
        do m=1,nca
          covar(n,m) = 0.0
          alpha(n,m) = 0.0
        enddo
      enddo

      chisq = 0.0
      alambda = -1.0
      stab = 0
      fnCall = 0
      chio = 0.0

C      Run the initialization call of mrqmin
      write(*,123) 1
      write(16,123) 1
      *****
      call mrqmin(x,y,sig,ndata,a,ia,ma,covar,alpha,nca,chisq,
        1      alambda,fnCall,contcut, atry,beta,da)
      *****
      inichi = chisq

      write(*,124) chisq, chisq-chio
      write(16,124) chisq, chisq-chio
      write(*,*) a
      write(16,*) a

C      Iterate to fit. We must have less than a 'sucess' fractional change 2 times in a row
      n=1
      do while ( (abs(chisq-chio)/chio.gt.sucess).or.(stab.lt.2) )

        chio = chisq

        write(*,123) n+2
        write(16,123) n+2
      123      format('Iteration: ', I4)

      *****
      call mrqmin(x,y,sig,ndata,a,ia,ma,covar,alpha,nca,chisq,
        1      alambda,fnCall,contcut, atry,beta,da)
      *****

      write(*,124) chisq, chisq-chio, (chisq-chio)/chio
      write(16,124) chisq, chisq-chio, (chisq-chio)/chio
      124      format('chi squared: ',F16.6,' change: ',F14.6,
        1      ' fractional change: ' F10.6)
      write(*,*) a
      write(16,*) a

      if(abs(chisq-chio).le.sucess) then
        stab = stab + 1
      else
        stab = 0
      endif

      n=n+1
    enddo

c      Run the finalization call of mrqmin and output the results

      alambda = 0.0
      write(*,*) 'Finalizing'

```

```

write(16,*) 'Finalizing'

*****
call mrqmin(x,y,sig,ndata,a,ia,ma,covar,alpha,nca,chisq,
1   alamda,fnCall,contcut, atry,beta,da)
*****

write(*,*) 'final fit param'
write(*,*) a
write(*,*) 'final chi squared and change'
write(*,*) chisq, chisq-inichi

write(16,*) 'covariance matrix'
do n=1,nca
  write(16,*) covar(n,1:nca)
enddo

write(16,*) 'final fit param'
write(16,*) a
write(16,*) 'final chi squared and change'
write(16,*) chisq, chisq-inichi

DEALLOCATE(x)
DEALLOCATE(y)
DEALLOCATE(sig)
DEALLOCATE(a)
DEALLOCATE(ia)
DEALLOCATE(covar)
DEALLOCATE(alpha)
DEALLOCATE(atry)
DEALLOCATE(beta)
DEALLOCATE(da)

c   thats 10 down

close(16)
c   close(19)

END

*****
*****
*****
C Levenberg-Marquard non-linear chi squared minimization routine
C based on the algorithm and code from Numerical Recipes (J-M's copy)

C The major fitting function. Has initialization (alamda < 0), iteration (alamda = 0),
c and finalization (alamda = 0) modes

C In Detail:
c Initialization: (initializes, runs zeeman, gets 1st chi^2 and derivatives)
c   sets mfit and alamda
c   calls mrqcof getting alpha beta and chisq (with inital parameters)
c   sets ochisq to chisq and atry to a
c   goes straight to the first real iteration
c Iteration: (uses derivatives to guss next a, runs zeeman with next a, gets chi^2 and derivatives,
c             keeps them if good otherwise reverts to the last iteration)
c   sets covar to alpha (with an augmented diagonal) and da to beta
c   runs gaussj (gauss jordain elimination to solve for the next step)
c   sets the next attempt values atry
c   calls mrqcof getting alpha beta and chisq (with atry parameters)
c   if it's sucessfull shrink alamda, set alpha to covar, beta to da, a to atry, and ochisq to chisq
c   if not grow alamda
c Finalization: (calls covsrt to get the covariance matrix and mrqcof to get a final spectrum)
c   still sets covar to alpha (with an augmented diagonal) and da to beta
c   still runs gaussj (gauss jordain elimination to solve for the next step)
c   calls covsrt to reorganize covar into the covariance matrix
c   calls mrqcof (using atry) to get the final spectrum (no derivatives this time)

C   x(ndata), y(ndata), sig = input data with 1 sigma uncertainties. ndata long.

```

```

C   a(ma) initial input parameters.  ma long.  ia(ma) parameters to fit (1=fit, 0=leave)
C   covar(nca,nca) = covariance matrix, returned also used as a workspace for alpha.
C   alpha(nca,nca) = modified curvature | Hessian matrix, eq 15.5.11, returned.
C   nca size of covar and alpha, >= ma, must be given.
C   chisq = chi squared.  alamda = new 'lamda', adjust the importance
C   of the diagonal elements in " a' ", alters our next pt guss.  Must be < 0 on first call
C   Must be = 0 for final evaluation, otherwise use what was returned.

SUBROUTINE mrqmin(x,y,sig,ndata,a,ia,ma,covar,alpha,nca,chisq,
1   alamda,fnCall,contcut, atry,beta,da)

IMPLICIT NONE

integer ma,nca,ndata,ia(ma),fnCall
c   ia = things to fit for (!= 0) ndata=size of data to fit,
c   ma = # param, nca (>= ma), fnCall mostly just perserved for fun (counts zeeman calls)
real alamda,chisq, a(ma), alpha(nca,nca), covar(nca,nca),
1   sig(ndata), x(ndata), y(ndata), contcut
c   alamda = change in lamda (or flag) chisq=obvious,
c   a = input param, alpha = eq15.5.11, covar = covariance matrix,
c   sig = uncertainties, x,y = data points
integer j,k,l,m,mfit
c   mfit = number of parameters were fitting <= ma
real ochisq, atry(ma), beta(ma), da(ma)
c   beta = eq 15.5.8, atry = temporary a, da = temporary beta
c   SAVE ochisq, atry, beta, da, mfit (numerical recipies used this with fixed length arrays)
SAVE ochisq, mfit
c   dummy, dummy2: just used to hold the output of the funcs subroutine
real dummy(ndata), dummy2(ndata,ma)

C   Initialization - use alamda < 0
C   normaly alamda is used to return the suggested change to the input parameters a

if(alamda .lt. 0.0)then
  mfit = 0.0
  do j=1, ma
    if (ia(j).ne.0) mfit=mfit+1
  enddo
c   set initial alamda value
  alamda = 0.001

*****
  call mrqcof(x,y,sig,ndata,a,ia,ma,alpha,beta,nca,chisq,
1   fnCall,alamda,contcut)
*****

  ochisq = chisq
  do j=1,ma
    atry(j)=a(j)
  enddo
  write(*,*) 'Iteration: 2'
  write(16,*) 'Iteration: 2'
endif

C   set up the covar matrix as the altered linearized fitting matrix
j=0
do l=1,ma
  if(ia(l).ne.0) then
    j=j+1
    k=0
    do m=1,ma
      if(ia(m).ne.0)then
        k=k+1
c   set the simple/standard elements
        covar(j,k)=alpha(j,k)
      endif
    enddo
c   set the (augmented) diagonal elements
    covar(j,j)=alpha(j,j)*(1.0+alamda)
    da(j)=beta(j)
  endif
enddo

```

```

        endif
    enddo

*****
    call gaussj(covar,mfit,nca,da,1,1)
c    find the matix solution (via Gauss Jordan Elimination)
*****

C    once converged evaluate once more and return the results
    if(alamda.eq.0.0)then

*****
        call covsrt(covar,nca,ma,ia,mfit)
*****
c    and make a pretty output
*****
        call funcs(x, a, ia, dummy, dummy2, ma, ndata,fnCall,alamda)
*****
    return
endif

C    did this iteration improve chi squared? ...
    j=0
    do l=1,ma
        if(ia(l).ne.0) then
            j=j+1
            atry(l)=a(l)+da(j)
        endif
    enddo
*****
    call mrqcof(x,y,sig,ndata,atry,ia,ma,covar,da,nca,chisq,
    1    fnCall,alamda,contcut)
*****

C    if so then accept the improved solution
    if(chisq.lt.ochisq)then
c    tighten alamda (default: multiply by 0.1)
        alamda=0.1*alamda
        ochisq=chisq
c    set alpha to the improved (covar) values
        j=0
        do l=1,ma
            if(ia(l).ne.0)then
                j=j+1
                k=0
                do m=1,ma
                    if(ia(l).ne.0)then
                        k=k+1
                        alpha(j,k)=covar(j,k)
                    endif
                enddo
c    accept the da (beta) and atry (a) values
                beta(j) = da(j)
                a(l) = atry(l)
            endif
        enddo
c    if not then increase alamda and leave the old best values
        else
            alamda = 10.0*alamda
c    chisq=ochisq
        endif

    return
END

```

```
*****
```

```

*****
*****
C mrqcof Evaluates the linearized fitting matrix alpha and the vector beta (eq 15.5.8)
C and calculates chi squared. Takes: x, y, sig, ndata, a, ia, ma, nalp, fnCall, alambda
C Returns alpha beta, chisq, fnCall (just passed from funcs)
C Same variable names used as in mrqmin, except nalp = nca
C and in one instance atry = a, covar = alpha, da = beta

C More explicitly it:
c   initialized alpha, beta and chisq to 0
c   calls funcs - the zeeman interface function
c   for calculated points != 0 and observed points > conlvl
c   add to the sum over all points for alpha beta and chisq

      SUBROUTINE mrqcof(x,y,sig,ndata,a,ia,ma,alpha,beta,nalp,
1      chisq,fnCall,alamda,contcut)

      IMPLICIT NONE

      integer ma, nalp, ndata, ia(ma),fnCall
c   ia = things to fit for (!= 0), ndata=size of data to fit,
c   ma = # param, nalp (>= ma), fnCall mostly just perserved for fun (counts zeeman calls)
      real chisq, a(ma), alpha(nalp,nalp), beta(ma), sig(ndata),
1      x(ndata), y(ndata), alambda, contcut
c   chisq=obvious, a = input param, alpha = eq15.5.11 ,beta = eq 15.5.8
c   sig = uncertainties, x,y = data points, alambda = here only flag for finalization (0.0=end)

      integer mfit, i, j, k, l, m
c   mfit = number of parameters were fitting <= ma
      real dy, sig2i, wt, ymod(ndata), dyda(ndata,ma), conlvl
c   dyda was MMAX long but MMAX has to be ma for this to work so I tried to make life eaiser

c   set mfit
      mfit = 0
      do j=1,ma
         if(ia(j).ne.0) mfit = mfit+1
      enddo
c   initialize (1/2 of symmetric) alpha and beta
      do j=1,mfit
         do k=1,j
            alpha(j,k)=0.0
         enddo
         beta(j)=0.0
      enddo
      chisq = 0.0

*****
      call funcs(x, a, ia, ymod, dyda, ma, ndata,fnCall,alamda)
C   zeeman calling function.
*****
cccccccccccccccccccccccccccccccccccccccccccccccccccccccccccc
      open(19, file="dump.dat", status='unknown')
cccccccccccccccccccccccccccccccccccccccccccccccccccccccccccc
c   Summation loop over all data
      do i=1,ndata
c   Only use points for which we have a calculated y
         if( (ymod(i).ne.0.0).and.(y(i).lt.contcut) )then
c   if(ymod(i).ne.0.0)then

c   set sig2i (sigma squared inverse) to 1/sigma^2
            sig2i = 1.0/(sig(i)*sig(i))
c   find the diff between obs and calc
            dy=y(i)-ymod(i)

C   calculate the new alpha and beta
            j=0
            do l=1,ma
               if(ia(l).ne.0)then
                  j=j+1
c   set the 'weighting' of this point: (1/sigma^2)*(dy/da_j)
                  wt=dyda(i,l)*sig2i

```



```

        if(ipiv(k).eq.0)then
c         if we have the biggest number yet the it's a good candidate, keep it
            if(abs(a(j,k)).ge.big)then
                big = abs(a(j,k))
                irow = j
                icol = k
            endif
            else if (ipiv(k).gt.1)then
                write(*,*) 'singular matrix in gaussj [1]'
                write(16,*) 'singular matrix in gaussj [1]'
c         error trapping. bad input?
            endif
        enddo
    endif
enddo

    ipiv(icol)=ipiv(icol)+1

c     Now we have a good pivot element we can interchange rows, if needed,
c     to put the pivot element on the diagonal. This is done by relabeling.
c     indxc(i), the column of the ith pivot element, is the ith column reduced,
c     while indxr(i) is the row in which that pivot element was originally located.
c     If indxc(i) != indxr(i) then there is an implied column interchange.
c     Thus the solution b's will end up in the correct order but the inverse
c     matrix will be scrawled by columns

        if (irow.ne.icol) then
            do l=1,n
                dum = a(irow,l)
                a(irow,l) = a(icol,l)
                a(icol,l) = dum
            enddo
            do l=1,m
                dum=b(irow,l)
                b(irow,l) = b(icol,l)
                b(icol,l) = dum
            enddo
        endif
c     Now we devide the pivot row by the pivot element (point at irow, icol) renormalizing
        indxr(i) = irow
        indxc(i) = icol
        if(a(icol,icol).eq.0.0) then
c     error trapping. bad input?
            write(*,*) 'singular matrix in gaussj [2]'
            write(16,*) 'singular matrix in gaussj [2]'
        endif
        pivinv = 1.0/a(icol,icol)
        a(icol,icol)=1.0
        do l=1,n
            a(icol,l)=a(icol,l)*pivinv
        enddo
        do l=1,m
            b(icol,l)=b(icol,l)*pivinv
        enddo
c     Now reduce the rows, except for the pivot row
        do ll=1,n
            if(ll.ne.icol)then
                dum=a(ll,icol)
                a(ll,icol)=0.0
                do l=1,n
                    a(ll,l)=a(ll,l)-a(icol,l)*dum
                enddo
                do l=1,m
                    b(ll,l)=b(ll,l)-b(icol,l)*dum
                enddo
            endif
        enddo
    enddo
enddo
c     end of the major loop over columns
c     now we just need to unscrawle the solution
c     interchange pairs of columns in the reverse order
do l=n,1,-1
    if(indxr(l).ne.indxc(l))then

```

```

      do k=1,n
        dum=a(k,indxr(1))
        a(k,indxr(1))=a(k,indxc(1))
        a(k,indxc(1))=dum
      enddo
    endif
  enddo

  return
END

```

```

*****
*****
*****

```

C covsrt Propogates the proper order of entries in back into the full ma X ma
 C covariance matrix 'covar'. Only really necessary to enshure proper output.
 C not important to me as I don't really care about the covariance of the input
 C parameters for zeeman (at least not now).

```

      SUBROUTINE covsrt(covar, npc, ma, ia, mfit)

```

```

C   covar = the covariance matrix (output) npc X npc large, npc = size of covar,
C   ma = size of ia (and a), ia = which parameters are free (1|0),
C   mfit = # of param to be fit

```

```

      IMPLICIT NONE

```

```

      integer ma, mfit, npc, ia(ma)
      real covar(npc,npc)

```

```

      integer i, j, k
      real swap

```

```

c   set unused elements of covar to 0
      do i = mfit+1,ma
        do j=1,i
          covar(i,j)=0
          covar(j,i)=0
        enddo
      enddo

```

```

c   interchange the non-zero elements of covar to give the right order
      k=mfit
      do j = ma,1,-1
        if(ia(j).ne.0)then
          do i=1,ma
            swap = covar(i,k)
            covar(i,k)=covar(i,j)
            covar(i,j)=swap
          enddo
          do i=1, ma
            swap = covar(k,j)
            covar(k,i)=covar(j,i)
            covar(j,i)=swap
          enddo
          k=k-1
        endif
      enddo
c   c'est tout
      return
END

```

```

*****
*****
*****
c   THE (zeeman) FUNCTION SUBROUTINE: funcs(x, a, ymod, dyda, ma, ndata)

```

```

*****
*****
*****

c   Definition of parameters in a(n) and ia(n):
c   n=1 => radial velocity (m/s)
c   n=2 => vsini (cm/s)
c   n=3 => micro turbulence (cm/s)
c   n=i (i=4,6,8,...) => atomic number
c   n=i+1 abundance for atom # in n=i

      SUBROUTINE funcs(x,a,ia,y,dyda,na,ndata,fnCall,alamda)
C     takes arrays: x, a, ia, real: alamda, and ints: na, ndata, fnCall
C     returns arrays y (for the corresponding x), and dyda (for the corresponding y and a)
      IMPLICIT NONE

      integer na, ndata
      real x(ndata), y(ndata), a(na), dyda(ndata,na), alamda
      integer ia(na)
c     here alamda = only a flag for finalization (0.0 = end)

      integer nWindows, fnCall, chkdyda
      real xt(ndata), yt(ndata), at(na), epsilon, epsilonE, epsilonV

      integer i,j,k,l

      nWindows = 0

c     the small _fractional_ shift in a parameter for it's numerical derivative
c     may need to be changed depending on the parameter's size and stability (this assumes ~1)
      epsilon = 0.02
c     elements specific epsilon (absolute)
      epsilonE = 0.05
c     velocities specific epsilon (absolute)
      epsilonV = 0.5E5

c     First check if inputs are in rage (-1..-13 dex in abundance)
c     If it's not then put it back in range and complaine.

      do i=5,na,2
        if(a(i).gt.-1.0)then
          write(*,231) i, a(i)
          write(16,231) i, a(i)
          a(i) = -1.0
        else if(a(i).lt.-13.0)then
          write(*,232) i, a(i)
          write(16,232) i, a(i)
          a(i) = -13.0
        endif
      enddo
231 format('ERROR: parameter ',I3,' too large: ',F9.4,
2       ' setting to -1.0')
232 format('ERROR: parameter ',I3,' too small: ',F9.4,
2       ' setting to -13.0')

c     And make sure microturbulence is >= 0
      if( (ia(3).ne.0) .and. (a(3).lt.0.0) )then
        write(*,233) a(3)
        write(16,233) a(3)
        a(3) = 0.0
      endif
233 format('ERROR: parameter 3 too small: ',E10.3,' setting to 0.0')

c     Setup, Run, and Read the results of Zeeman

*****
      call rewriter(a ,ia, na, nWindows)
c     write this iteration into zeeman's input file
c     currently an external file: rewriter.f
*****
*****

```

```

        call ZeeModel()
c      an external file, currently: z2.1v2mod1b-sub.f
*****
*****
        call interp(x, y, ndata, nWindows)
c      read zeeman's output and interpolate linearly
*****

        fnCall = fnCall+1
        write(*,226) fnCall
        write(*,*)
        write(16,226) fnCall
226  format('Function Calls:'I4)

c      Now we have the calculated y vales we need the derivatives
c      (done numericaly) (if we're not on the finalization call)

        if(alamda.ne.0.0)then
c      first back up the input parameters
        do i=1,na
            at(i) = a(i)
        enddo

c      then adjust each parameter in turn to find the change
        do i=1,na

            if(ia(i).ne.0)then

                if(i.le.3) then
                    epsilon = epsilonV
                else
                    epsilon = epsilonE
                endif

c                at(i) = at(i)+epsilon*a(i)
                at(i) = at(i)+epsilon

c      Now we need to evaluate the function again
*****
                call rewriter(at ,ia, na, nWindows)
c      write this iteration into zeeman's input file
c      currently an external file: rewriter.f
*****
*****
                call ZeeModel()
c      an external file, currently: z2.1v2mod1b-sub.f
*****
*****
                call interp(x, yt, ndata, nWindows)
c      read zeeman's output and interpolate linearly
*****

                fnCall = fnCall+1
                write(*,226) fnCall
                write(*,*)
                write(16,226) fnCall

                chkdyda=0
                do j=1,ndata
c                dyda(j,i) = (yt(j)-y(j))/(epsilon*a(i))
                dyda(j,i) = (yt(j)-y(j))/(epsilon)

                    if( abs(dyda(j,i)).gt.0.0)then
                        chkdyda=1
                    endif
                enddo

c      Simple error traping. If dyda has a row of 0s then there will be a error
c      (devide by 0) in the gauss jordan elimination subroutine. (better to catch it now)

```

```

                if(chkdyda.eq.0)then
                  write(*,230) i
                  write(16,230) i
                endif
230      format("Error: derivative of chi^2 wrt a = 0 for paramete
*r: ", I3)

                at(i) = a(i)

                endif
            enddo
        endif

        return
    END

*****
*****
*****
c      THE interp SUB-SUBROUTINE
c      reads and interpolates zeeman output files. Given a set of x values (observations)
c      the associated y values are calculated useing linear interpolation

C      Currently this assumes that the observed data is longer then the calculated (in wavelength)
C      Cannot currently deal with overlap in the observed spectrum
C      (asumes each line is at a > lambda then the last)
C      When there is overlap in the calculated windows it takes the second
C      (overwrites the 1st in the overlap reigon)
C      For points at observed wavelengths (x) where there is no calculated y value 1.0 is returned
C      (ie. the results are padded out to the observed spectrum length with 1.0s)

SUBROUTINE interp(x, y, ndata, nWindows)

IMPLICIT NONE

integer ndata, nWindows
real x(ndata), y(ndata)
c      x, y = observed values

c      the number of lines in one synthetic window
c      assume 15 A window length with a resolution of 0.01 A
c      this gives 1500 (+1) lines (ignore the last (the +1) line)
integer ncalc
PARAMETER(ncalc = 1501)

real xt(ncalc), yt(ncalc)
c      xt, yt = calculated x and y
integer i,j,k,l

character(5) fn1(40)
data fn1 /'.w01','.w02','.w03','.w04','.w05','.w06',
1      '.w07','.w08','.w09',
2      '.w10','.w11','.w12','.w13','.w14','.w15',
1      '.w16','.w17','.w18','.w19',
2      '.w20','.w21','.w22','.w23','.w24','.w25',
1      '.w26','.w27','.w28','.w29',
2      '.w30','.w31','.w32','.w33','.w34','.w35',
1      '.w36','.w37','.w38','.w39','.w40'/

c      initialize y to 0.0
do i=1,ndata
    y(i) = 0.0
enddo

c      first loop over all Zeeman's output files
do i=1,nWindows
    open(25,FILE=fn1(i) //'p01',STATUS='OLD')
c      read this output file

```

```

        do j=1,ncalc
          read(25,225) xt(j), yt(j)
        enddo
c      and close it before I forget
        close(25)

c      now we need to interpolate between calculated points to get the
c      appropriate value for the observed x point
c      (done in a somewhat simplistic & inflexible fashion) (I should improve this!)

        k=0
        l=0
c      so loop over all the x's we want a y for
        do j=1,ndata
c      find the first appropriate calculated point (if we haven't yet)
          if( (x(j).gt.xt(1)).and.(k.eq.0) )then
            k=1
c      (simple linear interpolation)
            y(j) = (yt(2)-yt(1) )*(x(j)-xt(1) )
1          / (xt(2)-xt(1) )+yt(1)

c      if we have previously found the first point and we haven't run out of cacluated points
          elseif( (k.gt.0).and.(l.le.(ncalc-1)) )then
c      scroll along to the next appropriate cacluated point (or stop when we run out)
            do while( (xt(1).lt.x(j)).and.(l.le.(ncalc-1)) )
              l=l+1
            enddo

c      if we haven't run out then use it
            if(l.le.(ncalc-1))then
              k=k+1

1          y(j) = (yt(l)-yt(l-1) )*(x(j)-xt(l-1) )
              / (xt(l)-xt(l-1) )+yt(l-1)
            endif
          endif

        enddo

        enddo

225 format(f10.4, f20.10)

        return
        END

```

B.3.2 ZEEMAN2 Input and Output: rewriter.f

The rewriter.f file, containing the input formatting for ZEEMAN2.

```

SUBROUTINE rewriter(a ,ia, na, nWindows)

IMPLICIT NONE

C edits the inzmodel.dat file
C available parameters for editing: vsini, abundances (elements must exist allredy)

integer MaxWindows
c the maximum number of windows allowed in inzemodle.dat
PARAMETER(MaxWindows = 40)

integer na, nWindows
real a(na)
integer ia(na)

```

```

integer i, j, k, nLines(MaxWindows), nEle
real vsini, vmic, abun(103,28)
character(26) comment

c unused but read in
double precision WLO(MaxWindows), ALINLS(103,14,40),
1 DPWL(103,40),rlland(103,40),ruland(103,40),FW,renorm,PHASE,
2 RAID, tau0l(103), tau0u(103), delta_abun(103), frh,frhe,
3 AMASS(100),T(100),RNE(100),RNATK(100),RHO(100),
4 BETAD,BPDD,ADD,BQ,BOCT,razang
integer KPL,NPHAS,NOBS,isflag(103,40,4), MU

OPEN(15,FILE='./data/inzmodel.dat',STATUS='OLD')

C PART 1: READ IN THE FILE

READ(15,115) nWindows
115 FORMAT(I4)
c the line list
do i=1, nWindows

READ(15,120) nLines(i),WLO(i)
120 FORMAT(I4,F10.3)

do j=1, nLines(i)
READ(15,130)(ALINLS(j,K,i),K=1,2),DPWL(j,i),
1 (ALINLS(j,K,i),K=4,14),rlland(j,i),ruland(j,i)
130 FORMAT(2F3.0,F10.4,6F4.1,F7.3,F10.3,3E10.3,2f6.3)
enddo

enddo

c # of phases, # observations??, instrumental profile, and renormalization
READ(15,151) NPHAS,NOBS,FW,renorm
151 FORMAT(2I4,2F10.0)

do i=1, nWindows
DO j=1,NPHAS
c phase and stokes flags for I, V, Q, U
READ(15,153) PHASE,(isflag(j,i,K),K=1,4)
153 FORMAT(F10.3,4I4)
ENDDO
enddo

c Read in 'RAID' (inclination angle of rotation axis to line of sight
c always 90 so far),
c vsini, microturbulence, and KPL (a flag for 'which intensity profile to plot',
c always -1) seems to be vestigial
READ(15,150) RAID,vsini,vmic,KPL
150 FORMAT(F10.0,24X,2E10.1,I4)

c Read in BETAD (angle between magnetic and rotation axes (usually 90)),
c BTDD (dipole magnetic field strength), ADD 'decentering parameter' for the dipole
c BQ (quadrupole field strength), BOCT (octupole strength)('co-linear with the rest),
c razang ('position angle of rotation axis projected on the sky')
READ(15,160) BETAD,BPDD,ADD,BQ,BOCT,razang
160 FORMAT(6F10.0)

c uncertainty here here, except for the 1st entry is the number of elements
READ(15,170) nEle
170 format(i4)

C Read In The Elements
do i=1,nEle
c in abun: 1 = element, 2 = ???, 3 = abundance!
READ(15,180) (abun(i,J),J=1,9),tau0l(i),tau0u(i),delta_abun(i)
180 FORMAT(F2.0,11F8.0)

enddo

c read the header for the modle atmosphere
c MU = # layers, comment = the original file
READ(15,101) MU,frh,frhe, comment
101 FORMAT(I2,F9.3,f13.3,A25)

```

```

C   The Model Atmosphere
do i=1,MU
  READ(15,110) AMASS(i),T(i),RNE(i),RNATK(i),RHO(i)
110  FORMAT(E16.9,1X,F9.0,1X,3(E12.6,1X))
enddo

C PART 2: EDIT VAULES
c   x only if the parameter is set to be fittable right now x
c   x otherwise we leave that line alone x
c   write all parameters with values in 'inlma.dat'

c   Change the vsini
c   if(ia(2) .ne. 0)then
vsini = a(2)
c   endif
c   Change the microturbulance
c   if(ia(3) .ne. 0)then
vmic = a(3)
c   endif
c   Change the element abundance
do i=1,nEle
  do j=4,na-1,2
c   if( (ia(j+1) .ne.0) .and.(a(j) .eq.abun(i,1)) )then
  if( a(j) .eq.abun(i,1) )then
    abun(i,3) = a(j+1)
  endif
enddo
enddo

C PART 3: WRITE THE FILE

REWIND(15)

WRITE(15,115) nWindows

do i=1, nWindows

  WRITE(15,121) nLines(i),WLO(i)
121  FORMAT(I4,F8.2)

c   The Line List
do j=1, nLines(i)

  WRITE(15,131) int(ALINLS(j,1,i)), int(ALINLS(j,2,i)),
1  DPWL(j,i), (ALINLS(j,K,i),K=4,14),rlland(j,i),ruland(j,i)
131  FORMAT(2I3,F10.4,6F4.1,F7.3,F10.3,3E10.3,2f6.3)

enddo

enddo

WRITE(15,152) NPHAS,NOBS,FW,renorm
152  FORMAT(I3,I4,F11.5, F7.2,1X)

do i=1, nWindows
  DO j=1,NPHAS
c   phase and stokes flags for I, V, Q, U
c   also ignored
  WRITE(15,154) PHASE,(isflag(j,i,K),K=1,4)
154  FORMAT(F8.3,4I4,1x)
  ENDDO
enddo

WRITE(15,155) RAID, 0.0, 2 ,0.0, vsini/1E5, vmic/1E5, KPL
155  FORMAT(F8.1,F10.2,I4,F10.2,2X,F6.1,'E+05',F6.1,'E+05',I4)

c   write the magnetic field parameters.
write(15,161) BETAD,BPDD,ADD,BQ,BOCT,razang
161  FORMAT(F8.1, 2X, SPF9.0, 1X, SF7.1, 3x, SPF10.1, F10.1, SF9.2)

```

```
c    got lazy here. No Idea what any of these are exopt for nEle
    write(15,171) nEle
171  format(i2," 0.001  00 1 1      ")

c    The Elements
    do i=1,nEle

        write(15,181) int(abun(i,1)),(abun(i,J),J=2,9),tau01(i),
1      tau0u(i),delta_abun(i)
181  FORMAT(I2,7F8.3,F8.2,2F8.3,SPF8.1)

    enddo

    WRITE(15,101) MU,frh,frhe,comment

C    The Model Atmosphere
    do i=1,MU
        WRITE(15,112) AMASS(i),T(i),RNE(i),RNATK(i),RHO(i)
112  FORMAT(ES16.9,' ',F8.1,' ',3(ES12.5,' '))
    enddo

    close(15)

111  format(1X)
    END
```